LATERAL DISTRIBUTION OF COSMIC RAY MUONS UNDERGROUND:

Results from the CosmoALEPH Experiment

DISSERTATION
zur Erlangung des Grades eines Doctors
der Naturwissenschaften

vorgelegt von
M.Sc.in Physics Rodica Tcaciuc
geb. am 08.07.1976 in Moldawien

genemight vom Fachbereich Physik
der Universität Siegen
Siegen 2006

LATERAL DISTRIBUTION OF COSMIC RAY MUONS UNDERGROUND:
Results from the CosmoALEPH Experiment

Rodica Tcaciuc

genehmigte

DISSERTATION
zur Erlangung des Grades eines Doctors
der Naturwissenschaften

1. Gutachter: Prof. Dr. Claus Grupen
2. Gutachter: Prof. Dr. Michael Schmelling

Tag der mündlichen Prüfung: 04.12.2006

ZUSAMMENFASSUNG

LATERALVERTEILUNG KOSMISCHER MYONEN UNTER DER ERDE: Ergebnisse des CosmoALEPH Experiments

Rodica Tcaciuc

Betreuung: Prof. Dr. Claus Grupen

Das CosmoALEPH Experiment am LEP e^+e^- Speicherring am CERN ist in einer Tiefe von 320 Metern Wasser Äquivalent installiert. Es wurde benutzt, um die chemische Zusammensetzung der primären kosmischen Strahlung bis zu Energien von 10 PeV aus den Daten hochenergetischer Myonen abzuleiten. Diese Myonen wurden in ausgedehnten Luftschauern ausgelöst durch Wechselwirkungen primärer Kerne in der Atmosphäre erzeugt. Die Zeit-Projections-Kammer (TPC) und das Hadron Kalorimeter (HCAL) des ALEPH Detectors und sechs Szintillatorstationen mit Abständen bis 1 km wurden benutzt, um die Dekohärenzkurve, die Multiplizität und die Transversalimpulsverteilung hochenergetischer Myonen zu bestimmen.

Die experimentellen Daten wurden mit Vorhersagen verschiedener Monte Carlo Modelle (MC) verglichen.

Aus dem Vergleich der gemessenen Dekohärenzkurve mit MC Vorhersagen für primäre Proton-, Helium- und Eisenkerne wurde auf der Basis des VENUS Modells eine Häufigkeit von (77 ± 11) % Protonen und (23 ± 11) % Eisen mit einer χ^2 - Wahrscheinlichkeit von 84 % bestimmt.

Die Dekohärenzkurve, unter Berücksichtigung der Korrelationen führt zu einer Häufigkeit von (88 ± 8) % Proton- und (12 ± 8) % Eisen Kernen bei einer χ^2 - Wahrscheinlichkeit von 53 %.

Der Vergleich zwischen den Multiplizitäts- und Transversalimpulsverteilungen mit MC Modellen führt ebenfalls zu einer Proton-Helium Dominanz.

Die Ergebnisse bezüglich der Häufigkeit der chemischen Elemente in der primären kosmischer Strahlung bis zu 10 PeV sind in Übereinstimung mit den Ergebnissen anderer Experimente.

ABSTRACT

LATERAL DISTRIBUTION OF COSMIC RAY MUONS UNDERGROUND: Results from the CosmoALEPH Experiment

Rodica Tcaciuc

Thesis Supervisor: Prof. Dr. Claus Grupen

The CosmoALEPH experiment, located underground at the LEP e^+e^- storage ring at CERN at a depth of 320 m water equivalent, was used to study the chemical composition of primary cosmic rays up to 10 PeV energies from the measurement of high energy muons, created in extensive air showers by interactions of primary nuclei in the atmosphere.

The Time Projection Chamber (TPC) and the Hadron Calorimeter of the ALEPH detector and six scintillator stations located at distances up to 1 km from each other were used to analyse the decoherence curve, multiplicity and transverse momentum distributions of energetic cosmic muons.

The experimental data were compared with predictions from different Monte Carlo (MC) models and mass composition approaches.

From a comparison between the measured decoherence distribution with CosmoALEPH and the MC predicted decoherence curves for proton, helium and iron, a primary composition of (77 ± 11) % protons and (23 ± 11) % iron nuclei with a χ^2 - probability of 84 % was determined, based on the predictions of the VENUS model with the constant mass composition approach. The analysis of the decoherence curve, with consideration of correlations between the measured CosmoALEPH parameters, leads to a composition of (88 ± 8) % protons and (12 ± 8) % iron nuclei for cosmic rays with a χ^2 - probability of 53 %.

The absolute comparison between the measured multiplicity and transverse momentum distributions in the TPC and those predicted by different Monte Carlo models results also in a dominant light composition. The experimental data are in a good agreement with MC data lying between proton and helium primaries.

The results obtained for the primary composition of cosmic rays up to the *knee* region are consistent with the results from other experiments.

Acknowledgements

First and foremost, I would like to thank Prof. Dr. Claus Grupen for the possibility to join his team for my PhD research, for guidance, advise, kindness and financial support he has provided during my student years.

Secondly, I would like to address many thanks to Prof. Dr. Michael Schmelling and Dr. Anke-Susane Müller for their interest and efforts, many ideas and a constant help during many stages of the analysis in my thesis.

Special thanks I would like to address Prof. Dr. Arif Mailov for his support, patience with my multitudes of questions, and great help through the whole timeframe of this thesis.

I also thank all CosmoALEPH collaboration members, who made possible the data taking during six years and a lot of collaboration meetings with fruitful presentations and discussions of the analysed results.

I would like to thank Prof. Dr. Buchholz and his team for the constant support in the computing problems, being able to perform all simulations needed for my research, for help and good time.

I thank also the support group of the CORSIKA program, namely Dr. Dieter Heck and Dr. Tanguy Pierog who helped to solve the problems of installation and running the software used for my Monte Carlo simulations.

I would like to address very many thanks to my whole family. I am especially grateful to my mother, my mother-in-law and my sister Silvia, who have provided a consistent support and loving care to my children during the time of my study.

Finally, this thesis would not have been possible without the patience and support of my husband Sergiu, and my wonderful sons Stefan and Dorian. Their love, encouragement and inspirations motivated me to daily hard work which resulted in this final document.

Contents

INTRODUCTION

Cosmic rays, discovered nearly a hundred years ago, are a phenomenon of the Nature and their origin is still uncertain. They come from outside of the Earth, may come from outside the Solar System, but mostly from within the galaxy. In general, the principal sources of cosmic rays are considered to be the Sun and other stars, supernovas and their remnants, pulsars, centers of active galactic nuclei and black holes.

First thoughts about the existence of cosmic rays came during the golden days of research in radioactivity. Sensitive instruments recorded radiation even when there was no radium or uranium nearby, and soon it was found that this new radiation did not originate from the Earth but came from somewhere outside. The austrian physicist Victor Hess made balloon flights in 1911 and observed a more intense radiation at high altitudes than at sea level. He explained this as “an extra-terrestrial source of penetrating radiation”. In 1936 he was awarded the Nobel Prize for the discovery of cosmic rays [1]. The name of *cosmic rays* [2] was introduced by the american physicist Robert Millikan.

The indication that cosmic rays are charged particles appeared early, in the study of the influence of the Earth’s magnetic field on the cosmic ray intensity [3]. It was observed that at the Earth’s poles, primary cosmic rays penetrate deeper into the atmosphere as at the equator. Compared to photons, charged particles are deflected by the geomagnetic field. Protons and electrons can’t move across magnetic field lines very easily (at the equator they are incident predominantly perpendicular to the magnetic field lines). They are forced to spiral around the magnetic field lines (see figure 1) and enter into the atmosphere at Earth’s poles traveling parallel to magnetic field lines. Crowded magnetic field lines near the poles cause some particles of certain momenta to be reflected and to move back in the same direction from which they came. As a result these particles bounce back and forth from one pole of the Earth to the other and form the so called van Allen belts (regions of magnetically trapped high energy charged particles discovered by van Allen).

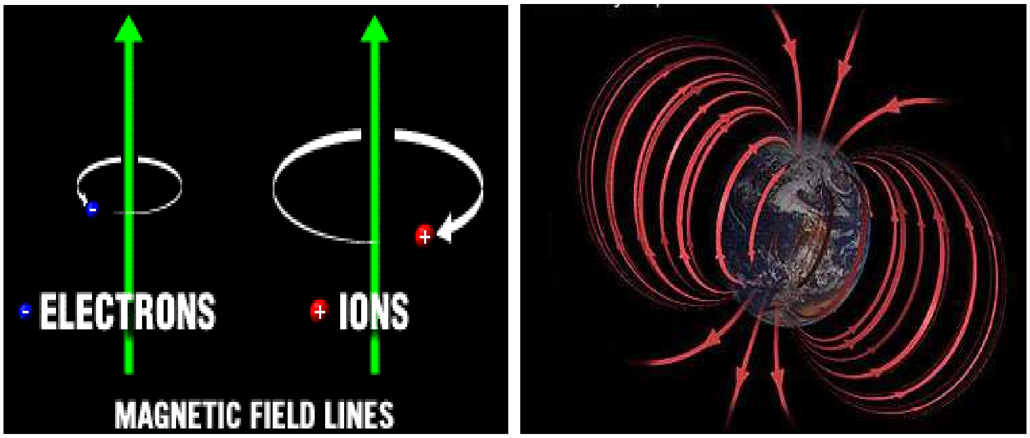

Figure 1: Effects of magnetic fields on charged particles. Electrons circle the field line in one direction, protons in the opposite direction [5].

Cosmic rays (CR) consist mostly of high-energy protons, with about nine percent helium and heavier nuclei and a small percentage of electrons and positrons.

The chemical composition of our universe reveals surprising particularities on the questions like: Why does the sun consist mostly of hydrogen and helium? Why is iron more abundant compared to heavy nuclei like gold? Why do these heavy nuclei exist at all and how are they produced? [4]

According to nuclear science, there is a dominance of even-Z elements in nature. This effect is associated with their nuclear stability. Relatively higher abundances of even-Z elements over odd-Z elements emphasize the importance of helium burning in sources of solar system material. Other stellar sources such as massive red giant stars (see figure 2) produce a variety of nuclei, some of which get accelerated and become galactic cosmic rays. It is considered that supernova explosions produce most of the heaviest cosmic ray nuclei.

Cosmic rays have a wide range of energies. Cosmic ray particles have been detected from the lower limit of a few GeV up to the energies exceeding 10^{20} eV. Experiments with combined ground based detectors, air fluorescence detectors and Cerenkov light detectors announced events with energies from 10^{18} eV up to more than 10^{20} eV (see Fly's Eye [6], AGASA [7], YAKUTSK [8], [9]).

On Earth, the highest energy that could be produced in an accelerator is of the order of 10^{12} eV at Fermilab's Tevatron and about 10^{13} eV at the

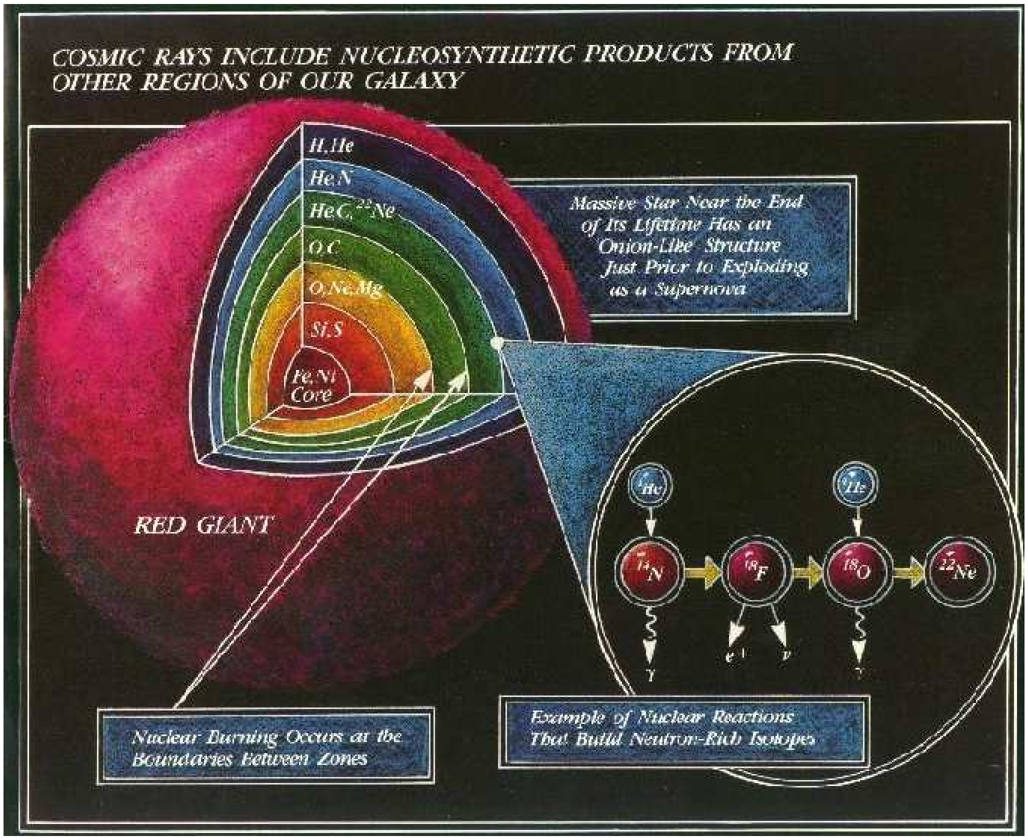

Figure 2: A massive red giant star [10].

proton-proton Large Hadron Collider at CERN in Geneva (for 2008, the planned proton-proton centre of mass energy of the collision is 14 TeV, equivalent to a laboratory energy in a fixed target experiment of 10^{17} eV).

In the known energy spectrum of primary cosmic rays are two clear signatures evident. A small spectral bend, the so-called *knee*, is seen near $5 \cdot 10^{15}$ eV. Experimental observations indicate a substantial decrease in the cosmic ray flux above this bend. Several models are proposed to explain this feature, the details are still in debate. Another spectral bend is seen near $3 \cdot 10^{18}$ eV, called the *ankle*, where the spectrum turns up again. Primary particles up to the knee are thought to be of galactic origin, up to the ankle and beyond the ankle it seems they may be to a certain extent extragalactic.

Cosmic rays continuously bombard the Earth and collide with air nuclei producing more particles (secondary particles) that can be detected throughout the atmosphere and sometimes deep underground. CR are studied using satellites and space probes, from balloons in the stratosphere, high-altitude airplanes and with giant detectors on and underneath the Earth's surface.

Cosmic rays represent also a natural source of relativistic particles that can be used to study the fundamental interactions of matter. Direct observations of primary and secondary cosmic rays with balloon experiments and ground detectors have led to the discovery of the e^+, $\pi^\pm$, $\mu^\pm$, $K^\pm$, K^0, Λ, Σ^+, and Ξ^- before the direct production of these particles at accelerators was possible. Due to the wide energy range (above 10^{20} eV), cosmic rays can provide information on partcle interactions at energies that may be never reproduced on Earth [11].

Many years after the discovery of cosmic rays in the beginning of the twentieth century, there are still unsolved problems. The knowledge of elemental composition and energy spectrum of primary cosmic rays may provide useful information about their sources, acceleration mechanisms, and their interaction characteristics in the galactic space.

Properties of high energy primary cosmic rays have to be deduced from reaction products, called Extensive Air Showers (EAS), which are formed within the atmosphere. Of great interest are energies above the TeV region which are inaccessible to direct observations due to the flux limitations. They can be investigated only indirectly by studying the properties of secondary particles produced in atmospheric cascades. Reconstruction of parameters like primary energy, direction and mass is not straightforward and it is only possible by comparison with accurate simulations of cosmic-ray induced air showers. Experiments at colliders have improved the understanding of nucleon-nucleon interactions at energies up to 1 PeV and allowed the development of reasonable models of the atmospheric cascade that reproduces the collider results as well as possible [12].

Objectives of the Thesis

This thesis is devoted to the studies of cosmic muons. These particles were discovered by Carl Anderson and Seth Neddermeyer in a cloud chamber in 1937 and were called muons. From their tracks it was estimated that they have the same unit of charge as electrons and a mass of 200 times the electron mass. Muons represent the most penetrating secondary charged particles produced in cosmic ray interactions in the atmosphere.

The muon content of EAS, due to their long range, carries a wealth of information about the shower development. The study of multi-muon events gives an insight into the primary cosmic ray composition and the physics of high energy hadronic interactions. The shape of the muon lateral distribution, which is dependent on the primary energy and mass composition [13], represents a conventional way to study the chemical composition of cosmic rays.

Many efforts are involved to investigate the observed *knee* above 10^{15} eV in the cosmic ray spectrum. Because the chemical composition of primary cosmic rays in this region can be determined just by indirect measurements, it is not a surprise that contradictory results are obtained for this feature. Thus, there is a lot of work yet to be done and the CosmoALEPH experiment contributes to this study. A Monte Carlo simulation of the number of muon coincidences underground at the CosmoALEPH level (muon separations up to 1 km), as function of the logarithm of primary energy for proton and iron primaries simulated with QGSJET (Quark Gluon String Jet) for energies from 1 TeV to 100 PeV, shows that CosmoALEPH is sensitive to a wide range of energies covering also the so called *knee* region (see Figure 3).

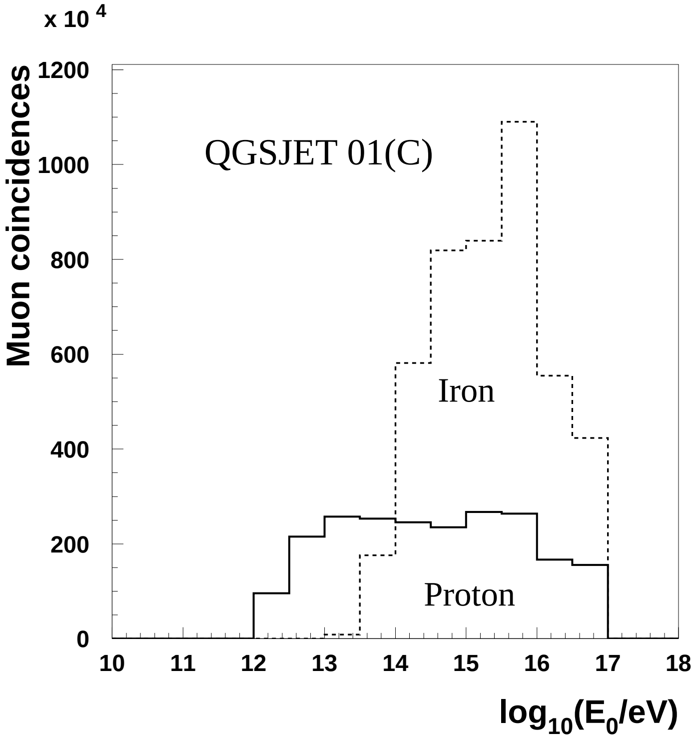

Figure 3: Sensitivity of the CosmoALEPH experiment to the cosmic ray energy spectrum.

The CosmoALEPH experiment consisted of the ALEPH detector and six scintillator stations installed underground, with distances up to 1 km between each other. The experiment was located at a depth of 320 meter water equivalent (mwe) at the e^+e^- storage ring LEP at CERN (see [14]) and offered interesting possibilities to detect and study single and multi-muon events underground.

The main aim of this work was to analyse:

- the muon lateral separation distribution (decoherence distribution) over distances of 1 km and to determine the chemical composition of primary cosmic rays
- the muon multiplicity and transverse momentum distributions to study the chemical composition and specific characteristics of the extensive air shower development.

For a quantitative comparison of the CosmoALEPH data with expectations from cosmic ray air showers simulations, a Monte Carlo (MC) was developed to study the decoherence distribution, muon multiplicity and transverse momentum distributions with different hadronic interaction models.

Extensive air showers initiated by high energy cosmic rays have been simulated using the MC CORSIKA program [87]. After the first interaction of primary nuclei in the atmosphere, only the hadronic component with hadrons decaying into muons was followed. The QGSJET, VENUS, SIBYLL and NEXUS high energy hadronic interaction models have been used [12]. Results of the simulations have been summarized in distributions of the multiplicity and transverse momentum, and a set of parameterizations which describe the lateral separations of muons for protons, helium and iron nuclei, for primary energies in the range from 170 GeV to 10 PeV and zenith angles varying from 0 to 89 degrees.

In the following chapter, the properties of cosmic rays are summarized. Chapters 2 and 3 describe the experimental setup and analysis of experimental data of the CosmoALEPH experiment. Monte Carlo interaction models used for simulations and the analysis of simulated data are introduced in Chapters 4 and 5. Chapter 6 contains results of the comparison of measured data with the CosmoALEPH experiment with predictions from different Monte Carlo models, followed by discussions about the evaluated chemical composition of primary cosmic rays from high energy cosmic muons.

Chapter 1

Properties of Cosmic Rays

1.1 The Measured Primary Energy Spectrum

The energy distribution of cosmic rays extends in an interval from a few GeV up to at least $3 \cdot 10^{20}$ eV [6]. For energies around 10 GeV, there is a flux of about 1 particle per cm^2 per second. Above 10^{20} eV it is expected to see about one particle per square kilometer in 100 years. Figure 1.1 shows the differential flux of all particles with different energies. From the shape of the energy spectrum we see that the number of particles per m^2 per second and per steradian decreases with increasing energy, proportionally to $E^{-\alpha}$:

$$\frac{dN}{dE} \sim E^{-\alpha}, \tag{1.1}$$

where E is the energy per nucleus, $\alpha(= \gamma + 1)$ is the differential spectral index of the cosmic ray flux and γ is the integral spectral index.

There is little variation in the spectral index of the energy spectrum up to 10^{15} eV with $\alpha = 2.7$. Then, the spectrum steepens up to 10^{19} eV where it has a value close to $\alpha = 3$. It can be assumed that these changes in α reflect the way of propagation of cosmic rays in the galaxy, different acceleration mechanisms and possibly additional energy losses.

According to different characteristics in the energy spectrum one can distinguish a few peculiarities:

- The change of the spectral index at about 4 PeV is called *knee*.
- A slight steepening around 400 PeV is called *second knee*. According to J.Hörandel [15], the two-knee structure is explained as a

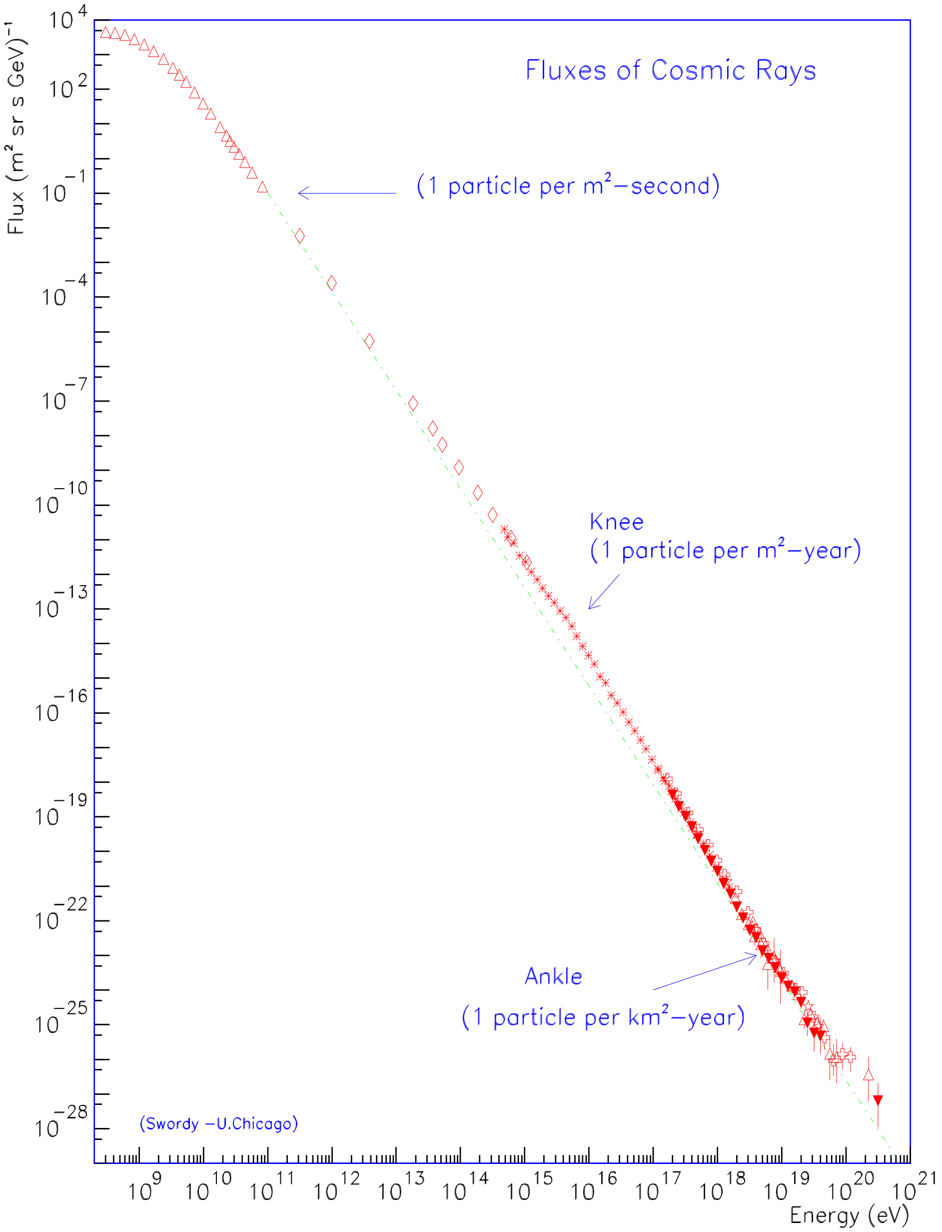

Figure 1.1: All-Particle-Spectrum, [16]

consequence of the all-particle spectrum being composed of individual spectra of elements with distinguished cut-offs. The first and most prominent *knee* is due to the subsequent cut-offs for all elements, starting with the proton component, and the *second knee* marks the end of the stable elements (Z = 92).

There are some reasonable hypotheses about the first *knee*. It is believed that in this region may be a less efficient acceleration mechanism of the cosmic rays in supernova shocks ("first order Fermi mechanism"), or a change in the propagation of cosmic rays from their source to the solar system is at work. The extrapolation of the "escape time" of cosmic rays from our galaxy to higher energies, according to $\tau_{esc} \sim E^{-\delta}$ with $\delta \approx 0.6$, breaks down at about $3 \cdot 10^{15}$ eV when $c \cdot \tau_{esc}$ approximates the value of the thickness of the galactic disc of ~ 300 *pc* [17] (1 $pc = 3.09 \cdot 10^{16}$ m, 1 light year = 0.3 pc).

Erlykin and Wolfendale [18] also support the theory of the knee origin from supernova remnants (SNR), but they propose this as a "single source" with an age of a SNR less than 10^5 years located in our Galaxy at 50 - 150 *pc* from our solar system.

Other theories assume a change of the hadronic interaction process. According to V.I.Yakovlev [19], above 10^{16} eV charmed particles, produced from the interaction of primary cosmic-ray particles in the atmosphere, play an important role. At sufficiently high energies, particles such as π and K mesons may interact in the atmosphere before decaying, with the result that short-lived particles may be produced. The unstable heavy charmed mesons (lifetime about 10^{-12} seconds) cannot be directly observed, because they decay very quickly. Their decay products (like "prompt" muons and neutrinos [20]) may be emitted with large transverse momenta at large angles from the incident direction, "demonstrating a seeming increase in the fraction of heavy mass primaries in cosmic radiation" [19].

An alternative picture of the interpretation of the knee proposed by Richard Wigmans [21] postulates the hypothesis "The change of the spectral index in the all-particle cosmic ray spectrum at an energy of ~ 3 PeV is caused by the onset of the reaction $p + \bar{\nu}_e \longrightarrow n + e^+$, which becomes energetically possible at this point". This process, that should take place for massive neutrinos of mass ~ 0.5 eV and energies of protons $E_p > \frac{1.695 \cdot 10^{15}}{m_\nu(eV)}$, would explain the light composition of cosmic rays up to the knee [17] and a heavier composition after the knee.

- The flattening at the highest energies around $3 \cdot 10^{18}$ eV is called *ankle* [22]. Up to the knee region, cosmic ray particles are thought to be of galactic origin and produced from supernova explosions. It is still unclear what physical processes accelerate particles to energies in the energy range from the knee to the ankle, although the ankle is sometimes interpreted as a crossover from a galactic to an extragalactic component.

  J. Wdowczyk and others [23], [22] suggest that cosmic rays above 10^{18} eV may be of extragalactic origin because of the large Larmor radii in the galactic magnetic field. A charged particle of charge q moving with velocity v in a magnetic field B will orbit around the magnetic field lines. The radius of this orbit is called the gyroradius, also known as the Larmor radius R_L:

  $$\frac{m \cdot v_\perp^2}{R_L} = q \cdot v_\perp \cdot B.$$

  The gyroradius is larger for faster or more massive particles and smaller for stronger magnetic fields.

  For highly relativistic particles of momentum P, the Larmor radii in the galactic magnetic field

  $$R_L = \frac{P}{q \cdot B}$$

  are too large to be contained in our Galaxy, which presents evidence that they originate from outside. At these energies, this may explain also the change in the chemical composition and in the slope of the spectrum. With increasing energy, the composition is becoming lighter again, going from a heavy (iron) composition below $10^{17.5}$ eV to a light (proton) composition near 10^{19} eV (see [24]).

  Also, in this region the manifestation of the Greisen,Zatsepin, Kuzmin (GZK) cut-off might be visible. The GZK limit is a theoretical upper limit on the energy of cosmic ray protons from distant sources. These physicists predicted that particles with energies above the threshold energy of nearly $5 \cdot 10^{19}$ eV would propagate just about 50 Mpc before they interact with cosmic microwave background photons to produce pions and lose most of their energy:

  $$\gamma + p \longrightarrow \Delta^+ \longrightarrow p + \pi^0$$

  $$\gamma + p \longrightarrow \Delta^+ \longrightarrow n + \pi^+.$$

These processes would continue until the particles'energy falls below the pion production threshold. Therefore, extragalactic cosmic rays from distances of more than 50 Mpc with energies greater than this threshold energy should never be observed on Earth. Data from Fly's Eye, HiRes and Yakutsk are consistent with the expected flux suppression above $5 \cdot 10^{19}$ eV due to the GZK cutoff. AGASA data show an excess of events above 10^{20} eV [25] (see Figure 1.2).

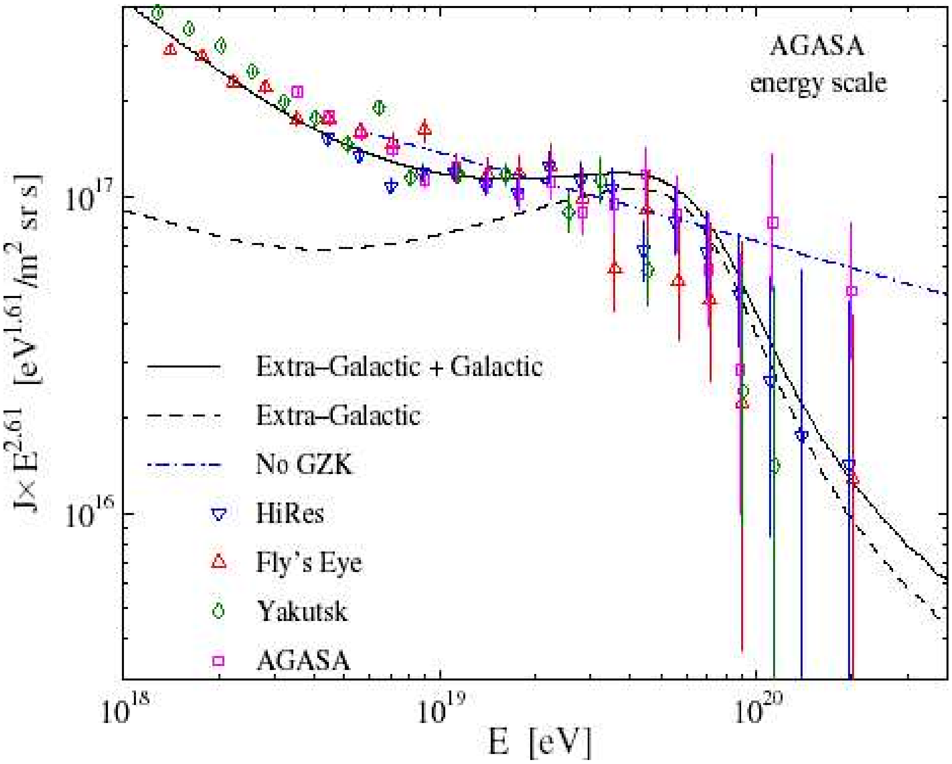

Figure 1.2: High energy primary spectrum [26].

A speculation suggests the involvement of ultra-high energy weakly interacting particles (for instance relic neutrinos) which might be created at great distances and later react locally, for example, with alpha particles:

$$\alpha + \nu_e \longrightarrow 3p + n + e^-$$

$$\alpha + \bar{\nu}_e \longrightarrow p + 3n + e^+.$$

The neutrons decay after a while into protons, giving rise to the particles observed in the high energy range above 10^{17} eV [21].

- The last structure which appears at the end of the spectrum at around a few tens of EeV is called *the toe* [27] and represents a total enigma in cosmic ray physics.

It has to be mentioned that in the low energy region of the primary spectrum the situation is also complex. Below a few GeV there are significant variations due to the solar modulation over the eleven year solar cycle which tends to reduce low energy cosmic rays at solar maximum [13]. The solar minimum and maximum cycle is 11 years and at every solar maximum the polarity of solar magnetic dipole reverses, thus imposing also a 22 year cycle [28].

Cosmic Rays (CR), entering the Solar System, lose part of their energy by collision with solar wind particles that create a solar magnetic field. The Sun ejects a constant stream of a fully ionized hydrogen/helium plasma, the so called *solar wind* from its upper atmosphere, which becomes turbulent at high solar activity. The solar wind consists of charged particles, predominantly of electrons, protons and a small admixture of α particles, that generates an additional magnetic field to the geomagnetic (30 - 60 μT [28]) and interplanetary fields (5 nT or 50 μG [28]).

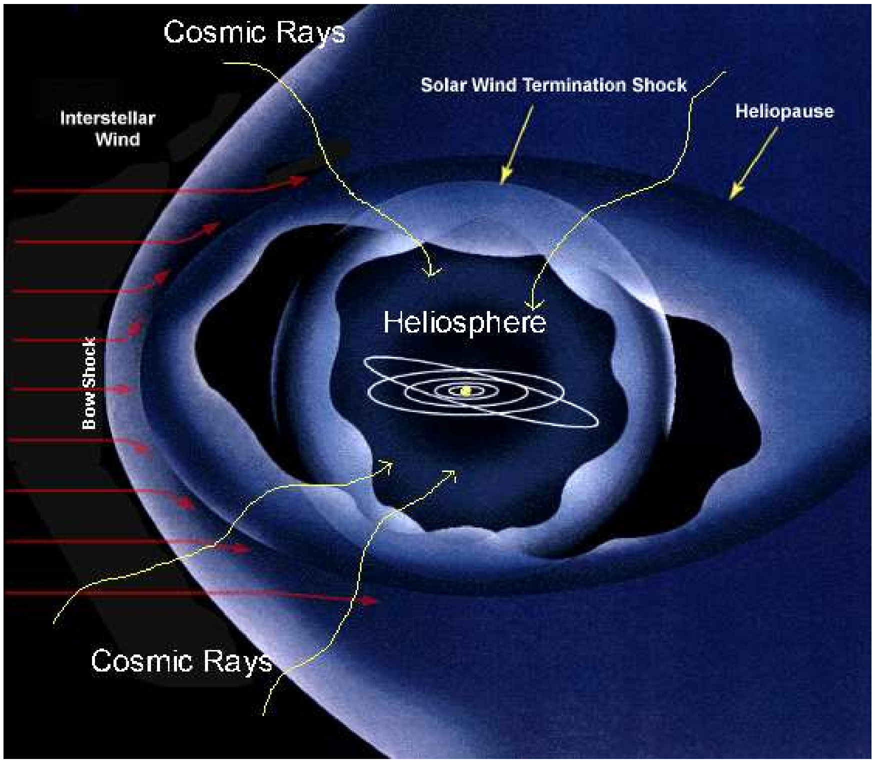

Figure 1.3: The Heliosphere with the solar system in the centre [29].

The solar wind expands out through the Heliosphere (see Figure 1.3), the region of the solar system that extends from the Sun's outer corona into space. Particles in the solar wind propagate at supersonic speed (400 km/s). In front of the Earth's magnetosphere (the local region of interplanetary space where the Earth's magnetic field largely excludes the solar wind), a shock front was observed at which the solar wind was decelerated, heated and deflected around the magnetosphere (see Figure 1.4).

The magnetic field of the magnetosphere works as a shield. If the solar activity is constant, the CR flux on Earth would be constant. When the Sun is active, the stream of solar wind particles creates an additional magnetic field, so the shield is stronger, and as a result fewer CR arrive in the vicinity of Earth. When the solar activity is low, the shield is weaker, and more CR arrive. The modulation of CR depends on their energy. Higher energy particles are less modulated by the solar cycle.

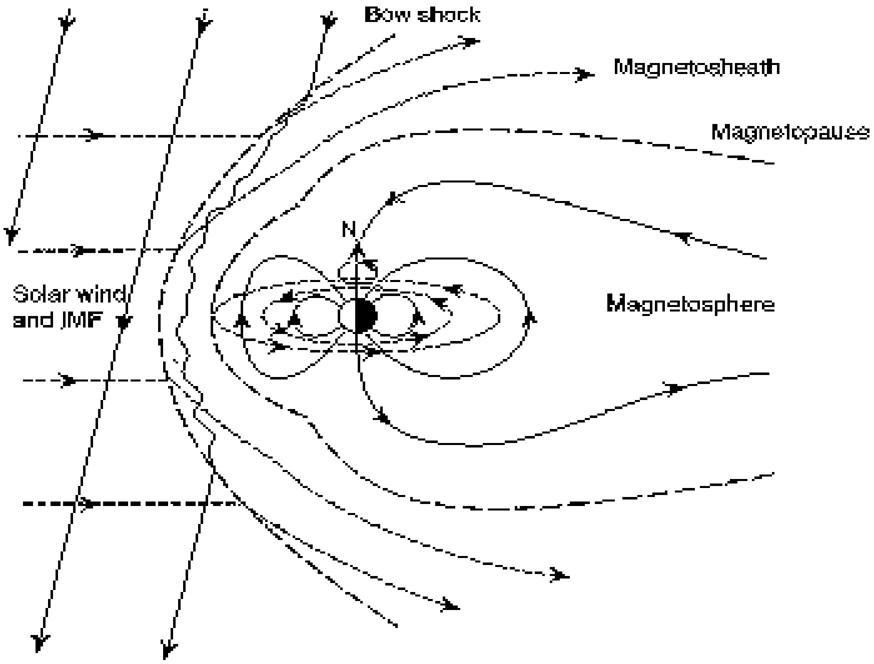

Figure 1.4: Structure of the Earth's magnetosphere in the noon-midnight meridian plane. The magnetopause is the region where the pressure of the Earth counterbalances the pressure of the solar wind [30].

1.2 Origin and Acceleration Mechanisms of Cosmic Rays

First studies of the origin of cosmic rays began in 1960's, when is has been possible to send detectors into space on the board of satellites, and is still a very topical question in high energy astrophysics research.

Electrically charged cosmic rays are bent by interstellar magnetic fields and do not travel in straight lines. From measuring their trajectory at Earth is impossible to tell where they came from, but the measurement of the chemical composition of galactic cosmic rays can provide information about the "average" sources. The heavier nuclei provide most information about the cosmic-ray origin through their elemental and isotopic composition.

The total energy density of cosmic rays measured above the atmosphere is dominated by particles of energies from 1 GeV to 10 GeV. Intensities at energies below 1 GeV are evidence for an origin from the Sun due to the solar activity. Thus, the Sun can also accelerate charged particles in electric fields, created due to the generation and decay of magnetic fields. These regions of turbulent plasma motions appear on the Sun as dark sunspots with lower temperature, because part of the thermal energy is transformed into magnetic field energy [3]. At higher energies from about 1 GeV up to the knee region, cosmic rays are confined to our galaxy. Mechanisms to accelerate particles up to energies of 10^{15} eV have been proposed and generally consist of binary star systems or supernova remnants (see figure 1.5). The mechanisms involved in producing the highest energy cosmic rays are still unknown. The region between the knee and the ankle, also beyond 10 EeV are less understood. Highest energy cosmic rays may come from outside our galaxy, and are much less deflected by the magnetic fields due to their high momenta. For this reason there is an increased interest in detecting large numbers of such particles in the hope of discovering where they come from. There are suggestions that these cosmic rays may have as sources Neutron Stars, X-Ray Binaries, Active Galactic Nuclei or Gamma Ray Bursts. Unfortunately these high energy cosmic rays are very rare (at 10^{20} eV only 1 cosmic ray hits each square kilometre of the Earth's surface per century) and so a giant air shower array must be built in order to detect them. The proposed Pierre Auger Observatory (Argentina) would be just such an array, along with the active large area experiments that use the fluorescence technique [42] like the US High Resolution Fly's Eye detector HiRes and the Japanese Telescope Array AGASA which measures the Cerenkov radiation that is generated when particles in the air shower pass through large tanks of pure water.

An important contribution to the discovery of the cosmic rays origin are represented by high energy cosmic neutrinos [35] and photons which could be produced in Supernovas, Microquasars, Active Galactic Nuclei or the extremely energetic Gamma Ray Bursts. It is considered that in these sources especially protons are accelerated to very high energies beyond 10^{15} eV. When such a high energy proton interacts with matter, also photons and neutrinos are produced. The neutrinos and photons are electrically neutral particles and during the propagation to the Earth, their trajectories are not affected by the Earth's, galactic or intergalactic magnetic fields, that is why they point directly to the source of their origin.

Because neutrinos interact rarely with matter, detectors with huge volumes (Ice Cube telescope $1km^3$ and AMANDA detector in the ice at the geographic South Pole, ANTARES and its succesor KM3NeT in the Mediteranian Sea, and the Baikal detector in the Baikal Sea) are needed. The working principle of these detectors is based on the detection of the Cherenkov light emitted by muons, which are produced when high energy neutrinos hit a nucleus of the ice atoms. In ice, charged particles can move with a velocity larger than the velocity of light and Cherenkov photons are emitted. The detected photon arrival times and amplitudes are used to reconstruct the track and locate its source in the sky.

Photons represent the medium of the natural observations of the sky in the visible spectrum from very old times. In our days, due to the high performance telescopes as the Hubble Space Telescope we are able to see objects and constellations far away at some megaparsec in the visible band and from radio-wavelength to gamma-astronomy spectra. Along with their infinite lifetime and large number, produced in all known astrophysical and nuclear processes, they carry in their spectrum information about their production like the temperature and chemical composition of their source or their environment. A disadvantage of photons is that they interact electromagnetically with cosmic material. Most of them are absorbed in the more dense regions such as dust clouds or directly in the regions where they were produced. High energy gamma-rays, in their propagation through the intergalactic space, may be absorbed by photons of the infrared and microwave backround via electron-positron pair production.

The detection of very high energy gamma rays allows to develop models of the source and the propagation of its emission through space. Some experiments (for more information see [36]) that investigate unexplored windows of γ-ray astrophysics from 10 GeV to 300 GeV are Cherenkov telescope based detectors like the High Energy Stereoscopic System (HESS) and the Major Atmospheric Gamma-ray Imaging Cherenkov Telescope (MAGIC), which detect the Cherenkov light emitted when the high energy photons initiate electromagnetic cascades in the atmosphere, thereby producing lots of electrons and positrons which create Cherenkov emission essentially in the forward direction. The Cherenkov photons arrive in large enough numbers on the surface of Earth to become an indirect image of the electromagnetic shower, allowing identification and reconstruction of the original particle's direction and energy.

Supernovae

A Supernova occurs when a star at the end of its lifetime explodes. The light intensity of the star increases by millions to billions orders of magnitude. For a short time its brightness will be comparable to the luminosity of a whole galaxy. Basically, there are two mechanisms of the star to became in a spectacular way a Supernova.

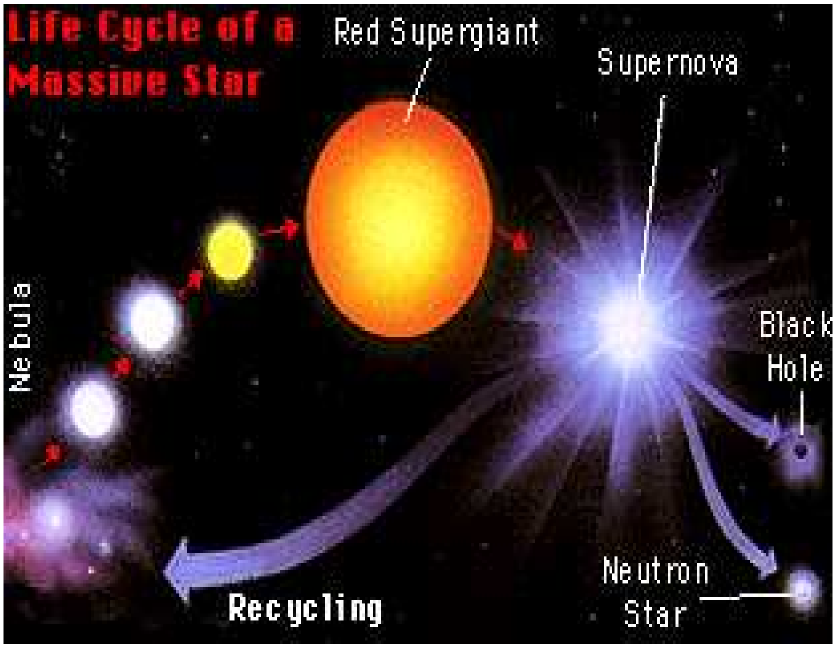

Figure 1.5: The Life Cycle of a Massive Star [40].

Massive stars with a mass more than eight times our Sun's mass [46], end their lives with a collapse of the core when there is no longer enough fuel for the fusion process to create an outward pressure which combats the inward gravitational pull of the star's great mass. These stars create sufficiently high temperatures and pressures needed to cause carbon fusion, once the star contracts at the end of the helium-burning stage. Cores of these massive stars become layered like onions (see Figure 2 on page 10) as progressively heavier atomic nuclei build up by fusion at the center, with an outermost layer of hydrogen gas, surrounded by a layer of hydrogen fusing into helium, surrounded by a layer of helium fusing into carbon, surrounded by layers that fuse to progressively heavier elements with releasing less and less energy until iron is produced (iron has the highest binding energy per nucleon of all the stable elements). First, the star will swell into a red supergiant (see figure 2), then the core collapses around the rapidly shrinking iron core and becomes hotter and denser, and in the last step due to the inverse beta-decay, electrons and protons combine to form a neutron star [46]. When the core contains essentially just iron with a temperature over 100 billion degrees, due to gravitational collapse, the outer layers of the star explode in a type II supernova and produce a shock wave. The nebula and the dense star that remains after the explosion is called the supernova remnant (see figure 1.6).

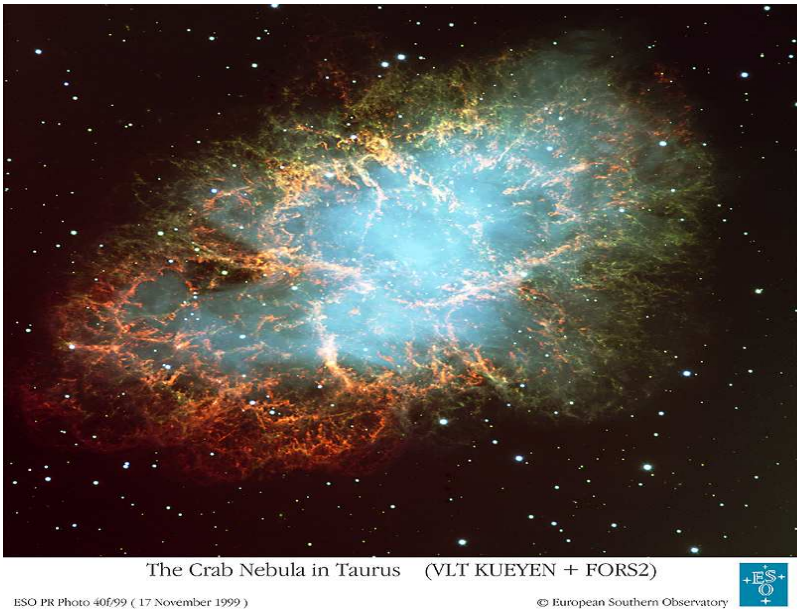

The Crab Nebula in Taurus (VLT KUEYEN + FORS2)

ESO PR Photo 40f/99 (17 November 1999)

© European Southern Observatory

Figure 1.6: The Crab Nebula is the result of a star that was seen to explode in 1054 AD. This spectacular supernova explosion was recorded by Chinese and (quite probably) Anasazi Indian astronomers. Here the red colour indicates electrons which are recombining with protons to form neutral hydrogen, while blue indicates electrons spiralling around the magnetic field of the inner nebula. In the nebula's very center lies a pulsar: a neutron star rotating, in this case, 30 times a second [31].

The powerful shock wave from the explosion expands into the interstellar medium and heats the material in the shock, also the material of the interstellar medium. New elements and radioactive isotopes are formed by the fusion process, or by slow or rapid neutron capture processes, depending on the density of this material. Some of the resulting protons, electrons and ions are accelerated in the shock wave from 10^{12} eV up to 10^{17} eV and may escape, thereby becoming cosmic rays. One assumes that the particles can be accelerated between two shock fronts, where being trapped, they are reflected back and forth from the fronts in the magnetic field of the remnant. This acceleration mechanism is called also the first order Fermi mechanism. In 1949 Enrico Fermi [44] proposed an explanation for the acceleration of cosmic rays, the so-called "second-order" Fermi mechanism, because the average gain in energy per collision between the moving particle against magnetic irregularities is proportional to $(u/c)^2$, where u is the relative velocity of the moving magnetized clouds in the interstellar medium and c is the velocity of light. In a collision, the particle may gain or lose energy. For protons with energies higher than 200 MeV, the gain of energy is more probable than energy losses due to ionization. Above this energy, radiative losses due to the acceleration in the interstellar magnetic fields becomes negligible for protons, compared to electrons for which this is the dominant process. After N collisions, a particle of mass m starting with non-relativistic energy will be accelerated to an energy

$$E = m \cdot c^2 \cdot exp(N \cdot (u/c)^2).$$

Both methods lead to a power law energy spectrum. Higher energies are not expected to originate from supernovae, due to the limited lifetime of the shocks and insufficient lifetime of strong magnetic fields.

When the mass of the star is too massive, the process of collapsing does not stop at a neutron star, it may undergo to become a black hole.

Small and medium sized stars may also undergo supernova explosions when they find themselves in a binary star system as white dwarfs. These kind of stars are not sufficiently heavy to generate core temperatures required to fuse carbon, produced by helium fusion in nucleosynthesis reactions. Having no further source of energy they cool down becoming a white dwarf with the densest forms of matter. White dwarf stars, if they have a nearby companion, may then become a type Ia supernovae. The binary companion may dump matter onto the white dwarf and its mass increases. As the density and temperature becomes higher, the fusion of carbon and oxygen into iron occurs in a runaway fashion and the white dwarf is converted into a fusion bomb. At the point when it may exceed the Chandrasekhar limit (about 1.5 times the mass of the Sun [41]), the white dwarf explodes violently and is completely destroyed, releasing a shock wave in which matter is ejected at high speeds on the order of 10,000 km/s. The energy released in the explosion also causes an extreme increase in luminosity. The matter that once was the white dwarf gets incinerated into radioactive elements, which decay over time, and continue to power the light curve of the supernova.

Neutron Star and Pulsars

A possible end of a star is the neutron star. After the explosion of the outer layers, the core of the massive star collapses more and more into an compact object of mass 1.4 times of our Sun's ($6 \cdot 10^{13} g/cm^3$ density [3]) and a diameter of 20 km, where the protons and electrons combine to form neutrons

$$p + e^- \longrightarrow n + \nu_e.$$

As a result of the gravitational contraction of a star, the formed neutron star can have extremely high magnetic fields (B $\simeq 10^8$ T) and they are also observed as Pulsars (rapidly rotating magnetized Neutron Star which generates regular pulses of radiation observed at radio wavelengths, also at optical, X-ray and gamma-ray energies). The periods of a Pulsar ($T_{Pulsar} = T_{Star} \cdot \frac{R^2_{Pulsar}}{R^2_{Star}}$) can take values of a few milliseconds and magnetic fields ($B_{Pulsar} = B_{Star} \cdot \frac{R^2_{Star}}{R^2_{Pulsar}}$) of $\sim 10^8$ T, depending, of course, on the stellar size, period and initial magnetic field. The rotational axis of Pulsars in generally does not coincide with the direction of the magnetic field. As a result, strong electric fields are produced in which particles can be accelerated [3]. Pulsars are considered to be able to accelerate cosmic rays up to energies of 10^{18} eV. Higher energies would not be possible because the protons would suffer energy losses in the strong magnetic field due to synchrotron radiation and would be trapped in the outer belt just as electrons and positrons.

X-Ray Binaries

Another possible source for high energies are X-ray binaries. In this case, a neutron star or a black hole accompanied by a normal star form the binary system. The strong gravitational force from the neutron star pulls material from the normal star. The dust and gas is accumulated onto the neutron star at its magentic poles (accretion process) forming an accretion disk (see figure 1.7). In the process of friction between the accretion disk layers, the material becomes very hot and very strong electromagnetic fields are produced, that can accelerate charged particles to high energies up to 10^{19} eV. These particles then radiate intense beams of energy which can be observed in the X-ray region.

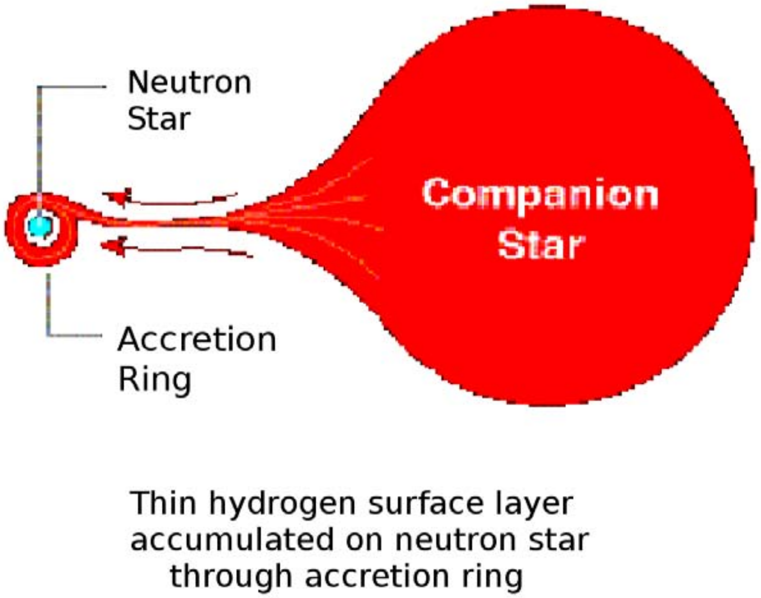

Figure 1.7: The Binary System [45].

Active Galactic Nuclei

There are assumptions that the sources of the highest energy cosmic rays are Active Galactic Nuclei (AGN) (see the figure 1.8). Astronomers define them as individual galaxies whose centers are emitting huge amounts of energy, beyond what can be attributed to normal processes from stars and the interstellar medium. In the unified model of Active Galactic Nuclei, active galaxies contain supermassive black holes at their centers. The surrounding galactic material moves toward the center and would form an accretion disk around the black hole. The inner part of the accretion disk is very hot and then would be capable to produce jets of hot gas and radiation streaming out of the nucleus along the axis of rotation of the disk. These jets would

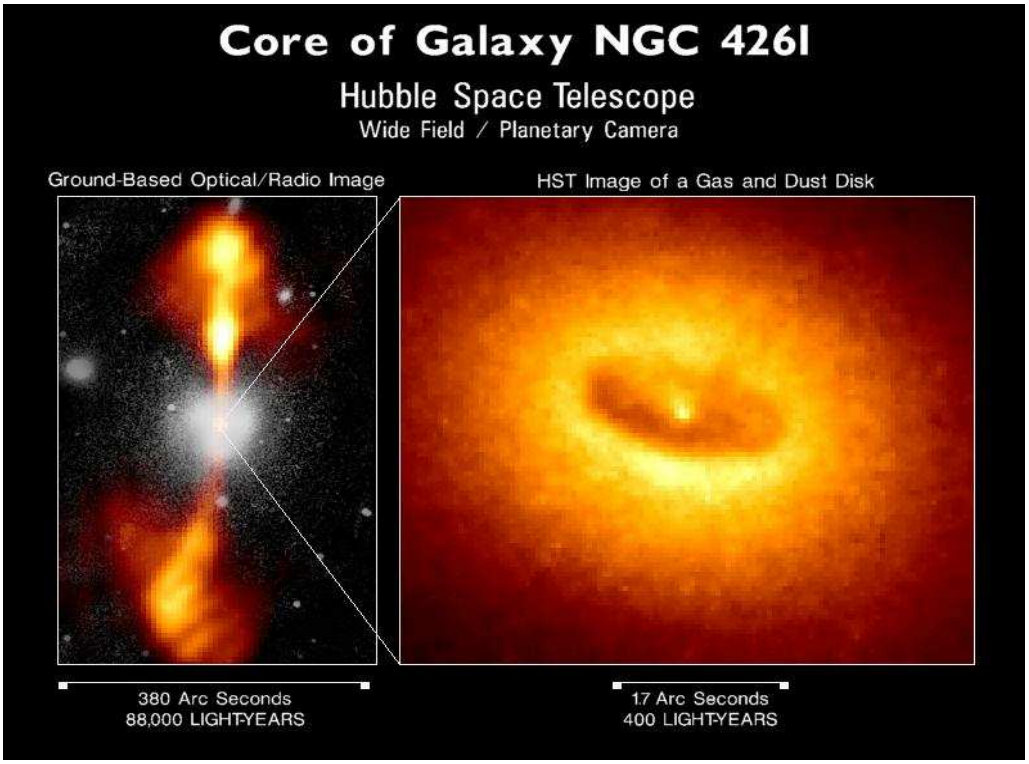

Figure 1.8: An active galactic nucleus (AGN) NGC-4261, one possible source of high energy cosmic rays. To the right is a close up image from the Hubble Space Telescope covering just 400 light years. It shows a doughnut shaped ring at the centre. This ring is thought to orbit a giant blackhole with a mass more than a hundred million times that of our sun [32].

be observable at radio wavelengths, X-ray and gamma ray bands. In these jets high energy particles can be accelerated. The accelerated charged particles (electrons and protons) emit gamma rays by synchrotron radiation and inverse Compton scattering on the synchrotron photons.

According to our viewing angle, the scientists distinguish several kinds of active galaxies: Seyfert galaxies, radio galaxies, quasars and blasars.

Gamma-Ray Bursts (GRBs)

GRBs are considered the most powerful events known in the Universe since the Big Bang and are thought to be a source for high energy cosmic rays. Their lifetime is short, from a few milliseconds to several minutes and they occur isotropicaly distributed in the sky approximately once per day in very distant galaxies (several billion light years away). This means that the gamma ray emission from gamma ray bursts that is observed now has been emitted billions of years ago, when the Universe was much younger. They can only be detected from space by satellites orbiting the Earth and space probes travelling through the Solar system because the Earth's atmosphere absorbs the gamma rays. Gamma ray bursts release extremely large amounts of energy up to $2 \cdot 10^{54}$ ergs [78] (or 10^{47} joules). This is equivalent to the amount of energy released by 1000 stars like the Sun over their entire lifetime. The progenitors of the GRBs are considered to be the very massive stars and binary systems composed of neutron stars or black holes. The collapse of the core of the massive stars, called also "hypernovae", is accompanied by the release of energy in the formation of the black hole that emerges out of the collapsed star in the form of a "long and soft" gamma ray burst.

In case of binary systems, the two objects in the system spiral toward each other and lose orbital angular momentum by gravitational wave radiation and eventually they merge into a single black hole with a sudden release of large amounts of gravitational energy sufficient to power a "short and hard" burst. Such an intense, localized and brief explosion implies the formation of an $e^{\pm}$, γ fireball expected to expand relativistically [79] into the surrounded plasma, that forms a shock wave with the possibility of Fermi acceleration. In the presence of turbulent magnetic fields built up behind the shocks, the electrons, that are accelerated in the fireball by multiple internal shocks as well as by the external and reversed shocks, produce a synchrotron power-law radiation spectrum, while the inverse Compton scattering of these synchrotron photons extends the spectrum into the GeV range. When the external shock starts decelerating, the electrons produce gamma-rays in the X-ray and optical range by the synchrotron mechanism, a process also called afterglow radiation [78]. According to E. Waxman ([80]), the protons are expected to be accelerated to high energies ($\sim 10^{20}$ eV) in the mildly relativistic shocks within an expanding ultrarelativistic GRB wind.

1.3 Mass Composition

The accurate determination of the elemental composition of primary cosmic rays could shed light on still puzzling features like the evolution of the Universe, the knee structure in the all-particle spectrum, the identification of specific source models and the propagation of cosmic rays through the interstellar medium from the source to Earth.

The most significant process that cosmic ray nuclei undergo in our galaxy is spallation [22]. This happens, when an atomic nucleus collides with another nucleus (proton) and breaks apart into a large number of nuclear fragments, α particles and neutrons [3], producing so called secondary nuclei. Primary nuclei, the survivors from the original time of their production, together with secondary nuclei (see Figure 1.9) provide information about the galactic chemical evolution, propagation and source models.

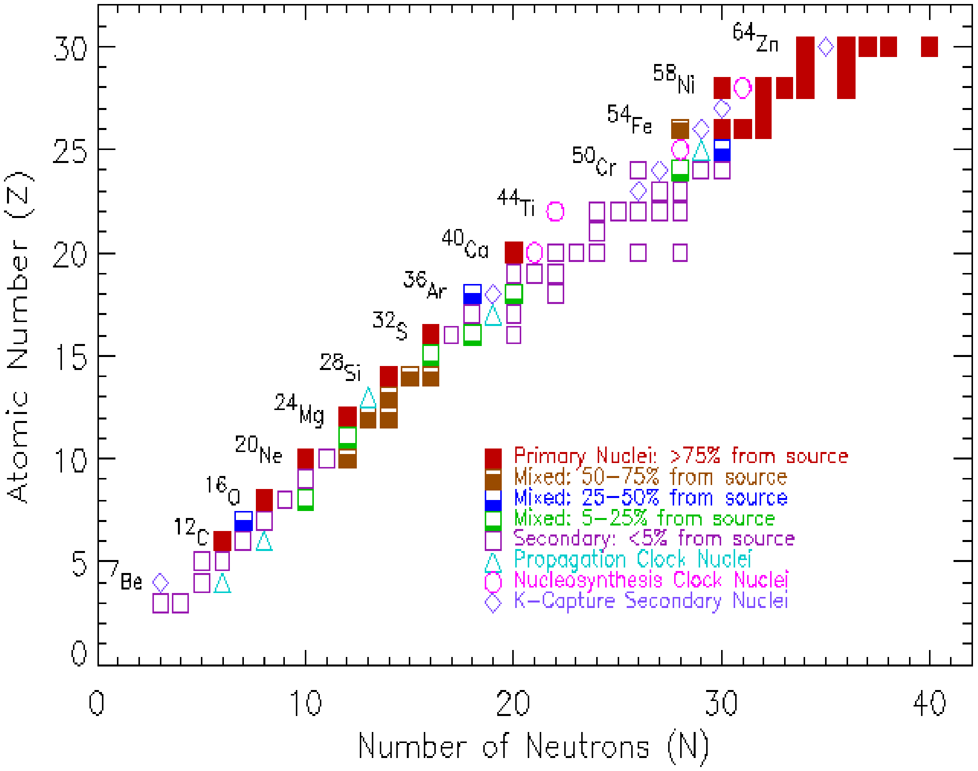

Figure 1.9: Types of cosmic ray nuclei [10]

Many secondaries (called also propagation clocks or radioactive clocks), after they are created, begin to decay and the fraction that reach us at Earth gives the time of transport and the age of these cosmic rays.

At low energies ($E < 10^{14}$ eV), the measurement of the mass composition is made directly in balloon or spacecraft experiments and some remarkable differences were observed.

Most notable is that three elements just below Carbon (Lithium (Li), Beryllium (Be) and Boron (B)) and five elements just below Iron (Scandium (Sc), Titanium (Ti), Vanadium (V), Chromium (Cr) and Manganese (Mn)) are much more abundant in cosmic radiation than in the solar system material (see Figure 1.10).

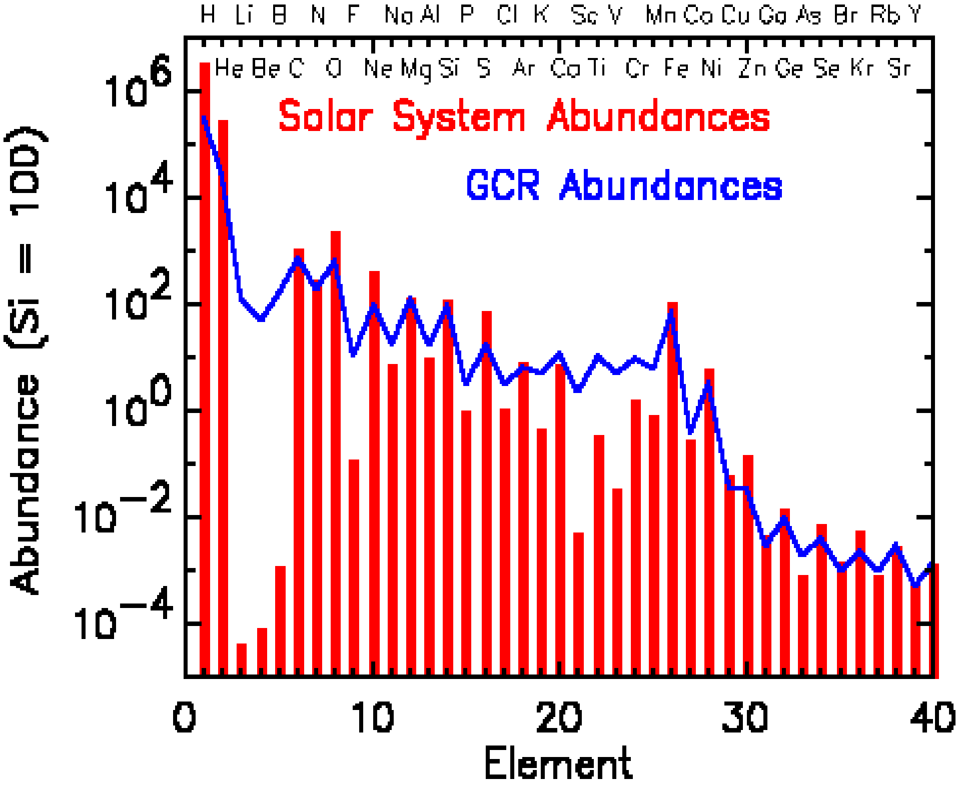

Figure 1.10: Solar and Galactic Cosmic Ray (GCR) Composition [34].

Also, the relative abundance of nuclei of hydrogen and helium atoms in cosmic rays compared to the solar system material is not really understood. One explanation could be that hydrogen and helium are harder to ionize for the injection into the acceleration process, or there is a difference in composition at the source ([13], [47]).

Hydrogen and helium are the most abundant elements in our solar system (see also Figure 1.10) [4]. This was determined from the spectral analysis of the Sunlight and from the chemical analysis of a special class of meteorites, the carboneous Chondrites, which would reflect a largely unmodified composition since the Big Bang. Hydrogen and helium were created together with lithium already in the course of the primordial nucleosynthesis shortly after the Big Bang, all heavy elements arose later in stars and star explosions. An analysis of the nuclei mass explains why in the Big Bang no heavy elements could be formed from ^1H and ^4He (the numbers are the mass numbers - the sum of the protons and neutrons in the nucleus). The fusion of two hydrogen nuclei gives ^2He, a hydrogen nucleus with helium yields ^5Li, and the merger (fusion) of two helium nuclei forms ^8Be, which is highly unstable.

Very specific for the ^2He, ^5Li and ^8Be is that, compared to the isotopes of lighter elements of usual occurence in stars and on the Earth, the decay of these nuclei into smaller fragments is energetically possible, because the total mass of the nuclear fragments is smaller than the mass of the initial nuclei. This mass difference is equivalent to the binding energy

$$E = mc^2,$$

(Einstein's formula), that is released in the decay. The lifetime of these nuclei is very short, $7 \cdot 10^{-17}$ s in case of ^8Be, that is why they are destroyed immediately after their production and exist in the Solar System just in minute quantities.

If the mass of ^8Be would be smaller by 0.1 %, this nucleus would be stable and the heavy elements would be produced already in the Big Bang with drastic consequences for the existence of stars.

The higher abundance of Li, Be and B nuclei in cosmic radiation appears to be due to spallation processes of very abundant carbon and oxygen nuclei.

The large excess of Scandium, Titanium, Vanadium, Chromium and Manganese in cosmic radiation is explained by collisions of the heavier cosmic rays Fe and Ni with nuclei of the interstellar medium [13]. Their relative abundance in our solar system is explained also by the difference between the mass of the formed nucleus and the sum of masses of daughter nuclei that fused. Elements just below Fe formed in such fusion processes are frequently unstable and may decay.

The presence of heavy nuclei in the Universe is explained by the chain of nuclear fusion reactions that happen in stars, with the formation of nuclei with higher binding energy from nuclei with lower binding energies, a process accompanied by release of energy. Because the nuclei of Fe and Ni show the highest binding energy per nucleon of all nuclei, this chain of fusion reactions stops at Fe and Ni (see Figure 1.11).

In such a way, heavy nuclei produced from Hydrogen and Helium are spread in the Universe, also in our solar system, through supernova explosions.

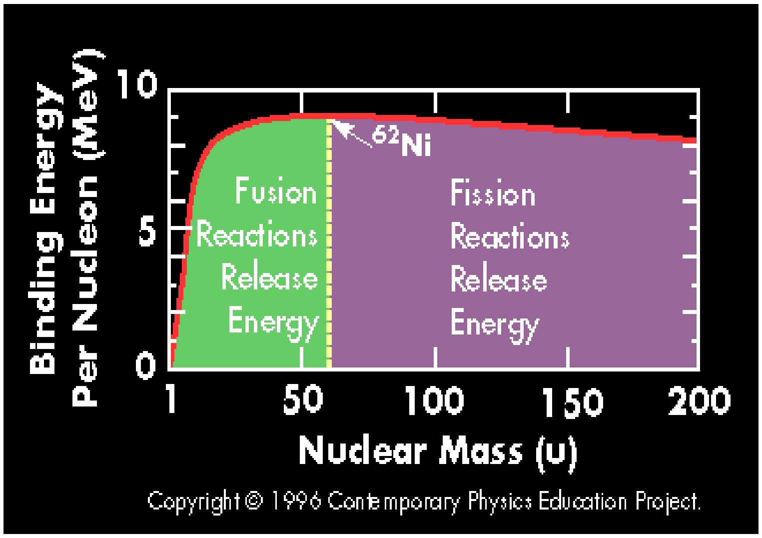

Figure 1.11: Binding energy [51]. In a fusion reaction, some reactant mass energy is converted to kinetic energy of the products. Binding energy, that correspond to $E = m \cdot c^2$, is the energy equivalent of the mass difference between a nucleus and its individual protons and neutrons constituents. For energy release in fusion to happen, the products need to have a higher binding energy per nucleon than the reactants.

Elements heavier than Fe, the so called "trans-Fe" elements, are less abundant in cosmic rays as well as in the solar system, explained also by the deficiency to create heavy elements by the s-process and r-process in stars and in supenovae [47]. It turns out that in the course of supernova explosions there are many non-equilibrium reactions, neutron capture processes, that build up very massive elements. A saturated nucleus captures at the same time a number of neutrons until a radioactive isotope is produced. In some cases these elements are stable, in many cases they are not and the process of radioactive decay (beta-decay) of heavy elements is just Nature's way of getting back into equilibrium. Neutron captures and beta-decay alternate such, that always successively heavier elements are formed.

According to the Nucleosynthesis theory, heavy elements in the mass region $A \geq 60$ are built through neutron capture processes: the slow s-process and the rapid r-process [48].

In the s-process most neutron captures are slower than beta-decays. This occurs when the neutron density is so small that the most unstable isotopes have time to decay through the beta-decay process to form again stable nuclei [50]. From the studies, it is concluded that the s-process occurs also today on the surface of the Asymptotic Giant Branch (AGB) stars and zero-metallicity stars [49] with masses between about one and eight solar masses. Many of them are characterized by a strong mass loss by ejecting the surface material into the interstellar medium, contributing thereby to the galactic chemical evolution. The AGB stars are old, mostly burnt-out stars with a degenerate carbon-oxygen core. They are supported by helium burning in a shell around this core. In this shell certain reactions release neutrons [50]:

$$^{22}Ne +^{4} He \longrightarrow^{25} Mg + n$$

$$^{13}C +^{4} He \longrightarrow^{16} O + n,$$

that start the neutron capture process by the Carbon (C), Nitrogen (N), Oxygen (O), Fluorine (F), and Neon (Ne) isotopes [49], and leads to the production of heavier nuclei up to Lead (Pb) and Bismuth (Bi). Beyond this point, no nuclei are stable enough to allow neutron capture to operate. Once s-process elements are formed, the AGB star conveniently convects these to the surface, where they may be released either in a stellar wind or in a subsequent supernova explosion.

The r-process accounts for the genesis of about half of the heavy nuclei beyond iron. The elements as Europium (Eu), Gold (Au), Platinum (Pt) or Uranium (U) derive exclusively from this process. The r-process occurs in an environment with very high neutron densities. Thus, neutron captures proceed much faster than beta-decays and thereby extremely beta-unstable exotic nuclei that rapidly decay to form stable neutron rich nuclei may be produced. Where and when this process takes place in the Universe is still an open question in astrophysics. There are suggestions that the r-process with the formation of heavy elements occurs in the explosive environments like supernovas of type II [48], in Gamma Ray Bursts or in the collision of two neutron stars in the Neutron Double Star System, which merge to form a black hole and thereby accelerate the neutron rich material [4].

The mass composition of high energy cosmic rays requires indirect methods of measurements. At present this is done with detectors with large areas, at the surface and underground (muon measurements), exposed for large periods of time. Many experiments have determined the elemental composition of cosmic rays from the comparison of Monte Carlo (MC) predictions with various measured parameters of extensive air showers like electromagnetic and muon lateral distributions, electron and muon multiplicities, Cherenkov lateral distributions (KASCADE, EAS-TOP [52], CASA/MIA/BLANCA [54] [55]) and underground muon pair separations (MACRO [56], CosmoALEPH [81]). Experimental results are very sensitive to the Monte Carlo hadronic interaction models, which makes a final conclusion on the chemical composition of primary cosmic rays difficult.

Recent results from the Pamir experiment favor a light mass composition [57] below the *knee* region and just 14% Fe above 10^{15} eV. The Indian - Japan GRAPES muon multiplicity distribution is best fit by simulated proton and helium primaries above 100 TeV [58].

Most of the experiments report a light composition dominance, mostly hydrogen and helium [59], below the *knee* (see Figure 1.12) which becomes heavier above the knee, returning again to a light composition near 10^{19} eV [24].

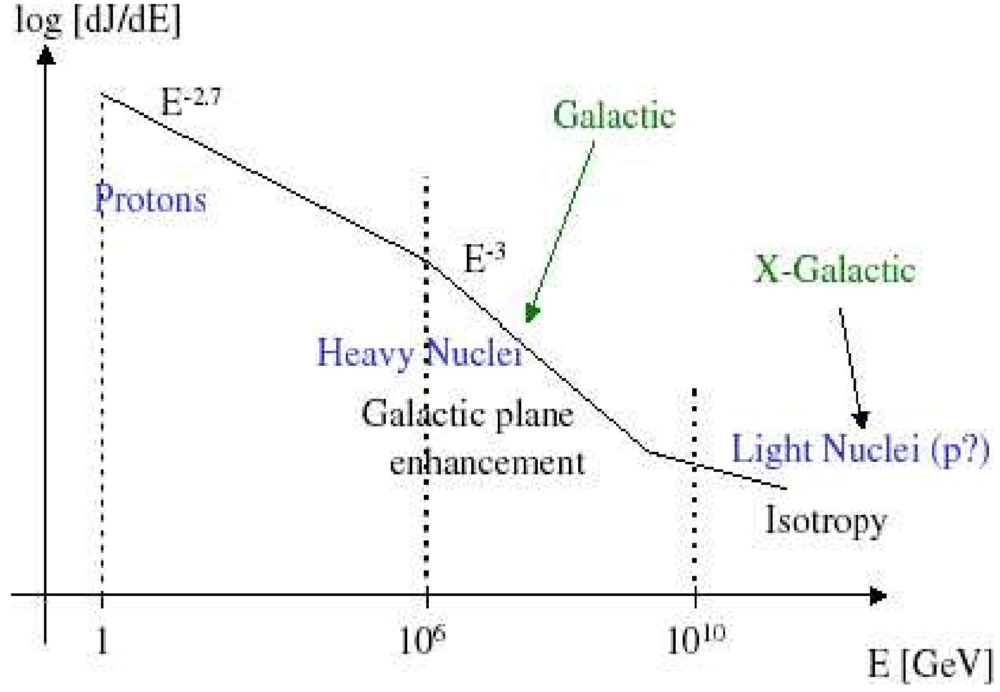

Figure 1.12: A schematic description of the differential spectrum and of the composition of cosmic rays observed on Earth [26].

The still puzzling *knee* phenomenon in the cosmic ray spectrum has started detailed investigations, and a lot of experiments are involved in the study of this region. The CASA-BLANCA detectors (charged particle distribution in extensive air showers, respectively lateral distribution of Cherenkov light) observe a light composition across the *knee*. The CASA-MIA experiment [55] which measures also muons underground, based on event by event analysis with discrimination between light and heavy primaries by comparison to simulated proton or iron induced air showers, indicates a heavier composition through the *knee*, while the measurements at the DICE/CASA/MIA air shower installation [60] find ~70% protons and helium near the 10 PeV energy region from a combination of the independent parameters of Cherenkov size, depth of shower maximum in the atmosphere, muon size and electron size at ground level.

Erlykin and Wolfendale [61] suggest a predominance of He in the *knee* region from the observation of the KASCADE N_μ - N_e distribution which is in contradiction with the measurements at the Tibet altitude, that indicate a composition heavier than proton and helium at the *knee* [62]. The EAS-TOP and MACRO (mass composition determined from the comparison of the measured muon multiplicity underground with two composition aproaches [64]) experiments report also a preference of light nuclei up to the knee region that agrees well with the direct measurements (JACEE experiment [63]). A break in the spectrum of H, He and CNO is observed, but not in the iron spectrum [65] and C.Morrelo presents a very good agreement of Monte Carlo simulations with experimental data for helium primaries [52].

The analysis of multiple muon events measured underground by the Soudan 2 Detector (northern Minnesota) favors a proton component in the energy region just before and around the knee, compatible with the expectation from Active Galactic Nuclei sources [53].

The indirect measurements of the composition of primary cosmic rays are difficult to interpret and from experiment to experiment they lead to contradictory results. Thus, the experiments initiated by a group from the University of Maryland identified hadrons produced from primary protons up to 100 TeV, above this energy from primary iron nuclei. These results are based on studies of the energetic (100 - 10000 TeV) hadrons near the cores of air showers [66] and their arraival time distributions [67]. They calculated the spectral indices of p, He, CNO, Si and Fe based on various Monte Carlo models proposing a heavy composition model with heavier nuclei dominance near the *knee* region of the cosmic ray spectrum.

The indication of a heavy composition beyond 10^{15} eV is supported by the SPACE/AMANDA multicomponent experiment [68]. They arrive at this conclusion from the combination of the electron and muon information collected with a scintillator array and the deep-ice Cherenkov telescope in coincidence at the South Pole. In a similar way, the Kolar Gold Field (KGF) underground detector [69] in India infers a heavy composition of primary cosmic rays beyond 10^{15} eV from the measured muon multiplicity underground.

For energies above 10^{16} eV there are indications that heavier nuclei compete with light nuclei or even a tendency to increasing heavy primaries is seen (see figure 1.13). This is well illustrated in the analyses of the KASCADE experiment ([17], [82], [83]).

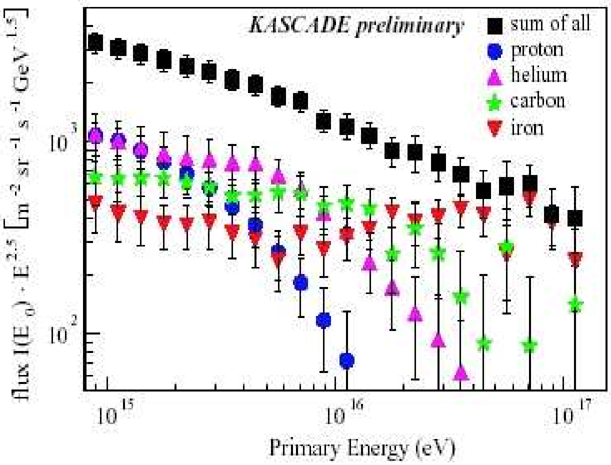

Figure 1.13: Preliminary energy distributions of four primary masses measured in the KASCADE experiment as obtained from an unfolding procedure. The sum of 4 individual distributions represents the all-particle CR-specrum (black squares). The vertical error bars represent the statistical uncertainties which are dominated by the statistical uncertainties of Monte Carlo simulations [83].

A study of shower size data of the Akeno experiment lead the physicists T.Stanev, P.L.Biermann and T.K.Gaisser to conclude that the region above the knee is dominated by Neon group nuclei, that turns off to a lighter component above 10^{16} eV with an extragalactic proton flux above 10^{17} eV [70]. The results of Utah Fly's Eye experiment, as those obtained by HiRes and Yakutsk extensive air shower arrays, observe also a light composition from $10^{17.5}$ eV to 10^{19} eV [24].

The extremely high energy cosmic rays are a mystery also nowadays. The knowledge of the mass composition above 10^{17} eV is poor with large uncertainties due to the limited flux of particles at such energies. From a systematic study of different measurements A.A.Watson [71] does not exclude the idea that above 10^{17} eV heavy nuclei might dominate as primary cosmic rays. The Haverah Park Array measurements are in favor of a bi-modal composition of 34% protons and the rest being iron in the energy range $2 \cdot 10^{17}$ - $3 \cdot 10^{18}$ eV [72]. A careful analysis of ultrahigh energy air showers detected by the SUGAR array shows that cosmic rays near 10^{19} eV are most likely iron nuclei, and at energies larger than $4 \cdot 10^{19}$ eV nuclei even heavier than iron occur[73].

There are hopes that the new large AUGER and KASCADE GRANDE experiments will solve many open questions regarding *knee*, *ankle* and *toe* features in the cosmic ray spectrum.

1.4 Air Showers

In 1938, Pierre Auger discovered *extensive air showers* [74], showers of secondary particles produced in collisions of high-energy primary cosmic rays with air nuclei. In his experiment high in the Alps, he observed that two particle detectors located many meters apart both signaled the arrival of particles at exactly the same time. From these measurements he assumed that the detected cosmic ray events are very energetic of order of 10^{15} eV which was ten million times higher than any known energy before.

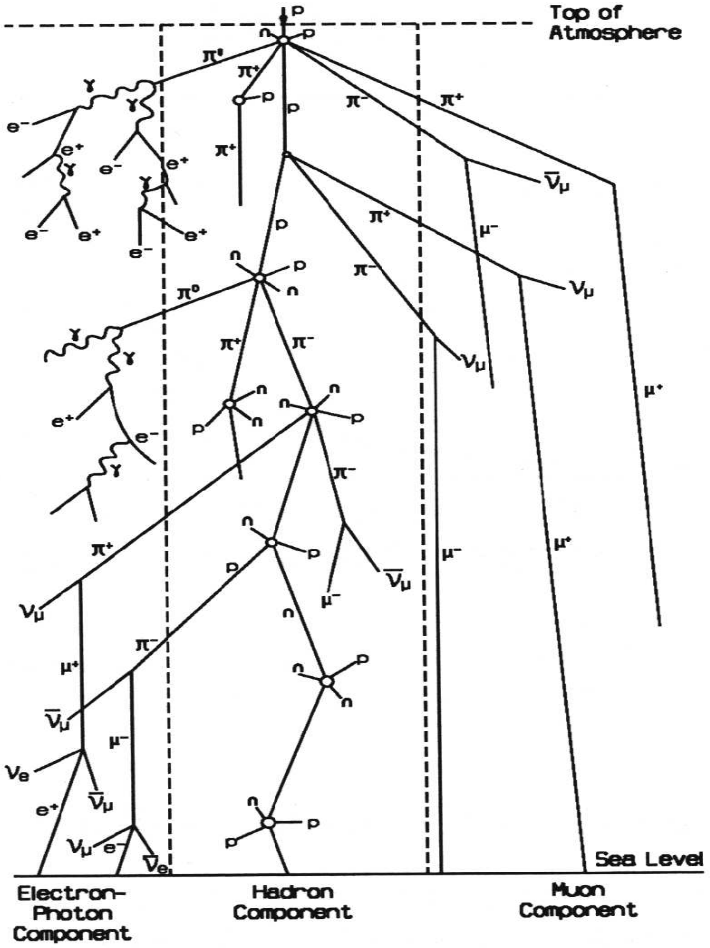

Figure 1.14: Schematic view of an air shower ([28], p. 22).

A high energetic primary cosmic ray nucleus A, interacting strongly with nuclei of the air (nitrogen and oxygen), produces neutral and charged pions

π, also several kaons K

$$A + Air \longrightarrow \pi, K + X.$$

This initiates an extensive air shower which consists of electromagnetic, hadronic and muon-neutrino components. Figure 1.14 shows a schematic view of the development of an air shower.

In the first interaction many secondary particles are produced. Nucleons and the created high energy hadrons, produced at the first interaction, interact further and induce the hadronic cascade. The pions can be categorized according to their transverse momentum. Low transverse momentum pions are the result of soft collisions with low momentum transfer. High P_T pions result from the hard scattering of point-like hadronic constituents and follow a $(1 + P_T/P_0)^{-n}$ differential cross section [11].

Neutral pions, due to their very short life time ($t = 8 \cdot 10^{-17}\ s$), decay predominantly into two photons $\pi^0 \longrightarrow 2\gamma$. The Dalitz decay $\pi^0 \longrightarrow e^+ + e^- + \gamma$ occurs only in 1.2 percent of the cases. Each high energy photon generates an electron-positron pair, which respectively radiate photons via bremsstrahlung. These two processes (pair production and bremsstrahlung) are the basis in the development of the electromagnetic cascade shower and they continue as long as the particles energy is large enough compared to the critical energy (according to P. Grieder [28], p.18, for electrons $E_c \simeq 84.2$ MeV, for muons $E_c \simeq 3.6$ TeV). Below the critical energy, the shower energy is dissipated in such processes as the ionization of the medium by electrons and positrons, by Compton scattering and by the photoeffect for photons with energies smaller than some hundred keV, until the electromagnetic component (soft-component) is absorbed.

Low energy charged pions and kaons are responsible for the muon- and neutrino-part in the shower development:

$$\pi^\pm \longrightarrow \mu^\pm + \nu_\mu(\bar{\nu}_\mu)$$

$$K^\pm \longrightarrow \mu^\pm + \nu_\mu(\bar{\nu}_\mu)$$
$$K^\pm \longrightarrow \pi^0 + \mu^\pm + \nu_\mu(\bar{\nu}_\mu).$$

At very high energies muons are produced from the decay of charmed mesons ($D^0 \longrightarrow K^-\mu^+\nu_\mu$, $D^+ \longrightarrow \bar{K}^0\mu^+\nu_\mu$, $D^- \longrightarrow K^0\mu^-\bar{\nu}_\mu$).

Experimentally an excess of positive cosmic ray muons is measured (the charge ratio of positive muons to negative muons $N(\mu^+)/N(\mu^-) \simeq 1.27$ [77]), explained by the produced excess of positive pions ($N(\pi^+)/N(\pi^-) = 1.25$) in the interactions of positive primary cosmic rays (mainly protons) with air nuclei [3].

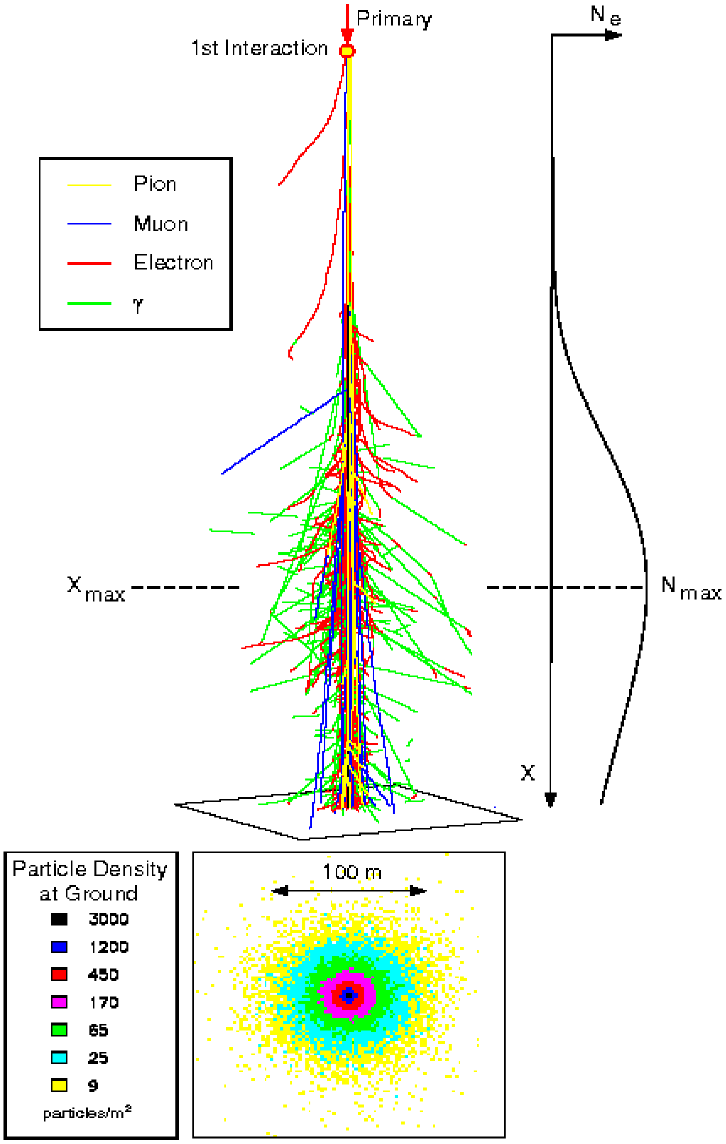

Figure 1.15: The simulated development of 1 PeV proton air-shower. The right hand plot shows the evolution of the total particle number with depth. The lower figure shows the distribution of particles at ground level [84].

Inelastic hadronic interactions of muons are very rare, they can essentially only decay (below 10 GeV) $\mu^{\pm} \longrightarrow e^{\pm} + \nu_e(\bar{\nu}_e) + \bar{\nu}_{\mu}(\nu_{\mu})$, or they lose energy via bremstrahlung, electron-positron pair production and ionisation.

Below the critical energy the energy loss via ionization of the medium becomes important. Non-decaying muons lose just a small part of their energy in the atmosphere ($\sim$ 1.8 GeV, that is why their flux is only somewhat attenuated (see figure 1.15) compared to the electrons and positrons which at an altitude below 15 km in the atmosphere are quickly absorbed [1].

Muons represent an important tool in the study of extensive air showers. Due to their small cross section for interactions, they are very penetrating and can be detected deep in the atmosphere or underground. Muons and neutrinos, due to their very penetrating properties, are called the hard component of the shower.

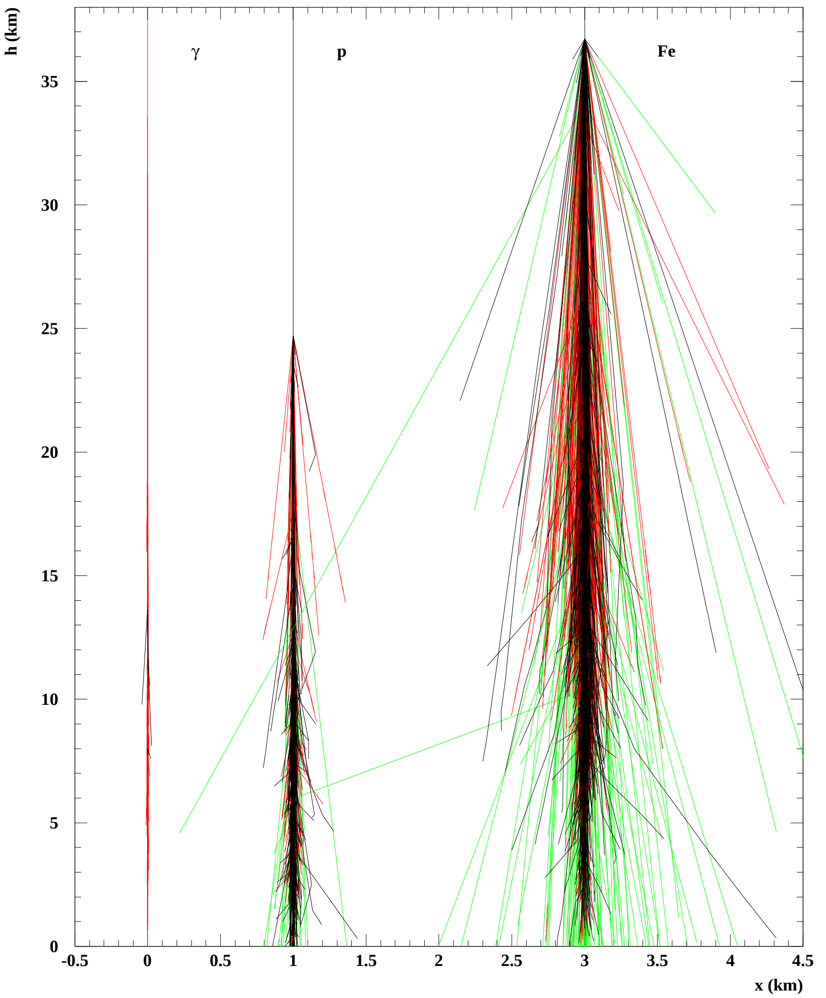

Figure 1.16: Simulated 100 TeV photon, proton and iron induced EAS with CORSIKA (VENUS) with a strong cut on the secondary energy. The red colour represents photons, black- hadrons, green- muons [85].

The longitudinal and lateral development of an extensive air shower depends on the type of the primary particle and its energy. As shown in figure

1.16, iron nuclei interact earlier in the atmosphere compared to photons and protons. Also, iron and proton induced air showers have a larger lateral width compared to a photon induced air shower, because the transverse momentum of the produced secondary particles in hadronic cascades is larger. In case of the electromagnetic component, the lateral size of the shower is caused by multiple scattering of electrons and positrons [75].

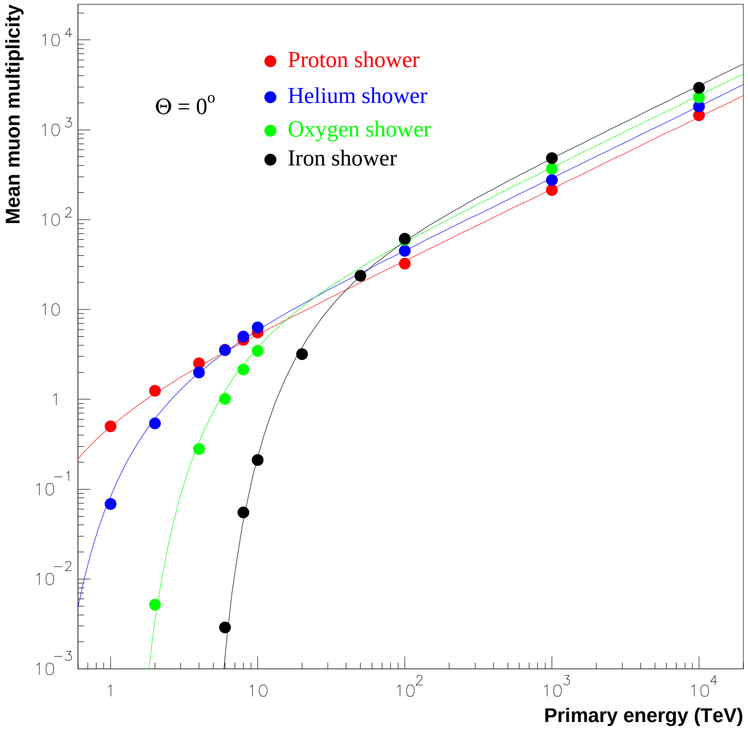

Figure 1.17: Mean muon multiplicity for p, He, O, and Fe simulated air showers with CORSIKA (QGSJET model) at different primary energies for a primary zenith angle $\theta = 0^0$. The points are the mean values of the multiplicity distributions for different primary energies [119].

An iron induced air shower contains more secondary particles, an effect that is evident with increasing primary energy (see figure 1.17) and the fluctuations are considerably smaller compared to proton induced air showers of the same energy (see figure 1.18).

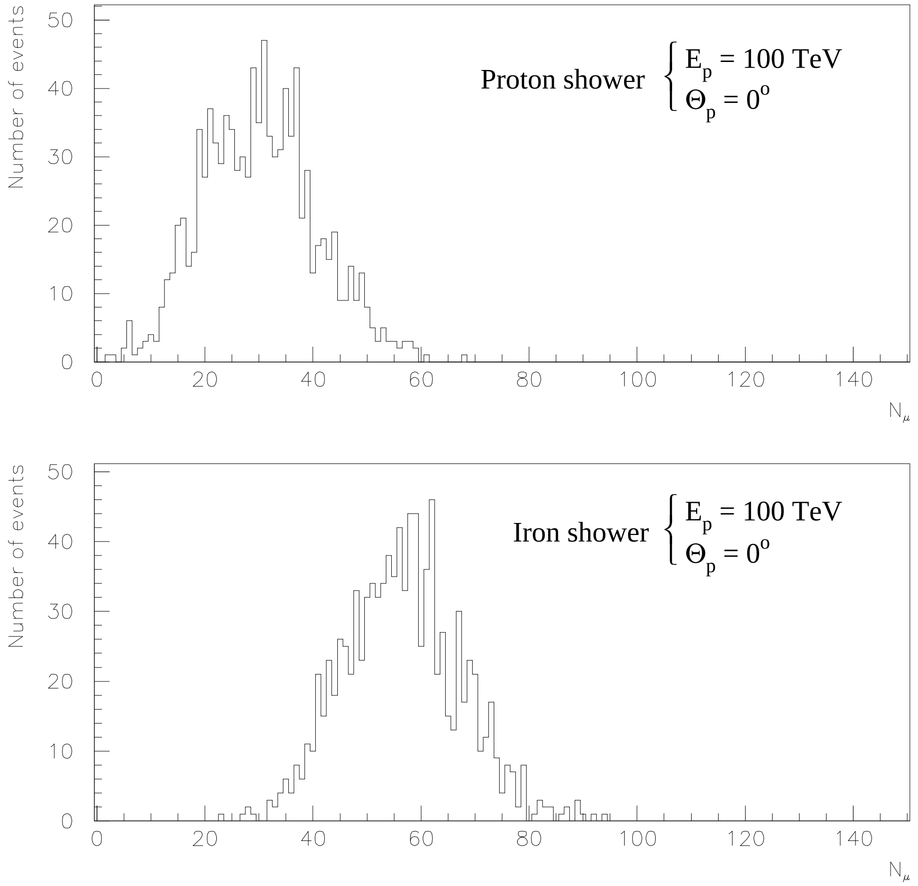

Figure 1.18: Multiplicity distribution of muons for Proton and Iron air showers simulated with DPMJET at a primary energy of 100 TeV and zenith angle $\theta = 0^0$.

According to N. Kalmykov [86] this is explained often in the context of the superposition model, in which a shower induced by a nucleus of iron of mass A=56 and energy E_0 is represented as the superposition of 56 nucleon showers of energy $E_0/56$.

The multiplicity and transverse momentum of high energy muons are sensitive to the mass composition of cosmic rays, because they are produced in the first interactions and carry the information of the primary cosmic nuclei. Due to the obtained transverse momentum, muons are characterised by a large lateral spread. The muon separation distribution, which is strongly correlated with the transverse momentum, is also sensitive to the primary composition. Thus, underground detectors allow to study the chemical composition of primary cosmic rays from the detection of high energy multiple muon events.

1.5 Muons in the atmosphere and underground

Muons are produced predominantly in pion decays. At sea level the majority of produced secondaries are muons, since pions are produced in large numbers in hadron cascades and their mean decay length s (directly proportional to the energy E and mean lifetime τ_μ of the particle) at moderate energies is very short compare to the muon mean decay length [3]

$$s = \gamma \cdot \tau_\mu \cdot c \qquad with \qquad \gamma = \frac{E}{m \cdot c^2} \ . \tag{1.2}$$

With increasing energy the relative intensity of muons, compared to that of pions, decreases, since the interaction probability for pions dominates.

The directional intensity of muons $I_\mu(\theta, \phi)$ is defined as the number of muons dN_μ incident on an element of area dA, per unit time dt, within an element of solid angle $d\Omega$ [28]

$$I_\mu(\theta, \phi) = \frac{dN_\mu}{dA \cdot dt \cdot d\Omega} \ , \qquad [cm^{-2} s^{-1} sr^{-1}]. \tag{1.3}$$

The intensity depends also on the energy, E. The *total intensity* integrated over all energies (integral energy spectrum) is determined as

$$I_\mu(\theta, \phi, \geq E, t) = \int_E^\infty \frac{dN_\mu(E)}{dA \cdot dt \cdot d\Omega} dE \qquad [cm^{-2} s^{-1} sr^{-1}], \tag{1.4}$$

or the *differential intensity* (differential energy spectrum) is

$$I_\mu(\theta, \phi, E, t) = \frac{dN_\mu(E)}{dE \cdot dA \cdot dt \cdot d\Omega} \ , \qquad [cm^{-2} s^{-1} sr^{-1} GeV^{-1}]. \tag{1.5}$$

Usually, the energy spectra are represented by a power law (see the equation (1.1) for the differential spectrum)

$$\frac{dN}{dE} = A \cdot E^{-(\gamma+1)}, \tag{1.6}$$

with A being a constant.

For the two body decays of pions and kaons ($\pi \longrightarrow \mu\nu \; K \longrightarrow \mu\nu$), T.K.Gaisser [107] deduced the production energy spectrum of muons observed in the atmosphere. The analytic expression is

$$\frac{dN_\mu}{dE_\mu} \approx \frac{0.14 \cdot E^{-2.7}}{cm^2 \cdot sr \cdot GeV} \cdot \left(\frac{1}{1 + \frac{1.1 E_\mu cos\theta}{115 GeV}} + \frac{0.054}{1 + \frac{1.1 E_\mu cos\theta}{850 GeV}} \right), \tag{1.7}$$

where E_μ and N_μ are the energy and intensity of the muon, and θ is the zenith angle. At low energies, below 10 GeV, this parameterization overestimates the muon flux, because it does not take into account the energy loss.

The integral flux of muons through a horizontal element of area dA, per unit time dt is

$$J_\mu = \int_0^{\frac{\pi}{2}} \int_E^\infty \frac{dN_\mu(E)}{dA \cdot dt} \cdot cos\theta \cdot d\Omega dE \qquad [cm^{-2} s^{-1}], \tag{1.8}$$

with $d\Omega = 2\pi \cdot sin\theta d\theta$ and the $\frac{dN_\mu(E)}{dE}$ given by equation (1.7).

Passing through matter, muons suffer non-continuous energy losses [3] by ionization, direct electron-positron pair production, bremsstralung, and nuclear interactions,

$$-\frac{dE}{dx} = a(E) + b(E) \cdot E. \tag{1.9}$$

The coefficient $a(E)$ stands for energy losses due to ionization and atomic excitation and at high energies it is essentially constant, because it has a week logarithmic energy dependence.

The coefficient $b(E)$ is an energy dependent term, $b(E) = b_{br}(E) + b_{pp}(E) + b_{nucl}(E)$, and represents the sum of the losses resulting from pair production, bremsstrahlung, and photo-nuclear interactions [28].

Integrating the above formula, the energy of the muons after penetrating the slant depth x (for inclined muons $x = h_d/cos\theta$, h_d [m w.e.] depends strongly on the density of matter and the vertical depth) is obtained. These muons, initially having at the surface level the energy E_0, and assuming that a and b are energy independent one gets

$$\int_{E_0}^{E} \frac{dE}{E + \frac{a}{b}} = -b \cdot \int_0^x dx; \qquad ln\frac{E + \frac{a}{b}}{E_0 + \frac{a}{b}} = -b \cdot \frac{h_d}{cos\theta} \, .$$

Taking the exponential of the last expression, we obtain:

$$E_\mu(h_d) = E = (E_0 + \frac{a}{b}) \cdot e^{-\frac{b \cdot h_d}{cos\theta}} - \frac{a}{b} \, . \tag{1.10}$$

In this case, the initial energy of the muon at the surface level, in order to penetrate underground and still having at the detector depth h_d the energy $E\mu$, is

$$E_0 = (E_\mu + \frac{a}{b}) \cdot e^{\frac{b \cdot h_d}{cos\theta}} - \frac{a}{b} \ . \tag{1.11}$$

A minimum energy for the muon at the surface to reach the depth h_d is obtained when $E\mu(h_d) = 0$:

$$E_0^{min} = \frac{a}{b} \cdot (e^{\frac{b \cdot h_d}{cos\theta}} - 1). \tag{1.12}$$

Measurements of muons underground have big advantages in the sense that the momentum and intensity at lower energies can be extrapolated to higher energies with the help of underground muons. Measured high energy muons with underground detectors permit to study the primary spectrum, also primary mass composition from multi-muon events.

From the integral energy spectrum (integration of the differential spectrum (1.6)) of high energy muons at sea level (from all arriving directions) and the energy loss (equation (1.12)) the average depth-intensity relation of muons is calculated as

$$N_\mu = A \cdot E^{-\gamma} = A \cdot \left(\frac{a}{b} \cdot (e^{\frac{b \cdot h_d}{cos\theta}} - 1)\right)^{-\gamma} , \tag{1.13}$$

where A is a constant and γ the spectral exponent. For high energies the exponential dominates, and the final relation for the depth-intensity is

$$N_\mu(h_d, \theta) = A \cdot \left(\frac{a}{b}\right)^{-\gamma} \cdot e^{\frac{-\gamma \cdot b \cdot h_d}{cos\theta}} \ . \tag{1.14}$$

The energy spectrum of muons underground depends on the energy spectrum on the surface, and can be written at the detector depth h_d as (see [13])

$$\frac{dN_\mu(h_d)}{dE_\mu(E_0)} = \frac{dN_\mu}{dE_0} \cdot \frac{dE_0}{dE_\mu} \ , \tag{1.15}$$

where from the equations 1.6 and 1.11 one obtains

$$\frac{dN_\mu}{dE_0} = A \cdot \left((E_\mu + \frac{a}{b}) \cdot e^{\frac{b \cdot h_d}{cos\theta}} - \frac{a}{b}\right)^{-(\gamma+1)}$$

and

$$\frac{dE_0}{dE_\mu} = e^{\frac{b \cdot h_d}{cos\theta}} \; .$$

For moderate zenith angles and depths, the integral muon spectrum can be expressed with a zenith angle dependence at sea level, as well as underground by ([3], [28])

$$I_\theta = I(\theta = 0^0) \cdot cos^n\theta, \tag{1.16}$$

where the exponent n [28]

$$n = 1.53 + 8 \cdot 10^{-4} \cdot X(mwe) + \epsilon$$

depends on the slant depth X [mwe] and ϵ. ϵ is a small correction that arises from muon decay and ionization losses at shallow depths only. The exponent n depends also on the low energy cutoff of the detector.

At intermediate depths or at large zenith angles at shallow depths, the above zenith angle distribution is expressed as

$$I(X, \theta) = I(X, \theta = 0^0) \cdot cos^{1.53}(\theta) \cdot e^{-8 \cdot 10^{-4} \cdot X \cdot (\frac{1}{cos\theta} - 1)} \; .$$

Chapter 2

CosmoALEPH Experimental Setup

2.1 Geometrical and Geographical Arrangement

The aim of the CosmoALEPH experiment was to measure high energy cosmic muons. The period of activity dates from 1995 to 2000. The ALEPH detector provided unique challenges to analyse underground angular distributions of muons, and the multiplicity of positive and negative high energy muons [76], [77]. Due to the presence of a magnetic field in the ALEPH detector, the momentum of these muons is measured. The additional scintillator stations in the LEP tunnel give the opportunity to look for long range coincidences of high energy muons up to 1000 *m*. Since the experiment was located underground at 320 *mwe* rock depth, this imposed a cutoff energy of about 75 GeV at vertical incidence.

Different experiments measured muon coincidence rates underground, but they either were located very deep underground or looked for coincidences at small muon separations.

These studies are very important because high energy muons are produced in the first interactions in the atmosphere, carrying direct information about the primary cosmic particle.

The CosmoALEPH experiment was located at the European Laboratory for Particle Physics CERN in Geneva. The detectors were situated in the ALEPH pit of the electron-positron storage ring of LEP at CERN underground at a depth of about 125 *m* (see figure 2.1). The circumference of the LEP ring is about 27 *km*. Bunches of electrons and positrons were accelerated in the LEP ring and focused for the collision in four detectors, one of them is the ALEPH detector, which also was used in the CosmoALEPH experiment for cosmic ray physics.

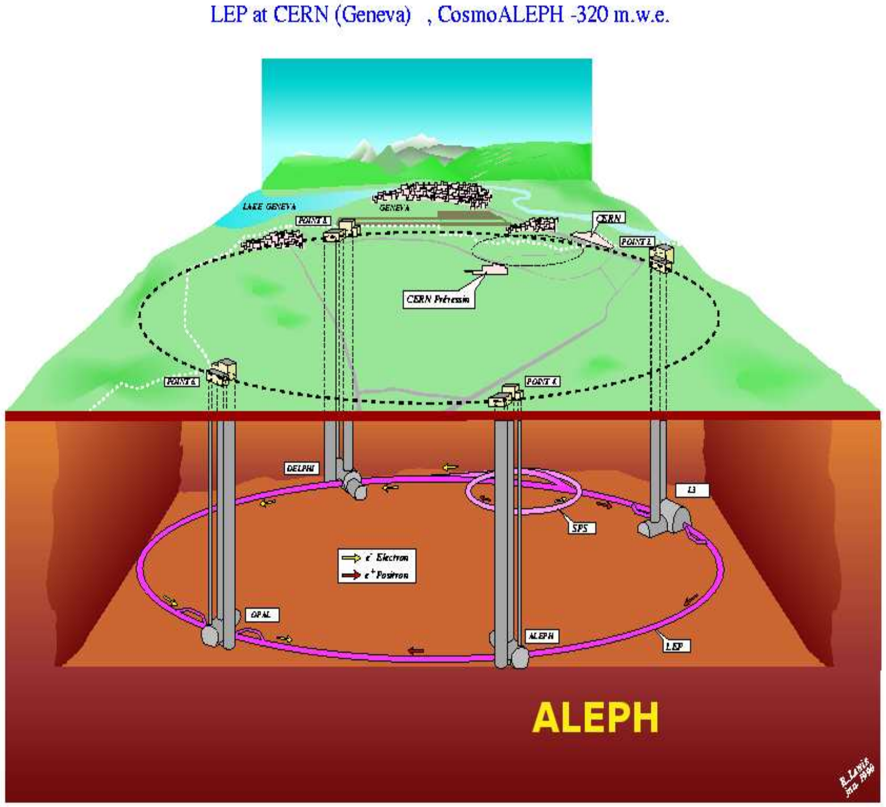

Figure 2.1: The Scheme of the LEP - ring and its detectors. The depth varies between 30 m (L3) and 125 m (ALEPH) [77].

The CosmoALEPH experiment used the Hadron Calorimeter (HCAL) of ALEPH and six scintillator stations: TROLLEY (Tro), GALLERY (Gal), BYPASS -A, -B, -C (ByA, ByB, ByC), and ALCOVE (Alc) positioned in the pit and the LEP tunnel at various distances up to 1 km (see figure 2.2), in order to study the spatial distribution of muon bundles underground.

The TROLLEY and GALLERY scintillators were placed in the ALEPH cavern close to the ALEPH detector. In 1995 the TROLLEY was placed at a distance of 7.3 ± 0.5 m from the side wall and 17 ± 1 m away from the Jura -side of the cavern. The position of the TROLLEY was changed from 1996 with a distance of 4 ± 1 m from the side of the cavern and 13 ± 1 m from the end face. The GALLERY scintillator station was active only in the year 1995, and was placed at 1.5 ± 0.5 m from the side wall of the cavern [111].

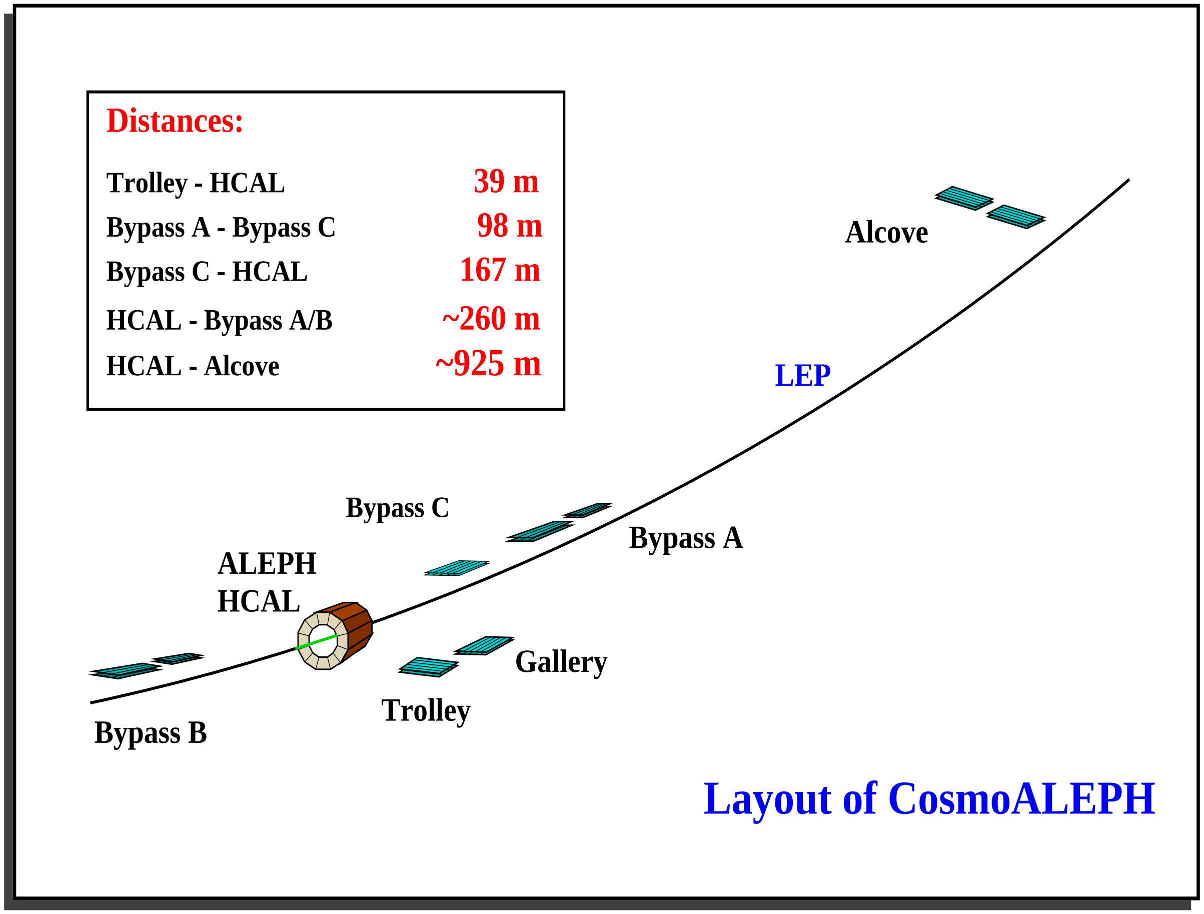

Figure 2.2: Geometrical positions of scintillator stations with respect to the ALEPH detector [108].

The BYPASSes and the ALCOVE scintillators were located in the LEP tunnel. The BYPASS C scintillator was located between ALEPH and BYPASS A. To calculate the distances between the detectors, the centre of the ALEPH detector was used as a reference with coordinates (0, 0, 0) ([110], [108], [111]). The coordinate system corresponds to the ALEPH coordinate system, with the z axis oriented along the beam pipe, y axis upwards and x axis in the direction of the LEP ring center. The coordinates of each detector are given in the Table 2.1.

Station	**Gal**	**Tro 1995**	**Tro**	**ByA**	**ByB**	**ByC**	**Alc**	**HCAL**
x [m]	54	36	39	- 10	- 10	- 13	- 110	0
y [m]	10	4.6	- 2	3	3	3	3	0
z [m]	- 4	- 2	- 6	- 262	262	- 166	- 920	0

Table 2.1: The coordinates x, y, z of individual detectors of the CosmoALEPH experiment. The Trolley station from 1996 was moved and the coordinates changed. Tro 1995 are the coordinates of the Trolley station in the year 1995.

The distances between detectors are given in the Table 2.2.

d [m]	**Gal**	**Tro 1995**	**Tro**	**ByA**	**ByB**	**ByC**	**Alc**	**HCAL**
Gal	0							
Tro 1995	18.1	0						
Tro	*	0	0					
ByA	*	*	260.6	0				
ByB	*	*	272.4	524	0			
ByC	*	*	168.2	96	428	0		
Alc	*	*	926.1	665.6	1186.2	760.2	0	
HCAL	54.1	36	39.5	262.2	262.2	166.5	926.5	0

Table 2.2: The distances between the CosmoALEPH detectors.

2.2 Scintillator Stations and Readout Electronics

Scintillator stations of the CosmoALEPH experiment consist of different numbers of stacks (see figure 2.3), each stack having two plastic scintillator counters on top of each other with readout photomultipliers at both ends ([110], [108]).

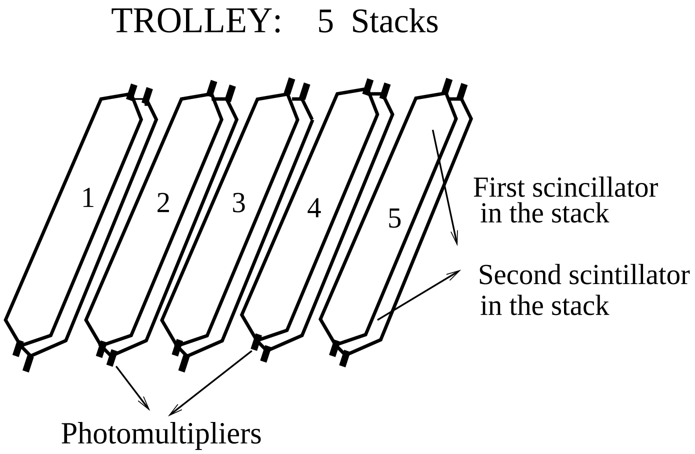

Figure 2.3: Geometry of the scintillator stacks.

Station	**Stacks**	**X x Z [m x m]**	$A^{\perp}$ [m^2]	**Y [cm]**	**Thickness [cm]**
Gal	5	0.4 x 2.2	4.40± 0.30	8	2
Tro	5	3.0 x 0.3	4.50± 0.34	8	1
ByA	1	0.4 x 2.2	5.28± 0.36	9	2
ByA	4	0.4 x 2.2		4	
ByA	1	0.4 x 2.2		16	
ByB	4	0.44 x 3.8	6.59± 0.35	10	2
ByC	2	0.4 x 2.2	4.59± 0.32	9	2
ByC	1	0.3 x 3.0		7	
ByC	1	0.3 x 3.0		10	1
ByC	1	0.5 x 2.05		15	
Alc	4	0.4 x 2.2	7.04± 0.48	7	2
Alc	4	0.4 x 2.2		8	

Table 2.3: Geometry of the stacks. The first column indicates the number of the stacks in a station, the second and the third columns give the dimensions of the scintillators in the stack, respectively the maximum area in case of vertical muons, and the fourth and the fifth columns specify the vertical separation between the scintillators in a stack and the thickness of the scintillators [110], [108], [109], [114].

Each scintillator station has a specific geometry. The number of stacks vary from station to station, the area of the scintillator counters and the separation between them vary as well. But, the pairs of two scintillators in one stack are always the same (see Table 2.3).

Uncorrelated errors of the perpendicular areas $A^{\perp}$ $[m^2]$ of the detectors are estimated assuming that the effective average width is uncertain by 2 cm and effective average length is uncertain by 10 cm [117].

Each scintillator is coupled to photomultipliers through a light guide, that is made of a material with adequate total reflection property to minimize photon losses.

To exclude electronic noise (old photomultipliers are noisy and give unwanted additional after pulses), all scintillators were red out with photomultipliers at both ends that operate in coincidence.

Signals from the photomultipliers are transmitted to a trigger data acquisition system, that consists of NIM electronics and one VME crate (see figure 2.4). The required threshold for the pulse height (above $\sim$ 70 mV [110]) at the discriminator and the scintillator coincidence, followed by a stack coincidence, reduces the non-random backround (after pulses) and random backround (caused by underground photons and thermal noise). The signals after the NIM modules were split via:

- a Delay Unit (100 ns) on a Pattern Unit, to equalize the time difference which the signal needed to pass through the Majority Logic Unit and the Trigger-Card
- and a Majority Logic Unit which did send the signal to a VME Interrupt generator. A trigger was activated when at least one of the scintillator stacks responded (a muon passing through both scintillators of one stack).

The time and the stack information were written to the VME Bus and read by the FIC (Fast Intelligent Controller). Later, all the data were transmitted from the FIC to the ALEPH-Online-Cluster ([109], [14]).

To measure the station coincidences, the time information of each event must be synchronized. For each event, a time stamp formed from the time of the readout processor, the radio frequency signal of LEP, and the BST-signal (Beam Synchronous Timing: every 88.9 μs, the time that a particle needs for one revolution in LEP) was assigned and interpolated by a 80 MHz Fast-Clock, that is provided by each station, giving a time window of 12.5 ns.

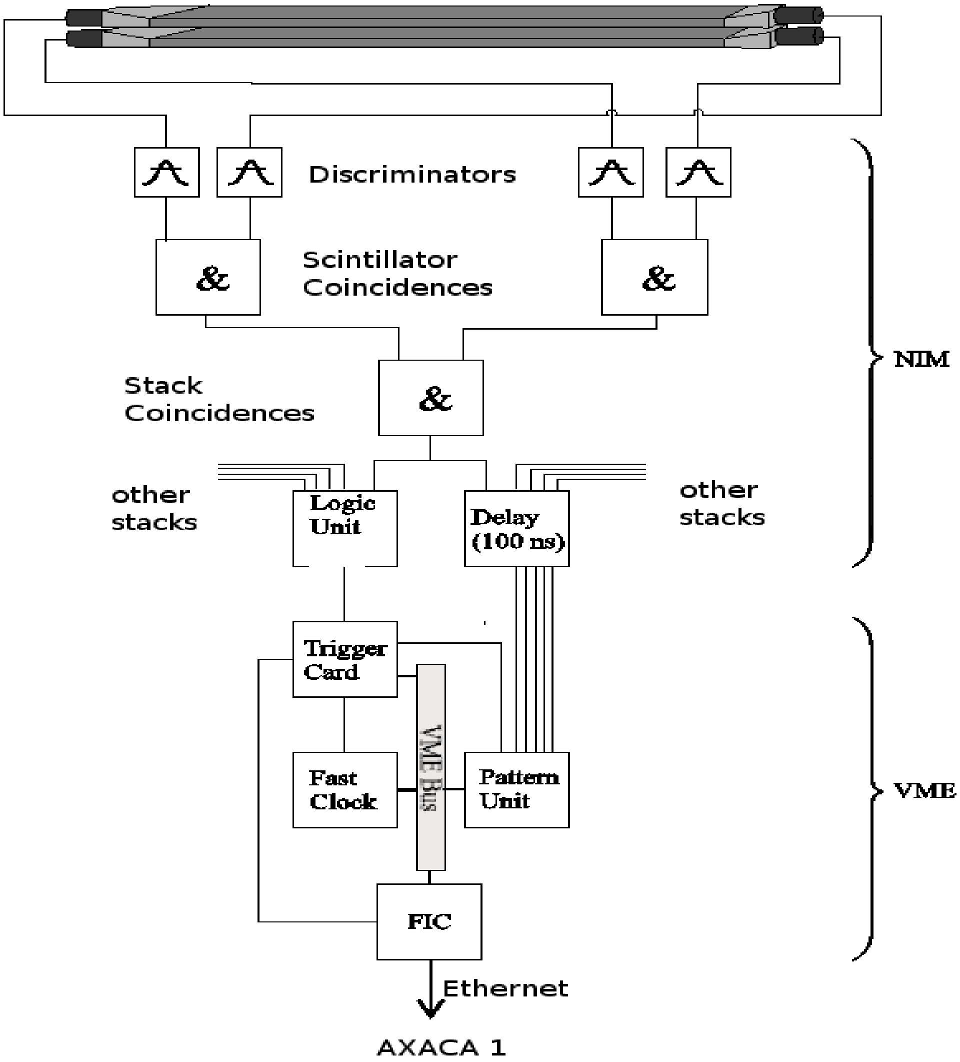

Figure 2.4: The readout electronics of the scintillator stations [108].

Thus, for a run, the time is specified by the reset cycle, turn clock reading and fast clock, both being written by the DAQ system in addition to the VAX-time of an event [117]. Scaling of the time through the BST-signal and Fast-Clock is followed in a time interval of 2.91 *seconds*, that corresponds to 32,768 counts. This interval was preset by the BST-Reset-signal. Each 2.91 *seconds* the turn clock is reset, and the VAX-time is used to infer the number of resets since the start of the run, calculating the absolute time of each event within the run. For the internal synchronization, the events were attributed to a BST-Reset-Interval with the help of the FIC-time. Global synchronization is done with a VAX of the ALEPH-online cluster, the differences of the Reset-Cycles between the stations being calculated and corrected ([109], [14]).

The readout of the data aquisition system was done by two programs, MISTDAQ for the scintillator stations and PARASITE for the ALEPH HCAL. Both programs were running on the CosmoALEPH online machine AXACA1 [110].

2.3 ALEPH Detector

The ALEPH detector was a massive installation composed of many subdetectors, with an onion arrangement of a cylindric form, to detect elementary particles produced at the collision of electron-positron bunches in the beam pipe of the detector (see figure 2.5).

The CosmoALEPH experiment used only the Hadron Calorimeter (HCAL) and the Time Projection Chamber (TPC), to measure the number of tracks for multi muon events, their direction and momentum.

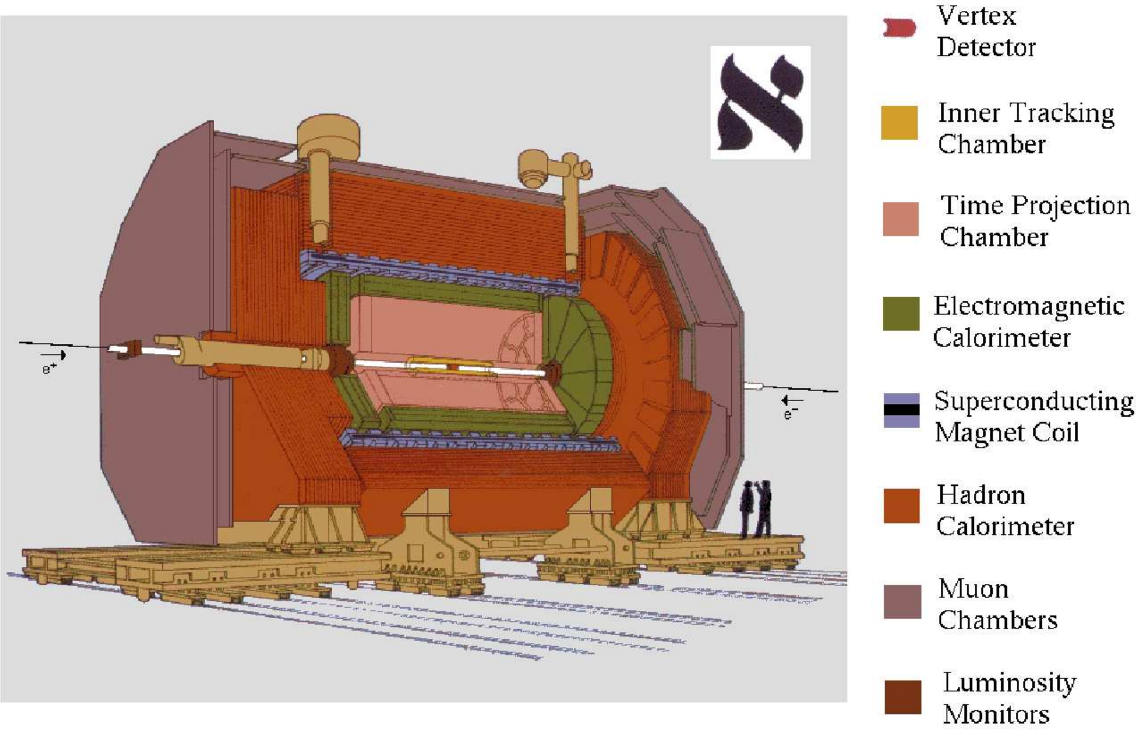

Figure 2.5: ALEPH detetor [115].

The **Hadron Calorimeter** [115] is structured into a central barrel of 7.24 *m* length with an outer radius of 4.68 *m* and inner radius of 3.0 *m*, closed with two end caps. During normal and dedicated CosmoALEPH runs, only the barrel was used for data taking. The barrel consists of 12 modules, each one split into two symmetrical parts called also supermodules (see the figure 2.6). Each module consists of 22 iron slabs of 5 *cm* thickness, spaced by air gaps in which layers of plastic streamer tubes have been inserted. The first detector layer was positioned in front of the first iron slab, thus 23 layers of plastic streamer tubes were used. The last layer of the HCAL is a iron slab of 10 cm thickness. The large iron structure of HCAL collects and returns the flux of the magnetic field. The magnetic field in the ALEPH detector was 1.5 Tesla oriented along beam line.

The streamer tubes consist of small plastic comb profiles of eight cells each with the internal surface of the comb painted with graphite. Each profile is inserted into a plastic box. On one side of the comb profile, aluminium strips of 4 *mm* are glued on a plastic support along the individual tube length. When the tube is fired, these strips provide a logic signal, that is important for the identification of muons.

In addition, outside the magnet, both in barrel and in the end-caps, two double layers of streamer tubes, called Muon Chambers, have been installed to identify tracks crossing the full amount of iron. The muon identification efficiency for HCAL together with the Muon Chambers is 86 % [115].

During normal runs, only HCAL was used for data taking. In order to accept a cosmic muon, the CosmoALEPH trigger [14] was activated if at least eight double planes in one HCAL supermodule and eight double planes in any of the three opposite supermodules fired simultaneously (see figure 2.6), a condition that is verified by the Memory Lookup Unit (MLU).

For the readout of the HCAL a special 5×64 bit pattern unit was used in connection with a FIC and the Fast Clock.

During dedicated runs taken without beams in the LEP ring the HCAL and the Time Projection Chamber were involved in the data taking process.

The **Time Projection Chamber** [115] was the central tracking detector of ALEPH with a cylindrical structure, divided into two parts by a central membrane. The electric drift field extended from each end-plate towards the membrane. The gas filling consisted of argon (91 %) and methane (9 %). The drift length was 2×2.2 *m* and the outer and inner radii were 1.8 *m*, respectively 0.31 *m*. A charged particle traversing the TPC loses energy and the electrons produced by ionization are drifted in the electric field towards one end-plate, where their arrival time and position were measured by wire chambers. The TPC measures 21 points in three dimensions on a track left by a charged particle.

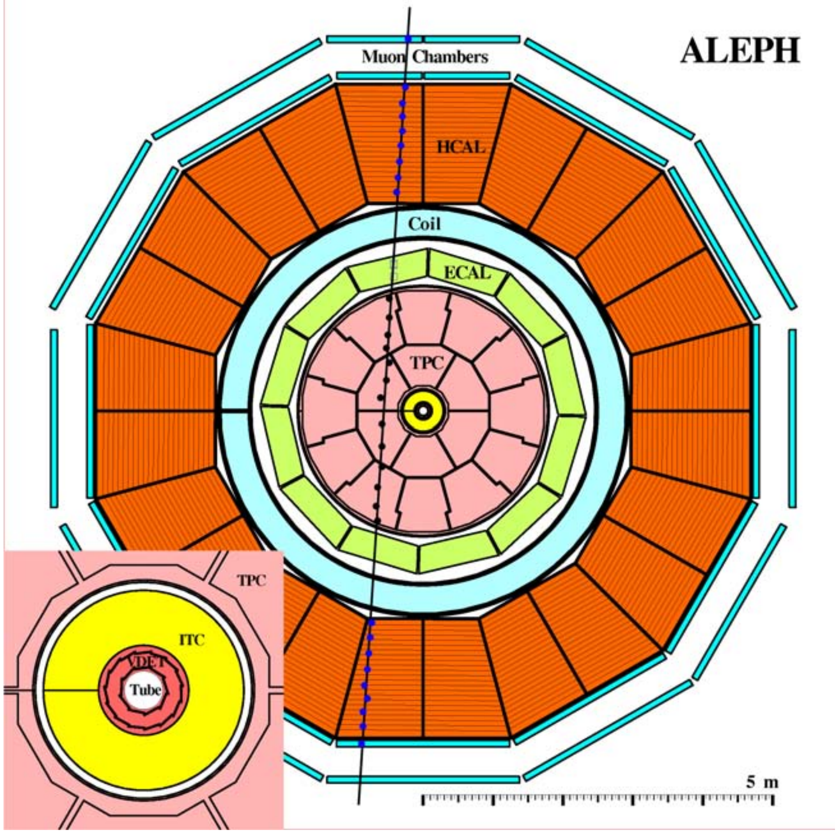

Figure 2.6: Accepted cosmic muon event by the HCAL trigger [77].

Due to the magnetic field, the trajectory of a charged particle in the TPC is curved. Measuring the radius of this helix, allows to determine the momentum of the particle. The TPC had a very high spatial ($\sim 160\ \mu m$) and momentum ($\Delta p/p \approx 2.5\%$ at 50 GeV/c and $\approx 60\%$ at 1.5 TeV/c) resolutions. This allowed to measure momenta up to about $3\, TeV$. The angular resolution was better than $2\ mrad$.

The TPC is a unique tool to investigate muon bundles also at small pair separations, that introduces an additional point at about $2\ m$ in the measured decoherence curve with scintillator stations and HCAL. Details of the analysis of muon coincidences in between the halves of the TPC are presented in the next chapter.

Chapter 3

Experimental Data Analysis

3.1 Definition of the Decoherence Curve in the CosmoALEPH Experiment

The analysis of the CosmoALEPH experimental data is based on the full data set taken between 1995 and 2000. During the data taking period about $0.9 \cdot 10^9$ events were collected with all scintillator stations within a time window of 200 μs. In addition, during dedicated CosmoALEPH runs, $1.4 \cdot 10^6$ events were recorded in the TPC in 1999 with a trigger rate of 2.5 Hz. In order to determine the muon separation distribution (pair rate as function of separations between detectors), coincidences between scintillator stations are measured. The analysis is performed separately for each year, and for the final decoherence distribution the results from all years were combined.

As described in Chapter 5, the MC simulations do not take into account the geometry and efficiency of CosmoALEPH detectors, also the overburden is not implemented. In order to compare the experimental data with MC results, the experimental data must be corrected for these parameters.

Thus, to calculate the coincidence rate at each distance $d_{i,j}$ between scintillator stations i and j, the following definition was used:

$$D\ (m^{-4}\ day^{-1}) = \frac{N_{coin}}{\varepsilon_i \varepsilon_j\ A_{eff_{i,j}}\ \epsilon_{ov_i} \epsilon_{ov_j}\ T_{i,j}}\ , \tag{3.1}$$

where

N_{coin} is the background-subtracted coincidence rate

$\varepsilon_{i,j}$ are single muon efficiencies of the stations

$A_{eff_{i,j}}$ is the combined effective area of detectors in coincidence

$\epsilon_{ov_{i,j}}$ correction factors for difference in thickness of the overburden on top of each detector

$T_{i,j}$ is the common effective up time of the stations in days

The analysis of the parameters used in the above definition is presented in the following sections.

3.2 Geometrical Acceptances

The geometry of the CosmoALEPH detectors limits the angular phase space. Because of their small dimensions and the distance between stacks, the detectors register only a small part of muons that hit the experimental installation.

For a homogeneous flux of muons through the surface of a scintillator with rotational symmetry around the vertical direction, the geometry factor or geometrical acceptance is defined as the ratio [113]

$$g = \frac{muon\ flux\ through\ upper\ and\ lower\ scintillator}{muon\ flux\ through\ the\ upper\ scintillator}\ . \tag{3.2}$$

In order to determine the geometrical acceptances, a full geometry simulation for each geometry configuration, for each scintillator station and HCAL, was performed ([14],[114]). To describe the zenith angle distribution of muons at shallow depths underground for the muon flux through a horizontal detector area at 320 mwe the following equation was used

$$\frac{dN}{d\theta} = cos^n\theta \cdot cos\theta \cdot sin\theta, \tag{3.3}$$

where the exponent $n = 1.79$ from the formula $n = 1.53 + 8 \cdot 10^4 \cdot X(mwe)$, was calculated for our depth.

On a horizontal area of 10 m × 10 m with variable orientation, single muon tracks for HCAL were uniformely generated according to the angular distribution (3.3). The intersection of muon tracks with the double planes of HCAL was calculated, for which the measured average efficiency of double planes of 0.862 was set. This analysis was done with the implemented 8 & 8 standard trigger verification algoritm [14].

The effective area A_{eff} of the HCAL was calculated as

$$A_{eff} = area\ of\ generation \cdot \frac{accepted\ tracks}{generated\ tracks} = 10.4\ m^2, \tag{3.4}$$

with a geometrical acceptance $g = 0.1039$ [114] calculated with the 8 & 8 trigger algoritm.

The geometrical acceptance without the 8 & 8 trigger algoritm for HCAL is assumed to be $g = 1.0 \pm 0.021$ [117].

In case of the scintillator stations, the acceptances were calculated as average over all stack types in all individual stations.

The values for geometrical acceptances of single CosmoALEPH detectors calculated for the maximum areas $A^{\perp}$ are presented in the table 3.1.

Station	**Max. Area** $[m^2]$	**Acceptance** (g)	A_{eff} $[m^2]$
Gal	4.40	0.8838±0.016	3.889
Tro	4.50	0.8501±0.017	3.825
ByA	5.28	0.8979±0.011	4.741
ByB	6.59	0.8765±0.010	5.862
ByC	4.59	0.8130±0.038	3.970
Alc	7.04	0.8839±0.025	6.220
HCAL	100.	0.1039±0.021	10.39

Table 3.1: Geometrical acceptances of CosmoALEPH detectors [114].

The uncorrelated errors of the geometrical acceptances were estimated from the uncertainty of the used angular distribution of muons in the MC simulation.

The combined effective area of the detectors in coincidence is determined as

$$A_{eff_{i,j}} = \rho_{i,j} \cdot A_i^{\perp} \cdot A_j^{\perp} \cdot g_i \cdot g_j,$$

where $\rho_{i,j}$ is a parameter responsible for the stack orientation.

The BYPASS C scintillator station had only a four stack configuration in the year 2000, which introduces a scaling factor of 0.8 for the numbers obtained for this configuration. The effective area and the geometrical acceptance for the detectors in coincidence are presented in the table 3.2.

Station 1	**Station 2**	$\mathbf{g_{i,j}}$	$\rho_{i,j}$	$A_{eff_{i,j}}$ $[m^2]$
Gal	**Tro**	0.7578	1.0086	15.005
Gal	**ByA**	0.8023	1.0107	18.640
Gal	**HCAL**	0.0899	0.9788	39.594
Tro	**HCAL**	0.0941	1.0643	42.339
Tro	**ByA**	0.7688	1.0072	18.267
Tro	**ByB**	0.7515	1.0078	22.617
Tro	**Alc**	0.7579	1.0087	24.012
ByA	**ByB**	0.7967	1.0113	28.133
ByA	**ByC**	0.7082	0.9690	18.266
ByA	**Alc**	0.8025	1.0109	29.829
ByA	**HCAL**	0.0917	0.9822	48.432
ByB	**ByC**	0.6945	0.9727	22.689
ByB	**Alc**	0.7861	1.0136	37.012
ByB	**HCAL**	0.0887	0.9720	59.308
ByC	**HCAL**	0.0784	0.9265	38.308
ByC	**Tro**	0.6681	0.9657	14.686
ByC	**Alc**	0.6990	0.9717	24.040
Alc	**HCAL**	0.0900	0.9793	63.381

Table 3.2: Combined acceptances and effective area of the CosmoALEPH detectors in coincidence [114], [117].

3.3 Efficiencies

A detailed study of the efficiencies of the CosmoALEPH detectors is presented in [14], [112], [113], [114], and [116].

HCAL efficiency

The HCAL efficiencies were determined from the PARASITE runs and the analysis is based on the following requirements:

- A single muon event must pass through exactly two supermodules, one in each hemisphere
- At least eight double planes must be hit in both supermodules (see figure 2.6), not counting the double plane whose efficiency is checked.

The efficiency of the double plane was calculated by

$$\varepsilon = \frac{n}{N} \, , \tag{3.5}$$

where n is the number of events registered by the fired double plane in question, and N is the total numbers of triggers. Statistical errors are calculated from the binomial distribution

$$\Delta\varepsilon = \sqrt{\frac{1}{N} \cdot \varepsilon \cdot (1-\varepsilon)} \ . \tag{3.6}$$

The average efficiency of the double plane $\bar{\varepsilon}_{dpl}$ was calculated from the single plane efficiency ε_{spl}, in case when the efficiencies of single planes are identical

$$\bar{\varepsilon}_{dpl} = 2 \cdot \varepsilon_{spl} - \varepsilon_{spl}^2 \ . \tag{3.7}$$

A global error for the double planes was estimated and is equal to $\varepsilon = \pm 0.02$ [116].

This analysis was performed for all years of the data taking period with HCAL. The average efficiency of the double planes for all years are presented in the table 3.3.

Years	**1995**	**1996**	**1997**	**1998**	**1999**	**2000**
$\langle\varepsilon\rangle$	0.850	0.860	0.862	0.866	0.867	0.868

Table 3.3: Average efficiencies of the HCAL double planes for all years of the run [116].

From these numbers an average efficiency of the double planes of HCAL for all years is set to 0.862.

Scintillator station efficiencies

In order to determine the efficiencies of the scintillator stations, special efficiency runs were analysed. For this, one time every year the electronics of each station was recabled [110]. During at least a 24 hour run, one layer was declared as trigger layer, then the trigger and readout layer were swapped and a new efficiency run was started with the same time duration. To register only muons, for the layers that trigger, the threshold of the discriminators of the upper or lower scintillators of the station were increased. The total rate on a single scintillator was set to about 0.5 Hz [112]. Even this condition did not exclude the triggering by photons present in large amounts at the CosmoALEPH experiment level due to radioactive decays from the overburden material.

The efficiency of the upper scintillator in the selected sample of runs is calculated when the lower scintillator is set as trigger. The efficiency of the lower scintillator is then determined when the upper scintillator was selected as trigger. Knowing the geometry factor for each station (see table 3.1), the true efficiency of a single stack for vertical muons was determined as

$$\varepsilon = \frac{\varepsilon_{up.scint.} \cdot \varepsilon_{low.scint.}}{g^2} \, , \tag{3.8}$$

since the scintillator efficiencies already include the geometric acceptance of the stack by design.

The efficiency analysis was performed with the following condition ([114], [112]):

- Trigger plus single stack scheme.

To determine the efficiency of the readout layer of a stack, a hit in the trigger layer of this stack was required, plus a coincidence in one of the other stacks of the station (see the figure 3.1). Since the analysis is done for the single muon efficiency, an error of 5 % for this method is assumed.

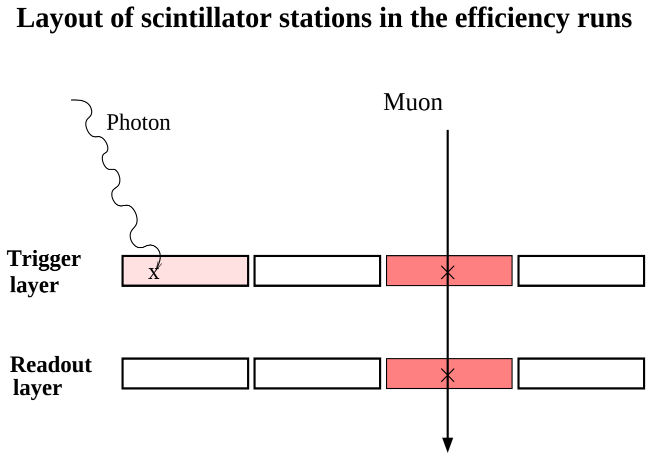

Figure 3.1: Efficiency analysis of the scintillators with the scheme "trigger plus single stack".

A problem arises from the fact that, imposing a high threshold, the trigger efficiency for muons is low, and inclined muons that travel a long distance through the scintillator are preferred. This reduces the geometry factors and, thus affects also the efficiencies.

This effect was corrected from the data for the coincidence analysis. A true geometry factor g_t was calculated assuming that muons which hit the upper trigger layer but miss the lower readout layer will hit the left or the right neighbour (see figure 3.2).

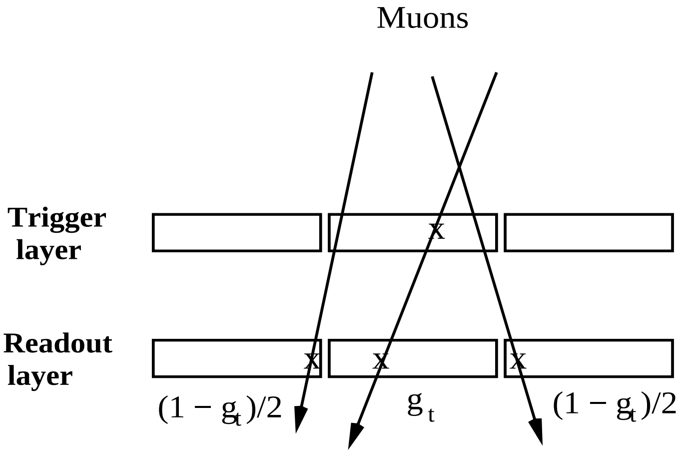

Figure 3.2: Efficiency analysis of the scintillators with the scheme "trigger plus single stack".

For the raw efficiencies of the stacks ε_1, ε_2, calculated according to the equation

$$\varepsilon_{stack} = \varepsilon_{up.scint.} \cdot \varepsilon_{low.scint.} \ ,$$

The number of hits n_1 in the readout scintillator under the trigger, and the number of hits n_2 in the neighbouring scintillator, are determined by

$$n_1 = N \cdot \varepsilon_1 \cdot g_t \qquad and \qquad n_2 = N \cdot \varepsilon_2 \frac{1 - g_t}{2} \ ,$$

where N is the number of muons that gave a trigger. From these two equations g_t is deduced as

$$g_t = \frac{1}{1 + 2 \cdot (n_2 \cdot \varepsilon_1)/(n_1 \cdot \varepsilon_1)} \ .$$

The obtained geometry factor is valid only for the case when there is no gap between the stacks. The true geometrical factors calculated from the data for each station are presented for all years of data taking in table 3.4.

Thus, the nominal geometry factors (table 3.1) are corrected by a scaling factor determined as $s = g_t/g$. From this consideration, with the corrected geometry factor, the true efficiency of a single stack for vertical muons was calculated as

$$\varepsilon = \frac{\varepsilon_{up.scint.} \cdot \varepsilon_{low.scint.}}{(g \cdot s)^2} = \frac{\varepsilon_{stack}}{(g \cdot s)^2} \ , \qquad (3.9)$$

The final efficiencies of the scintillator stations and true geometry factors are presented in the table 3.4.

Station	**Year(s)**	**Raw Efficiency** (ε_{stack})	$\mathbf{g_t}$
Gal	95/11	0.469 ± 0.014 (0.012, 0.007)	0.792 ± 0.033
Tro	95/11	0.530 ± 0.029 (0.023, 0.018)	0.785 ± 0.038
	96/12	0.563 ± 0.023 (0.017, 0.015)	0.766 ± 0.020
	97/12	0.530 ± 0.020 (0.016, 0.012)	0.766 ± 0.025
	99/03	0.549 ± 0.016 (0.011, 0.012)	0.762 ± 0.028
	99/08	0.561 ± 0.027 (0.021, 0.017)	0.761 ± 0.024
	00/02	0.554 ± 0.016 (0.011, 0.012)	0.758 ± 0.024
	Combined	**0.549 ± 0.015 (0.006, 0.014)**	**0.764 ± 0.010**
ByA	97/12	0.610 ± 0.015 (0.008, 0.013)	0.926 ± 0.024
	99/03	0.612 ± 0.013 (0.006, 0.012)	0.925 ± 0.026
	99/08	0.581 ± 0.015 (0.007, 0.013)	0.927 ± 0.021
	00/02	0.615 ± 0.014 (0.005, 0.013)	0.924 ± 0.026
	Combined	**0.607 ± 0.013 (0.003, 0.013)**	**0.926 ± 0.012**
ByB	99/03	0.714 ± 0.051 (0.007, 0.051)	0.776 ± 0.022
	99/08	0.728 ± 0.038 (0.006, 0.037)	0.767 ± 0.023
	00/02	0.736 ± 0.029 (0.007, 0.028)	0.764 ± 0.028
	Combined	**0.726 ± 0.039 (0.004, 0.039)**	**0.770 ± 0.014**
ByC	99/08	0.448 ± 0.021 (0.006, 0.020)	0.829 ± 0.037
	00/02	0.456 ± 0.021 (0.005, 0.020)	0.830 ± 0.051
	Combined	**0.453 ± 0.020 (0.004, 0.020)**	**0.820 ± 0.030**
Alc	97/12	0.581 ± 0.012 (0.007, 0.010)	0.839 ± 0.063
	00/02	0.578 ± 0.009 (0.005, 0.017)	0.843 ± 0.022
	Combined	**0.579 ± 0.015 (0.004, 0.014)**	**0.842 ± 0.021**

Table 3.4: True geometry factors calculated from the data and stack efficiencies of the scintillator stations with the total errors. Statistical and systematic errors are presented in parentheses [117].

The errors of the stack efficiency represent a combination of statistical and systematical errors. For a general scaling of the geometry factor, the scaling factor is considered to be $s = 0.9$ for scintillator stations and s = 1 for HCAL [117].

3.4 Overburden Corrections

The CosmoALEPH scintillator stations are situated in the ALEPH cavern and the LEP tunnel at different depths, and to present the muon separation distribution, the muon coincidence rates between the CosmoALEPH detectors require to be corrected for the difference in overburden, which will bring all stations to the same depth.

The analysis of the overburden corrections [111] is based on the determination of the muon flux for each individual station, values which are corrected to a reference muon flux at the depth of 320 *mwe* below the surface.

The overburden above ALEPH and LEP consists mainly of moraine and molasse material, with a density of 2.2 g/cm^3, and 2.5 g/cm^3 respectively. The overburden from the ceiling of the cavern to the surface is 125 *m*, which corresponds to 300 ± 2 *mwe*. Taking into account the

- increased topography over the LEP construction, which is about 5 ± 3 *m* of moraine with an equivalent of 11 ± 6.6 *mwe*,
- infrastructure at the surface of 1.0 ± 0.5 *m* of concrete, or 2.5 ± 1.2 *mwe*, since the density of concrete is the same as for molasse,
- the fact that the moraine layers contain water in the range of about 10 %, that introduce an additional 1 *mwe*,

the total overburden for the cavern amounts to 314.5 ± 7 *mwe*.

The overburden over HCAL was estimated from the account of the influence of the curved ceiling in the cavern. With a MC simulation, generating muons over the effective area of 10.4 m^2 of HCAL, the difference between the average height where the muon enters the wall and the apex of the cavern was determined. This corresponds to an extra overburden of 1.4 *m* concrete or 3.5 *mwe*. Summing this to the total overburden, 319 ± 7 *mwe* is obtained for HCAL.

The TROLLEY and GALLERY scintillator stations were also situated in the ALEPH cavern. Since the TROLLEY was moved in 1996 from its place closer to the side wall and taking into account the radius of the ceiling, which is 10.7 *m*, for the TROLLEY an overburden of 323 ± 7 *mwe* for 1995, and an overburden of 326 ± 7 *mwe* for years 1996 - 2000 were determined.

The GALLERY was situated even closer to the wall, 1.5 *m* from the wall. The uncertainty of the overburden are in the case of the stations in the cavern dominated by the distance from the wall, since the effect of the ceiling determinates more or less overburden over the detectors. For the GALLERY an extra overburden of 4.9 ± 0.4 *m* molasse, or 12.2 ± 1 *mwe* was determined, that, summed to the 314.5 ± 7 *mwe*, gives a total overburden of 327 ± 7 *mwe*.

The BYPASS A, -B, -C and ALCOVE stations were situated in the LEP tunnel close to the ceiling with a radius of 2.5 m, that introduces an extra overburden of 8.2 m of molasse in comparison to the ceiling of the ALEPH cavern. Taking into account that the LEP tunnel was constructed with a small inclination of about one degree, which results in a decrease of the amount of overburden in the directions away from the ALEPH cavern, and using the information from the topographic maps, the difference in the thickness of the moraine above ALEPH and different stations was calculated. The total overburden for all CosmoALEPH detectors are summarized in table 3.5.

Stations	**Overburden [mwe]**
Reference	320
Gal	327 ± 7
Tro 1995	323 ± 7
Tro	326 ± 7
ByA	311 ± 7
ByB	311 ± 7
ByC	344 ± 7
Alc	289 ± 7
ALEPH	319 ± 7

Table 3.5: The overburden over the CosmoALEPH stations. The errors in the cavern are fully correlated, the errors in the tunnel are independent [111].

The flux of muons underground can be calculated from the muon spectrum at the surface and the energy loss through the overburden.

To determine the expected flux for each CosmoALEPH detector, the equation for the integral flux through a horizontal area (1.8) was used, with the differential muon spectrum at the surface level given by the Bogdanova parameterization [125]

$$\frac{d^2N}{d\Omega \cdot dP} = \frac{18}{P \cdot cos\theta + 145} \cdot (P + 2.7 \cdot sec\theta)^{-2.7} \cdot \frac{P+5}{P+sec\theta} \ . \tag{3.10}$$

The muon momentum P is measured in the range $1 \leq P \leq 10^5$ GeV/c, and θ is the zenith angle of the muon. This parameterization is compared with the Gaisser parameterization (see equation (1.7)), which is valid for energies above 100 GeV (see the figure 3.3). Due to differences in the region of 100 GeV - 1 TeV, a systematic error of 5 % is added to the total flux that is calculated for each CosmoALEPH detector.

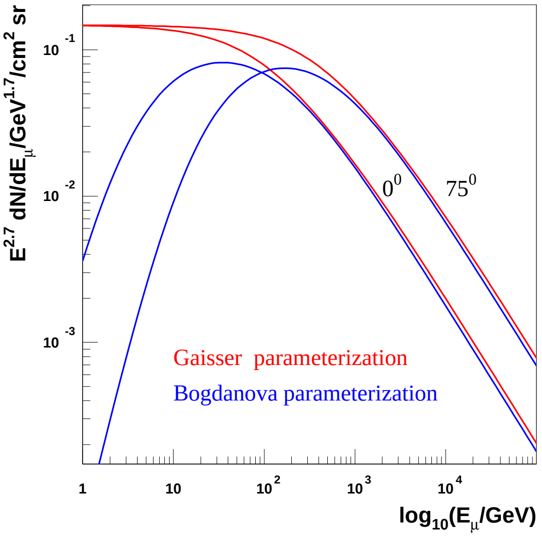

Figure 3.3: The muon energy spectra at sea level for the energy interval $1 \leq P \leq 10^5$ GeV, at 0^0 and 75^0 zenith angle, with Bogdanova (blue line) and Gaisser (red line) parameterizations.

The minimum value of the lower integration limit is determined according to equation (1.12) with the requirement of a minimum energy at the detector depth in case of scintillator stations, and equation (1.11) in case of HCAL. Muons should have an energy of 8 ± 3 GeV to pass through HCAL. The thickness of the overburden for each CosmoALEPH detector is taken from table 3.5.

The parameters a and b are considered constant and they were determined for Standard Rock (SR) (density 2.69 g/cm^3, Z = 11, A = 22) being close to the chemical composition of the CERN soil $\frac{Z}{A} = 0.5$ [111]. Since we expect an energy cut-off larger than 100 GeV for all zenith angles of muons on average, a value of $4 \cdot 10^{-6}$ cm^2/g is assumed for the coefficient b from its energy dependence (see [28], p.463). a was taken as $a = 2.2\ MeV \cdot cm^2/g$.

The $\frac{1}{cos\theta}$ term in the equation for the energy loss (1.12), according to the angular distribution $dN/dcos\theta \sim cos^n\theta$, is averaged over all zenith angles

$$\langle\frac{1}{cos\theta}\rangle = \frac{\int_0^1 \frac{1}{cos\theta} \cdot cos^n\theta\ d(cos\theta)}{\int_0^1 cos^n\theta d(cos\theta)} = \frac{n+1}{n},$$

where n at the CosmoALEPH depth has the value $n(320mwe) = 1.79 \pm 0.20$

Stations	**Flux (F_0 [Hz/m^2])**
Reference	0.320
Gal	0.304 ± 0.017
Tro 1995	0.313 ± 0.017
Tro	0.306 ± 0.017
ByA	0.342 ± 0.021
ByB	0.342 ± 0.021
ByC	0.269 ± 0.015
Alc	0.406 ± 0.025
ALEPH	0.267 ± 0.023

Table 3.6: Flux expected for the CosmoALEPH detectors [111].

obtained from the parameterization [14]

$$n = 1.53 + 8 \cdot 10^{-4} \cdot X/mwe \ .$$

After the integration of equation (3.10) according to the definition for the integral flux (1.8), with the lower energy limit calculated from the energy loss relation (1.12) and with zenith angles varying from 0^0 to 90^0, the values for the flux are obtained for each CosmoALEPH detector (see table 3.6).

The errors here originate from the uncertainty of the overburden depth, and from the uncertainty of the overburden chemical composition. For HCAL, an uncertainty arises from the energy cut, which is estimated to be 8 ± 3 GeV.

The overburden corrections are calculated from the obtained flux for each station as the ratio of the expected flux for each station and the expected muon flux at the reference depth of 320 mwe.

Station	**Flux ratio (ϵ_{ov_i})**	**Gal**	**Tro 1995**	**Tro**	**ByA**	**ByB**	**ByC**	**Alc**
Gal	0.950 ± 0.053							
Tro 1995	0.978 ± 0.055	1.00						
Tro	0.956 ± 0.053	1.00	1.00					
ByA	1.069 ± 0.066	0.16	0.16	0.16				
ByB	1.069 ± 0.066	0.16	0.16	0.16	0.15			
ByC	0.841 ± 0.047	0.16	0.16	0.16	0.15	0.15		
Alc	1.269 ± 0.078	0.15	0.15	0.15	0.14	0.14	0.14	
ALEPH	0.834 ± 0.072	0.61	0.61	0.61	0.10	0.10	0.10	0.09

Table 3.7: Correction factors for the overburden to the 320 *mwe* reference with their errors and correlation matrix [111].

A study of the decoherence distribution at different depths with different Monte Carlo interaction models showed that the actual overburden corrections for coincidence rates depend on the distance between detectors, mostly at small distances (see Appendix B). Since this dependence is of the order of 5 %, an error of 5 % is added to the overburden corrections. The final correction factors for different values of the overburden ϵ_{ov_i} for station i are presented in table 3.7 along with their errors and correlation coefficients.

3.5 Data Quality Requirements and Coincidences between CosmoALEPH detectors

The procedure of the analysis of coincidences between different stations follows after the determination of the absolute time calibration for each event, and the uptime of the station in the period of activity. The CosmoALEPH hardware had a deadtime between 1 and 3 ms. In the coincidence analysis a uniform deadtime of 4 ms was introduced by software and taken into account in the uptime calculation. For coincidences between detector stations, the combined uptime was determined from the overlap of the uptimes of the detectors in the coincidence.

A very detailed description of the data analysis is presented in [117]. The analysis of coincidence rates is based on some data quality requirements:

- A correction was introduced from the information of the deadtime. All events which are closer than 4 ms to the previous one were rejected. Thus, a deadtime of 4 ms per event was enforced.
- In the fast clock distributions (see figure 3.4) distinct spikes were observed which appeared because the fast clock was synchronized to the LEP frequency. These spikes were removed in the data analysis.

To reject the problematic runs for each scintillator station the following cuts were defined [117]:

- The number of accepted events is required to be larger than 10.
- The fraction of rejected events is required to be less than 0.1
- The fraction of empty events within a run is required to be less than 1 %. Empty events with time information are explained as delayed signals in the pattern unit which have missed the gate of the coincidence units.

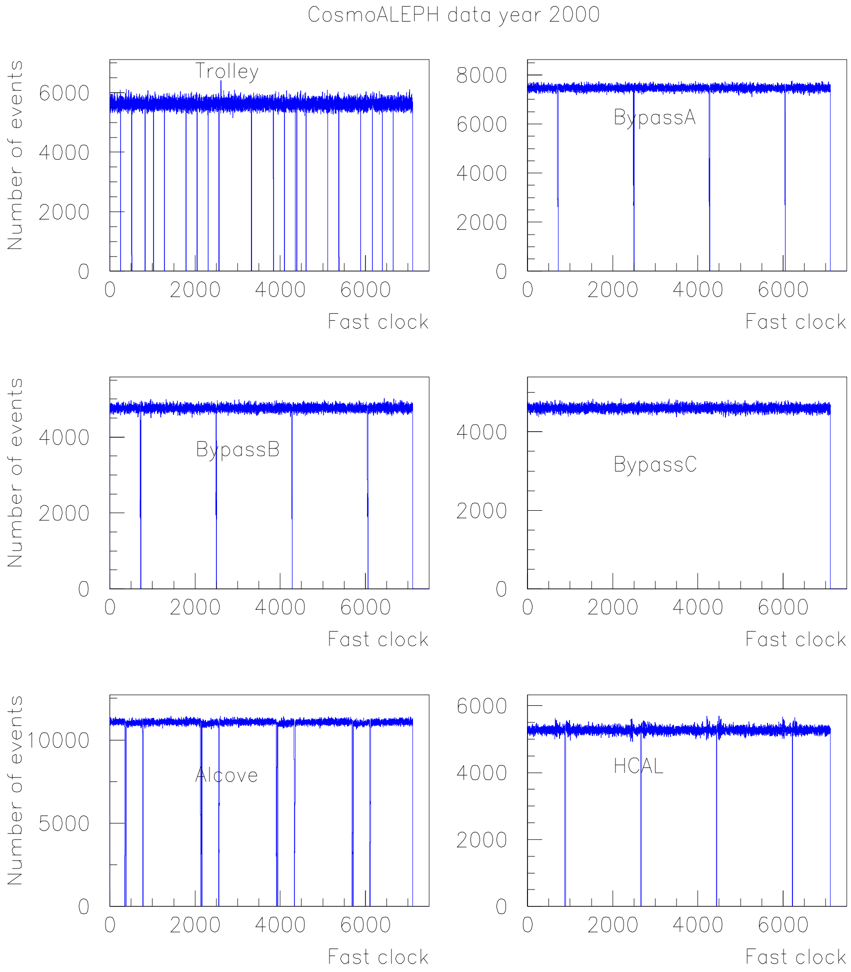

Figure 3.4: Fast clock reading for some CosmoALEPH detectors.

- The average time between subsequent events is required to be less than the cut parameter for the time difference (*dtcut*) which is based on the muon flux, station areas and efficiencies:

$$\langle dt \rangle = \frac{1}{F_0 \cdot A^{\perp} \cdot g \cdot \varepsilon},$$

where F_0 $[Hz/m^2]$ is the expected flux for the CosmoALEPH detectors (see table 3.6), g are the geometrical acceptances of the CosmoALEPH detectors (see table 3.1), ε is the efficiency of a single stack for vertical muons given by equation (3.9) with the values of raw efficiencies given in table 3.4. $A^{\perp}$ $[m^2]$ represents the maximum area for each detector with the values given in table 2.3. The cut parameter for the time difference is not equal to $\langle dt \rangle$ in case of HCAL, since there is no photon background. In case of Bypass B (the obtained efficiency of this station from the efficiency runs is not reliable) and HCAL, the cut parameter *dtcut* was adjusted by hand to match the measured rates [117]. In figures figures 3.5 and 3.6 the measured coincidence rates with each CosmoALEPH detector for all years of activity are presented.

- The equivalent number of active stacks in a station

  $$n_{eq} = \frac{[\sum_i (number\ of\ hits\ seen\ on\ stack\ i)]^2}{\sum_i (number\ of\ hits\ seen\ on\ stack\ i)^2}$$

  must be greater than a defined cut parameter $ncut = n - 0.5$.

  n_{eq} is equal to the physical number of stacks n if all stacks in a scintillator station have fired and have the same number of hits. An exception is the ALCOVE station which was placed very close to the LEP beam, and the expected background from multiple scattered photons may be very large. Thus, for the ALCOVE station a cut of $n_{eq} > n - 1.5$ was imposed.

The values for both cut parameters: time difference and number of equivalent stacks are presented in the table 3.8.

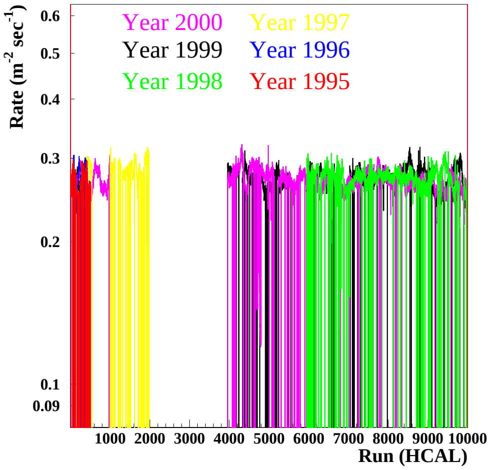

Figure 3.5: The cosmic muon rates of ALEPH's HCAL.

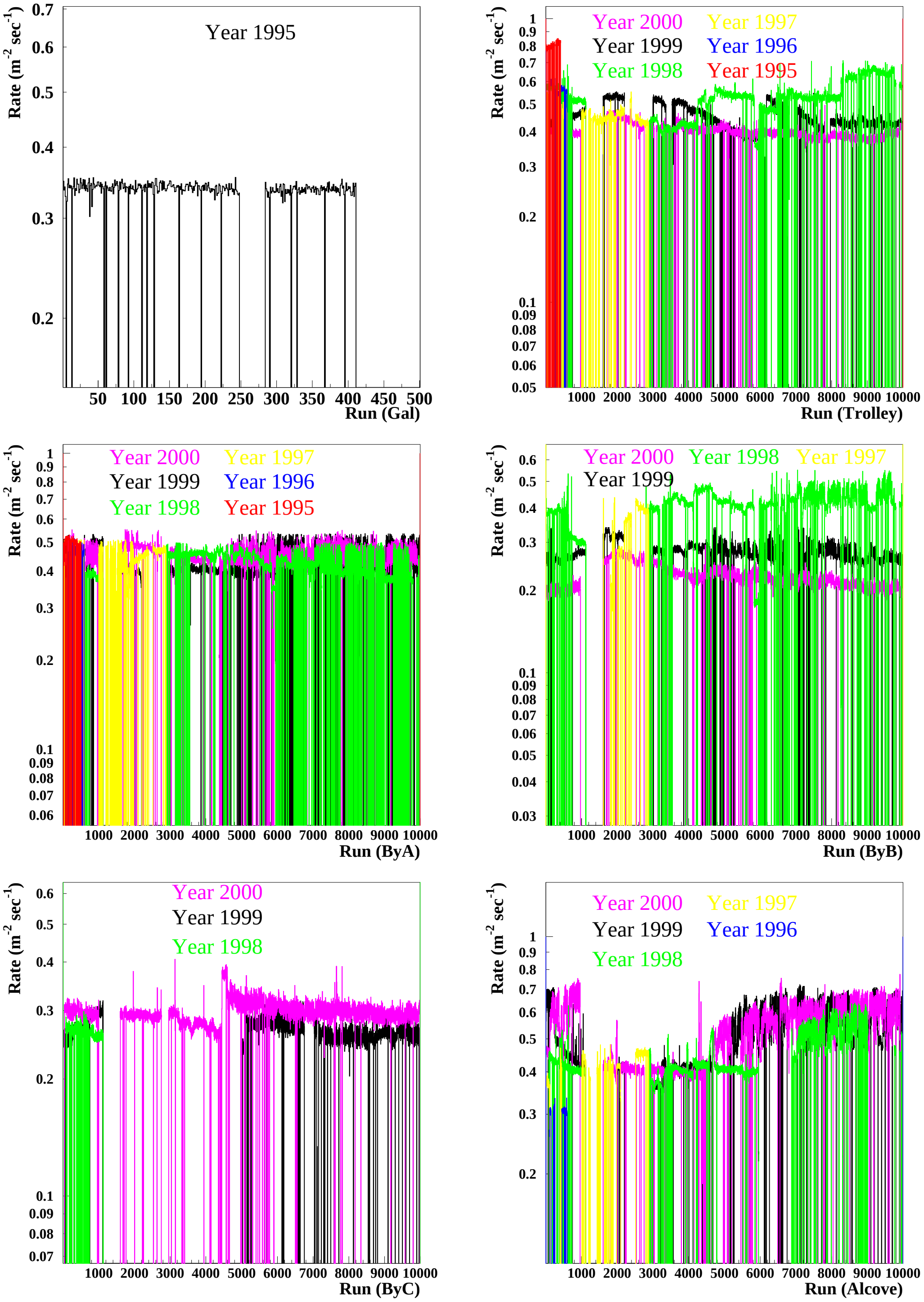

Figure 3.6: Cosmic muon rates of CosmoALEPH scintillator stations normalized on time and area.

Station	$\langle dt \rangle$ [s]	**dtcut**	**ncut**
Gal	1.141	1.141	4.5
Tro	0.911	0.911	4.5
ByA	0.664	0.664	5.5
ByB	0.428	0.850	3.5
ByC	1.105	1.105	4.5
Alc	0.425	0.425	6.5
HCAL	0.360	0.500	*

Table 3.8: Cut values for the expected average time difference between events and for the equivalent number of active stacks [117].

- A test variable
  $$E = \sqrt{n} \cdot (\frac{n \cdot S_2}{2 \cdot S_1^2} - 1) > 2.5 \ ,$$
  which is gaussian distributed with a mean value of zero and standard deviation one was introduced to verify the exponential shape of the distribution of time differences between subsequently accepted events. The variable E was calculated for $x = dt - 4 \ ms$ in order to correct for dead time, where for n events $S_k = \sum_{i=1}^{n} x_i^k$. In case of runs with limited statistics there are deviations from the gaussian shape. Thus, runs with a non-exponential time difference distribution were excluded from the analysis.

For all runs, which satisfied the data quality cuts, the coincidences between the CosmoALEPH detectors were analysed year by year.

The coincidence window was set to $\pm(1\mu s + \sum \mathit{cable\ delays})$ around $\Delta t = 0$. Cable delays are given in table 3.9.

Station	**Gal**	**Tro**	**ByA**	**ByB**	**ByC**	**Alc**	**HCAL**
delay [ns]	800	727	1311	1199	824	3897	0

Table 3.9: The cable delays of the CosmoALEPH detectors [118].

The interval, where the background is calculated, was defined as:

$$20 \ \mu s \ < \mid \Delta t \mid < \ 70 \ \mu s.$$

Results of the coincidences in different years were combined by a weighted average and presented in a single number. An exception is the combination of Trolley with HCAL, since Trolley was moved from its place since 1996. For this combination two values for the coincidence rate, for the year 1995, and an averaged value for the years 1996 - 2000, were calculated.

The distances between the CosmoALEPH detectors were calculated in the horizontal plane xz from the centers of the detectors in the pair. The errors of the distances are $\sigma_d = \sqrt{\sum_{i=1,2} A_i^{\perp}}$. The values of the distances $d_{i,j}$ between detectors and the coincidences normalised on time $N_{coin}/T_{i,j}$ [coincidences/day] are presented in table 3.10.

The distributions of muon arrival time differences are presented in figure 3.7.

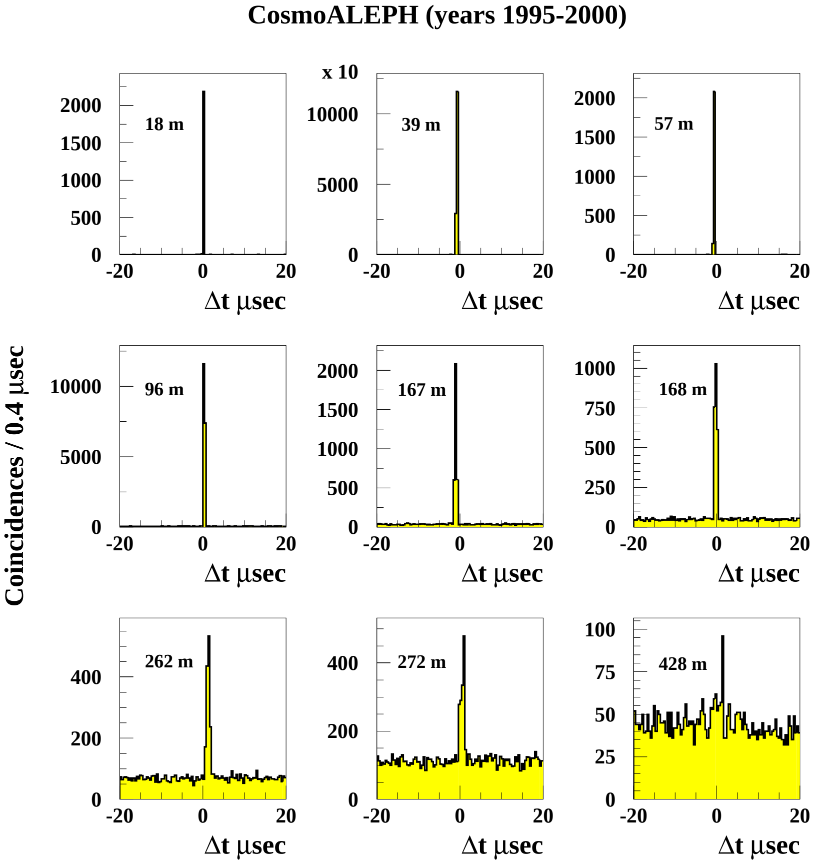

Figure 3.7: Distributions of the muon arrival time differences for the detectors in coincidence. The y axis shows the number of muon coincidences [120].

The distance between pairs of stations is given in meters. Signals due to muon coincidences are clearly seen and indicate the presence of Extensive Air Showers with a lateral spread up to 500 m. Above 500 m there is no clear signal peak observed, but in the analysis the slight excess over the backround in the signal regions was taken.

Station i	**Station j**	**Years**	$d_{i,j}$ **[m]**	$N_{coin}/T_{i,j}$ **[coin./day]**
Gal	**Tro**	1995	18.11 ± 2.98	199.72 ± 4.41
Tro	**HCAL**	1995	36.06 ± 5.11	395.61 ± 6.26
Tro	**HCAL**	1996-2000	39.46 ± 5.11	338.05 ± 26.81
Gal	**HCAL**	1995	54.14 ± 5.10	205.13 ± 4.5
ByA	**ByC**	1999-2000	96.05 ± 3.19	37.23 ± 0.316
ByC	**HCAL**	1999-2000	166.5 ± 5.17	11.25 ± 0.218
Tro	**ByC**	1999-2000	168.24 ± 3.06	4.46 ± 0.127
Tro	**ByA**	1997-2000	260.65 ± 3.13	1.54 ± 0.089
ByA	**HCAL**	1997-2000	262.19 ± 5.18	3.29 ± 0.130
ByB	**HCAL**	1998-2000	262.19 ± 5.32	2.88 ± 0.119
Tro	**ByB**	1998-2000	272.44 ± 3.34	1.41 ± 0.082
ByB	**ByC**	1999-2000	428.01 ± 3.40	0.26 ± 0.062
ByA	**ByB**	1998-2000	524.00 ± 3.46	0.11 ± 0.071
ByA	**Alc**	1997-2000	665.56 ± 3.51	0.16 ± 0.139
ByC	**Alc**	1999-2000	760.21 ± 3.45	0.106 ± 0.13
Tro	**Alc**	1997-2000	926.07 ± 3.40	0.0054 ± 0.13
Alc	**HCAL**	1997-2000	926.55 ± 5.35	0.2732 ± 0.18

Table 3.10: Coincidence rates and distances between the CosmoALEPH detectors [117].

3.6 Coincidence Rates at Small Separations (dedicated runs in the year 1999)

For the evaluation of the coincidence rate of muons at small separations the ALEPH TPC is used. In the analysis only those events are selected which have muon tracks fully contained in each half of the fiducial volume of the TPC along the z-direction. A typical selected event with two muons registered in the TPC is shown in figure 3.8.

Helices of muon tracks in the magnetic field (1.5 Tesla) in the TPC are crossing the plane xz and are reconstructed using the JULIA software package

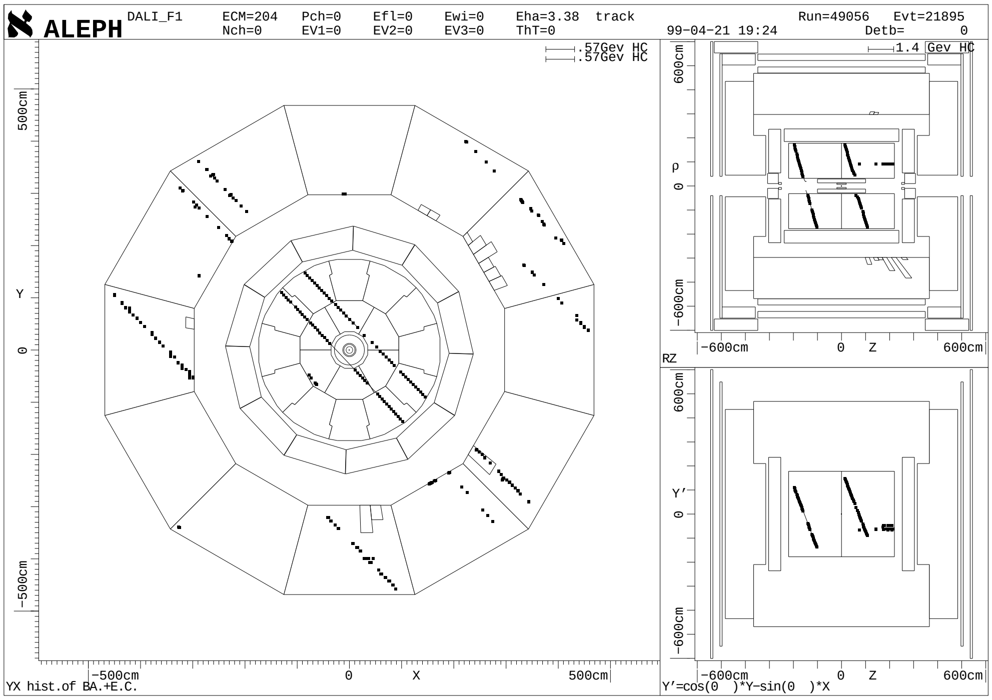

Figure 3.8: Display of a multi-muon event with two muon tracks detected in the TPC (central part of the ALEPH detector) and additional muons traversing HCAL.

[126] (see Appendix D) and an additional program developed to merge two segments into one track of single cosmic muons [120].

The JULIA software package performs fits and extracts information only for single track segments, since this program was developed for the analysis of ALEPH e^+e^- data, where the tracks of particles originate in the detector from the interaction vertex in the beam pipe. The JULIA software package was designed such, that it does not allow any modifications from the users, but the information provided by JULIA about one segment can be used in the reconstruction of the full track for a cosmic muon.

Only those tracks were accepted for the analysis, that have at least four hits in the segment. Because a cosmic muon track is defined as a combination of two segments, at least four hits in one segment and four hits in other segment of the track are required.

In case of multi-muon events, the JULIA software package provides information about all individual segments, without knowing to which track these segments belong. That is why an additional program was developed [120] to link correctlly those two segments that correspond to a muon track that has passed through the TPC. This is done in an iteration procedure by combining one segment with all other segments. The χ^2 of the helix fit was used to decide the best way of linking two segments to one track from all possible combination pairs of one segment with all other segments.

To study the quality of the fit, the momentum resolution as a funtion of momentum and as a function of number of hits N for the segments (information only from JULIA) and for the fully fit tracks are compared (see figure 3.9).

Figure 3.9 shows that the momentum resolution is much better for full tracks. As a result, fitting the full track of cosmic muons in the TPC, high momentum muons up to 3000 GeV/c are reconstructed with a good momentum resolution ($\sigma_p/p < 0.75$) compared to the momenta of the segments, which can be reconstructed at most up to 1000 GeV/c with $\sigma_p/p < 1$.

From the first two plots (left and right) in figure 3.9, the obtained σ_p/p^2 as function of the number of TPC hits N and as function of momentum is in agreement with calculations presented in [75] using the general equation for the track resolution

$$\frac{\sigma_p}{p} = \frac{\sigma_x}{0.3 \cdot B \cdot L^2} \cdot \sqrt{\frac{720}{(N+4)}} \cdot p \, ,$$

with N points equally distributed over the magnet length L and with track measurements errors σ_x.

For fixed values of magnetic field B, N, L and σ_x, the following values for ALEPH track resolution are obtained:

$$\frac{\sigma_p}{p^2} \approx 10^{-3} \, (GeV/c)^{-1} \, ,$$

and

$$\frac{\sigma_p}{p^2} \sim L^{-5/2} \, (GeV/c)^{-1} \, ,$$

where $L = k \cdot N$ represents the N measurements distributed over L in k equidistant intervals.

The χ^2 per degree of freedom for the full track fit with a mean value of 1.2 looks resonable for most reconstructed muon tracks.

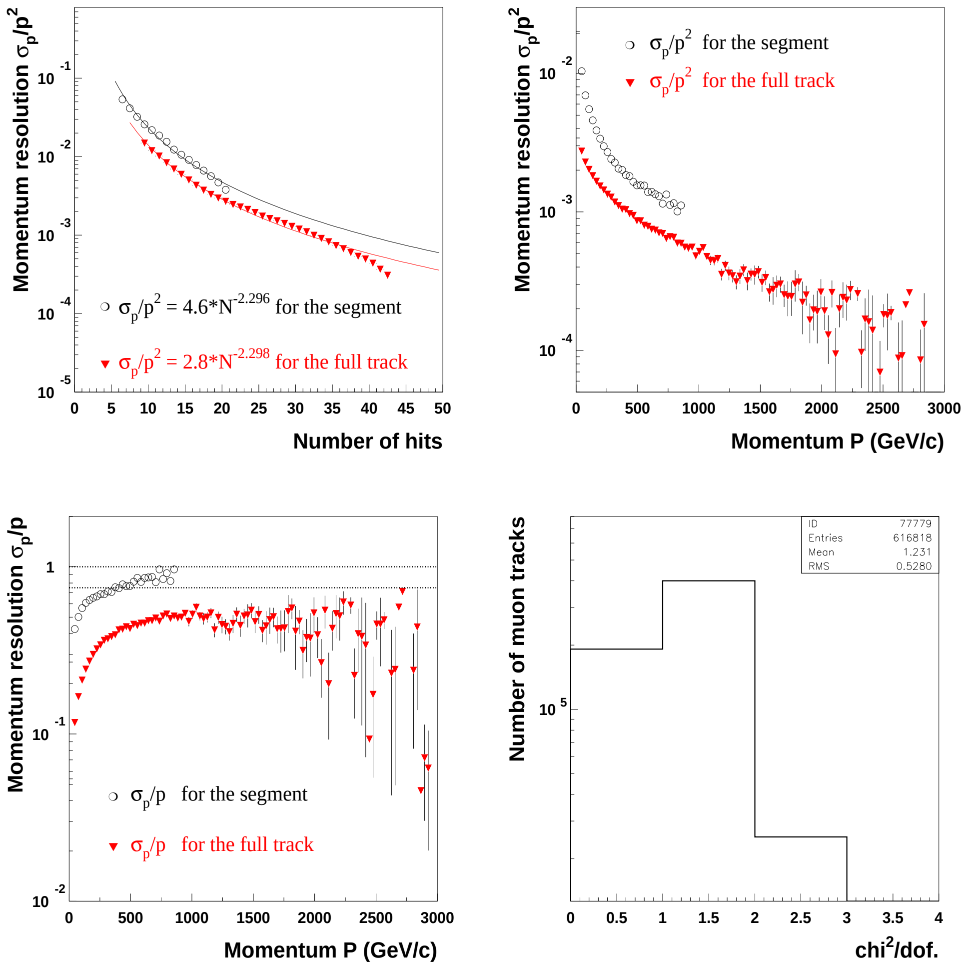

Figure 3.9: Momentum resolution (σ_p/p^2, σ_p/p) for JULIA muon segments and fitted full muon tracks as function of the number of hits and momentum in the TPC, and the χ^2/dof of the helix fit for the full muon track.

The following selection criteria were used for the analysis of coicidences between halves of the TPC

- Muon tracks were analysed for momenta $p > 5$ GeV/c and a momentum resolution $\Delta p/p < 1$
- Only events with at least two muons with the requirement that at least one muon passes through one half of the TPC and another muon of this event passes through the second half of the TPC
- Muon tracks must be fully contained in the fiducial volume and cross the plane xz of both halves of the TPC.

The coordinates x and z of the point, where the muon track intersects the plane xz, are saved. Such kind of events contribute to coincidences in the TPC and the distance between the first muon in the first half and the first muon in the second half of the TPC for one multiple muon event is computed.

The effective up-time of the TPC in dedicated runs was calculated from the JULIA data files that were produced from raw data files, by summing up the time differences between subsequent events in one run. This procedure was done for all runs. Empty events with hit information in HCAL, but no hit information in the TPC, which amount to about 25 %, were not considered in the calculation of the total open time.

An open time of 5.17 days was computed when the TPC was active. With the chosen selection requirements, 1653 ± 150 coincidences between muons in two halves of the TPC at an average distance of 2.6 ± 0.7 m were detected (see figure 3.10). The error of the number of coicidences is determined from the cuts on the momentum and momentum resolution. The effect of the momentum resolution cut is very small, while the momentum cuts at 1.5 GeV and 10 GeV introduce a systematic effect for the calculated number of coincidences of ± 146.

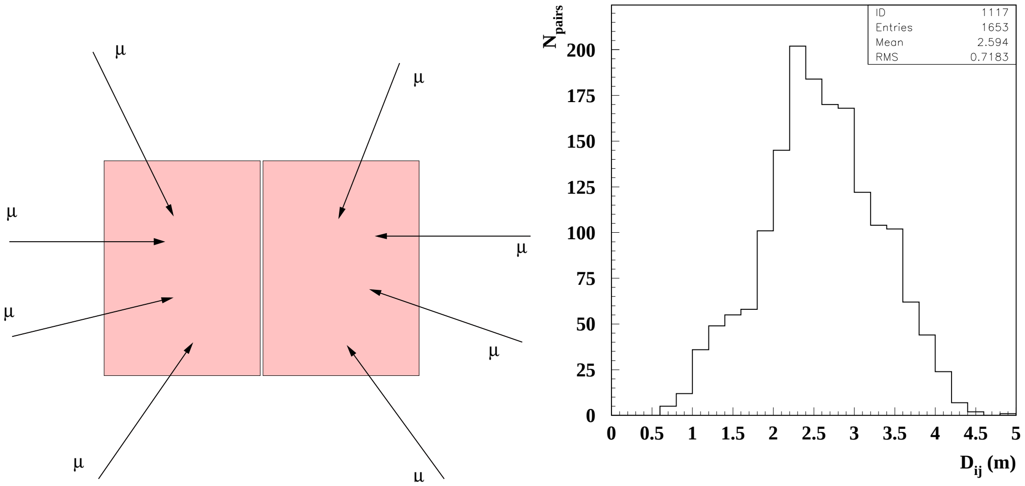

Figure 3.10: The number of coincidences between the two halves of the TPC at an average separation of 2.6 m, for muon tracks that are fully contained in the two halves of the ALEPH TPC separated by the membrane of the TPC along the z -direction.

Geometrical acceptances and reconstruction efficiencies [120] of each half of the TPC detector are determined using a full Monte Carlo simulation [120] including muon propagation in the overburden and hit digitization of the muon track in the detector. The simulation of muon events is based on the CERN package GEANT 3.21 [127].

The development of proton primary showers in the atmosphere were simulated with the VENUS model (see section 5.1). The information of the simulated muon momentum, zenith and azimuthal angles were transfered to the GEANT program for the transportation of these muons through the overburden to the depth of 320 *mwe*. To determine the geometrical acceptance of one half of the TPC, only those muons at the surface level were sampled, which point to the fiducial volume of the ALEPH detector underground.

Thus, the geometrical acceptance for one half of the TPC was calculated as the ratio of the number of generated muons fully contained in the considered half of the TPC which also intersect the plane xz, and the total number of generated muons pointing to the fiducial volume of the ALEPH detector after transportation through the overburden. Muons that do not reach the detector due to energy loss or multiple scattering processes are not considered for this calculation. Since the GEANT program is designed to handle only single primary particle events, and the VENUS simulated muons in the atmosphere are transfered to the GEANT program as primary particles, the geometrical acceptances of both halves of the TPC were determined in a two step analysis: firstly for one half, then in a repeated procedure for the second half of the TPC.

For both halves of the TPC a geometrical acceptance with its statistical error of $g = 0.88 \pm 0.04$ [120] is obtained, where the error depends on how many muons were generated at the surface level.

The obtained value for the geometrical acceptance for one half of the TPC shows the capacity of even one half of TPC to register cosmic muons in a large interval of zenith agles. The zenith angle distribution of muons fully contained in the fiducial volume of one half of the TPC, obtained from the experimental data, is presented in figure 3.11.

The zenith angle and azimuthal angle of a muon track in the TPC were determined at the closest approach to the z axis.

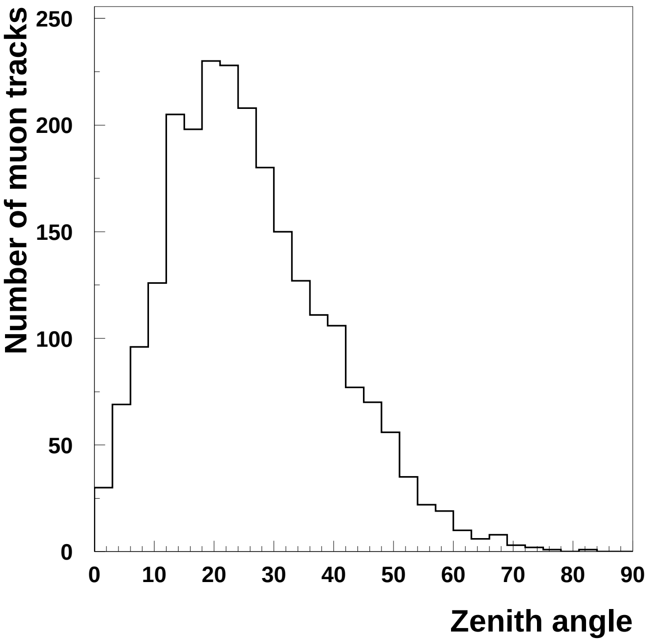

Figure 3.11: Zenith angle distribution of muon tracks registered in one half of the TPC.

The muon track reconstruction efficiency was determined in five stages: VENUS - GEANT - GALEPH - JULIA - ALPHA.

Muons transported through the atmosphere (simulated extensive air showers initiated by primary protons simulated with the high energy hadronic interaction model VENUS of the CORSIKA program) and overburden (GEANT) up to the ALEPH detector are transferred to GALEPH [128], a program that simulates the interactions of the generated particles in the implemented geometry and chemical composition of the material of ALEPH with all its sub-detectors, on their passage through the different materials. The output format of GALEPH is the same as for a real event in the experimental data (raw data).

As in case of experimental data, the JULIA reconstruction program is used to produce the files which contain information on the detected event or true simulated event, depending on whether experimental data or generated events are reconstructed.

The final stage is to fit the segments into full tracks with the developed program [120], which is an interface for using variables analysed by the ALPHA package [129].

To determine the track reconstruction efficiency for one half of the TPC, the ratio of the number of reconstructed true muons and number of accepted true muons for reconstruction is calculated and an average value for both halves of $\varepsilon = 96\ \% \pm 3\ \%$ [120] is obtained. A statistical error of 3 % was calculated by varying the number of simulated muons at the surface.

The effective areas in the xz plane of each half of the TPC were determined as

$$A_{eff} = A^{\perp}_{TPC_{1/2}} \cdot g,$$

where g is the geometrical acceptance of the considered half of the ALEPH TPC and

$$A^{\perp}_{TPC_{1/2}} = 2.2 \times 3.6 = 7.92\ \ [m^2]$$

is the maximal area of one half of the TPC in the xz plane. The effective areas of each half of the TPC are presented in figure 3.12.

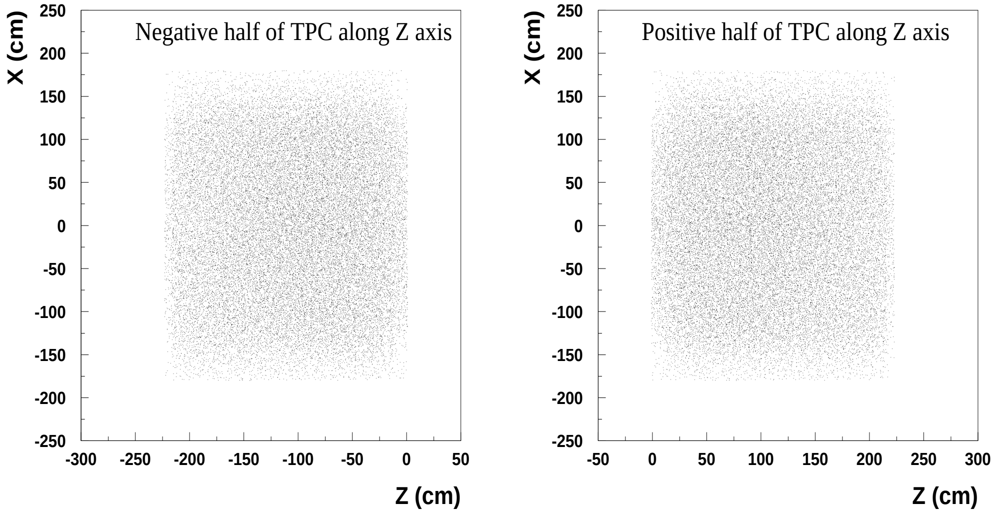

Figure 3.12: Crossing areas of the negative (left plot) and positive (right plot) halves of the TPC at the intersection of muon tracks with the xz plane along the z axis.

According to equation (3.1), the coincidence rate between the two halves of the TPC must be corrected for geometrical acceptance, track reconstruction efficiency and overburden.

Thus, for symmetric halves of the TPC with

$$\varepsilon_1 = \varepsilon_2 = 0.96 \pm 0.03\ , \qquad g_1 = g_2 = 0.88 \pm 0.04,$$

$$N = 1653 \pm 150 \text{ coincidences},$$

$$A_1^{\perp} = A_2^{\perp} = 7.92\ m^2, \qquad T = 5.167\ days$$

and considering the correction factor of 0.834 ± 0.07 for the overburden on top of the ALEPH detector, the coincidence rate between the two halves of the TPC detector is calculated as:

$$Rate = \frac{1653}{0.834^2 \cdot 0.96^2 \cdot 0.88^2 \cdot 7.92^2 \cdot 5.167} = 10.28 \pm 3.84 \quad [m^{-4} \cdot day^{-1}]$$

For the coincidence rate between the two halves of the TPC, the trigger efficiency of HCAL ϵ is assumed to be on average 100 %, since only events with at least two muons are considered for the analysis. The amount of such multiple muon events in the TPC, compared to single muon events, is about 0.5 %. The trigger efficiency of the HCAL for single muon events $\epsilon_{=1}$ registered in the TPC is about 87 %, as it is ilustrated in the analysis presented in section 3.8. Thus, $\epsilon_{\geq 2} \geq 1 - (1 - \epsilon_{=1})^2 = 98.3$ %.

The coincidence rate error was calculated according to the standard error propagation

$$\sigma_y^2 = \sum_i \left(\frac{\partial y}{\partial x_i}\right)^2 \cdot \sigma_{x_i}^2\ .$$

In the calculation, a 10 % error to the overburden correction is added, as obtained from the Monte Carlo studies of the decoherence distribution at different depths (see Appendix B).

The evaluated coincidence rate between the two halves of the TPC at an average small separation:

$$d = 2.6 \pm 0.7\ [m] \qquad Rate_{2.6m} = 10.28 \pm 3.84 \qquad [m^{-4} \cdot day^{-1}]$$

is added to the CosmoALEPH decoherence curve with coincidence rates up to 1 km, obtained from the measurements with scintillator stations and HCAL (see the next section).

Due to a very good momentum resolution of $\sigma_p/p \approx 2.5\%$ at 50 GeV/c and $\approx 60\%$ at 1.5 TeV/c, spatial resolution of $\sim 160\ \mu m$, and angular resolution $< 2\ mrad$, the TPC of the ALEPH detector was used also to analyse the multiplicity and transverse momentum distributions of single and multiple cosmic muon events in the total fiducial volume of the TPC (see section 3.8).

3.7 Measured Decoherence Distribution

With the information from the previous sections for the coincidence rates, effective areas, overburden corrections and efficiencies of all scintillator stations, the decoherence distribution is determined according to equation (3.1).

The error matrix was determined by an error Monte Carlo program [117] as

$$C_{ij} = \langle (D_i - \bar{D}_i) \cdot (D_j - \bar{D}_j) \rangle,$$

where the D_i are obtained from equation (3.1) by fluctuating all inputs within their errors, and $\bar{D}_i$ were obtained by using the central values of all quantities in equation (3.1). Quantities from the equation (3.1) were smeared with a gaussian distribution around their central values. The ratio s of geometry factors in efficiency and normal runs and areas of the scintillator stations were generated with a uniform distribution within $\pm\sigma$ around their central values.

The final values for the decoherence distribution parameters are given in table 3.11.

distance [m]	**Rate** $[m^{-4}\ day^{-1}]$
2.60 ± 0.700	10.2800 ± 3.8429
18.1 ± 3.000	20.6066 ± 4.2373 (0.4532, 4.2130)
36.1 ± 5.100	12.2049 ± 2.0907 (0.1935, 2.0817)
39.5 ± 5.100	10.6678 ± 2.0235 (0.8460, 1.8381)
54.1 ± 5.100	8.8212 ± 1.5169 (0.1931, 1.5045)
96.0 ± 3.200	2.8855 ± 0.5668 (0.0245, 0.5663)
166.5 ± 5.20	0.4948 ± 0.0808 (0.0096, 0.0803)
168.2 ± 3.10	0.4755 ± 0.0965 (0.0136, 0.0956)
260.6 ± 3.10	0.0948 ± 0.0185 (0.0054, 0.0177)
262.2 ± 5.20	0.0819 ± 0.0128 (0.0032, 0.0124)
272.4 ± 3.30	0.0980 ± 0.0215 (0.0080, 0.0199)
428.0 ± 3.40	0.0223 ± 0.0075 (0.0056, 0.0049)
524.0 ± 3.50	0.0057 ± 0.0040 (0.0036, 0.0018)
665.6 ± 3.50	0.0047 ± 0.0043 (0.0041, 0.0014)
760.2 ± 3.50	0.0053 ± 0.0067 (0.0063, 0.0022)
926.1 ± 3.40	0.0002 ± 0.0052 (0.0050, 0.0015)
926.5 ± 5.30	0.0045 ± 0.0031 (0.0030, 0.0010)

Table 3.11: Coincidence rates and distances between CosmoALEPH detectors that form the decoherence distribution. The errors are the total errors with statistical and systematical components presented in parenthesis [117].

The elements of lower left part of the symmetric correlation matrix are:
1.
0.75 1.
0.68 0.81 1.
0.74 0.80 0.73 1.
0.56 0.37 0.34 0.37 1.
0.56 0.66 0.60 0.66 0.65 1.
0.76 0.61 0.56 0.52 0.77 0.72 1.
0.74 0.61 0.55 0.52 0.71 0.49 0.71 1.
0.53 0.66 0.60 0.66 0.56 0.59 0.47 0.64 1.
0.67 0.55 0.50 0.47 0.64 0.44 0.63 0.75 0.71 1.
0.33 0.22 0.20 0.22 0.55 0.38 0.46 0.41 0.41 0.50 1.
0.15 0.10 0.09 0.10 0.23 0.11 0.15 0.23 0.25 0.27 0.17 1.
0.12 0.07 0.06 0.07 0.16 0.08 0.12 0.15 0.11 0.13 0.09 0.05 1.
0.09 0.06 0.06 0.06 0.13 0.10 0.12 0.10 0.07 0.08 0.07 0.03 0.03 1.
0.01 0.01 0.00 0.01 0.01 0.01 0.01 0.01 0.01 0.01 0.00 0.00 0.00 0.00 1.
0.13 0.15 0.14 0.15 0.10 0.14 0.12 0.11 0.13 0.10 0.05 0.03 0.03 0.02 0.00 1.

The coincidence rate determined from an independent measurement of cosmic muons in the Time Projection Chamber of the ALEPH detector is not included in the correlation matrix, since it does not correlate with the measurements obtained with scintillator stations and HCAL. The decoherence distribution measured with the CosmoALEPH detectors at 320 *mwe* is plotted in figure 3.13.

From table 3.11 it is clearly seen that the rates at small distances are dominated by the systematics, while at large distances by the statistics. However, the CosmoALEPH decoherence distribution measured up to 1 *km* is smooth within the calculated errors.

In Chapter 6, the comparison between the measured and MC predicted decoherence distributions is presented.

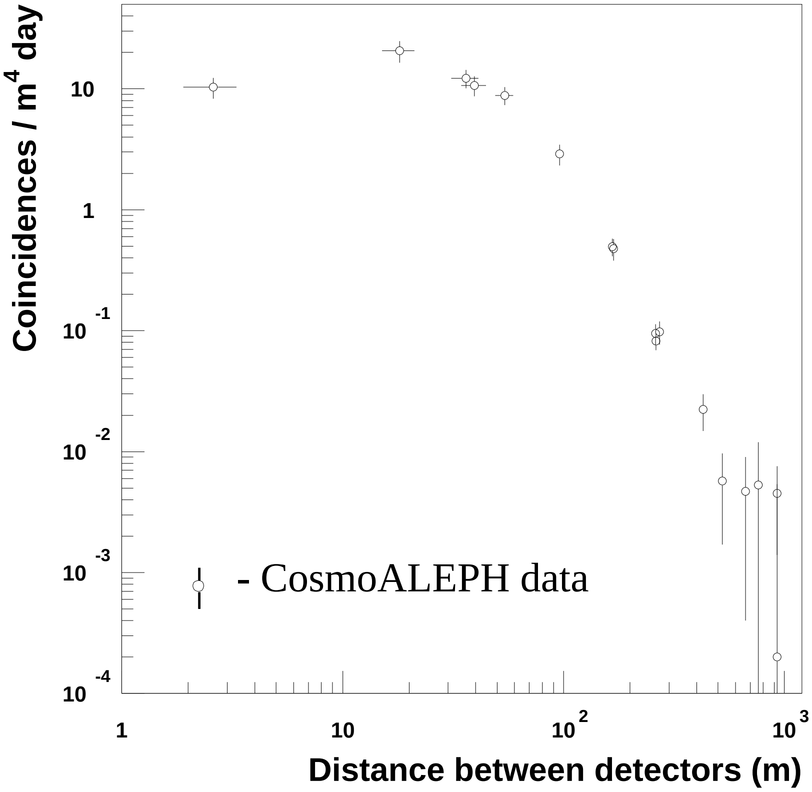

Figure 3.13: Measured decoherence distribution with CosmoALEPH.

3.8 Multiplicity and Transverse Momentum Distributions in the ALEPH TPC

The Time Projection Chamber (TPC) of the ALEPH detector provides an opportunity to study the chemical composition of primary cosmic rays from measurements of multiplicity and transverse momentum (with respect to vertical incidence) distributions of high energy muons underground at the depth of 320 *mwe*. The measured multiplicity and transverse momenta are compared with predictions from different MC models, which also have been used to study the mass composition of primary cosmic rays from the decoherence curve measured with the CosmoALEPH detectors.

The results from these two independent measurements should consolidate and confirm the results for the chemical composition of primary cosmic rays.

The procedure of the analysis of muon tracks in the TPC is the same as for the TPC halves (section 3.6), with the difference that the TPC is treated as the integral volume with an active area in the xz plane of $A = 4.4 \times 3.60$ $[m^2]$. Thus, $1.1 \cdot 10^6$ muon events were recorded in the TPC during dedicated CosmoALEPH runs in 1999. The analysis here is done in three stages: Raw data - JULIA - ALPHA. The JULIA program prepares EPIO files with track fit information about each of the two segments of a cosmic muon registered in the TPC.

These segments were fitted into a full muon track in the TPC with a program [120] based on the ALEPH software (the same program for fitting two segments into one muon track as used to study coincidences at small separations in the TPC). After the track fitting procedure, only events with at least one muon were saved if the following criteria are satisfied:

- Momentum P > 5.0 GeV/c and momentum resolution $\frac{dP}{P} < 1.0$
- The muon track crosses the xz plane of the TPC
- The length of the full muon track is larger than 1.6 m

As a result, muon tracks fulfilling the above conditions are saved and the multiplicity and transverse momentum of single and multiple muon events are plotted.

These two distributions require a correction for track reconstruction efficiency and HCAL trigger efficiency.

To calculate the trigger efficiency of the HCAL (at least eight planes in one HCAL module and eight planes in any of the three opposite modules fired simultaneously) as function of muon multiplicity and transverse momentum for single and multiple muon events, the ALEPH preselected e^+e^- data from the year 1999 were used. During e^+e^- runs, all ALEPH subdetectors were functioning properly. Naturally also, high energy cosmic events were recorded.

However, because of synchonizing the ALEPH trigger with the moment of beam crossing for e^+e^- runs, the short duty cycle for cosmic muon detection resulted in about 90 % loss of statistics.

Using the JULIA software package, segments belonging to cosmic muon events were preselected if there was no vertex reconstructed by JULIA with the following quality cuts [120]:

- momentum of each segment $P > 5$ GeV/c
- number of TPC hits of each segment ≥ 5

and fiducial volume cuts:

- distance of closest approach to beam axis $\mid Q \mid > 0.5\ cm$
- z coordinate of the track point where $\mid Q \mid$ is measured is $\mid z \mid > 4\ cm$.

In figure 3.14 a cosmic muon event preselected from the ALEPH e^+e^- data with hits also in the Muon Chambers is presented.

The EPIO files prepared with the JULIA software package were further analysed with a program developed to match two segments into one track [120]. The analysis is performed for each muon track with the conditions that:

- momentum P $>$ 5.0 GeV/c
- momentum resolution $\frac{dP}{P} < 1.0$
- at least one hit in one of the two layers of the Muon Chambers [115] is required to define a muon.

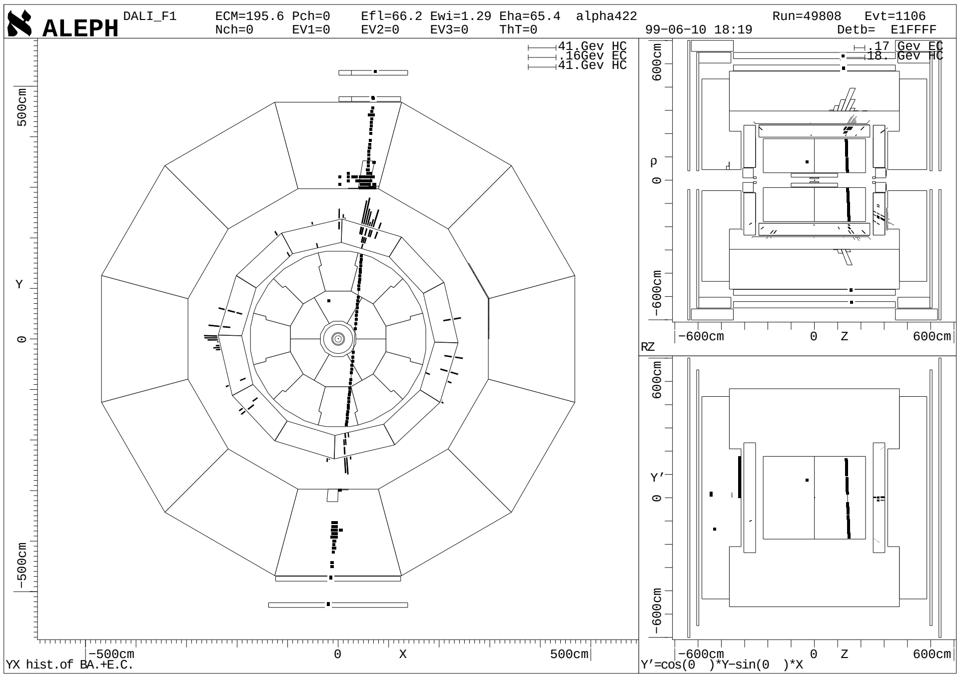

Figure 3.14: Event display of a preselected single-muon event from the ALEPH e^+e^- data with hits of the tracks detected in TPC, HCAL and the Muon Chambers.

To ensure that muon tracks cross the HCAL barrel, at least two hits in the barrel of HCAL (one hit for the first segment and one hit for the second segment that were merged into a track) were required.

The HCAL trigger efficiency for single muon events was calculated as the ratio of the number of muons satisfying the CosmoALEPH trigger condition and the number of muons without the trigger condition.

The HCAL trigger efficiency as a function of the muon transverse momentum was calculated by normalizing the transverse momentum distribution obtained with 8 & 8 CosmoALEPH trigger condition on the transverse momentum distribution obtained without trigger condition.

The obtained efficiency for the transverse momentum was fitted with a polynomial of first order. In figure 3.15 it is shown that with increasing transverse momentum the HCAL trigger efficiency decreases slowly, which means that the tail of the transverse momentum distribution must be slightly corrected.

In the case of muon multiplicity, the HCAL trigger efficiency only for single muon events was determined with a value of (86.6 ± 2.0) %.

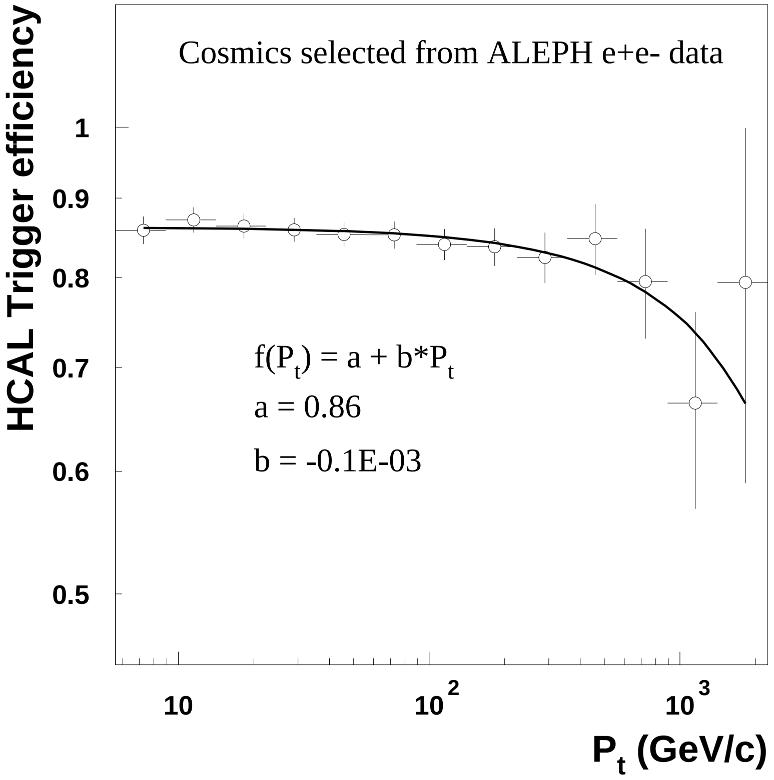

Figure 3.15: The efficiency of the 8 & 8 HCAL trigger for single and multiple muon events measured from ALEPH e^+e^- preselected data taken in the year 1999.

The HCAL trigger efficiency for multiple muon events is assumed to be around 100 %, because the probability, that HCAL will trigger, increases for a double or multiple muon event compared to a single muon event.

In the case of transverse momentum, there is no significant impact on the HCAL trigger efficiency from the track reconstruction efficiency. This is explained by the fact that single muon events represent about 99.5 % of the total statistics. In the range from low to high transverse momenta they are uniformly distributed and their tracks are reconstructed with a high efficiency.

The muon track reconstruction efficiency [120] as a function of transverse momentum was determined from a full MC simulation of muon propagation through the atmosphere, overburden and the ALEPH detector following the same steps as described in section 3.6. With the same cuts for momentum and momentum resolution mentioned above, the reconstruction efficiency of muon tracks in the TPC was calculated as the ratio of transverse momentum distribution for reconstructed muons and transverse momentum distribution before reconstruction for all muons entering the TPC. In both distributions, before and after track reconstruction, the information of the true momentum is used. The resulting distribution for the track reconstruction efficiency was fitted with a polynomial of second order. In figure 3.16 the track reconstruction efficiency is presented as a function of transverse momentum.

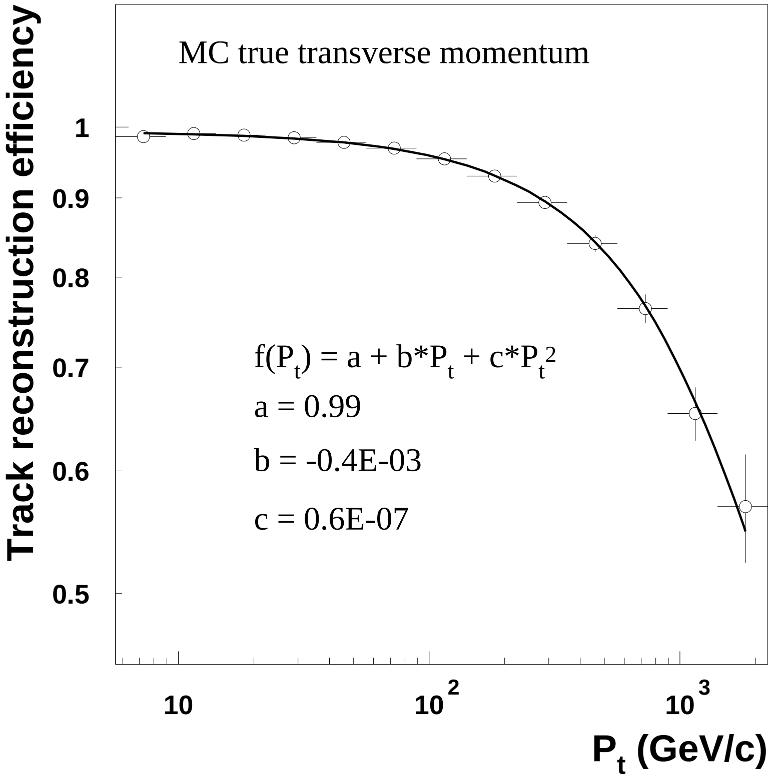

Figure 3.16: Efficiency of the muon track reconstruction in the TPC.

The track reconstruction efficiency contains only information about single muon events, since the GEANT program, which transports VENUS muons through the overburden, cannot handle multiple muon events. As a result, the track reconstruction efficiency in the case of the muon multiplicity was calculated only for single muon events as the ratio of the number of muons in the TPC after reconstruction and the number of all muons that enter the TPC before reconstruction yielding a value of 95 ± 2 %.

The errors of the HCAL trigger efficiency and track reconstruction efficiency were calculated by a standard error propagation procedure for each histogram bin separately.

The following plots show the transverse momentum distribution (see figure 3.17) and muon multiplicity distribution (see figure 3.19) before corrections and after corrections for HCAL trigger efficiency and track reconstruction efficiency.

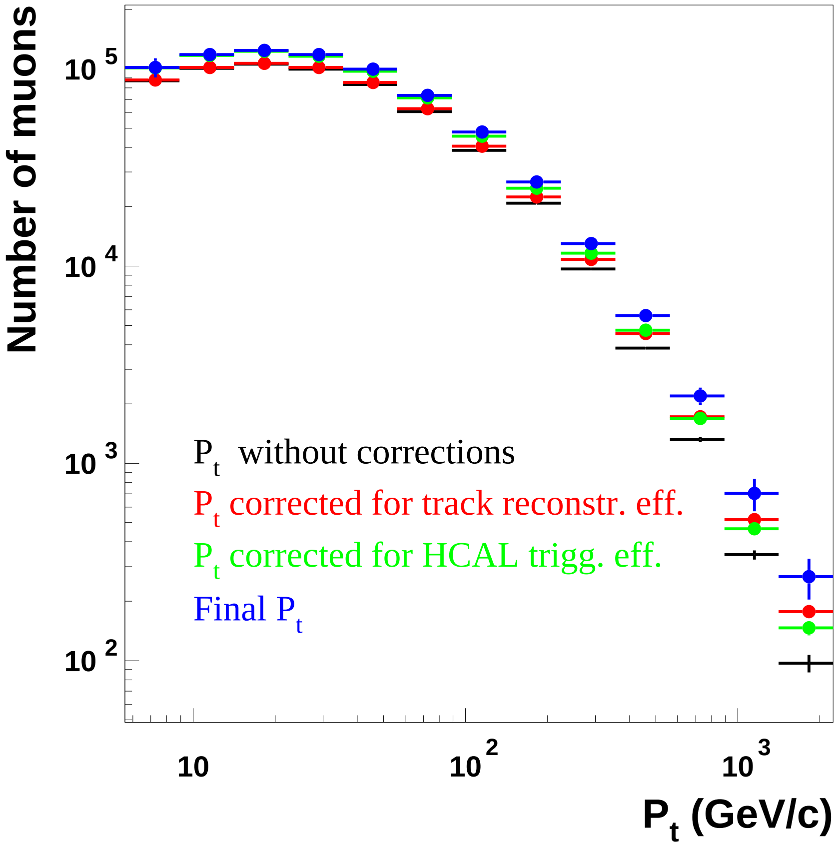

Figure 3.17: The transverse momentum distribution of single and multiple muon events measured at the CosmoALEPH depth of 320 *mwe* underground with the ALEPH TPC. The horizontal lines represent the bin width.

In the transverse momentum distribution the total errors are presented as a combination of systematical and statistical errrors which are quadratically summed as

$$\sigma = \sqrt{\sigma^2_{sys:P_t} + \sigma^2_{sys:\Delta p/p} + \sigma^2_{statist}}\ .$$

Systematical errors were calculated by varying the cuts for mometum and momentum resolution. To calculate the error of the first bin in the transverse momentum distribution, an analysis for muon tracks with momenta $P_t > 5$ GeV/c and $P_t > 6$ GeV/c was performed. The result of the subtraction of the bin contents between the transverse momentum distributions for these two cuts provides an uncertainty of $\sigma_{sys:P_t} = 13\%$ for low transverse momenta. Another error comes from the cut on the momentum resolution. The analysis was performed for $P_t > 5$ GeV/c with $\Delta p/p < 1$, $\Delta p/p < 0.9$ and $\Delta p/p < 1.1$. The uncertainty from these cuts is of the order of $\sigma_{sys:\Delta p/p} = 12$ % for higher momenta.

Because the transverse momentum distribution is corrected for the HCAL trigger efficiency ε_{trigg} and track reconstruction efficiency ε_{track}, the statistical errors were calculated according to the standard error propagation procedure for the ratio

$$r = \frac{bin\ content(i)}{\varepsilon_{trigg}(i) \cdot \varepsilon_{track}(i)}\ .$$

For high transverse momenta there is a contribution of about 62 % from statistical errors.

The distribution of the total relative errors is presented in figure 3.18.

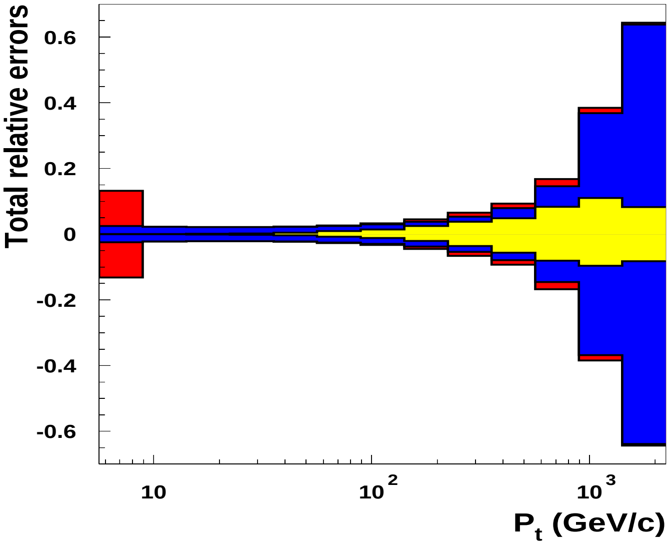

Figure 3.18: The distribution of systematical errors (yellow), statistical errors (blue) and total errors (red).

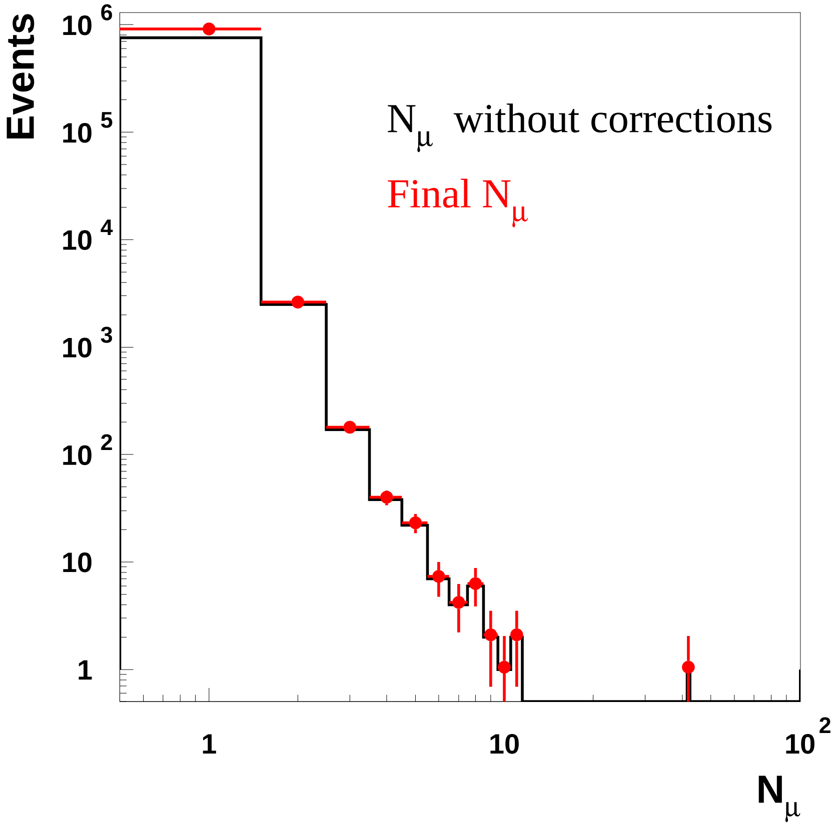

Figure 3.19: The multiplicity distribution of single and multiple muon events measured with the ALEPH TPC at the CosmoALEPH depth of 320 *mwe* undergroung, presented before corrections (black histogram) and after corrections (red points). Only statistical errors are presented.

To study the chemical composition of primary cosmic rays, the obtained multiplicity and transverse momentum distributions are compared with the distributions predicted by different Monte Carlo models and the results are presented in section 6.2.

The implementation of the TPC and analysis of the multiplicity and transverse momentum distributions for proton, helium and iron initiated showers, simulated with QGSJET, VENUS, SIBYLL and NEXUS are presented in section 5.5, together with the azimuthal, zenith and track length distributions of cosmic muons measured and simulated in the TPC.

Chapter 4

Concept of the Monte Carlo Simulation Program

4.1 CORSIKA: A Program for Air Shower Simulation

CORSIKA (COsmic Ray SImulation for KAscade) is a detailed Monte Carlo program to study the 4-dimensional evolution of Extensive Air Showers (EAS) in the atmosphere initiated by various cosmic ray particles. Originally it was developed to perform simulations for the KASCADE experiment at Karlsruhe. The first version of CORSIKA was proposed in 1989 and represents a complete set of standard FORTRAN routines. CORSIKA is a combination of programs which allow to simulate interactions and decays of nuclei, hadrons, muons, electrons and photons which appear in the development of EAS up to the highest energies observed ($E > 10^{20}$ eV). It provides type, energy, location, direction and arrival times of all secondary particles that are created in an air shower.

The CORSIKA program is structured basically in four parts. The first part is a general program frame handling the in- and output, and treats the decay of unstable particles taking into account all decay modes with branching ratios down to the one percent level with correct kinematics also in three body decays. During particle transport, which includes particle ranges defined by the particle lifetime and its cross-section, ionization energy losses, the deflection of charged particles by the Earth's magnetic field and also the deflection by multiple scattering are considered. The second part treats hadronic interactions of nuclei and hadrons with air nuclei at energies above 80 GeV. The third part simulates hadronic interactions at energies below 80 GeV and the fourth part describes the interactions of electrons, positrons and photons.

The main problem of the CORSIKA program is the large amount of computing time consumption for simulations of EAS with increasing primary energy. To reduce the CPU time, the so-called *thin sampling* algorithm or *variance reduction* method is used in this program [12]. According to this procedure only a few secondary particles are followed down to the ground. The decision at which point of the EAS development the thin sampling should start is given by the thinning level energy E_{thin}, expressed by the fraction ε_{thin} of the primary energy E_0

$$\varepsilon_{thin} = E_{thin}/E_0. \tag{4.1}$$

The respective particle is randomly selected, considering its survival probability according to its energy fraction of the energy summed over all secondary particles emerging from the interaction under consideration.

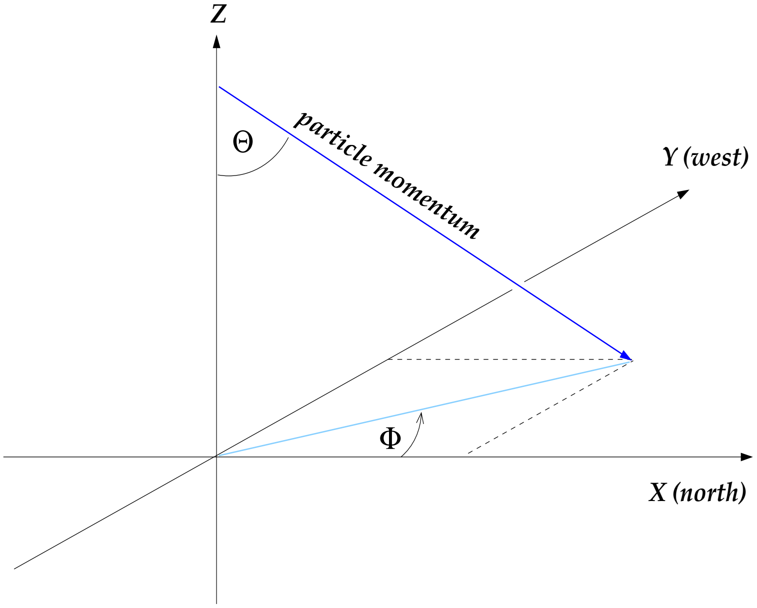

Figure 4.1: Coordinate system in CORSIKA

The Cartesian coordinate system chosen in CORSIKA is shown in figure 4.1. It defines the positive x-axis oriented to the North, the positive y-axis to the West, and the positive z-axis upwards. The origin is located at sea level. The zenith angle θ of a particle trajectory is measured between the particle momentum vector and the negative z-axis. The azimuthal angle ϕ is counted counterclockwise between the positive x-axis and the x-y-component of the particle's momentum vector.

Technical details of CORSIKA program are specified in [87].

4.2 Global Simulation Parameters and Interaction Models

To control the simulation, CORSIKA offers the possibility to choose between a variety of parameters. The type and the flux of primary cosmic ray particles have to be defined. The energy and the primary angle of incidence can be chosen as fixed values or randomly picked within a range. Also the slope of the energy spectrum that describes the steeply falling energy spectrum with increasing energy must be specified.

The atmosphere in CORSIKA consists of N_2, O_2, and Ar with volume fractions of 78.1%, 21.0%, and 0.9% and it is divided into 5-layers according to the exponential dependence (in the lower four of them) of the density (column density $T(h)$ of the atmosphere) on the altitude h:

$$T(h) = a_i + b_i e^{-h/c_i} \qquad i = 1, \cdots, 4, \tag{4.2}$$

where a_i, b_i, and c_i are atmospheric parameters. In the fifth layer the column density decreases linearly with height

$$T(h) = a_5 - b_5 \frac{h}{c_i}. \tag{4.3}$$

Various parameter sets can be selected to study seasonal influences [87].

Recent additions to CORSIKA permit to adopt not only a flat atmosphere which limits simulations to zenith angles $\theta < 70^0$, but also a spherical atmosphere for large zenith angles $\theta > 70^0$, for which the influence of the Earth's surface curvature must be taken into account [88]. Within CORSIKA 50 elementary particles are defined:

- leptons γ, $e^\pm$, $\mu^\pm$, optionally electronic and muonic neutrinos,
- mesons π^0, $\pi^\pm$, $K^\pm$, $K^0_{S/L}$, η,
- baryons p, n, Λ, $\Sigma^\pm$, Σ^0, Ξ^0, Ξ^-, Ω^-, and the corresponding anti-baryons,
- resonance states $\rho^\pm$, ρ^0, $K^{*\pm}$, K^{*0}, $\overline{K}^{*0}$, Δ^{++}, Δ^+, Δ^-, Δ^0, and the corresponding anti-baryonic resonances,
- also nuclei with mass number $A \leq 60$ can be simulated.

All these particles are tracked explicitly and may undergo interactions or decay (in case of unstable particles).

In CORSIKA simulations, particles above a defined threshold energy are tracked in detail, for smaller energies they are discarded. The continuous *energy loss by ionization dE/dx* of a single charged hadron or muon traversing matter of thickness dx along its track is calculated by the Bethe-Bloch stopping power formula

$$\frac{dE}{dx} = \frac{z^2}{\beta^2} k_1 (ln(\gamma^2 - 1) - \beta^2 + k_2) \;, \tag{4.4}$$

where $\beta = v/c$ is particle velocity in the laboratory frame, γ is the Lorentz factor, and z is the charge of the ionizing particle in units of e. $k_1 = 0.1533$ MeV $g^{-1} cm^2$ and $k_2 = 9.3862$ are constants derived for dry air [90].

In CORSIKA, multiple scattering of charged particles in the Coulomb field of the nuclei is considered only for muons. Multiple scattering is treated according to Moliere's Theory and only once for each tracking step in the middle of the tracking interval.

Charged paricles are deflected in the Earth's magnetic field and this effect is taken into consideration by the CORSIKA program. Within CORSIKA, the magnetic field components B_x and B_z may be specified for the geographical location of the experiment, the B_y component is zero by definition. The direction of a charged particle of charge z that travels with momentum $\vec{p}$ along the path length l in the magnetic field $\vec{B}$, is changed by the angle α, which for small angles is approximated by

$$\alpha \approx l \cdot z \cdot \frac{\vec{p} \times \vec{B}}{p^2} \;. \tag{4.5}$$

A detailed description of CORSIKA's physics content is given in [12].

4.3 Models for Hadronic Interactions

Cosmic ray interactions which are predominantly nucleon-nucleus or nucleus-nucleus interactions are modelled on the basis of the present knowledge about nucleon-nucleon reactions, provided by recent experiments at $p\overline{p}$ colliders up to centre of mass energies of 1.8 TeV. To cover the high energy region, theoretical models based on collider results have to be extrapolated far into unknown regions of energy. This represents the dominant uncertainty of the interaction models. Another uncertainty comes from the fact that secondary particles which are emitted in the forward direction cannot be detected in collider experiments, however, these particles are the most important ones for the development of EAS, because they carry the largest part of the energy deep down into the atmosphere.

Hadronic interactions are classified into various groups according to the reaction type.

In elastic scattering processes, the colliding particles in the centre of mass system lose no energy, while in inelastic processes, a large part of the centre of mass energy is used to produce new particles.

Characteristic to inelastic interactions are the diffractive scattering processes. The single diffractive scattering has the same kinematics as elastic interaction, with the difference that one of the colliding particles remains intact and transfers only a small part of its energy to the other particle, which is excited to a higher energy state thereby becoming unstable with the consequence that it decays, producing secondary particles. In double diffractive scattering, both colliding particles are excited and may decay. The projectile fragments carry the energy of the initial projectile deep into the atmosphere.

In non-diffractive processes, essentially inelastic scattering, both, the target and the projectile particles are destroyed and the whole centre of mass energy ($\sqrt{s}$) is used to produce secondary particles.

Strong interaction processes, in which jets are produced, play an important role with increasing centre of mass energy. In semi-hard interactions minijets in the range of a few GeV are produced. The minijet cross section depends strongly on the transverse momentum cutoff and in models with minijets this is about 2 GeV. Above this threshould, the QCD coupling is weak enough to use perturbation theory. The contribution to the minijet inclusive cross section can be calculated by integrating a sum of terms like [107]:

$$\frac{d\sigma_{jet}}{dx_1 dx_2 d(cos\theta)} = F(x_1)F(x_2)\frac{d\sigma}{d(cos\theta)} , \tag{4.6}$$

where $F(x)$ are the structure functions of quarks or gluons, which count the number of partons in the given x-range that are available for scattering, and σ is the elementary cross section for the scattering of partons. The quantity of Feyman x is defined by $x = \frac{P}{P_{max}} = \frac{2 \cdot P}{\sqrt{s}}$. The number of pairs of minijets is

$$< N >= \frac{\sigma_{jet}}{\sigma_{inel}} . \tag{4.7}$$

The understanding of the minijet cross section is the key to understand the particle production at high energies, and the determination of the transverse momentum cutoff is of great importance [91]. This allows to extrapolate kinematic regions explored by the accelerator experiments to higher energies.

The total cross section for hadronic reactions is

$$\sigma_{tot} = \sigma_{el} + \sigma_{inel}, \tag{4.8}$$

with $\sigma_{inel} = \sigma_{non-diff} + \sigma_{diff}$. All hadronic models in CORSIKA contain diffractive events. The hadron-nucleon and hadron-nucleus interactions are described by the multiple scattering theory of Glauber [12]. The simplified version of the full theory is given by the formula

$$\sigma_{tot} - \sigma_{el} = \int d^2b(1 - exp[-\sigma T(b)]). \tag{4.9}$$

where σ is the hadron-nucleon cross section. The function

$$T(b) = \int \rho_N(b)dz \tag{4.10}$$

represents the number of target nucleons/cm^2 in the nucleus at an impact parameter b, and ρ_N is the number density of nucleons at a distance $r = \sqrt{b^2 + z^2}$ from the center of the nucleus [107].

In CORSIKA the low energy hadronic interactions (below $E_{lab} < 80$ GeV) are simulated by the **GHEISHA** code. The alternative program for the low energy hadronic interactions is **UrQMD** (Ultra-relativistic Quantum Molecular Dynamics program) developed for heavy ion collision experiments.

Electrons and gammas are treated separately by the **EGS4** Monte Carlo code or alternatively by the much faster form of the analytic **NKG** formula. Optionally, Cherenkov photons may be generated.

High energy hadronic interactions are simulated with six different reaction codes which provide the chance to derive systematic uncertainties of predictions from different simulations. In air showers, the inelastic interactions that cannot be described by QCD play a central role, thus, they are described with models based on the Gribov-Regge theory (GRT). This theory allows multiple interactions to occur in parallel with compex phenomenological objects called "Pomerons", representing an elementary interaction [92].

A Pomeron is represented by a ladder of gluons and quark loops according to the topological expansion of quantum chromodynamics, and the production of particles in inelastic collisions is determined by a specific cut.

In Monte Carlo applications, GRT based models conserve well the energy that needs to be shared between many Pomerons in case of multiple scattering when calculating the particle production, however, in case of the cross section calculation the energy is not conserved [92], and this represents a disadvantage for this approach.

Gribov-Regge theory (GRT) type models are:

- The **VENUS** (Very Energetic NUclear Scattering) model is designed for simulation of ultra relativistic heavy ion collisions with a detailed simulation of creation, interaction, and fragmentation of colour strings.

Here, cutting of the Pomerons is realized by forming colour strings which subsequently fragment into colour neutral hadrons. In collisions of heavy nuclei at high densities, massive quark-matter droplets may be formed. Also, diffractive and non-diffractive collisions are treated. Jet production is not considered, that is why the VENUS model reaches only a maximum energy of 2×10^7 GeV [12].

- The **QGSJET** (Quark Gluon String model with JETs) model is an extension of the QGS model ([12], [89]) based on the Gribov-Regge theory, to treat nucleus-nucleus interactions and semihard processes. This model additionally includes minijets to describe hard interactions which are important at highest energies.

  A high energy collision is represented as a superposition of a number of elementary processes, Pomeron exchanges, by a small number of adjustable parameters and by a parameter-free generalization to hadron-nucleus and nucleus-nucleus interactions [93].

  Using the optical theorem and calculating various unitarity cuts of elastic scattering diagrams according to Abramovskii-Gribov-Kanceli rules, the expressions for the total and inelastic cross sections, also for the relative probabilities of particular interaction configurations may be obtained [94].

  The interaction between the projectile and the target hadron are mediated by microscopic parton cascades, that consist of "soft" and "semihard" Pomerons. After performing the energy-momentum sharing among soft and semihard Pomerons, as well as sharing among the soft and hard pieces of the latter one, the number of charged particles in the partonic cascade is obtained generalizing the method of multiple production of hadrons (soft Pomeron showers) [103].

  Here, the nucleus-nucleus interaction [86] is treated in the Glauber approach, where the nucleus is seen as a cluster of accumulated independent nucleons.

- The **DPMJET** (Dual Parton Model with JETs production, see [95]) model describes the particle production in hadron-nucleus and nucleus-nucleus collisions at high energies. High energy projectiles undergo multiple scattering, in which particle production is realized by the fragmentation of colourless parton-parton chains constructed from the quark content of the interacting hadrons. The Dual Parton Model is based on two components. The soft component is described by a supercritical

Pomeron, while for the hard component additionaly hard Pomerons are introduced.

The other three MC models are:

- **HDPM** is a phenomenological generator HDPM inspired by the Dual Parton Model and adjusted where possible to experimental data.
- **SIBYLL** is a minijet model essentially designed for the use in EAS Monte Carlo simulations. The model uses a critical Pomeron with only one soft chain pair [96]. Strings originating from hard collisions with minijet production of high transverse momenta are considered. Nucleus-nucleus collisions are treated according to a semi-superposition model [96], in which a nucleus of mass A and energy E0 is represented as the superposition of A nucleons of energy E0/A, but the distribution of interaction lengths, here, depends on the type of the nucleus. According to J. Knapp [89] this model is somewhere in between the purely phenomenological ones and the GRT models.
- **NeXus** is the newest model and combines algorithms of VENUS and QGSJET ([88],[97]). It is by construction a link between the Gribov-Regge approach and the parton model and this approach is called "parton-based Gribov-Regge theory" with unified soft and hard interactions. In this model the multiple scattering aspect in case of hadron-nucleus collisions (multiple scattering diagrams represented as a sum of soft and semi-hard Pomerons, where the latter are obtained from the perturbative QCD calculations) is treated rigorously, with energy conservation not only for particle production calculations, but also for cross sections. In both cases the energy is properly shared between different interactions that occur in parallel [98]. All theoretical improvements in this model cost a large amount of computer time. This motivated the NEXUS developers to follow an alternative approach, namely the air shower development in terms of cascade equations [98].

At present only the QGSJET, DPMJET and SIBYLL models (with minijets) reach the highest energies up to $> 10^{20}$ eV. The maximum energy for HDPM and NeXus are 10^8 GeV and 2×10^8 GeV respectively. The VENUS model reaches a maximum energy of 2×10^7 GeV.

Simulation results of these models are adjusted to experimental data wherever available. As demonstrated in [99], [100], [101], [102] VENUS and especially QGSJET provide the best agreement of simulations with experimental data up to the primary energy of $\approx 10^{16}$ eV. Thus the muonic component of EAS simulations with muon energies exceeding some 100 GeV may be predicted with uncertainties $\leq 20\%$.

Chapter 5

Monte Carlo Data Analysis

5.1 Simulations

Extensive Air Showers (EAS) were simulated using the CORSIKA program version 6.203 [87]. The considered interaction models are **QGSJET**, **VENUS**, **SIBYLL** and **NEXUS**.

The coordinates in the CORSIKA program are defined with respect to a coordinate system with the origin located at observation level (sea level). The shower axis is always pointing to the origin of the coordinate system. For simulations of air showers up to zenith angles $\approx 90°$, where the Earth atmosphere is no longer flat, the curved atmosphere option is used, which takes into account the influence of the Earth's surface curvature (see figure 5.1).

The U.S. standard atmosphere parameterized according to J. Linsley was adopted:

Layer i	Altitude h (km)	a_i (g/cm^2)	b_i (g/cm^2)	c_i (cm)
1	$0 \cdots 4$	-186.5562	1222.6562	994186.38
2	$4 \cdots 10$	-94.919	1144.9069	878153.55
3	$10 \cdots 40$	0.61289	1305.5948	636143.04
4	$40 \cdots 100$	0.0	540.1778	772170.16
5	> 100	0.01128292	1	10^9

Table 5.1: Parameters of the U.S. standard atmosphere. [87]

For low energy hadron-nucleus collisions the GHEISHA model was selected, motivated by the considerations that it is very fast and will not affect our results, because CosmoALEPH energies are beyond the range of validity of GHEISHA (≤ 80 GeV).

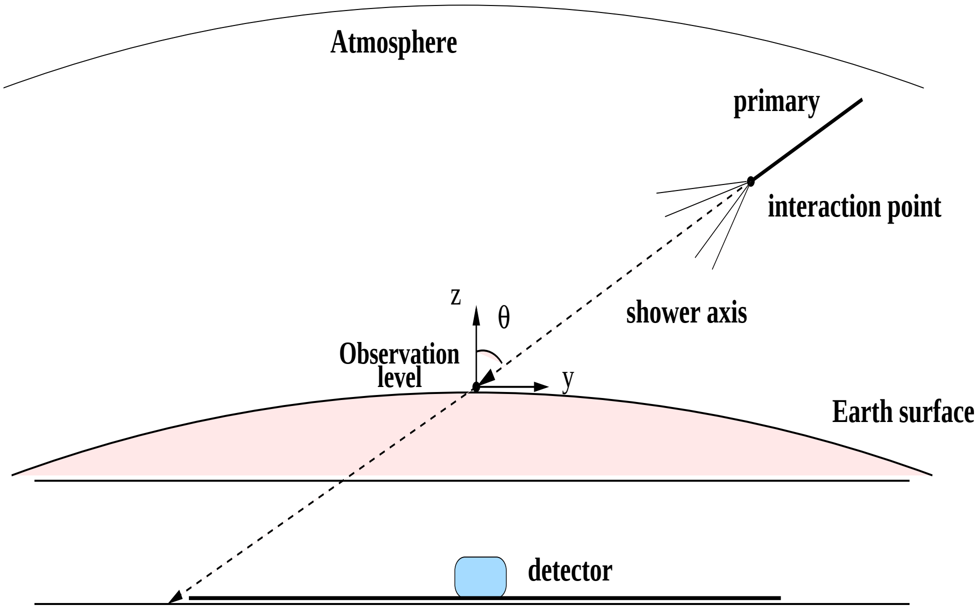

Figure 5.1: The geometry used in the curved atmosphere option in CORSIKA [120].

The simulations were performed for

- about $\mathbf{10^8}$ air showers of **H**, **He** and **Fe** primaries
- in the primary zenith angle θ range from $\mathbf{0}^\circ$ to $\mathbf{89}^\circ$

according to the differential energy spectrum (see equation (1.1)). For the present study two mass compositon models were considered: Constant mass composition (CMC) with the same spectral slope $\alpha = 2.7$ for all considered primary elements and the Maryland composition model (MCM) [106] with varying spectral index and energy cutoff $E_c \ (GeV)$ (see the table 5.2).

Composition model	Elements	α	E_c (GeV)	α $(E > E_c)$
MCM	**proton**	**2.75**	$\mathbf{3.0 \cdot 10^5}$	**3.35**
	helium	**2.77**	$\mathbf{6.0 \cdot 10^5}$	**3.37**
	iron	**2.50**	$\mathbf{8.4 \cdot 10^6}$	**3.10**

Table 5.2: Heavy composition model proposed by the Maryland group [106].

CORSIKA allows to specify only one spectral index. In order to be able to specify two spectral indices for the primary energy spectrum with a continuous transition from the spectrum with one slope to the spectrum with the other slope, an α_1 from the minimum selected energy E_{min} up to the energy cutoff E_c, and an α_2 from the $E_0 > E_c$ up to a maximum selected energy E_{max} were introduced. The CORSIKA code was changed, according to the cumulative transformation method which gives the probability $P(x)$ that x has a value greater than or equal to x [124].

Thus, up to the energy cutoff, the primary energy is sampled according to the formula:

$$E_{prim0} = [E_1 + RAN0 \cdot (E_{31} - E_1)]^{\frac{-1}{(\alpha_1 - 1)}} \ . \tag{5.1}$$

For $E_{prim0} > E_c$, the primary energy is sampled according to the formula

$$E_{prim1} = [E_2 + RAN1 \cdot (E_{32} - E_2)]^{\frac{-1}{(\alpha_2 - 1)}} \ , \tag{5.2}$$

with

$$E_1 = E_{min}^{-(\alpha_1 - 1)} \ , \tag{5.3}$$

$$E_{31} = E_c^{-(\alpha_1 - 1)} \ , \tag{5.4}$$

$$E_{32} = E_{max}^{-(\alpha_2 - 1)} \ , \tag{5.5}$$

$$E_2 = E_c^{-(\alpha_2 - 1)} \ . \tag{5.6}$$

RAN0 and RAN1 are random numbers initialized by the uniform random number generator RM48 from CERN-LIB; E_{min} and E_{max} correspond to the minimum and maximum values of the chosen interval for the primary energy.

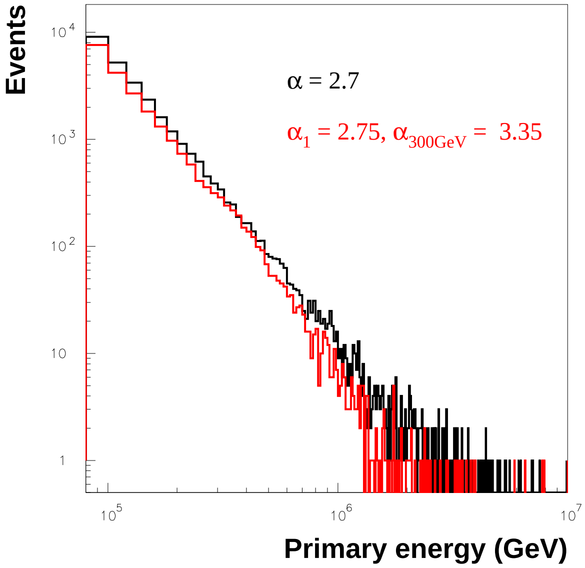

Figure 5.2: Primary energy spectrum normalized on the same number of events simulated with SIBYLL for primary proton showers in the energy range 1 TeV - 10 PeV with $\alpha = 2.7$ (black distribution), and $\alpha_1 = 2.75$ and for $\alpha_2 = 3.35$ ($E > 300$ TeV) (red distribution).

The simulations were done

- for primary energies in the range from 170 GeV to 10 PeV for CMC. In this case the simulations for the SIBYLL model were performed from 1 TeV to 10 PeV for p and He and from 10 TeV to 10 PeV for Fe, since SIBYLL is a semi-superposition model and for heavy nuclei a larger primary energy is required
- for primary energies in the range from 1 TeV to 10 PeV for MCM.

In the present study the interactions and decay processes in the atmosphere for hadrons and muons are simulated above 75 GeV. The electromagnetic component was completely discarded.

The magnetic field was considered for the location Geneva with the horizontal component of the Earth's magnetic field $B_x = 20.0\ \mu$T, and the vertical component of the Earth's magnetic field $B_z = 42.8\mu$ T. No limitations for the detector area were used.

At production, only muons with energies exceeding the energy cut-off (see equation 1.12)

$$E_\mu = 0.55 \cdot (e^{\frac{0.4 \cdot 0.32}{\cos\theta}} - 1) \qquad [TeV] \ , \tag{5.7}$$

were saved for further analysis. The energy cut-off depends on the zenith angle of muons and detector depth, and it was determined using the GEANT [127] program for Monte Carlo simulation of muon propagation through the overburden composed of rock and molasse and through the Hadron Calorimeter of the ALEPH detector, all together with a thickness of 320 *mwe*. The energy loss spectrum was fitted and the parameters 0.55 and 0.4 in equation (5.7) were obtained from the fit [122]. The presented formula for the energy cut is in agreement with results obtained in [123].

This procedure is performed with the aim to establish the decoherence distributions, multiplicity and transverse momentum distributions of muons underground at the CosmoALEPH experiment level for the considered primary particles and Monte Carlo models.

5.2 Influence of Multiple Scattering and Magnetic Field on Energetic Muons Underground

To compare experimental results on cosmic rays with predictions from Monte Carlo simulations, always a large amount of data is needed. This is difficult to realize, especially with increasing energy of primary particles, since the flux decreases very rapidly according to a power law $\sim E^{-2.7}$.

For this analysis, the study of the muon component underground with the CosmoALEPH experiment, sheltered by an overburden of 320 *mwe*, which introduces a threshold energy of 75 GeV for vertical incidence, it was decided to use directly CORSIKA muons produced in the atmosphere, having energies greater than the energy cutoff (see equation (5.7)), and to analyze them underground. This decision is based on the analysis, as described in detail in Appendix A.

To proceed with this analysis, two important factors had to be checked: the influence of the Earth's magnetic field and the effect of multiple scattering of muons in the overburden.

Because muons are charged particles, they are deflected in the Earth's magnetic field. How much this deflection will be, depends both, on the momentum of muon P and on the magnetic field B, according to the equation:

$$P = e \cdot B \cdot R_L, \tag{5.8}$$

where e is the electric charge $e = 1.6 \cdot 10^{-19}\ C$ and R_L represents the Larmor radius (bending radius of the track in the magnetic field) [75]. Multiplying both sides of the above equation (5.8) with the velocity of light $c = 3 \cdot 10^8$ m/s results:

$$c \cdot P[J] = 1.6 \cdot 10^{-19}[C] \cdot B[\frac{V \cdot s}{m^2}] \cdot R_L[m] \cdot 3 \cdot 10^8[\frac{m}{s}],$$

where 1 $Tesla = \frac{V \cdot s}{m^2}$ and 1 $J = C \cdot V$. Converting the left side from Joule [J] to electron Volt [eV], 1 $J = 1eV/1.6 \cdot 10^{-19}$, one obtains

$$c \cdot P[eV] = 3 \cdot 10^8 \cdot B \cdot R_L \ . \tag{5.9}$$

For 75 GeV/c muons (energy cutoff for CosmoALEPH), and a magnetic field for Central Europe of $B \approx 20\ \mu T$, the Larmor radius becomes

$$R_L = 12.5 \cdot 10^6 \quad m \ .$$

The obtained bending radius for the considered magnetic field and energy is very large compared to a depth of H = 125 m and the deflection angle can be approximated to [75]:

$$\theta = \frac{H}{R_L} \ . \tag{5.10}$$

Calculating the above ratio, one gets a maximum deflection angle of

$$\theta = 0.00057^0 \ .$$

From this value it can be concluded, that the influence of the magnetic field for this depth interval (125 m) is negligible.

Another characteristic of charged particles is that they are scattered by the Coulomb potential of nuclei and electrons in matter. Particles suffer a large number of scattering processes with very low deviations from the original path. For small scattering angles, the distribution of scattering angles is symmetrical around $\theta = 0^0$.

Frequently, charged particles suffer also larger scattering angles. Summing up the many relatively small random changes of the of flight direction in passing through an absorber, the so called "average scattering angle" $\sqrt{\langle\theta^2\rangle}$ of the projected angular distribution of scattering angles [75] is obtained:

$$\sqrt{\langle\theta^2\rangle} = \theta_{plane} = \frac{13.6MeV}{\beta \cdot c \cdot p} \cdot z \cdot \sqrt{\frac{x}{X_0}} \cdot \{1 + 0.038 \cdot ln(\frac{x}{X_0})\}, \tag{5.11}$$

where p is the momentum (in MeV/c), $\beta \cdot c$ the velocity, z the charge of the scattered particle, and x/X_0 is the thickness of the scattered medium x, measured in units of the radiation length X_0.

For muons of energy 75 GeV/c, traversing a medium of thickness $320 \cdot 10^2$ g/cm^2 (CosmoALEPH depth) with a radiation length of about 30 g/cm^2, the average scattering angle is

$$\theta_{plane} = 0.0063 \, rad = 0.36^0 \; .$$

These calculations show that the influence of the Earth's magnetic field and the multiple scattering process on the muons that can reach the CosmoALEPH experiment is relatively small. These results again motivate for a direct analysis of CORSIKA muons underground at the CosmoALEPH experiment depth without considering the effects of magnetic deflection and multiple scattering. A possibility would have been to combine CORSIKA, which simulates extensive air showers in the atmosphere with GEANT [127] -a program for MC simulations of muon propagation through the overburden. But the disavantage of GEANT is that this program operates only with single muon events, and this work is based on the analysis of multiple muon events; namely the decoherence distribution of muons and the multiplicity of muons underground.

5.3 Description of the MC Analysis Method

Based on the results obtained in the previous section, it is assumed that energetic muons simulated with CORSIKA at sea level propagate underground without changing their direction. The coordinates of muons which have an energy greater than the energy-cut-off (see equation (5.7)) were calculated at the depth of $h = 125$ m using the coordinates for these muons at the sea level provided by CORSIKA. Figure 5.3 illustrates the geometrical view of this assumption.

According to figure 5.3, the coordinates of muons underground at the CosmoALEPH level are:

$$x_1 = x_0 + h \cdot tg\theta \cdot cos\varphi \; [m] \qquad y_1 = y_0 + h \cdot tg\theta \cdot sin\varphi \; [m] \; , \qquad (5.12)$$

where x_0 and y_0 are the coordinates of muons at sea level.

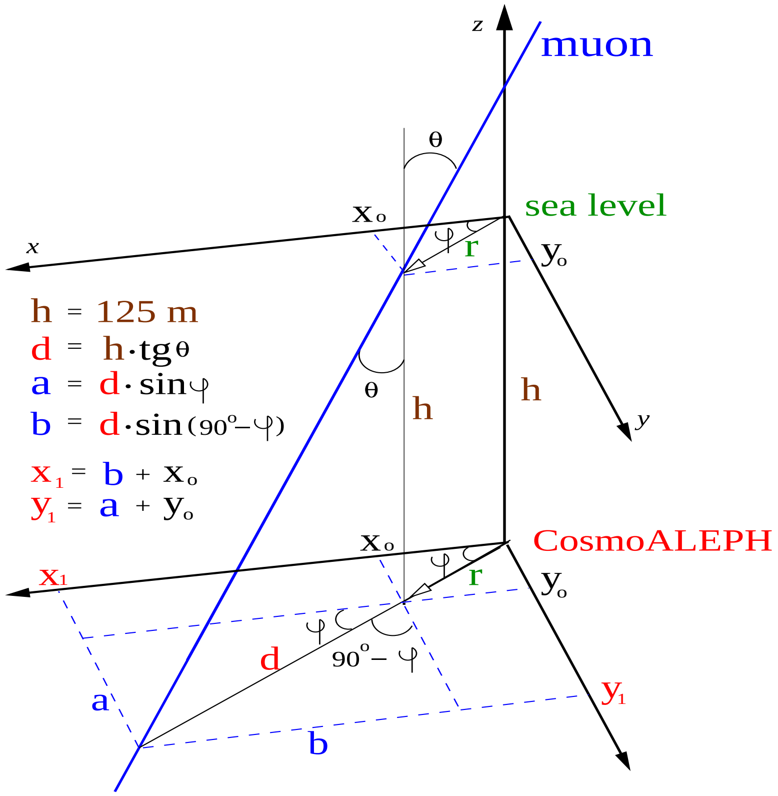

Figure 5.3: The x and y coordinates of muons underground at 320 mwe.

θ and φ are the zenith and azimuth angles of the muon. The radial distance of muons from the shower axis at the CosmoALEPH depth is

$$R = r + d = \sqrt{x_1^2 + y_1^2} \qquad [m], \tag{5.13}$$

where r is the radial distance of muons from the shower axis at sea level:

$$r = \sqrt{x_0^2 + y_0^2} \qquad [m] \; .$$

Figure 5.5, where the coordinates of muons at sea level and at the CosmoALEPH level are presented, shows that the distribution of the x and y coordinates underground at the CosmoALEPH level suffers an expected widening along x and y axes. An explanation of this behavior is provided by the zenith angle distribution at sea level (see figure 5.4), which shows that muons of energies above 70 GeV in a shower are produced predominantly under $40° - 50°$. Such muons, which at sea level are concentrated around the center of the coordinate system, will spread out more at the CosmoALEPH level.

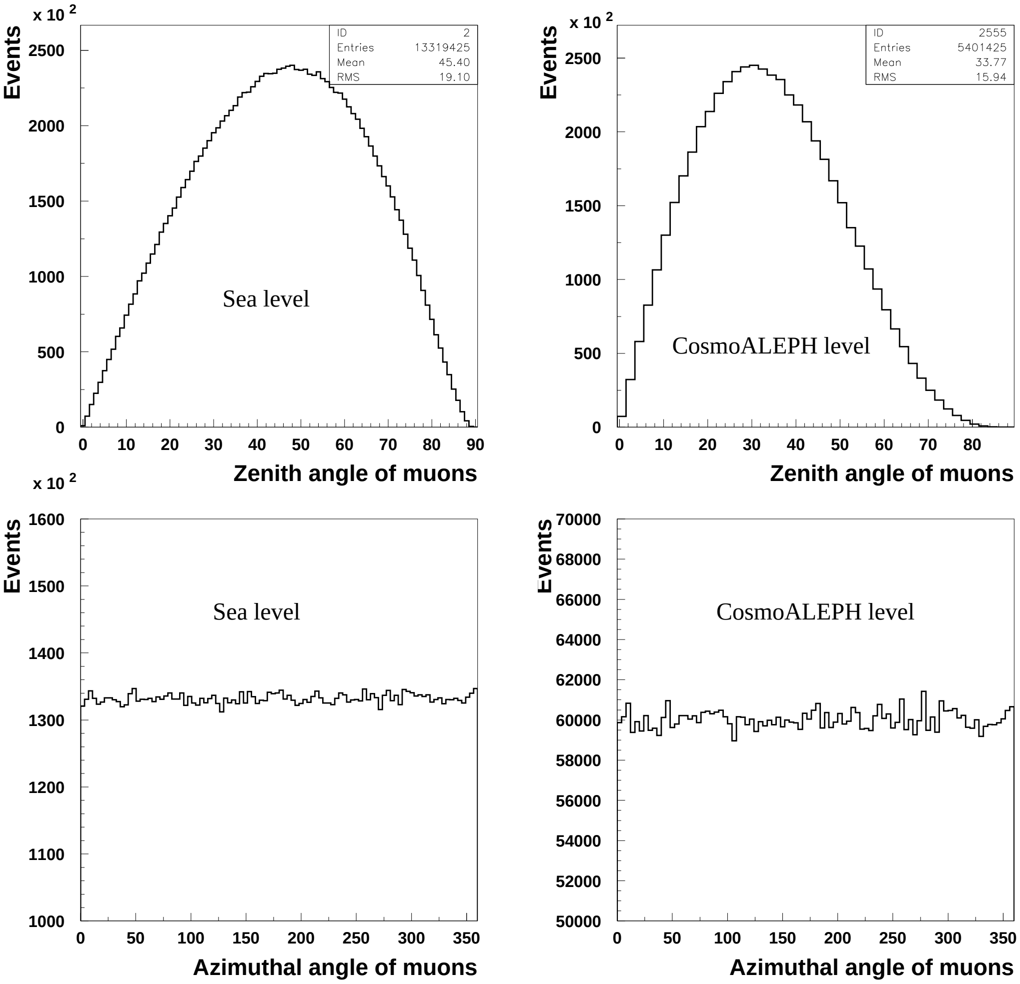

Figure 5.4: Zenith angle and azimuthal angle distributions of muons for 10^8 proton showers simulated with QGSJET for primary energies from 170 GeV to 10 PeV and zenith angles from 0^0 to 89^0 at sea level and at the CosmoALEPH depth of 320 *mwe*.

Figure 5.4 presents the muon zenith and azimuthal angle distributions at sea level and at CosmoALEPH level. From the zenith angle distribution it is seen that the number of muons reaching the CosmoALEPH level decreases by more than a factor of two, also a shift of the maximum from $40° - 50°$ to $25° - 35°$ is observed. This effect is well understood, being due to the energy loss in the overburden that depends on the zenith angle. The azimuthal angle distribution is uniformly distributed at sea level as well as at the CosmoALEPH level.

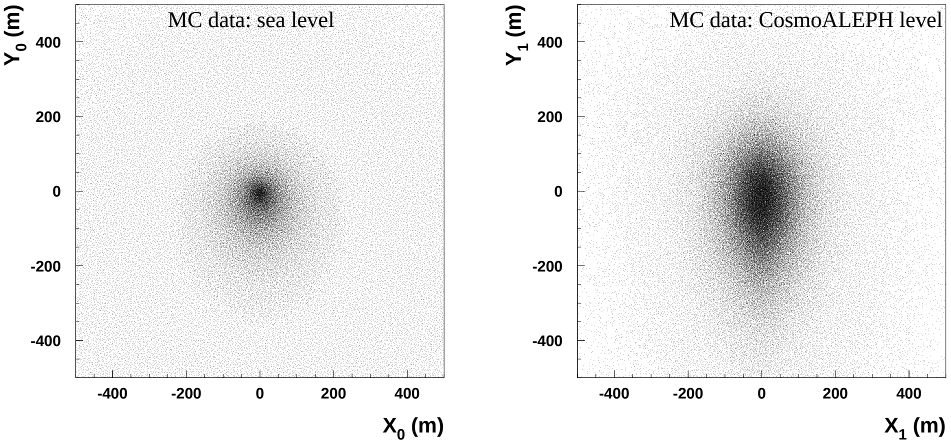

Figure 5.5: The x and y coordinates of muons at sea level (left plot) and at the CosmoALEPH depth (right plot) produced with the QGSJET model for proton primaries simulated for primary energies from 170 GeV to 10 PeV and zenith angles from 0^0 to 89^0.

For a depth of $h = 125\ m$ and an energy of muons at sea level E_μ, the energy of muons at this depth is determined as $E_{125m} = E_\mu - E_{cut-off}$. The total time of flight since the first interaction of the primary particle in the atmosphere, until this depth is reached is $t = t_{sealevel} + t_{125}$ (see figure 5.6), where $t_{sealevel}$ is the time of flight since the first interaction of the primary particle in the atmosphere up to sea level, provided by CORSIKA. t_{125} is the time of flight from sea level through the overburden up to the CosmoALEPH depth.

In the CORSIKA program [12], the time of flight of a paticle, that moves along its path, is computed by dividing the particle's particular path length l by the avarage velocity β

$$dt = \frac{l}{c \cdot \beta} = \frac{l}{c \cdot \frac{v}{c}}, \tag{5.14}$$

where β is the arithmetic mean of the laboratory velocities of the particle at the beginning and the end of the trajectory. The total time elapsed since the first interaction is the sum of all time intervals accumulated by the successive particles to the observational level.

For

$$l = \frac{h}{cos\theta}, \qquad v = \frac{P \cdot c^2}{E},$$

and a momentum of

$$P = \frac{1}{c} \cdot \sqrt{E^2 - m_0^2 \cdot c^4},$$

the time of flight from sea level up to the CosmoALEPH depth is:

$$t_{125m} = \frac{125m}{cos\theta} \cdot \frac{1}{c^2 \cdot \frac{P_{125m}}{E_{125m}}} = \frac{125m}{cos\theta} \cdot \frac{E_{125m}}{c \cdot \sqrt{E_{125m}^2 - m_0^2 \cdot c^4}.} \qquad [\mu s] \quad (5.15)$$

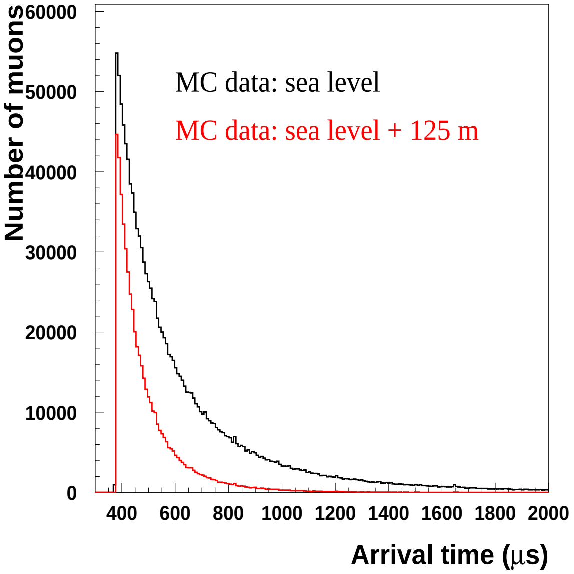

Figure 5.6: Arrival time of muons at sea level (black distribution) and total arrival time at the CosmoALEPH level (red distribution).

Thus, knowing the x and y coordinates and the arrival time t of each muon at the CosmoALEPH depth, for each shower with two or more than two muons underground, the distance

$$d_{\mu_1 \mu_2} = \sqrt{(x_{\mu_1} - x_{\mu_2})^2 + (y_{\mu_1} - y_{\mu_2})^2}$$

and time difference

$$\Delta t = t_{\mu_1} - t_{\mu_2} \ ,$$

in the plane of the CosmoALEPH detectors, for all possible pairs of two muons in a shower, were calculated. These calculations were performed for all simulated showers.

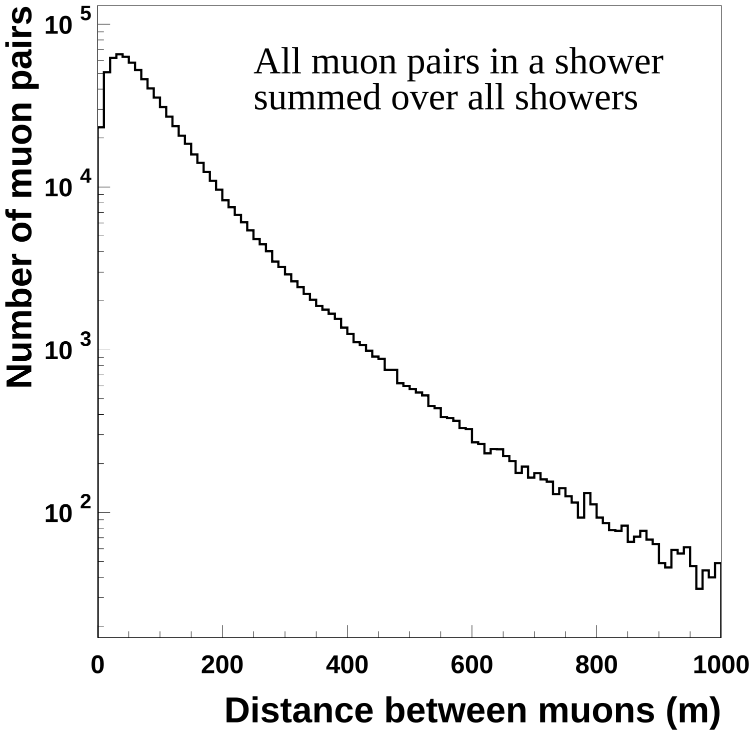

Figure 5.7: Distance between muons in one shower summed over all showers simulated with QGSJET

To obtain the coincidence rate at specified separations between muons, 20 values from 1 m to 1186 m were chosen,

d_{ij} [m]									
1,	2,	4,	6,	8,	12,	14,	18,	39,	54,
96,	167,	262,	272,	428,	524,	666,	760,	927,	1186

and only those muon pairs with distances equal to one of these 20 values in the interval ±0.5 m and in the time window of ±20 μs were saved (see figure 5.8).

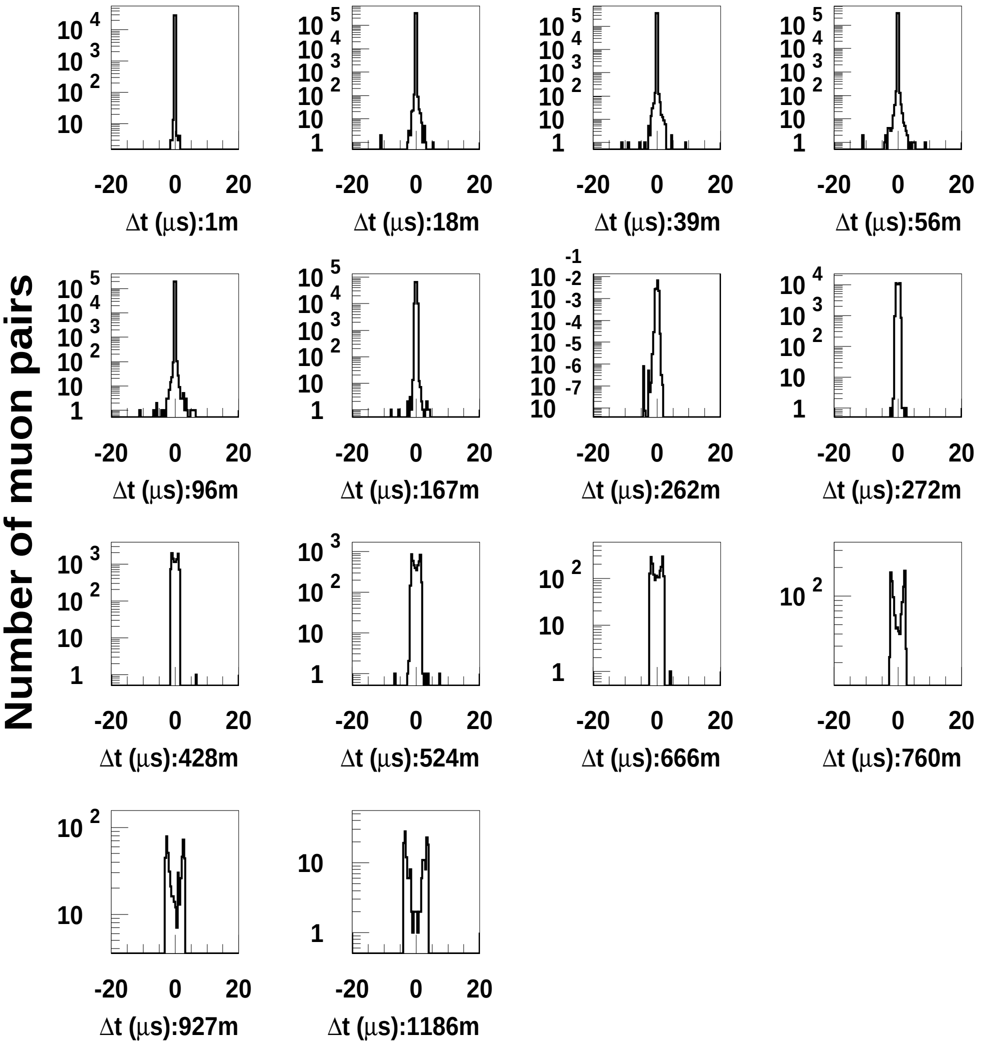

Figure 5.8: The distributions of muon arrival time differences at various separations obtained from $5 \cdot 10^8$ PROTON showers, simulated with the VENUS model for energies from 170 GeV to 10 PeV and zenith angles from 0^0 to 89^0.

In figure 5.8 one sees that with increasing distance between muons, the number of muon pairs decreases, and the time difference distributions become wider as it is expected exhibiting a splitting, observed also in experimental data. A likely explanation is that at large distances there are mostly inclined showers.

The next important point is to normalize the obtained coincidence rates of muons on the area product of the pair of detectors. Since the geometry of detectors in MC is not implemented (it would be required to simulate about $10^{16} - 10^{18}$ primary showers in order to cover the 1 km interval with sufficient coincidences at large separations, which is not realistic for the present capacities), the method of ellipsoidal rings is used.

Figure 5.10 shows that muons in the xy plane of the detectors at the CosmoALEPH depth see an ellipsoid, not a circle. Thus, the radial distance of each muon from the shower axis R was projected onto a plane normal to the particular shower axis and labeled as R_0 (see figure 5.9).

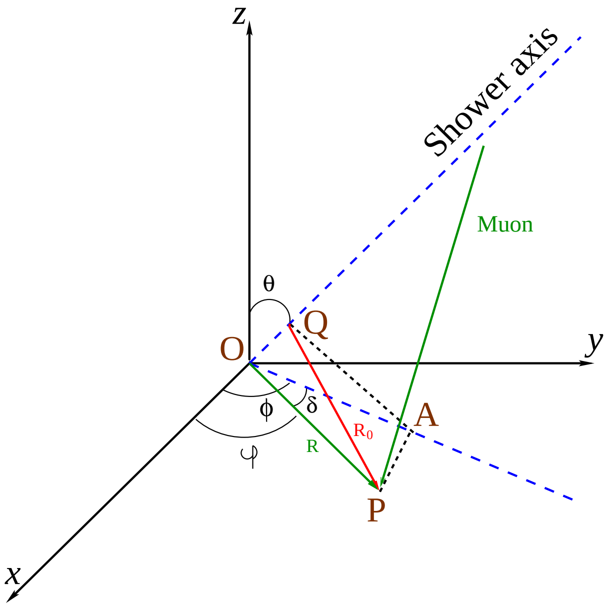

Figure 5.9: Radial perpendicular distance of muons from the shower axis.

In the above figure 5.9, Θ and Φ are the zenith and azimuth angles of the primary particle, φ is the azimuth angle of the muon, with $\delta = \Phi - \varphi$. Projecting PQ $\perp$ OQ and PA $\perp$ OA, leads to PA $\perp$ QA and OQ $\perp$ QA. The angle between OQ and OA is $90^0 - \Theta$. Thus, the radial perpendicular distance of muons from the shower axis can be inffered from the triangle QAP as

$$R_0 = \sqrt{PA^2 + QA^2}\,, \tag{5.16}$$

where $PA = R \cdot sin\delta$ and $QA = OA \cdot sin(90^0 - \Theta) = OA \cdot cos\Theta$, with $OA = R \cdot cos\delta$. Based on these derivations, a final expression for the radial perpendicular distance of muons from the shower axis is obtained:

$$R_0 = R \cdot \sqrt{1 - cos^2\delta \cdot sin^2\Theta} \qquad [m]\,. \tag{5.17}$$

If the area of the circle of radius R_0 which is in the plane normal to the shower axis is projected on the xy detector plane, one obtains an ellipse in the xy plane with radii R and R_0 (see the figure 5.10)

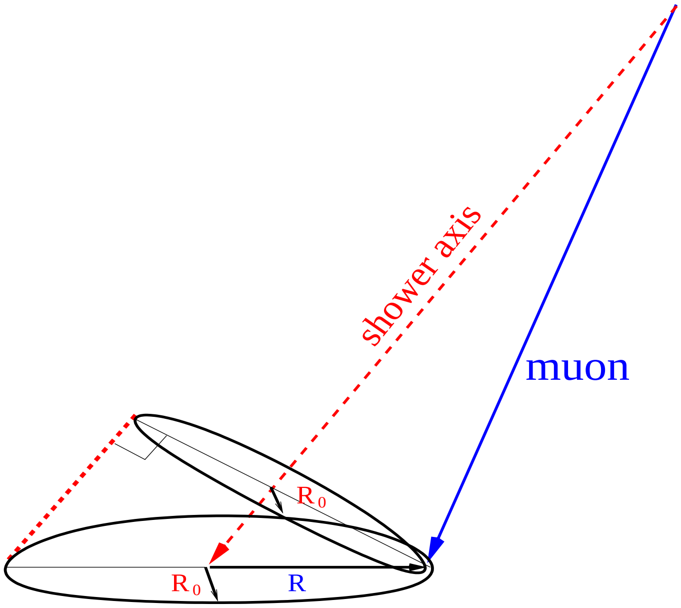

Figure 5.10: The projection of a circle in the plane normal to the shower axis on the xy plane of the detectors.

Adding and substracting 50 cm from these radii, an ellipsoidal ring for each muon in the pair is obtained. Each muon pair at a particular separation is weighted by normalization to the product of the areas of the obtained ellipsoidal rings for each muon in the pair:

$$W = \frac{1}{S_{\mu_1} \cdot S_{\mu_2}} \qquad [m^{-4}], \tag{5.18}$$

where

$$S_{\mu_1} = \pi \cdot \{(R_{0\mu_1} + 0.5)(R_{\mu_1} + 0.5) - (R_{0\mu_1} - 0.5)(R_{\mu_1} - 0.5)\} \tag{5.19}$$

$$S_{\mu_2} = \pi \cdot \{(R_{0\mu_2} + 0.5)(R_{\mu_2} + 0.5) - (R_{0\mu_2} - 0.5)(R_{\mu_2} - 0.5)\}. \tag{5.20}$$

This analysis was performed for each simulated primary element using four considered CORSIKA models in case of constant mass composition and Maryland composition approaches (the results are presented in the next section).

5.4 Decoherence Distribution predicted by MC Models

In this section the analysis of the MC decoherence distributions is presented. The procedure described in the previous section is applied to three simulated primary elements p, He and Fe using the high energy hadronic models QGSJET, VENUS, SIBYLL and NEXUS, for two considered mass composition approaches: constant (CMC) and Maryland (MCM) compositions.

For each simulated primary element, the coincidence rates for 20 different muon separations normalized to m^4 were calculated. The decoherence distributions are represented by the coincidence rate as a function of distance between muons, that in a large part correspond to the separations between the CosmoALEPH detectors.

In the next figures the shapes for the decoherence distribution for all the considered set of parameters are presented.

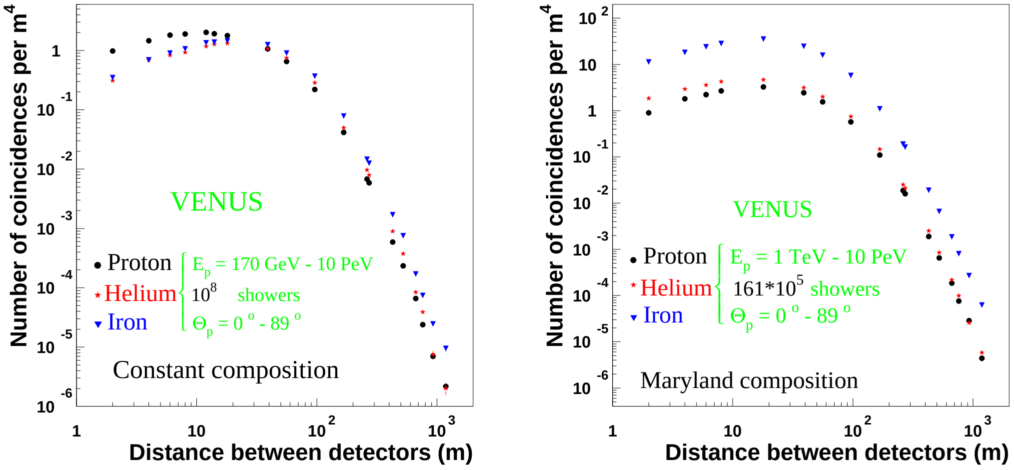

Figure 5.11: The decoherence distribution for p, He and Fe primaries simulated with VENUS for CMC and MCM .

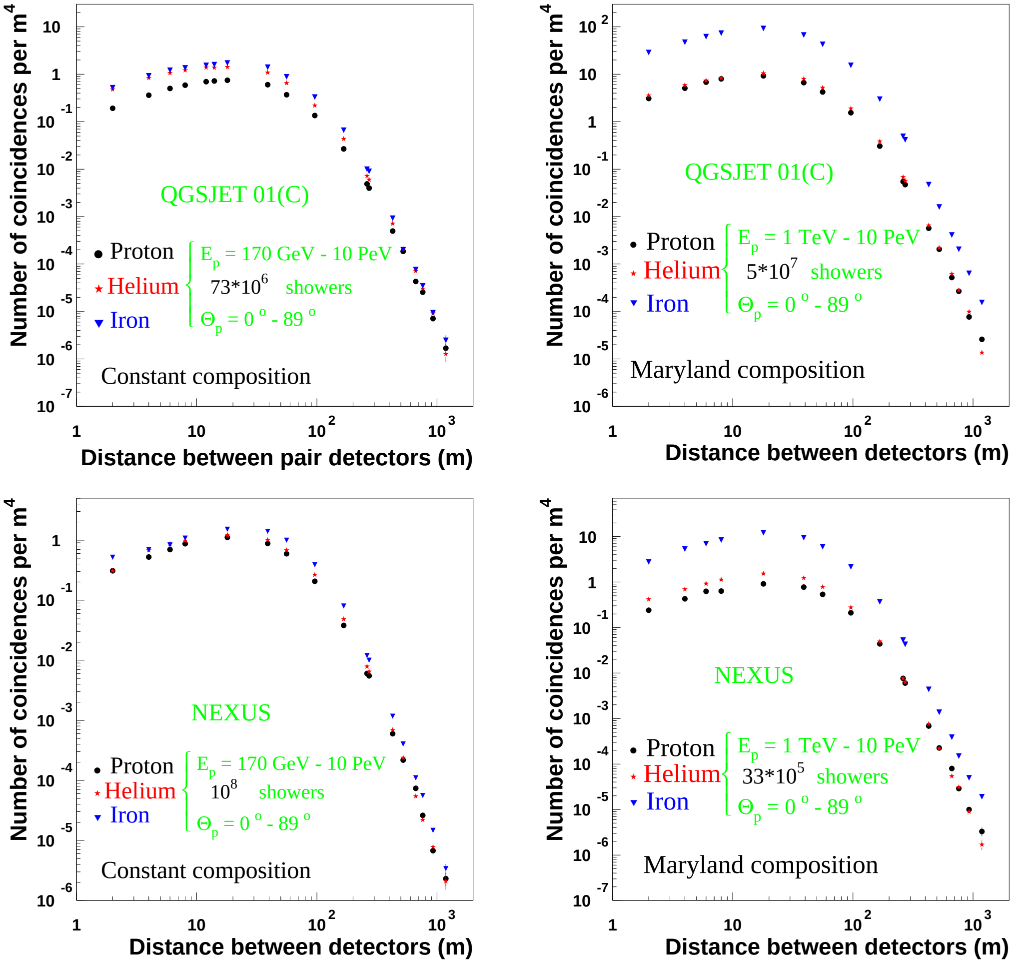

Figure 5.12: The decoherence distribution for p, He and Fe primaries simulated with QGSJET and NEXUS for CMC and MCM.

The shapes of the decoherence distribution for the SIBYLL model are presented in figure 5.13. As specified in section 5.1, the elements for this model are simulated for a different primary energy interval, namely proton and helium in the range from 1 TeV to 10 PeV, and iron in the energy range from 10 TeV - 10 PeV. As a result, the amplitude for the iron decoherence curve is higher compare to those of proton and helium.

From the above plots it is clearly seen that decoherence curves determined with CORSIKA for different primary elements do not differ too much from each other.

A slight difference between proton, helium and iron shapes is observed at small separations in case of all considered hadronic interaction models, while the decoherence shapes at large separations seem to be very similar for all elements.

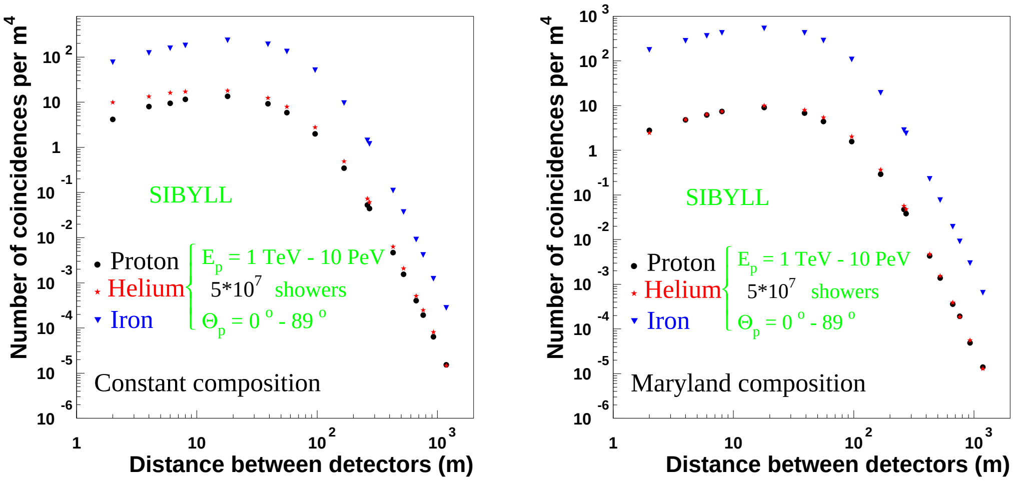

Figure 5.13: The decoherence distribution for p, He and Fe promaries simulated with SIBYLL for CMC and MCM.

Thus, in the study of the chemical composition with CORSIKA hadronic interaction models, the information at small separations plays an decisive role.

The obtained shapes for the decoherence distribution were best fitted with the Nishimura-Kamata-Greisen (NKG) formula:

$$f(R) = a \cdot \left(\frac{R}{R_0}\right)^b \left(1 + \frac{R}{R_0}\right)^c , \tag{5.21}$$

where a, b, c, and R_0 are parameters obtained from the fit, and R $[m]$ represents the distance between the detectors, or in this case, between muons at separations that correspond to the CosmoALEPH detectors. In the next figures 5.14, 5.15, 5.16, and 5.17 the results of the fit with the NKG formula are presented. The values obtained for the free parameters are given in table 5.3.

Model	Elements	a	b	c	R_0 [m]
VENUS CMC	**proton**	**16.980**	**0.650**	**- 7.230**	**121.08**
	helium	**31.290**	**1.034**	**-8.520**	**147.00**
	iron	**32.084**	**1.020**	**- 8.050**	**146.80**
VENUS MCM	**proton**	**64.010**	**0.990**	**- 7.740**	**121.80**
	helium	**54.460**	**0.740**	**-7.930**	**146.95**
	iron	**611.02**	**0.950**	**- 7.700**	**122.99**
QGSJET CMC	**proton**	**16.580**	**1.056**	**- 7.700**	**118.00**
	helium	**24.590**	**0.910**	**-7.930**	**129.00**
	iron	**33.130**	**0.930**	**- 8.690**	**157.00**
QGSJET MCM	**proton**	**151.11**	**0.918**	**- 7.460**	**119.70**
	helium	**171.80**	**0.886**	**-8.057**	**143.00**
	iron	**1706.1**	**0.960**	**- 7.930**	**128.00**
SIBYLL CMC	**proton**	**259.28**	**0.964**	**- 7.990**	**121.00**
	helium	**210.78**	**0.699**	**-8.329**	**154.00**
	iron	**5176.5**	**0.965**	**- 8.878**	**160.00**
SIBYLL MCM	**proton**	**179.13**	**0.967**	**- 8.170**	**133.00**
	helium	**250.38**	**1.050**	**-8.637**	**143.00**
	iron	**11702.0**	**0.977**	**- 8.579**	**146.00**
NEXUS CMC	**proton**	**27.340**	**1.074**	**- 8.090**	**125.00**
	helium	**28.270**	**0.996**	**-8.620**	**150.00**
	iron	**52.864**	**1.190**	**- 8.587**	**140.00**
NEXUS CMC	**proton**	**20.500**	**0.990**	**- 8.700**	**161.30**
	helium	**38.100**	**1.040**	**-8.830**	**144.80**
	iron	**347.98**	**1.110**	**- 8.980**	**140.20**

Table 5.3: The values of the free parameters a, b, c, and R_0 obtained from the fit with the NKG formula (5.21) on the shapes of the decoherence distribution of each element simulated with VENUS, QGSJET, SIBYLL and NEXUS for constant mass composition (CMC) and Maryland composition (MCM) approaches.

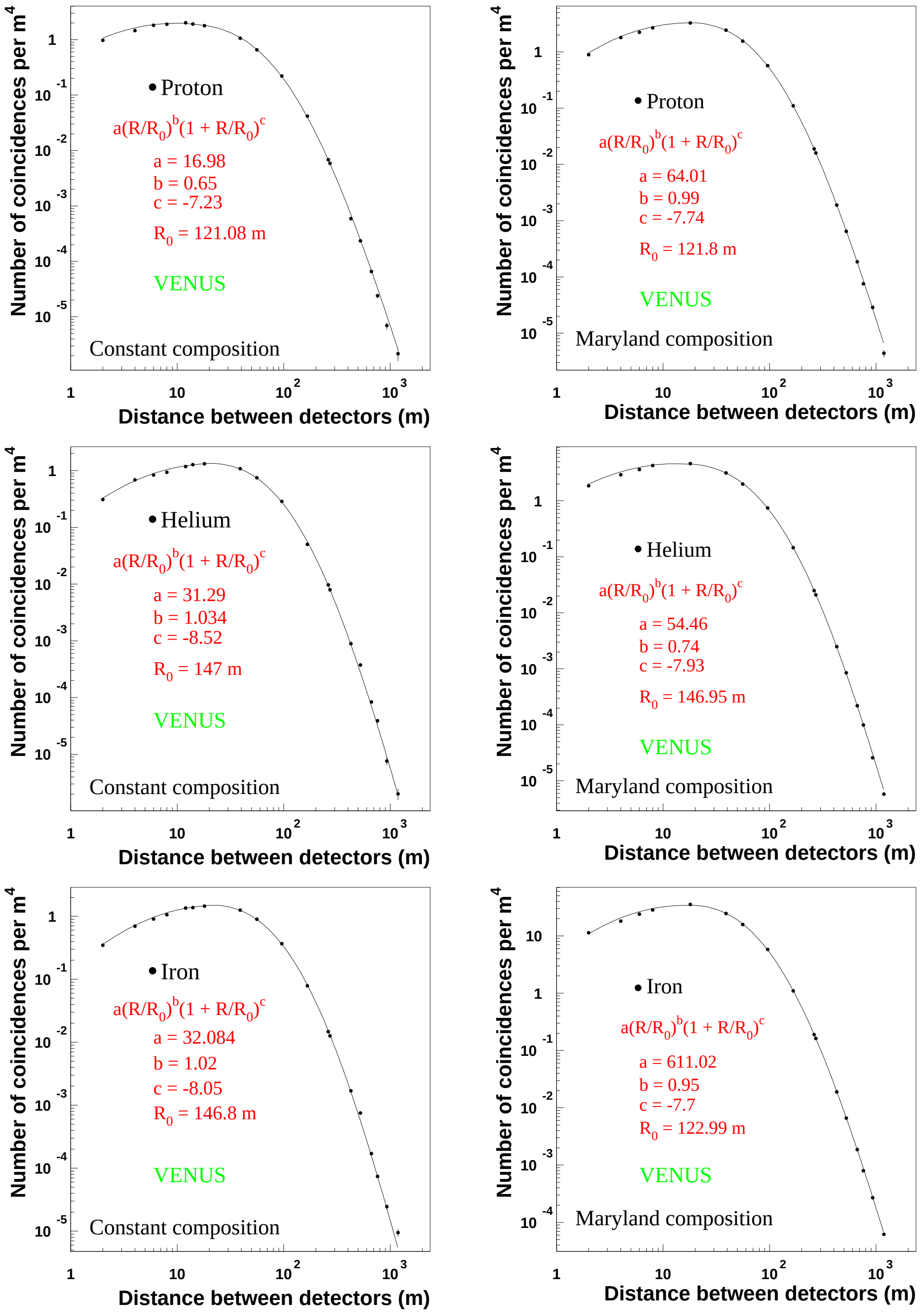

Figure 5.14: Fitted decoherence distributions for p, He and Fe with NKG for VENUS in case of Constant mass and Maryland composition models.

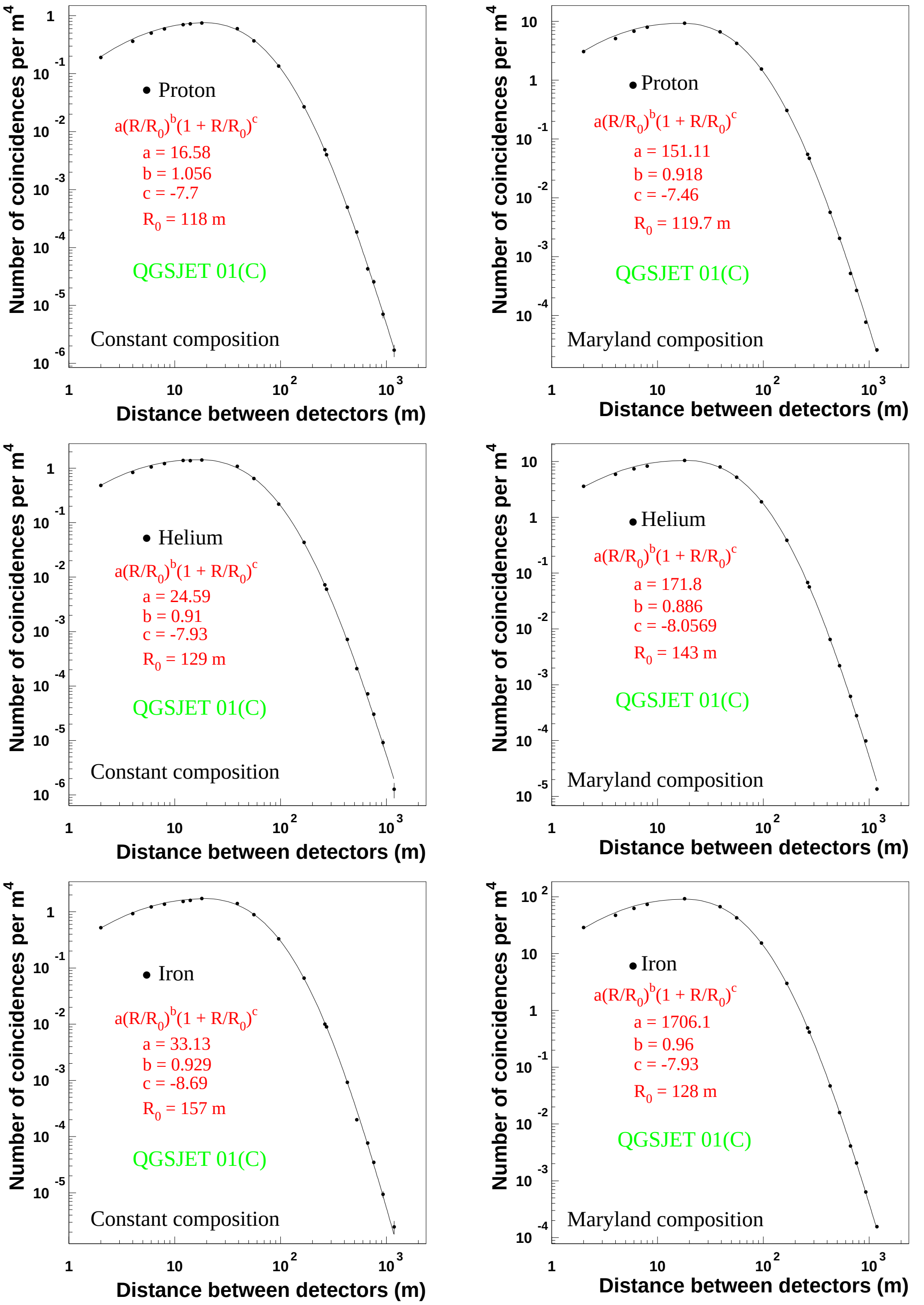

Figure 5.15: Fitted decoherence distributions for p, He and Fe with NKG for QGSJET in case of Constant mass and Maryland composition models.

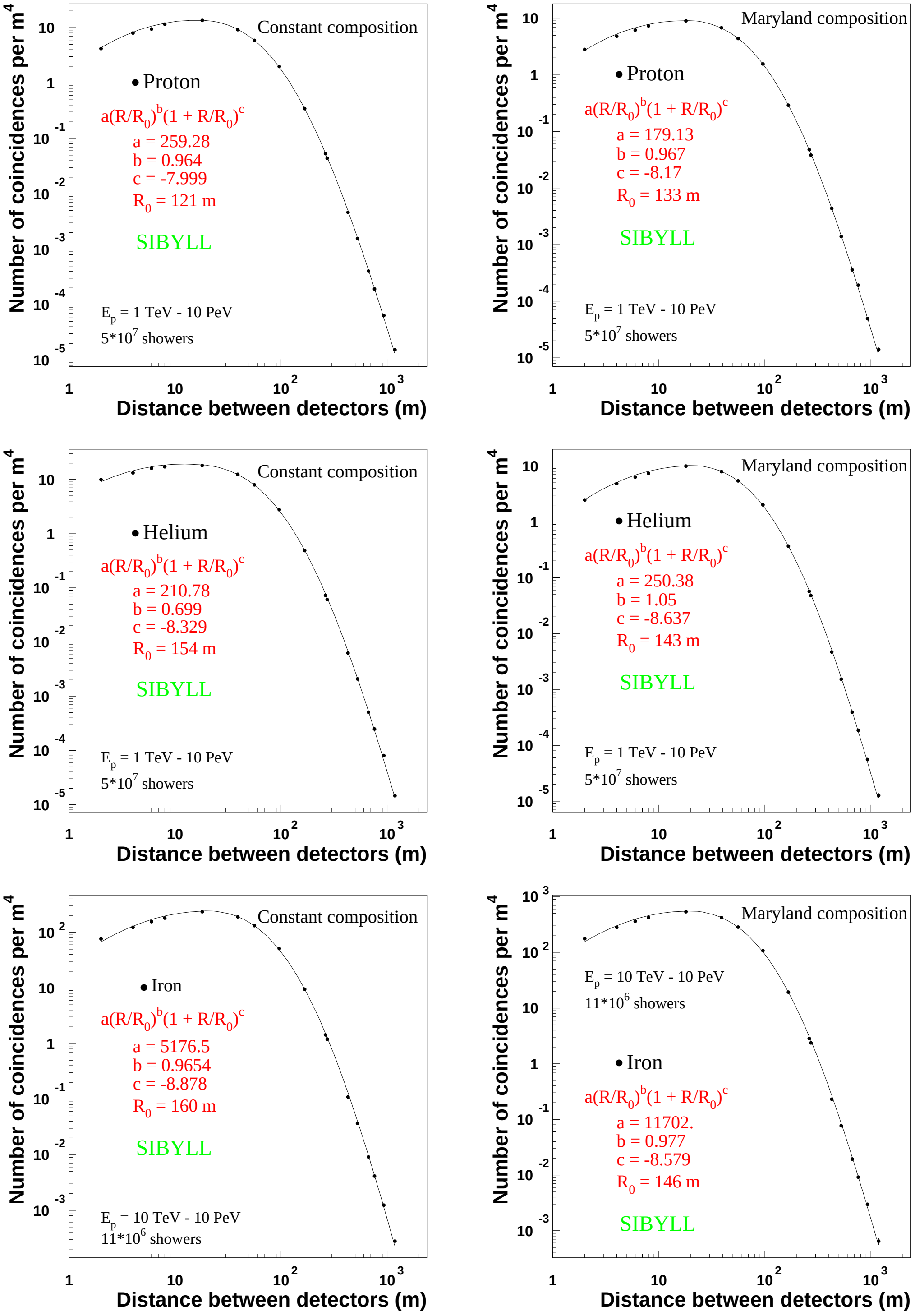

Figure 5.16: Fitted decoherence distributions for p, He and Fe with NKG for SIBYLL in case of Constant mass and Maryland composition models.

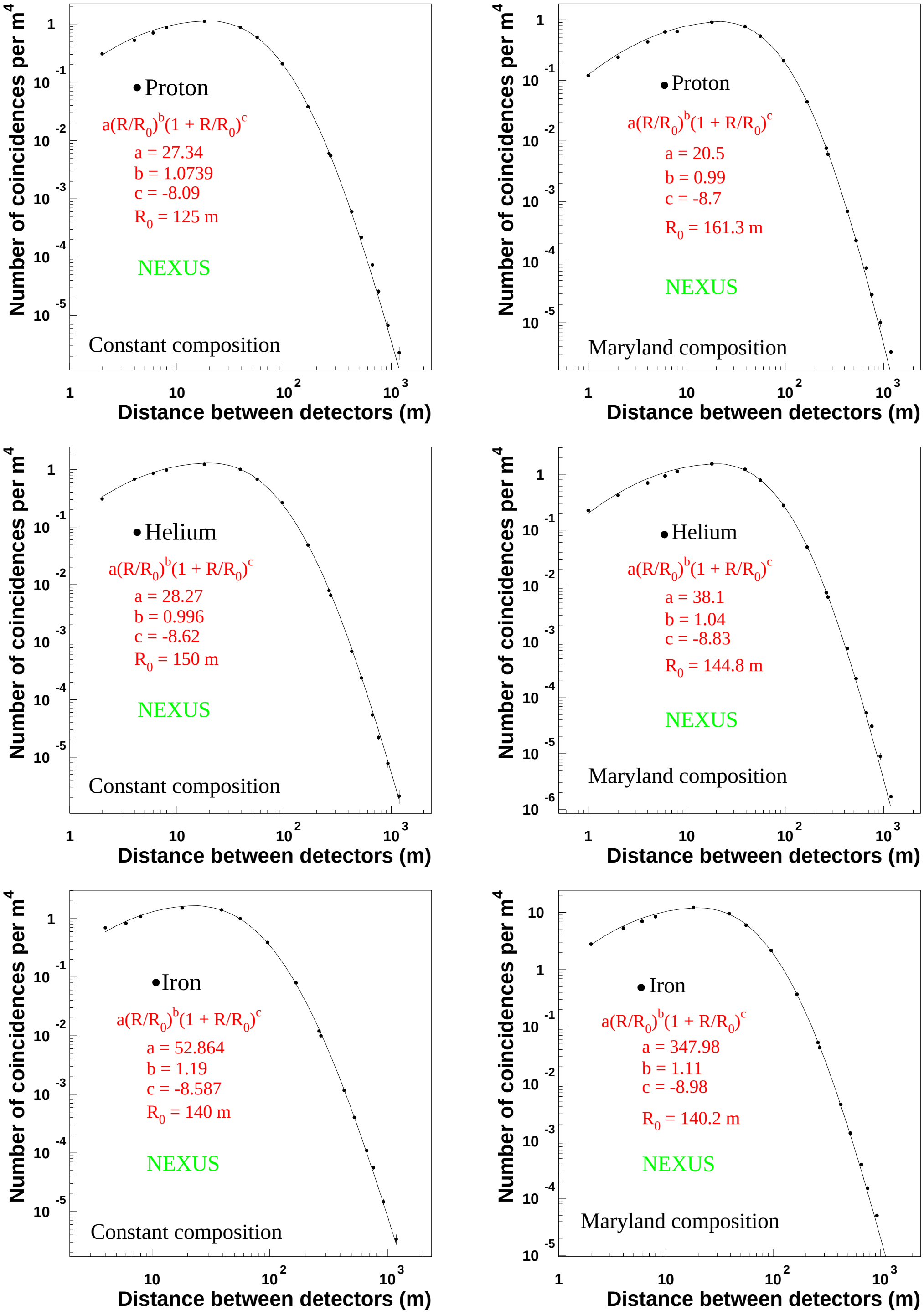

Figure 5.17: Fitted decoherence distributions for p, He and Fe with NKG for NEXUS in case of Constant mass and Maryland composition models.

From these figures it is seen that the NKG formula is in very good agreement with the decoherence distributions obtained for all considered primary elements simulated with different hadronic models and composition approaches.

The errors are treated according to Poisson statistics [75] ($n \pm \sqrt{n}$). In this analysis, the coincidence rates for each particular separation between muons i ($i = 1, 20$) (see figure 5.8) are determined by summing up the weighted (on the product of ellipsoidal areas) bin content of the time difference distributions. By dividing the number of muon pairs for a particular separation i to the coincidence rate, obtained from the time difference distribution, an average area S_i $[m^4]$ is calculated as :

$$S_i = \frac{Number\ of\ muon\ pairs\ for\ distance\ i}{Coincidence\ rate\ for\ distance\ i}\ . \tag{5.22}$$

Thus, this area is constant for each chosen value i for distances between muons, and the statistical error for the coincidence rate i will be

$$Err_i = \frac{\sqrt{Number\ of\ muon\ pairs\ for\ distance\ i}}{S_i}. \tag{5.23}$$

Since the number of muon pairs is large, statistical errors are small, therefore they are invisible in the above figures.

The obtained parametrizations for the decoherence distribution for each primary element are compared with the experimental decoherence distribution, with the aim to determine the primary composition of cosmic rays. Results of the comparison are presented in Chapter 6.

5.5 Multiplicity and Transverse Momentum Distributions of CORSIKA Muons measured in the TPC

For the analysis of the multiplicity and transverse momentum distributions in the Time Projection Chamber with CORSIKA high energy hadronic interaction models, simulation data for the constant mass composition approach were selected (see the section 5.1).

To have an absolute comparison of the measured multiplicity and transverse momenta in the TPC of the ALEPH detector with those predicted by CORSIKA, the number of simulated air showers should correspond to the run time of the TPC during dedicated runs, which was computed and corresponds to 5.167 *days* or 446428.8 *seconds*. To determine the flux that should be simulated with CORSIKA for 5.167 days, the differential primary spectrum is used

$$\frac{dN}{dE \cdot dS \cdot d\Omega \cdot dt} \approx E^{-2.7} \qquad (cm^2 \cdot sec \cdot sr \cdot GeV)^{-1} \; . \tag{5.24}$$

The primary integral flux at sea level for primary energies varying from E_{min} to E_{max} and zenith angles θ from 0° to 89° is given by

$$N = \int\limits_{E_{min}}^{E_{max}} E^{-2.7} \, dE \int\limits_{0}^{\frac{\pi}{2}} sin\theta \, d\theta \int\limits_{0}^{2\pi} d\phi \int\limits_{0}^{A} dS \int\limits_{0}^{T} dt \; , \tag{5.25}$$

where the solid angle is defined as

$$d\Omega = \int\limits_{0}^{\frac{\pi}{2}} sin\theta \, d\theta \int\limits_{0}^{2\pi} d\phi = 2\pi \; , \tag{5.26}$$

which assumes an isotropic flux of primary particles at the edge of the atmosphere extrapolated to the Earth's surface. The azimuth angle ϕ is taken between 0° and 360°. A is the sampling area of the position of interaction points of primary particles at the edge of the atmosphere with the shower axis pointing in the centre of the coordinate system at the surface (see figure 5.18).

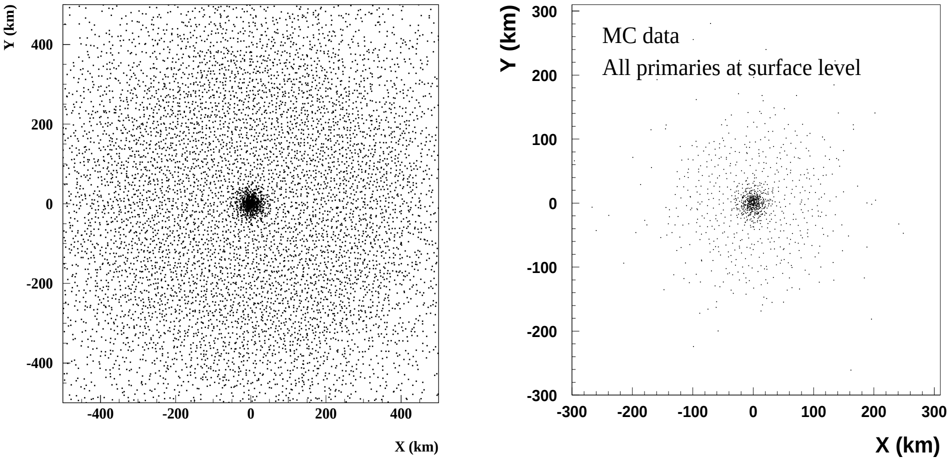

Figure 5.18: The sampling area of the interaction points of primary particles around the centre of the coordinate system at sea level for events with muons at sea level (left plot), and only for events with muons unterground at 125 m depth (right plot).

The distribution of the interaction points of primary particles around the origin of the coordinate system at the surface taken from the CORSIKA simulation is shown in figure 5.18. As seen from this figure the interaction points are spread over large distances from the impact point of the shower axis. The coordinates in this figure are given in units of kilometers. It is clear that the detector size (the length of the ALEPH detector is about 7 m along the z direction) is too small compared to the sampling volume provided by the CORSIKA program. Also, one must take into account that at a given depth underground not all produced muons will reach the detection level and this will require the generation of a very large number of showers in the time interval corresponding to the recording time of the experimental data.

The integral flux of primary particle showers with muons capable to reach a certain depth underground is

$$N \approx \int_{E_{min}}^{E_{max}} E^{-2.7}\, dE \int_{0}^{\frac{\pi}{2}} sin\theta\, d\theta \int_{0}^{2\pi} d\phi \int_{0}^{A_{eff}} dS \int_{0}^{T} dt\ . \tag{5.27}$$

$A_{eff} = \pi R^2$ is the sampling area of impact points of showers axis underground of a radius R around the origin of the coordinate system. This effective area takes into account the muon survival probability ϵ_μ at a certain depth underground so that $A_{eff} = \epsilon_\mu \cdot A$. Since the area A of the impact points of the shower axis at the surface is very large and does not have an exact definition, the effective area underground was determined from the CORSIKA results.

Plotting the coordinates of impact points of primaries underground at the CosmoALEPH experiment depth, but only for events with muons at this depth (see figure 5.19), it can be seen that the radius of the sampling area of impact points of primaries is in the range of meters, not kilometers. The geometry of the ALEPH TPC (a detailed explanation will follow) was implemented underground at a depth of 125 m with the centre placed below the origin of the coordinate system defined by the intersection point of the shower axis at sea level. The analysis, performed only for events with muons detected in the implemented TPC, showed that the coordinates of impact points of primaries underground at the CosmoALEPH experiment depth extends over an area which is more compact in comparison to the sampling area of impact points of those primaries with muons anywere underground (see figure 5.19).

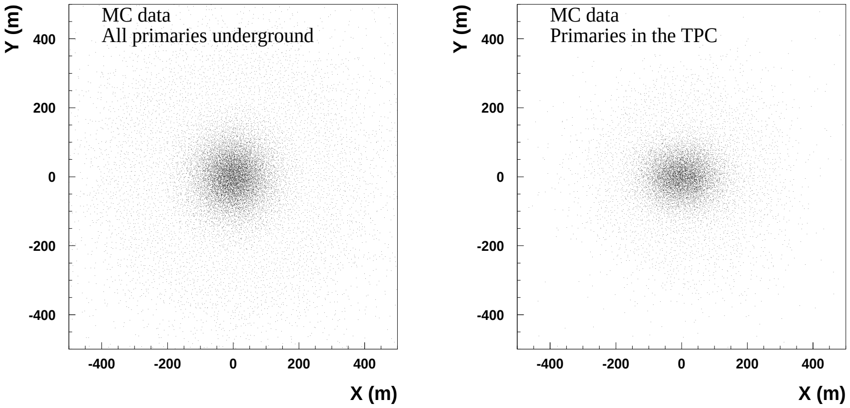

Figure 5.19: Effective sampling area of the shower axis underground for events with muons unterground at 125 m depth (left plot) and with muons unterground at 125 m depth in the TPC (rightplot).

Thus, for the analysis of the muon component at the CosmoALEPH depth, a sampling area of the showers axis with a radius of 500 m is assumed. The effective area can be written as $A_{eff} = \pi \cdot 500^2 = 7.85 \cdot 10^9$ $[cm^2]$.

For different primary energy intervals, the primary flux will be different, ilustrated in following points:

- **The primary flux for the energy range** 170 **GeV -** 10^7 **GeV**

Calculating the integral

$$\int_{170\ GeV}^{10^7\ GeV} E^{-2.7}\, dE = \frac{E^{-1.7}}{(-1.7)} \Bigg|_{170\ GeV}^{10^7\ GeV} = 95.02 \cdot 10^{-6}\ (cm^2 \cdot sec \cdot sr)^{-1}$$

and substituting this value into equation (5.27), the corresponding real collection time for 10^8 showers simulated with CORSIKA for this primary energy range is estimated as

$$T = \frac{10^8}{95.02 \cdot 10^{-6} \cdot 2\pi \cdot 7.85 \cdot 10^9} \approx 21.33\ sec\ . \tag{5.28}$$

If 10^8 simulated events correspond to 21.33 sec, then the flux that should be simulated in $446428, 8$ $seconds$ is

$$N = \frac{10^8 \cdot 446428.8}{21.33}\ . \tag{5.29}$$

Thus, for this energy $E_{min} = 170$ GeV $\rightarrow$ $N_{5.167\ days} \approx 20933.0 \cdot 10^8\ showers$ have to be simulated.

- **The primary flux for the energy range 10^3 GeV - 10^7 GeV**

Calculating the integral

$$\int_{10^3\ GeV}^{10^7\ GeV} E^{-2.7}\, dE = \frac{E^{-1.7}}{(-1.7)}\Bigg|_{10^3\ GeV}^{10^7\ GeV} = 4.6725183 \cdot 10^{-6}\ (cm^2 \cdot sec \cdot sr)^{-1}$$

and substituting this value into equation (5.27), the corresponding real collection time for $5 \cdot 10^7$ showers simulated with CORSIKA for this primary energy range is estimated as

$$T = \frac{5 \cdot 10^7}{4.6725183 \cdot 10^{-6} \cdot 2\pi \cdot 7.85 \cdot 10^9} \approx 216.858654\ sec\ . \tag{5.30}$$

If $5 \cdot 10^7$ simulated events correspond to 216.858654 *sec*, then the flux that should be simulated in 446428.8 *seconds* is

$$N = \frac{5 \cdot 10^7 \cdot 446428.8}{216.858654}\ . \tag{5.31}$$

Thus, for this energy $E_{min} = 10^3\ \ GeV\ \ \rightarrow\ \ N_{5.167\ days} \approx 10293.0 \cdot 10^7\ showers$ have to be simulated.

- **The primary flux for the energy range 10^4 GeV - 10^7 GeV**

Calculating the integral

$$\int_{10^4\ GeV}^{10^7\ GeV} E^{-2.7}\, dE = \frac{E^{-1.7}}{(-1.7)}\Bigg|_{10^4\ GeV}^{10^7\ GeV} = 0.9322827 \cdot 10^{-7}\ (cm^2 \cdot sec \cdot sr)^{-1}$$

and substituting this value into equation (5.27), the corresponding real collection time for the 10^7 showers simulated with CORSIKA for this primary energy range is estimated as

$$T = \frac{10^7}{0.9322827 \cdot 10^{-7} \cdot 2\pi \cdot 7.85 \cdot 10^9} \approx 2173.601\ sec\ . \tag{5.32}$$

If 10^7 simulated events correspond to 2173.601 *sec*, then the flux that should be simulated in 446428.8 *seconds* is

$$N = \frac{10^7 \cdot 446428.8}{2173.601}\ . \tag{5.33}$$

Thus, for this energy $E_{min} = 10^4$ GeV $\rightarrow$ $N_{5.167\ days} \approx 205.0 \cdot 10^7$ *showers* have to be simulated.

These calculations show that the simulated showers with CORSIKA are insufficient for an absolute comparison with experimental data. To speed up the simulation, in order to accumulate the necessary primary flux that will correspond to 446428.8 *seconds* in the considered radius of 500 m, the position of the TPC centre is moved many times for each simulated event matching the calculated above flux for 5.167 days. For example, for the primary energy range 170 GeV - 10^7 GeV, the position of the TPC is changed 20933 times in the area of 500 m around the shower axis, as illustrated in figure 5.20. The x_d and y_d coordinates of the centre of the TPC detector are selected randomly with the RANLUX random function in this area.

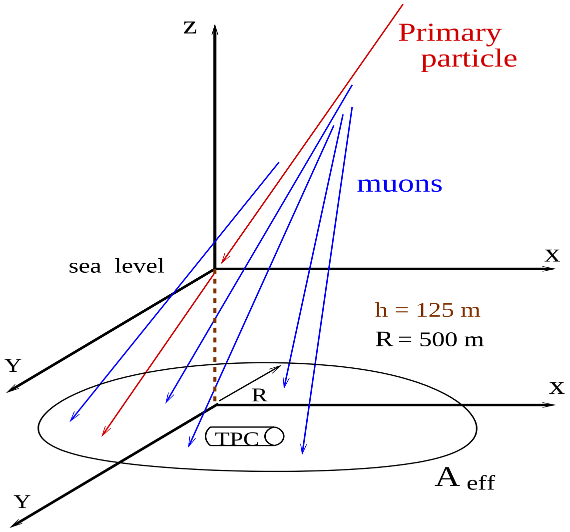

Figure 5.20: Sampling area for the TPC in MC.

- **CORSIKA muons through the TPC volume**

All events with at least one muon that penetrates to the CosmoALEPH experiment depth (320 *mwe*) were considered for the analysis.

The TPC centre is chosen to be at 125 m underground with ± 1.8 m intervals along the vertical direction, that corresponds to its outer radius. For the interval 123.2 m - 126.8 m an imaginary track for each muon with 37 hits with a step width of 0.1 cm on the vertical direction is defined. For each 0.1 cm step, the coordinates x, y and z for each muon are saved (see figure 5.21).

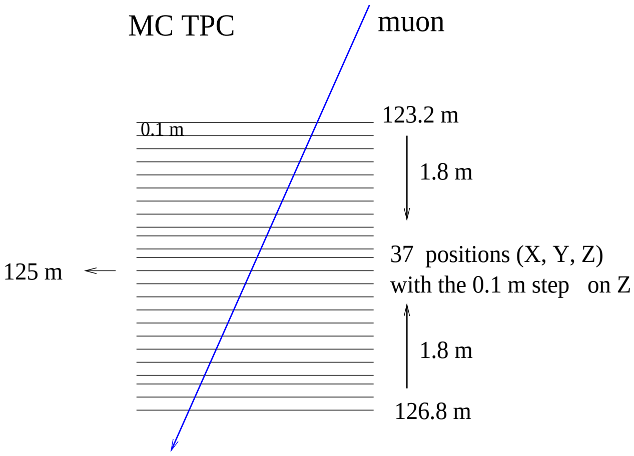

Figure 5.21: MC muon track.

All 37 hits of a muon are checked if they are inside the TPC according to a simple implemented geometry: a circle of radius R in the yz plane varying along the x direction in the interval from $-2.2\ m$ to $+2.2\ m$

$$R = \sqrt{(125.0 - z_\mu(hit))^2 - (y_d - y_\mu(hit))^2}\ . \tag{5.34}$$

If $R \leq 1.8\ m$, then it is checked if this hit is inside the xy plane

$$abs(x_d - x_\mu(hit)) \leq 2.2m. \tag{5.35}$$

The TPC is aligned along the x direction in MC (see the figure 5.22), in the experimental data along the z direction.

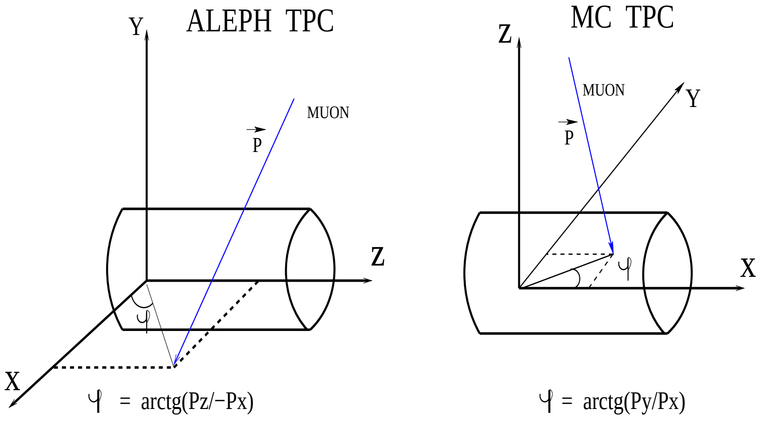

Figure 5.22: The positioning of the TPC in MC and in the experiment.

This positioning, required by the different definitions of the coordinate systems in the experiment and MC, was respected during the analysis, and for the comparison with the experimental data the corresponding planes in both cases (MC and experiment) were used.

Because in the experimental data only tracks through the barrel were analysed, this is handled in the MC in the following way: the endcap hits were counted in a band of 0.1 m in the x direction for both endcaps of the TPC if they satisfied the following conditions:

$$abs((x_d - x_\mu(hit)) - 2.2m) \leq 0.1m \tag{5.36}$$

$$abs((x_d - x_\mu(hit)) + 2.2m) \leq 0.1m. \tag{5.37}$$

If the number of endcap hits for both endcaps was simultaneously zero, the muon track was accepted for the analysis. This resulted in the appearance of two maxima in the azimuthal angle distribution, the gaps reflecting lost tracks through the barrel-endcap transition (see figure 5.23).

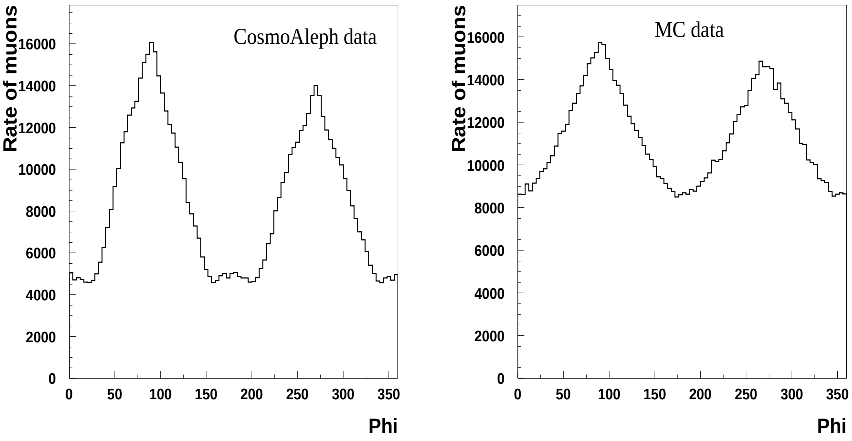

Figure 5.23: Azimuthal angle distribution

In CORSIKA, the azimuthal angle of the muon is calculated as

$$\varphi = arctg(\frac{P_y}{P_x}) \ ,$$

as can be seen from figure 5.22. In the experimental data, the azimuthal angle is calculated as

$$\varphi = arctg(\frac{P_z}{-P_x}) \ ,$$

since the axis orientation of the coordinate system differs from the CORSIKA axis definition. Also, in the experimental data, due to the presence of the magnetic field in the TPC, muon tracks are curved in form of a helix, and the azimuthal angle is determined by a tangent to this helix at the closest approach to the interaction point in the beam pipe.

Thus, figure 5.23 represents a relative comparison between the experimental and MC azimuthal angles (the differences are clearly seen), which shows the two peak structure. Figures 5.24 and 5.25 show the distributions of hit coordinates of muon tracks in the TPC. These plots demonstrate the correctness of the implemented TPC geometry in MC. To check that the geometry of the TPC is correctly implemented, the distributions of hit coordinates in the TPC are plotted and illustrated in figure 5.24.

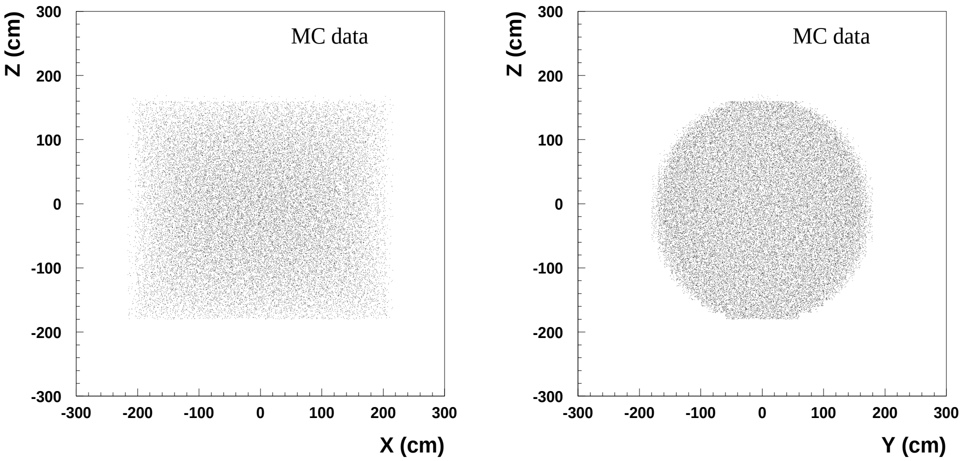

Figure 5.24: The effective area of the TPC in the xz plane (left plot) and in the yz plane (right plot)

Finally, the selection criteria to accept a muon for this analysis in the TPC at the CosmoALEPH depth are specified in the following points:

- Momentum $P_\mu > 5$ GeV/c
- Number of endcap hits for both endcaps simultaneously are zero
- The distance between the first and the last hit in the TPC is > 1.6 m
- The track of the muon crosses the plane xy of the TPC

The cross checks of these conditions are presented in the following figures. In figure 5.25 it is visible that the TPC in the experiment is separated into two halves by a membrane, while in the MC this membrane is absent. The track length and zenith angle distributions, presented for CosmoALEPH data and MC data are in acceptable agreement.

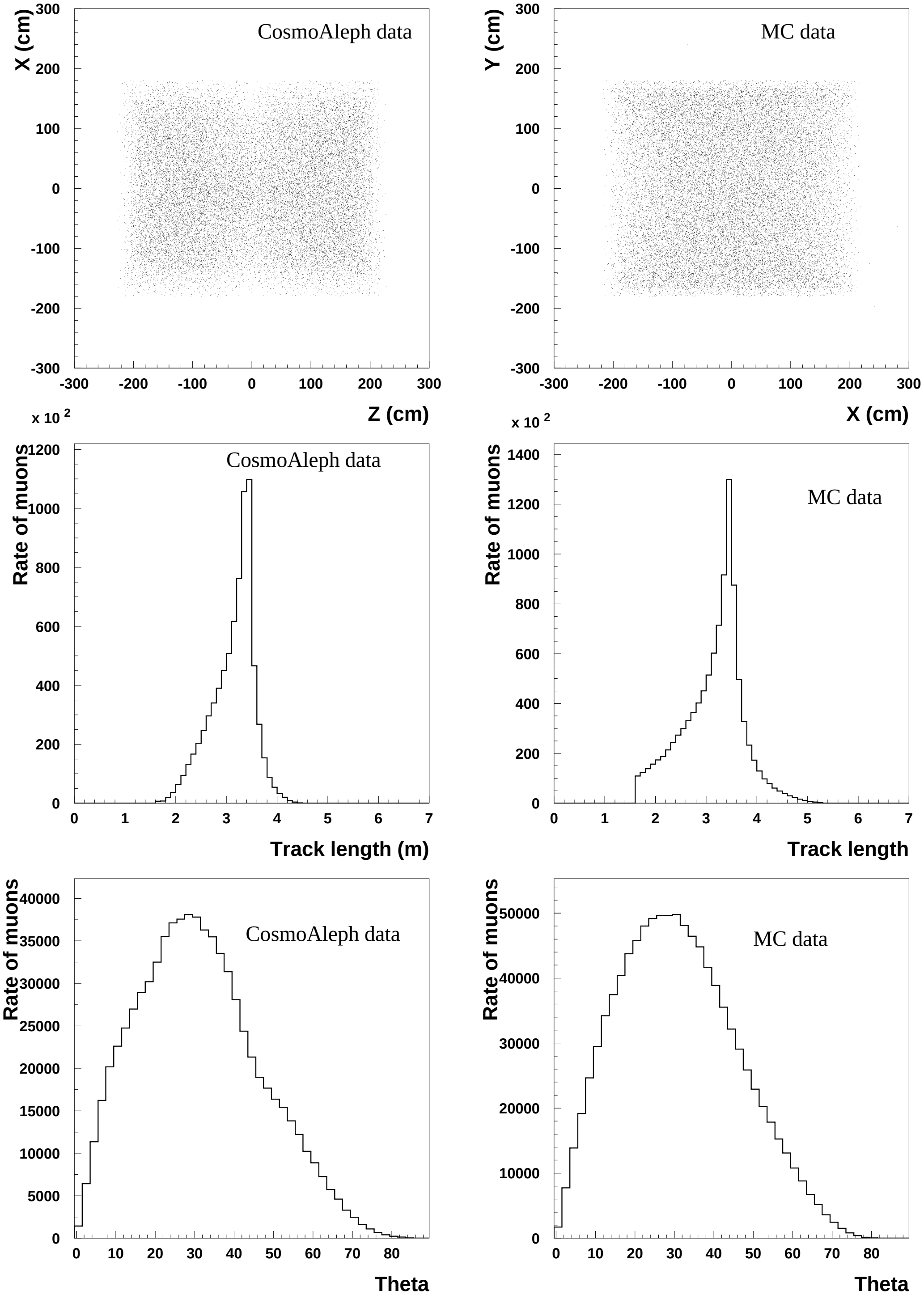

Figure 5.25: The distribition of the muon track intersection points with xz and xy TPC planes, the track length and zenith angle distributions for CosmoALEPH and MC data.

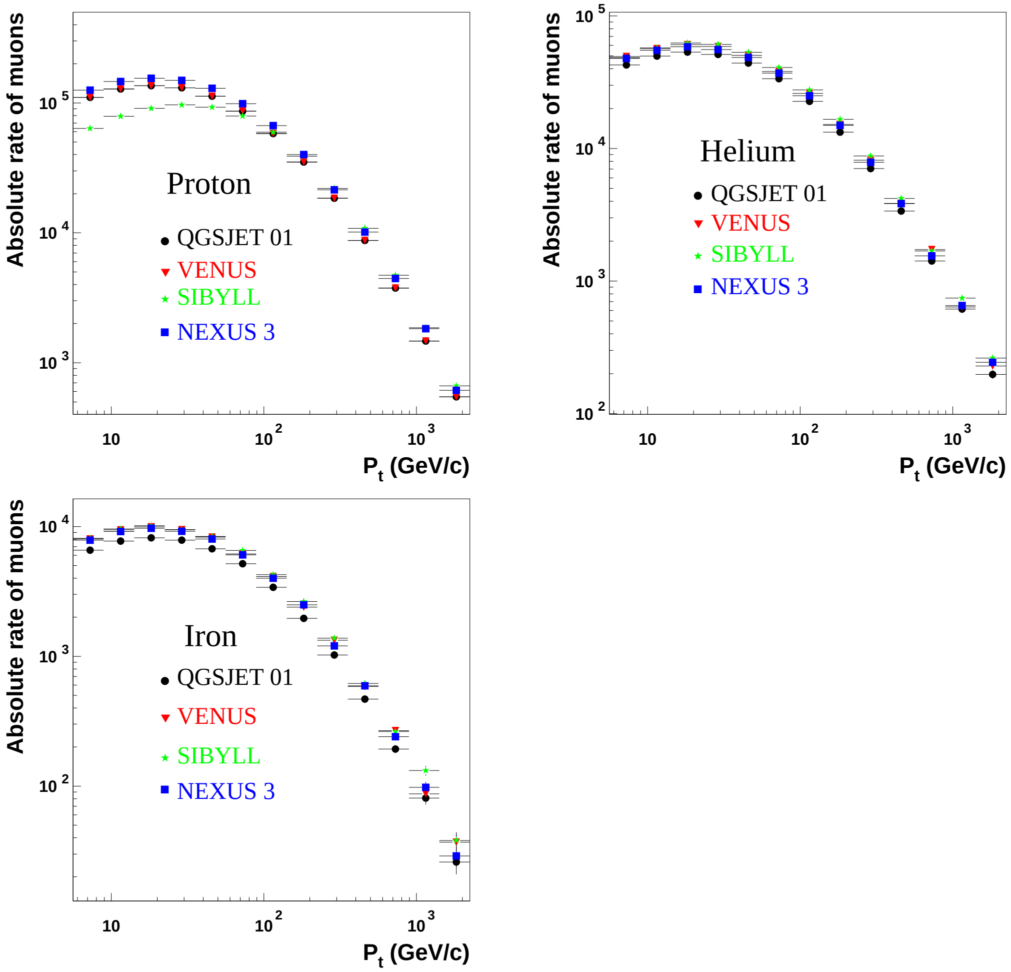

Figure 5.26: Transverse momentum distributions for p, He and Fe primaries simulated with QGSJET, VENUS, SIBYLL and NEXUS with a statistics corresponding to the TPC uptime of 5.167 days.

In the final step, the muon transverse momentum was calculated with respect to the vertical incidence and presented in figure 5.26 for proton, helium and iron primaries simulated with the QGSJET, VENUS, SIBYLL and NEXUS models for the constant mass compostion approach. From these figures it can be seen that the transverse momentum distributions for a primary element are very similar for different MC models. An exeption is SIBYLL for proton primaries, which contributes with less muons at low transverse momenta compared to the other models. A more detailed analysis of shapes of the transverse momentum distributions showed good agreement with the Nishimura-Kamata-Greisen formula (see Appendix C).

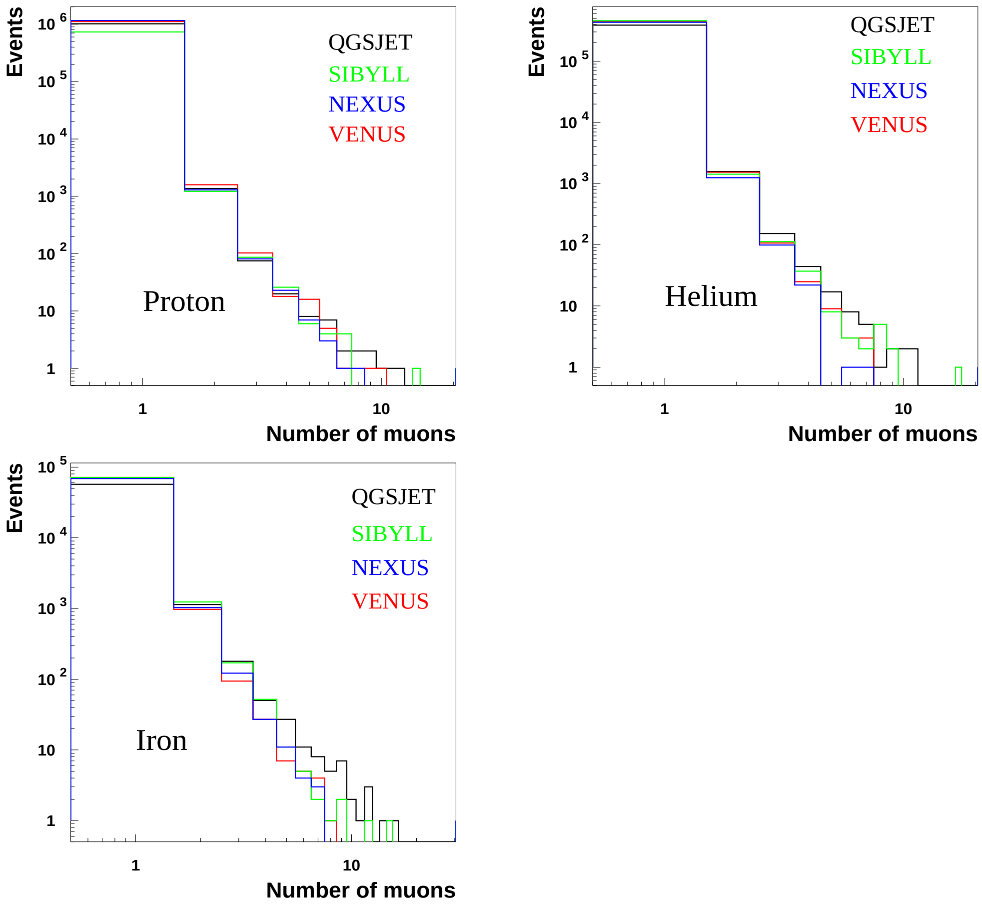

Figure 5.27: Muon multiplicity distributions for p, He and Fe primaries simulated with QGSJET, VENUS, SIBYLL and NEXUS with a statistics corresponding to the TPC uptime of 5.167 days.

The muon multiplicity distributions for simulated proton, helium and iron showers are presented in comparison for the considered CORSIKA models (see figure 5.27). The obtained muon multiplicity distributions for simulated primaries with different models do not show evident differences. The exception is only SIBYLL, which shows less single muon events for simulated proton primaries. This effect could be explained by the considered higher energy range for the simulation (see section 5.1). The mean value of these distributions is around unity with very litle variations for different elements and models.

The comparison of simulated transverse momentum and multiplicity distributions of muons with CosmoALEPH experimental data is presented in Chapter 6.

Chapter 6

Results

6.1 CosmoALEPH and the MC Decoherence Distribution

In the previous chapters the decoherence curve measured underground at a depth of 320 *mwe* with the CosmoALEPH detectors and the decoherence curves simulated with different high energy hadronic interaction models of the CORSIKA program were determined. The final step is to compare the measured and MC predicted decoherence distributions in order to extract the elemental composition of primary cosmic rays.

The CosmoALEPH decoherence curve is fitted with a sum of parameterizations obtained for **p**, **He**, and **Fe** for each considered hadronic model and composition approach:

$$f(x) = par(1) \cdot f_p + par(2) \cdot f_{He} + par(3) \cdot f_{Fe}, \tag{6.1}$$

where f_p, f_{He}, and f_{Fe} are the Nishimura-Kamata-Greisen (NKG) parametrizations

$$f(R) = a \cdot \left(\frac{R}{R_0}\right)^b \left(1 + \frac{R}{R_0}\right)^c$$

with parameters a, b, c, and R_0 given in table 5.3. For the fit, the parameters par(1), par(2), and par(3) are varied to analyse the shape of the above function (6.1) around its minimum. The values obtained for the parameters are used to determine the contributions of primary cosmic elements.

In order to prevent unphysical values of the parameters used in the fit of the measured CosmoALEPH data, a constrained fit with imposed limits on the parameters was performed.

The fitting procedure uses the MINIUT Function for minimization and error analysis [131].

Two types of fits were performed on the decoherence curve measured with CosmoALEPH: namely a diagonal fit that takes into account the total errors of the measurements, which represent a combination of systematical and statistical errors (see table 3.11) and a covariance matrix fit that takes into account error correlations (see section 3.7).

Diagonal fit

To compute the parameter values and their uncertainties, the fit is performed taking into account the errors on the y axis and x axis with the simplified expression of χ^2 for statistically independent observations based on the diagonal elements $(\sigma_{y_i}^2 + (f_d \cdot \sigma_{x_i})^2)$ of the inverse covariance matrix:

$$\chi^2 = \sum_i \frac{(y_i - f(x))^2}{(\sigma_{y_i}^2 + (f_d \cdot \sigma_{x_i})^2)}, \tag{6.2}$$

where σ_{y_i} and σ_{x_i} are the measurement errors and the index i runs from 1 to 17, since there are 17 points in the CosmoALEPH decoherence curve. $f(x)$ is the function that determines the shape of the MC decoherence curve given by equation (6.1). The function f_d is represented by the first derivatives with respect to the distance of the determined NKG parameterizations:

$$f_d = par(1) \cdot \frac{\partial f_p}{\partial x} + par(2) \cdot \frac{\partial f_{He}}{\partial x} + par(3) \cdot \frac{\partial f_{Fe}}{\partial x}. \tag{6.3}$$

Covariance matrix fit

The most general expression of χ^2 is

$$\chi^2 = \sum_{i,j} (y_i - f_i(x)) \cdot C_{ij}^{-1} \cdot (y_j - f_j(x)), \tag{6.4}$$

where C_{ij}^{-1} is the inverse error matrix determined from the full covariance matrix C_{ij}.

The full covariance matrix of y observations (coincidence rates) is formed by the product of the total errors of the individual coincidence rates with the elements of the 16 × 16 correlation matrix ρ_{ij} given in section 3.7:

$$C_{ij} = \sigma_{y_i} \cdot \sigma_{y_j} \cdot \rho_{ij}. \tag{6.5}$$

The first point in the decoherence curve at the distance of 2.6 m is not included in the covarince matrix, since it represents an independent measurement of the coincidence rate between two halves of the TPC from the dedicated runs. For this point, the χ^2 was calculated only once according to equation (6.2) where also errors on the x axis are included (errors of the distance between detectors). For the fit that takes into account only errors on the y axis (errors of coincidence rates), the χ^2 was calculated according to the equation

$$\chi^2 = \sum_i \frac{(y_i - f(x))^2}{\sigma_{y_i}^2} \ .$$

To include the x errors into the covariance matrix, a term $(f_d \cdot \sigma_{x_i})^2$ is added to the diagonal elements of the covariance matrix. To start the fitting procedure, firstly a fit without x errors was performed, and the last computed values for f_d were saved only for the diagonal elements. Then, the values of $(f_d \cdot \sigma_{x_i})^2$ were added to the diagonal elements of the covariance matrix and after this, the obtained covariance matrix is inverted. The fit procedure is repeated for a few iterations taking into account the x and y errors, always saving the last 16 values of f_d and using them in the next iteration.

After testing the covariance matrix fit on the experimental data in different aspects, it was concluded that the fits are not satisfactory because the fitted curve is everywhere on one side of the data. An explanation is that the models are not fully consistent with the data, and, if the correlations are taken into account, it costs very little to move the fit to one side of the data. On the other hand, the correlations cannot be ignored, since, for example, an uncertainty in the efficiency or in the up-time of one of the scintillator stations affects all coincidences with this station [130].

To solve this problem, the penalty method [132] was implemented to minimize

$$\chi^2 + C \cdot p^2(y) \ ,$$

where p(y) represents the penalty function which can have different forms and C is the penalty coefficient.

The proposed penalty function which has been used in this analysis has the form [130]

$$p(y) = \sum_i \frac{(y_i - f_i(x))}{\sigma_{y_i}} \ .$$

The penalty coeficient has to be large enough to ensure a reliable solution. If the constraint is not satified, the penalty function becomes very large and tends toward infinity.

Thus, the minimization procedure was performed according to the equation

$$\sum_{i,j} (y_i - f_i(x)) \cdot C_{ij}^{-1} \cdot (y_j - f_j(x)) + 10^6 \cdot \left(\sum_i \frac{(y_i - f_i(x))}{\sigma_{y_i}} \right)^2 \ .$$

The fitting procedure was started with a small penalty coefficient and increased up to 10^6 to find the best minimum of the fitted MC curve.

In the fit with the penalty function the final value for χ^2 gets larger, even if the fitted MC curve is in a good agreement with the experimental data. A positive observation from the normal fit with the covariance matrix (equation 6.4) and from the fit with the penalty function is that the resulting contributions for the considered primary elements for both fits are very similar with small deviations that can be considered negligible.

Elemental contributions

From the fit, the contribution of each element **p**, **He**, and **Fe** is estimated as:

$$Element_i = E_i = \frac{par(i) \cdot 100\%}{\sum_i par(i)}, \tag{6.6}$$

where $Element_i$ represents the contribution in % for proton, helium and iron. The uncertainties of these contributions are calculated according to the standard error propagation procedure

$$\sigma_{E_i} = \sqrt{\sum_{j=1,3} \left(\frac{\partial E_i}{\partial par(j)} \cdot \sigma_{par(j)} \right)^2}, \tag{6.7}$$

where $\sigma_{par(j)}$ are the errors of the parameters $par(j)$ computed by the MINUIT fitting function. For correlated variables the formula for σ_{E_i} is

$$\sigma_{E_i} = \sqrt{\sum_{k,l} \frac{\partial E_i}{\partial par(k)} \cdot \frac{\partial E_j}{\partial par(l)} \cdot C_{kl}(par)}, \tag{6.8}$$

where $C_{kl}(par)$ represent the error matrix of parameters.

For the fit with covariance matrix and penalty function, the number of degrees of freedom is increased by one unit. In a constraint fit, the parameters cannot vary independently. If two parameters are given, then the third one is determined by the constraint as implemented in the penalty function [130], which reduces the number of free parameters by one.

The contribution and uncertainty of each element to the chemical composition of primary cosmic rays and their χ^2 per degree of freedom are summarized in table 6.1 for the diagonal fit and in table 6.2 for the covariance matrix fit with penalty function. Final results of the fit of the measured decoherence curve with shapes obtained from the MC for the decoherence distribution are presented in figures 6.1 and 6.2 for the diagonal fit and in figures 6.3 and 6.4 for the covariance matrix fit with penalty function.

It is to mention that in both fitting methods, the experimental points are in a good agreement with the MC fitted line, differences appear only in the values of χ^2. The contributions that were determined for the primary elements with both methods are very similar with only small differences.

From these plots it can be seen, that the shapes obtained for the decoherence curve for high energy cosmic muons simulated with different high energy hadronic interaction models and also two composition approaches, describe the experimental decoherence curve well, preferring a light composition of proton and helium.

Only in case of the VENUS model for the constant mass composition approach there is a more pronounced contribution for iron up to 20 % compared to other models, some of them giving only 2 % or even less iron.

Looking at the shapes for the decoherence distribution presented in figures 5.11, 5.12 and 5.13 from section 5.4, it is seen that in VENUS (CMC), proton primaries provide higher muon coincidence rates at small separations (behavior very similar also for the measured coicidence rates at small separations with CosmoALEPH) compared to helium and iron primaries. At large separations, there is a clear evidence that iron primaries contribute with a higher muon rate compared to proton and helium primaries, an effect which can explain the iron contribution with VENUS (CMC). For the other models, this effect is not observed, the tails of the decoherence shapes for all elements seem to be more or less parallel. From these figures, is also quite evident that the CosmoALEPH decoherence curve favors the shape obtained for helium in case of QGSJET (CMC), VENUS (MCM), SIBYLL (CMC) and NEXUS (MCM), since the coincidence rates at small separations for helium are somewhat higher. These observations are confirmed by the results obtained from the fit (see tables 6.1 and 6.2).

From the MC shapes on the experimental data, and also from the values of χ^2 per degree of freedom is clearly seen that the best fit is achieved for the VENUS model with the constant mass composition approach.

Shapes of the decoherence curve, obtained with NEXUS, describe the experimental data well, but in both cases of the diagonal fit and the covariance matrix fit, the model does not describe the point at small separations (at 2.6 m), since the simulated coincidence rates in this region are lower compared to the other models.

Results from the diagonal fit : QGSJET and VENUS

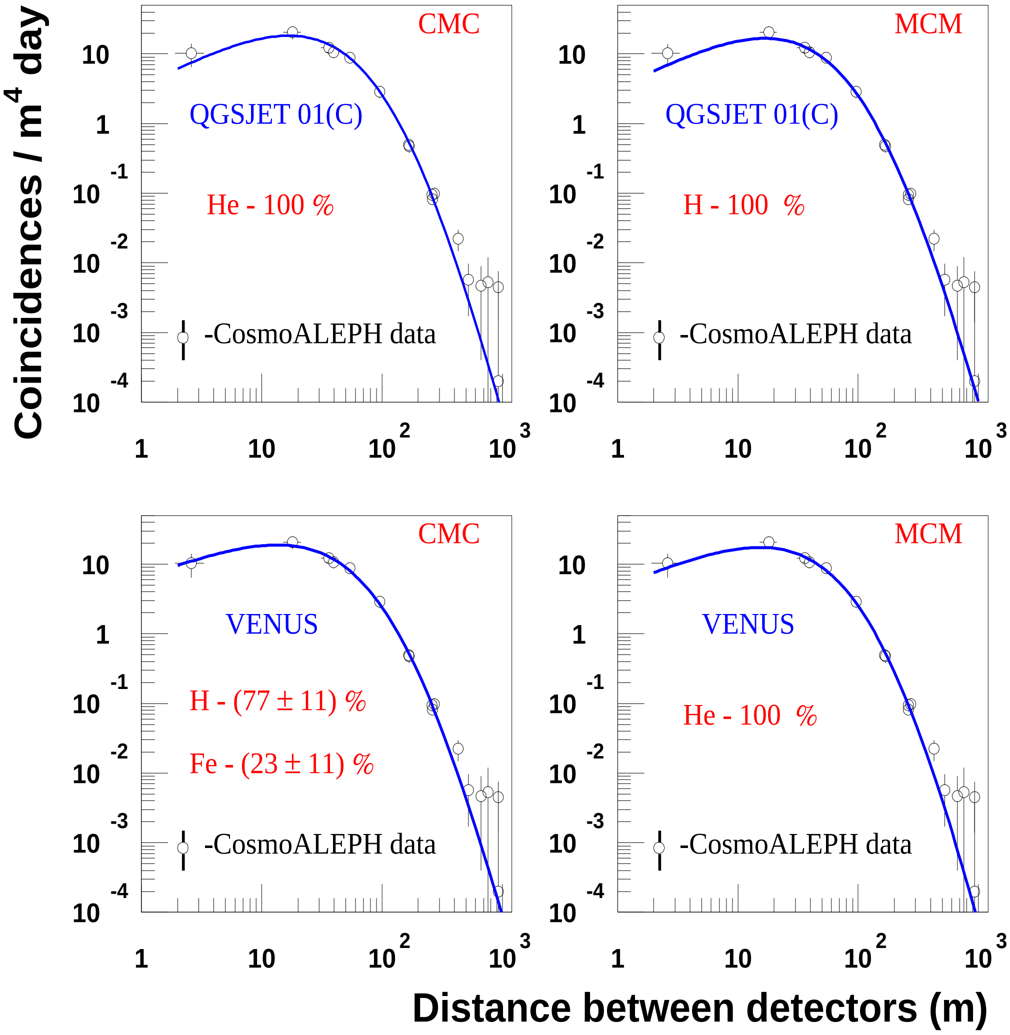

Figure 6.1: Comparison of the measured CosmoALEPH decoherence distribution underground with the shapes obtained for the decoherence distribution with QGSJET and VENUS in case of constant (CMC) and Maryland (MCM) composition approaches. The open circles are the measured coincidence rates per unit time and area at seventeen different distances between CosmoALEPH detectors, and the line is the fit of the experimental data with the sum of p, He and Fe NKG parameterizations obtained from extensive air showers simulations.

Results from the diagonal fit : SIBYLL and NEXUS

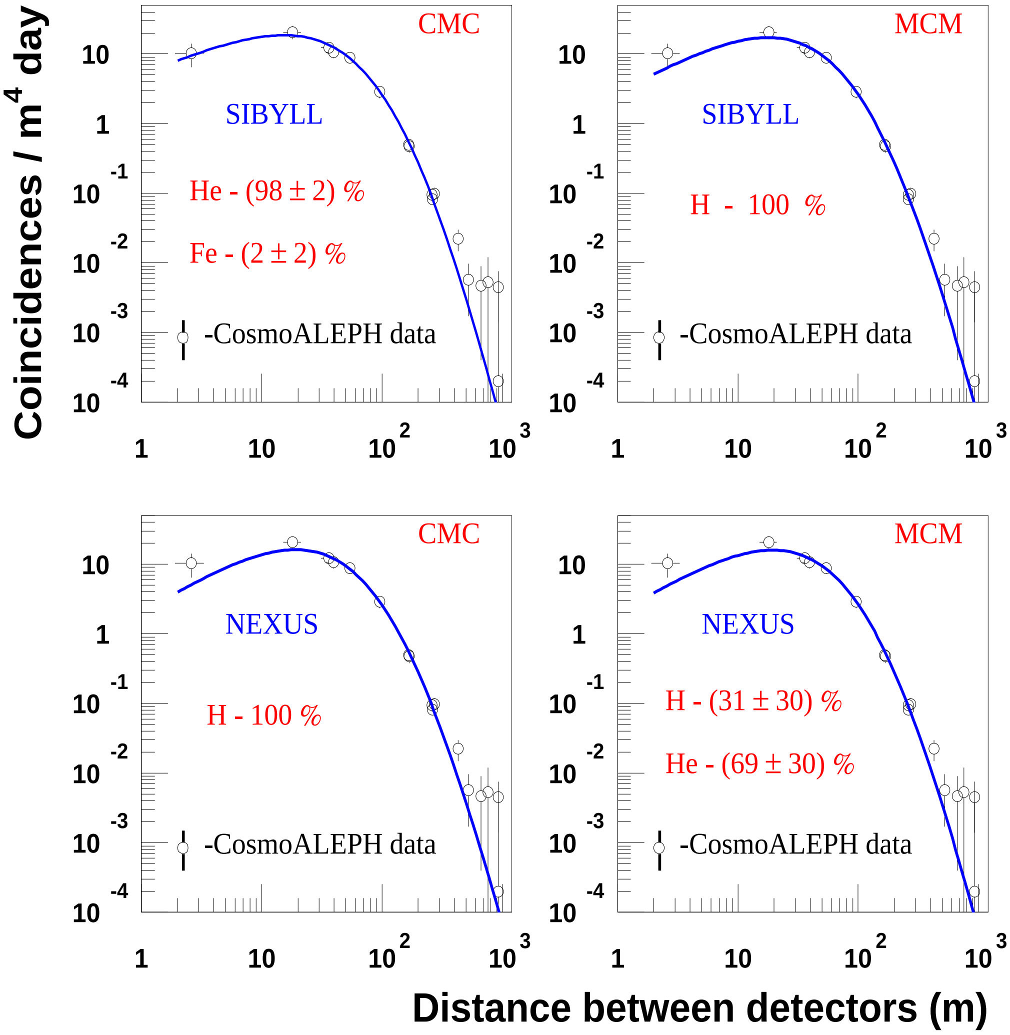

Figure 6.2: Comparison of the measured CosmoALEPH decoherence distribution underground with the shapes obtained for the decoherence distribution with SIBYLL and NEXUS in case of constant (CMC) and Maryland (MCM) composition approaches. The open circles are the measured coincidence rates per unit time and area at seventeen different distances between CosmoALEPH detectors, and the line is the fit of the experimental data with the sum of p, He and Fe NKG parameterizations obtained from extensive air showers simulations.

Covariance matrix fit with penalty function : QGSJET and VENUS

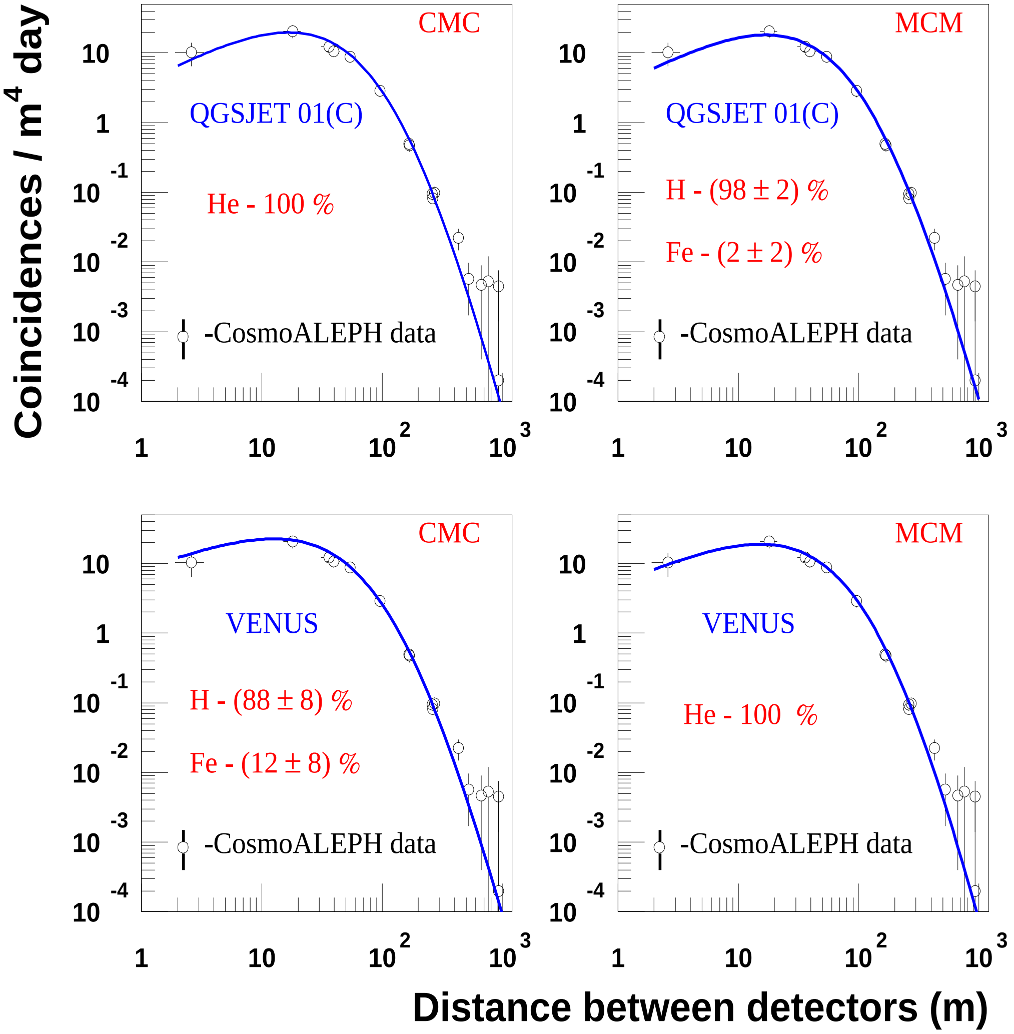

Figure 6.3: Comparison of the measured CosmoALEPH decoherence distribution underground with the shapes obtained for the decoherence distribution with QGSJET and VENUS in case of constant (CMC) and Maryland (MCM) composition approaches. The open circles are the measured coincidence rates per unit time and area at seventeen different distances between CosmoALEPH detectors, and the line is the fit of the experimental data with the sum of p, He and Fe NKG parameterizations obtained from extensive air showers simulations.

Covariance matrix fit with penalty function : SIBYLL and NEXUS

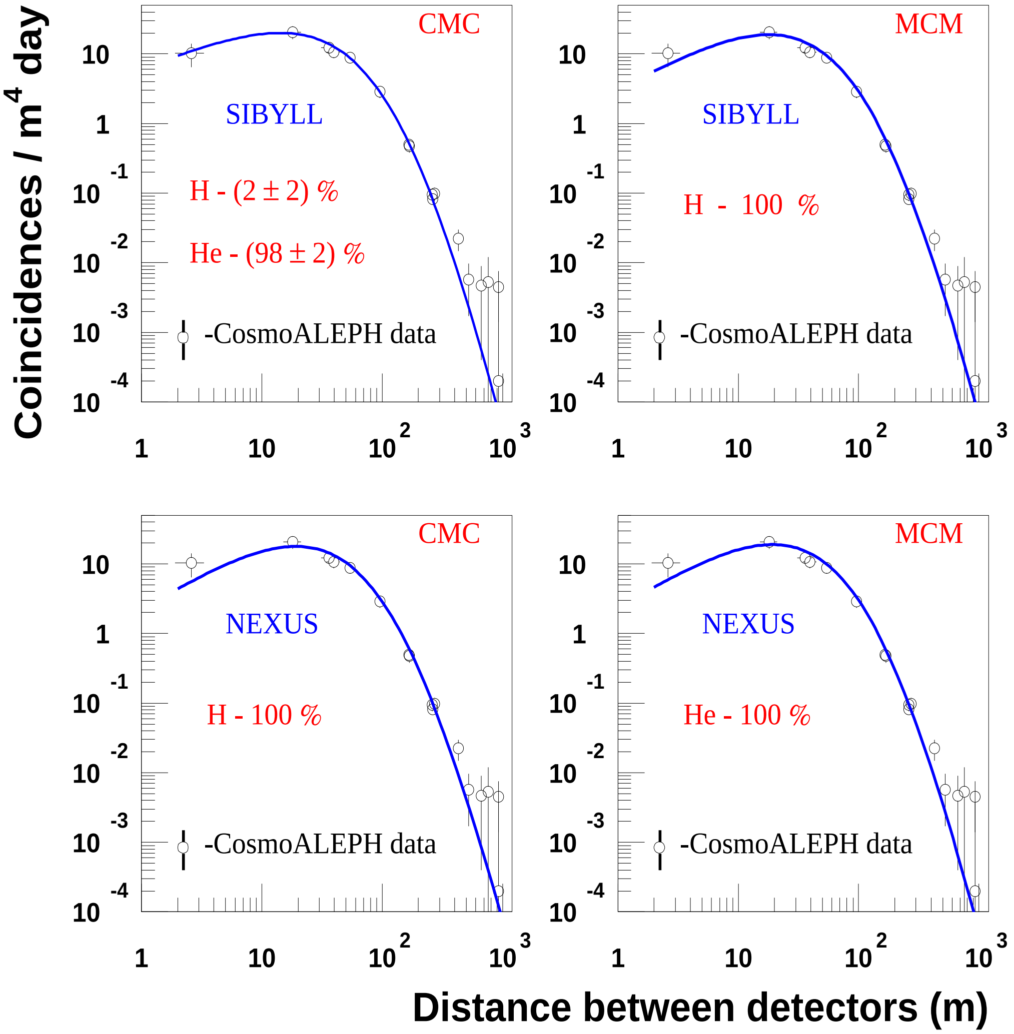

Figure 6.4: Comparison of the measured CosmoALEPH decoherence distribution underground with the shapes obtained for the decoherence distribution with SIBYLL and NEXUS in case of constant (CMC) and Maryland (MCM) composition approaches. The open circles are the measured coincidence rates per unit time and area at seventeen different distances between CosmoALEPH detectors, and the line is the fit of the experimental data with the sum of p, He and Fe NKG parameterizations obtained from extensive air showers simulations.

Results from the diagonal fit

Hadronic model	**CMC**	$\frac{\chi^2}{d.o.f}$ (prob. %)	**MCM**	$\frac{\chi^2}{d.o.f}$ (prob. %)
QGSJET	He - 100 %	$\frac{10.7}{14} = 0.8$ (71)	H - 100 %	$\frac{10.2}{14} = 0.7$ (75)
VENUS	H - (77 ± 11) % Fe - (23 ± 11) %	$\frac{8.9}{14} = 0.6$ (84)	He - 100 %	$\frac{10.}{14} = 0.7$ (76)
SIBYLL	He - (98 ± 2) % Fe - (2 ± 2) %	$\frac{11.5}{14} = 0.82$ (65)	H - 100 %	$\frac{11.8}{14} = 0.8$ (62)
NEXUS	H - 100 %	$\frac{12.4}{14} = 0.9$ (57)	H - (31 ± 30) % He - (69 ± 30) %	$\frac{14.}{14} = 1.0$ (45)

Table 6.1:

Results from the covariance matrix fit with penalty function

Hadronic model	**CMC**	$\frac{\chi^2}{d.o.f}$ (prob. %)	**MCM**	$\frac{\chi^2}{d.o.f}$ (prob. %)
QGSJET	He - 100 %	$\frac{17.5}{15} = 1.2$ (29)	H - (98 ± 2) % Fe - (2 ± 2) %	$\frac{20.5}{15} = 1.4$ (15)
VENUS	H - (88 ± 8) % Fe - (12 ± 8) %	$\frac{13.9}{15} = 0.93$ (53)	He - 100 %	$\frac{19.12}{15} = 1.3$ (21)
SIBYLL	H - (2 ± 2) % He - (98 ± 2) %	$\frac{16.9}{15} = 1.1$ (32)	H - 100 %	$\frac{20.3}{15} = 1.4$ (16)
NEXUS	H - 100 %	$\frac{23.4}{15} = 1.6$ (8)	He - 100 %	$\frac{24.6}{14} = 1.7$ (6)

Table 6.2: Chemical composition of primary cosmic rays (presented in percentage) obtained from a comparison of CosmoALEPH data with data simulated with QGSJET, VENUS, SIBYLL and NEXUS for constant (CMC) and Maryland (MCM) composition approaches. The χ^2 per degree of freedom and the probability of χ^2 are presented for clarity.

The results obtained for the chemical composition of primary cosmic rays from the CosmoALEPH muon decoherence distribution, measured underground at a depth of 320 *mwe* are in agreement with the results obtained by other experiments for the mass composition up to the *knee* region.

Based on the χ^2 values, the CosmoALEPH experiment determined a composition of 77±11 % protons and 23±11 % iron nuclei with a χ^2 - probability of 84 % for VENUS with CMC. If correlations between the measured parameters are taken into account, the CosmoALEPH experiment determines a composition of 88 ± 8 % protons and 12 ± 8 % iron nuclei with a χ^2 - probability of 53 %. Thus, the analysis of the decoherence curve, with the consideration of the presence of correlations, allows to determine the chemical composition of primary cosmic rays with a reduced probability.

The measurements performed with the Homestake Liquid Scintillation Hodoscope [11] in the 10^{14} - 10^{16} *eV* energy range determined a composition of 83 ± 13 % protons and 17 % iron with 67.4 % χ^2 probability.

Experiments like DICE/CASA/MIA, KASKADE, EAS-TOP, and MACRO (see the section 1.3) report a preference of a light composition up to the *knee*, balancing between the predominance of proton or helium, which is observed also from CosmoALEPH experimental data.

From these results it can be concluded that there is a strong model dependence in the analysis of the chemical composition of primary cosmic rays.

6.2 CosmoALEPH and MC Multiplicity and Transverse Momentum Distributions

The multiplicity and transverse momentum distributions of cosmic muons, measured with the Time Projection Chamber (TPC) of the ALEPH detector at a depth of 320 *mwe*, are presented in an absolute comparison with the distributions predicted by the QGSJET, VENUS, SIBYLL and NEXUS models for proton, helium and iron simulated air showers for the constant mass composition approach.

Results of the comparison are presented in figures 6.5 and 6.6.

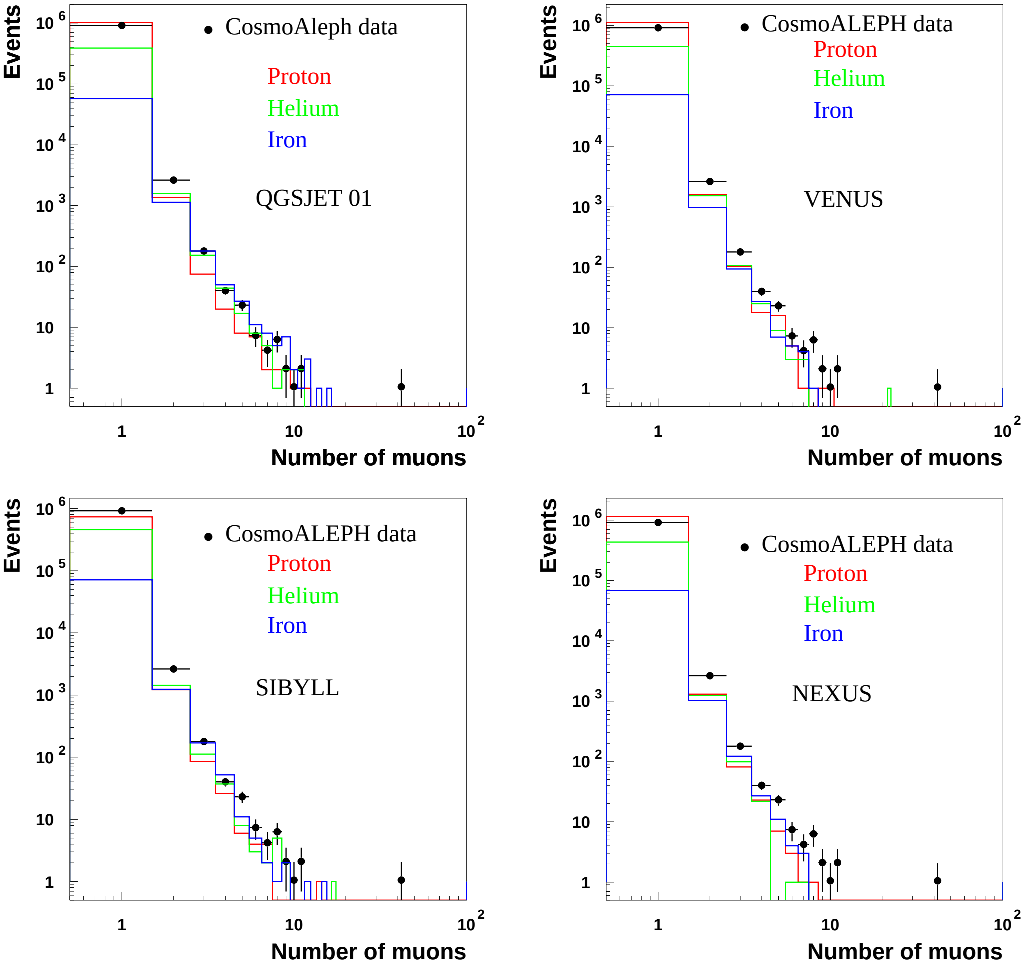

Figure 6.5: The comparison of muon multiplicity distributions for p (red), He (green) and Fe (blue) primaries simulated with QGSJET VENUS, SIBYLL and NEXUS with the multiplicity distribution of muons measured in the ALEPH TPC (black). Experimental data are presented with statistical errors.

From these distributions is clearly seen that the experimental data are in a good agreement with the simulated single muon events, while at higher multiplicities the experimental data dominate. An event with a high multiplicity of about forty is observed in experimental data compared to MC data. These results show that the MC models are not able to reproduce events with high multiplicities, with the message that high energy particle interactions occur in the atmosphere that are not well understood and implemented in MC models.

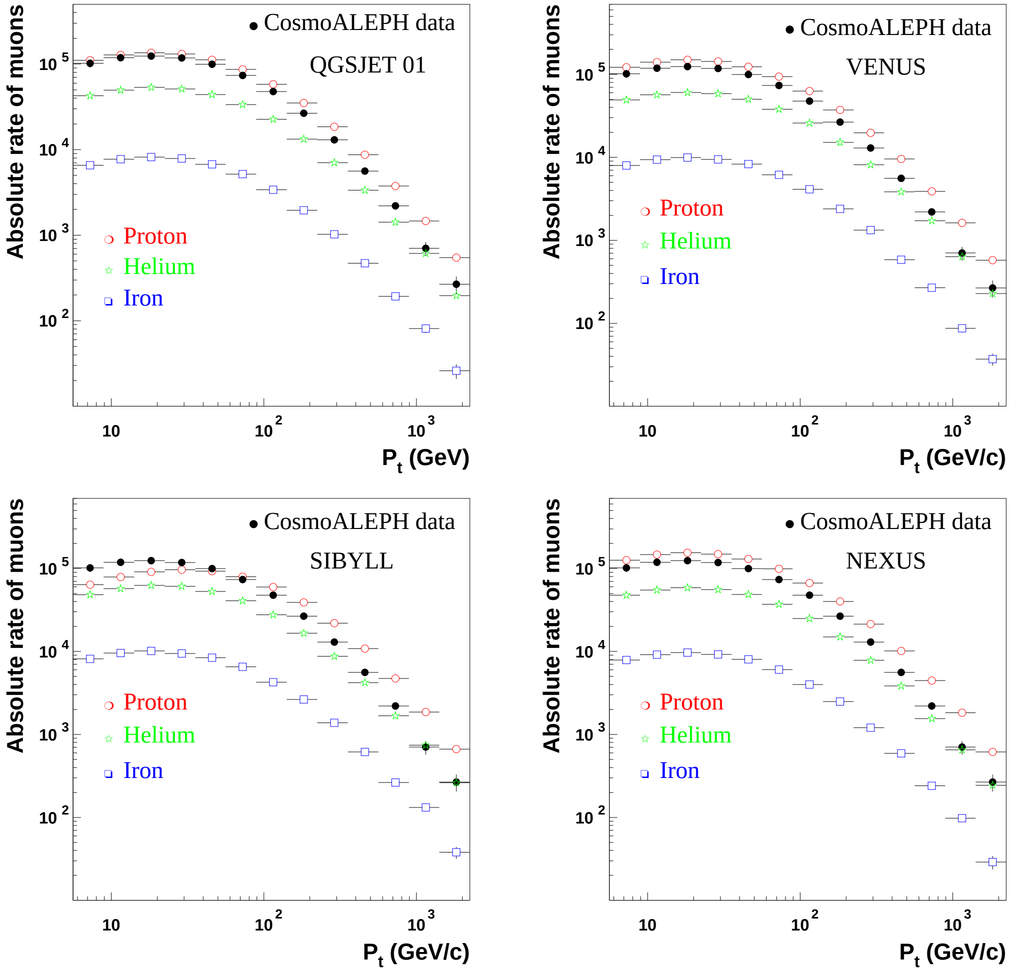

Figure 6.6: The comparison of muon transverse momentum distributions for p (red), He (green) and Fe (blue) primaries simulated with QGSJET, VENUS, SIBYLL and NEXUS with the transverse momentum distribution of muons measured in the ALEPH TPC (black). Lines along the x axis represent the bin width.

As we learned from experimental and MC data, more than 99 % of all primary showers represent single muon events. Following only the result of single muon events in the multiplicity distribution, it can be seen that the

CosmoALEPH data lie between proton and helium primaries. The same observations are valid for the CosmoALEPH transverse momentum distribution, that lies between proton and helium primaries in the considered range of momenta.

The only model that seems to describe the experimental data not too well is SIBYLL, which shows a reduced number of muon events at low momenta, as well as less single muon proton primaries.

Thus, from the absolute comparison of the multiplicity and transverse momentum distributions with MC predictions, it can be concluded that the experimental data prefer a light compostion. A detailed analysis of the chemical composition from the transverse momentum distribution would be possible after an unfolding of the measured transverse momentum distribution, also a detailed propagation of CORSIKA muons through the ALEPH detector.

CONCLUSIONS

In this work the muon component of extensive air showers at a rock depth of about 320 meter water equivalent, which corresponds to a threshold energy of 75 GeV for vertical incidence, was studied.

The CosmoALEPH experiment, located underground at the LEP e^+e^- storage ring at CERN at a depth of about 125 *m*, was used to study the chemical composition of primary cosmic rays up to 10 PeV energies from the measurements of high energy cosmic muons, created in extensive air showers by interactions of primary nuclei in the atmosphere.

The Hadron Calorimeter of the ALEPH detector and six scintillator stations provided information about muon coincidences for distances up to about 1 *km*, being the largest distance between a pair of CosmoALEPH stations. Time Projection Chamber (TPC) of the ALEPH detector with its very good momentum, spatial and angular resolutions was used to analyse multiplicity and transverse momentum distributions of single and multiple muon events up to about 3 TeV energies.

The results of the experimental data were compared with predictions from different Monte Carlo models.

For the simulation of extensive air showers the CORSIKA program was used with QGSJET, VENUS, SIBYLL and NEXUS high energy hadronic interaction models and two composition approaches; the light composition with constant spectral index $\alpha = 2.7$ and Maryland composition as heavy composition model.

The results of the simulations were summarised in parameterizations for the muon decoherence curves for proton, helium and iron primaries. Multiplicity and transverse momentum distributions of single and multiple muon events at the CosmoALEPH depth were analysed for a generated statistics which corresponds to the effective uptime of the TPC during dedicated CosmoALEPH runs.

From the comparison between the measured decoherence distribution with CosmoALEPH and the predicted decoherence curves for proton, helium and iron by the considered Monte Carlo models and composition approaches, a primary composition of (77 ± 11) % protons and (23 ± 11) % iron nuclei for cosmic rays with a χ^2 - probability of about 84 %, based on the predictions of the VENUS model and constant mass composition approach, was determined. The analysis of the decoherence curve, with the consideration of correlations between the measured CosmoALEPH parameters, leads to a composition of (88 ± 8) % protons and (12 ± 8) % iron nuclei for cosmic rays with a χ^2 - probability of 53 %. Thus, taking into account the correlations, the chemical composition from CosmoALEPH measurements can be predicted with a reduced probability.

Other MC models describe the CosmoALEPH decoherence curve with a lower χ^2 - probability, preferring a light mass composition, balancing between proton and helium primaries. The results on the chemical composition of primary cosmic rays from the lateral distributions at ground level as well as underground are very sensitive to the interaction model used.

The absolute comparison between the measured multiplicity and transverse momentum distributions in the TPC and those predicted by different Monte Carlo models results also in a dominant light composition. The experimental data are in a good agreement with MC data lying between proton and helium primaries.

The obtained results for the primary composition of cosmic rays up to the *knee* region are consistent with the results from other experiments.

Some discrepancies were observed for the SIBYLL model, which generates less single muon events and a lower number of muons at low transverse momenta for proton initiated showers compared to other models.

A comparison of the measured muon multiplicity in the TPC with muon multiplicities predicted by different MC models shows that MC models are unable to reproduce events with high multiplicities, with the message that high energy particle interactions occur in the atmosphere that are not well understood and implemented in the MC models.

An important message from our measurements is that we need a better and consistent understanding of the interactions of high energy particles in the atmosphere.

A more detailed study of the chemical composition of primary cosmic rays from the CosmoALEPH data can be performed after unfolding of the measured transverse momentum distribution and a proper propagation of muons simulated with CORSIKA through the ALEPH detector, which will provide the possibility to analyse CORSIKA data in identical conditions as experimental data.

Appendix A

Study of Correlations between Muon Lateral and Multiplicity Distributions

The main purpose for the Monte Carlo (MC) simulations was to produce muon separation distributions for various primary elements simulated with various MC models and to compare these to the experimentally measured separation distribution for multiple muon events detected underground by the CosmoALEPH detectors. One of the fundamental problems that appeared was the fact that with increasing energy, the flux of primary cosmic particles decreases according to a power law (see equation (1.1)). Thus, to have satisfactory statistics for muon coincidences at large separations up to 1 km, a huge amount of primaries must be simulated, which is not realistic for the available computer power and with the available Monte Carlo programs.

The initial idea was to prepare a fast MC simulation program with the implemented geometry of the CosmoALEPH detectors, based on parameterizations for the mean muon multiplicity and muon lateral distributions, which will sample from these distributions in a short time a large statistics with a fast random function. The mean muon multiplicity and muon lateral distributions were obtained from CORSIKA simulations of p, He, O and Fe primary nuclei at the surface [119], but only for those muons with an energy greater than the energy cutoff. The multiplicity of muons could be successfully reproduced, but for the muon lateral distribution a very complicated formula (depending on mass, primary energy, zenith angle, detector depth) was obtained, making hard to reproduce its shape and additionally it slowed down the fast MC program significantly.

Because of this, the question arose: why not use a fast random function generator like HRNDM [121] to sample air shower events from CORSIKA distributions by many orders of magnitude more and faster ? Then, to combine the information in order to determine the muon separation distribution up to 1 km for various primaries, also for different MC high energy hadronic models available in CORSIKA.

To proceed with this, firstly questions like: Does a correlation between muon multiplicity and muon lateral distriution and between other parameters exist? Reproduces the chosen HRNDM function, which generates random numbers from the histograms, correctly the CORSIKA results? should be answered.

To answer this questions, proton air showers were simulated at various primary energies and zenith angles $\theta = 0^0, 30^0, 50^0$ (see the table 1) according to the power law (1.1) with the same spectral index $\alpha = -2.7$, with CORSIKA (curved version, U.S. standard atmosphere, GHEISHA as low energy model) using the high energy hadronic interaction models VENUS and DPMJET.

E_p (TeV)	1	10	50	10^3
# showers	10^6	10^6	10^5	10^3

Table 1: Number of proton air showers simulated at zenith angles $\theta = 0^0, 30^0, 50^0$ with VENUS and DPMJET.

For this analysis, showers that reach the surface level with at least two muons were selected and in each shower the distances between all possible pairs of two muons (for all showers) at the surface were computed. For proton showers simulated with VENUS, the mean distance between muons as function of multiplicity in each shower was plotted and presented in figure 1.

From figure 1 it can be seen that the mean distance between muons increases with the multiplicity of muons in a shower. Events with large multiplicity occur at large distances. C.Forti, Th.K.Gaisser and T.Stanev [106] explained that events starting unusually high in the atmosphere will tend to produce more muons because the parent mesons decay easily in the more rare part of the atmosphere. Muons from such events at the surface level are spread out at large distances from the shower axis. This correlation is expected to be less significant for heavy primaries because of the smaller fluctuations in showers initiated by heavy nuclei.

For high energies this effect is not so pronounced, because the higher the primary energy the smaller are the fluctuations of muon lateral distributions (see figure 2) and most energetic muons are concentrated in a small area near the shower axis.

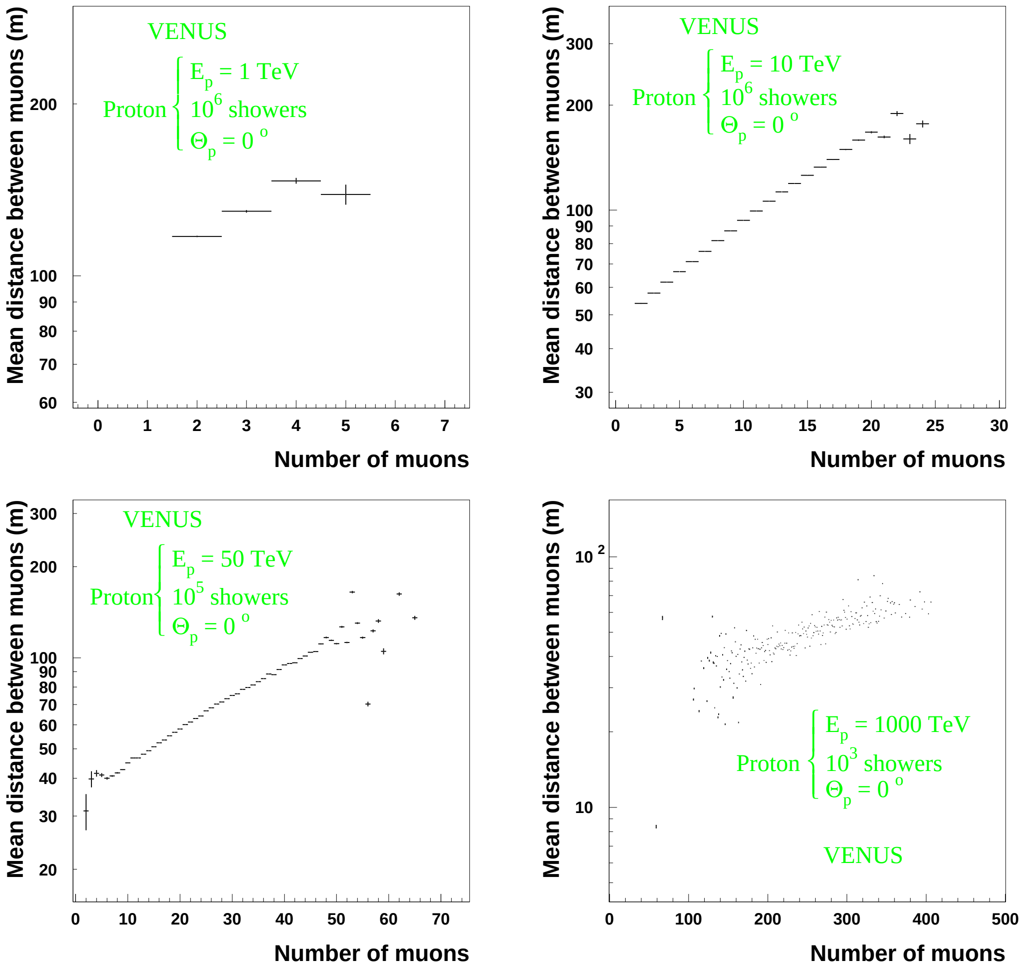

Figure 1: Analysis of the correlation between muon multiplicity and lateral distributions for vertical proton showers simulated with VENUS at 1 TeV, 10 TeV, 50 TeV and 1000 TeV.

Thus, trying to sample one of these parameters (multiplicity or lateral distribution) without taking into account this correlation, means loosing important aspects of physics.

A more detailed study of the correlations between various parameters, also the effect of the random generator HRNDM, was performed with two methods.

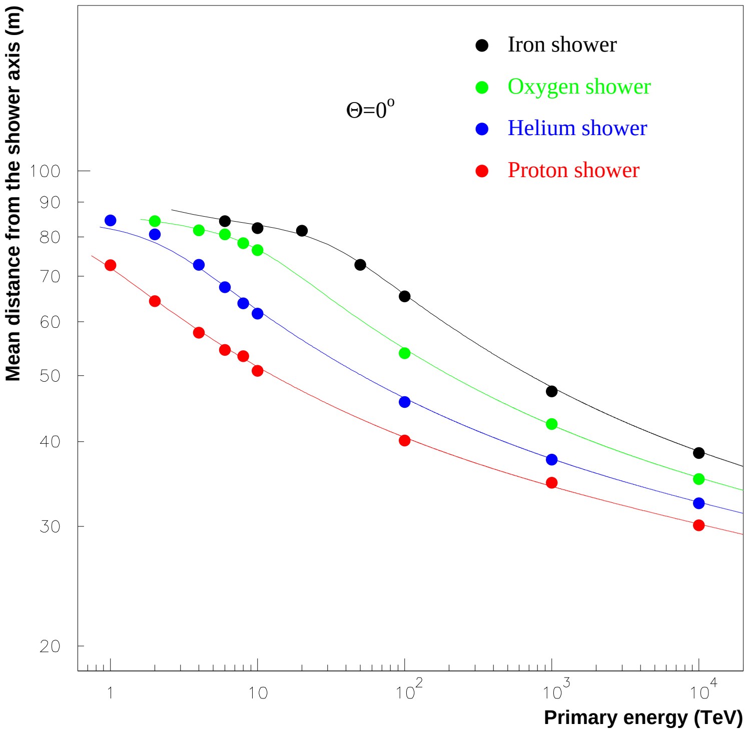

Figure 2: The mean perpendicular distance of muons from the shower axis for p, He, O and Fe simulated air showers with CORSIKA (QGSJET model) at different primary energies for a primary zenith angle $\theta = 0^0$. The points are mean values of the lateral distributions for different primary energies [119].

In both methods, the multiplicity and the radial distance from the shower axis

$$R = \sqrt{x^2 + y^2}$$

with x and y being the coordinates of the muons at the surface, and the azimutal distribution of the generated muons with CORSIKA at the surface were analysed.

Due to the interest in the muon separation distribution, the CORSIKA information (multiplicity, radial distance R from the shower axis, and azimutal angle φ of muons) is sampled with the HRNDM function at a high statistics and used to calculate all possible distances between muons in one randomly generated shower and this is summed for all showers. These results are compared with the distribution of distances between muons in one shower (summed over all showers) initially simulated with CORSIKA to see if HRNDM reproduces the CORSIKA results.

The muon separation distribution is analysed for two cases: a) - information of the muon lateral distribution and muon azimuthal angle distribution taken from all types of showers (single and multiple muon events), and b) - from events with only one muon (single muon events). For the last case, the multiplicity is generated according to the CORSIKA muon multiplicity, but the information for the muons in one generated event is randomly taken from the muon lateral distribution and muon azimuthal angle distribution for single muon events.

First method

According to the muon multiplicity obtained with CORSIKA, new events are generated using the HRNDM1 function.

- 1a: According to the CORSIKA muon lateral distribution, new radial distances of muons from the shower axis using HRNDM1 function are generated
- 2a: According to the CORSIKA muon azimuthal angle distribution, new muon azimuthal angles are generated and the x and y coordinates of new muons with the new radial distances R and new muon azimuthal angles φ were determined as

$$x\ [m] = R \cdot cos\varphi\ , \qquad y\ [m] = R \cdot sin\varphi\ .$$

Simulated distributions with CORSIKA and generated distributions with the HRNDM1 function from the CORSIKA distributions are compared in figure 3.

The azimuthal angle distribution is not uniformly distributed because the simulations were done at fixed energies in the presence of the Earth's magnetic field. Alternatively, when the simulations are done in an interval of primary energies in the presence of the magnetic field, the azimuthal distribution of muons becomes uniformly distributed (see figure 5.4 in section 5.3).

Parallel to this, the lateral distribution and zenith angle distribution are generated from the CORSIKA zenith angle and lateral distributions of muons originating from single muon events:

- 1b: according to the single muon lateral distribution (one muon events), new radial distances of muons from the shower axis using HRNDM1 function are generated

- 2b: according to the single muon azimuthal angle distribution (one muon events), new muon azimuthal angles are generated and the x and y coordinates of new muons with the new radial distances and zenith angles were determined.

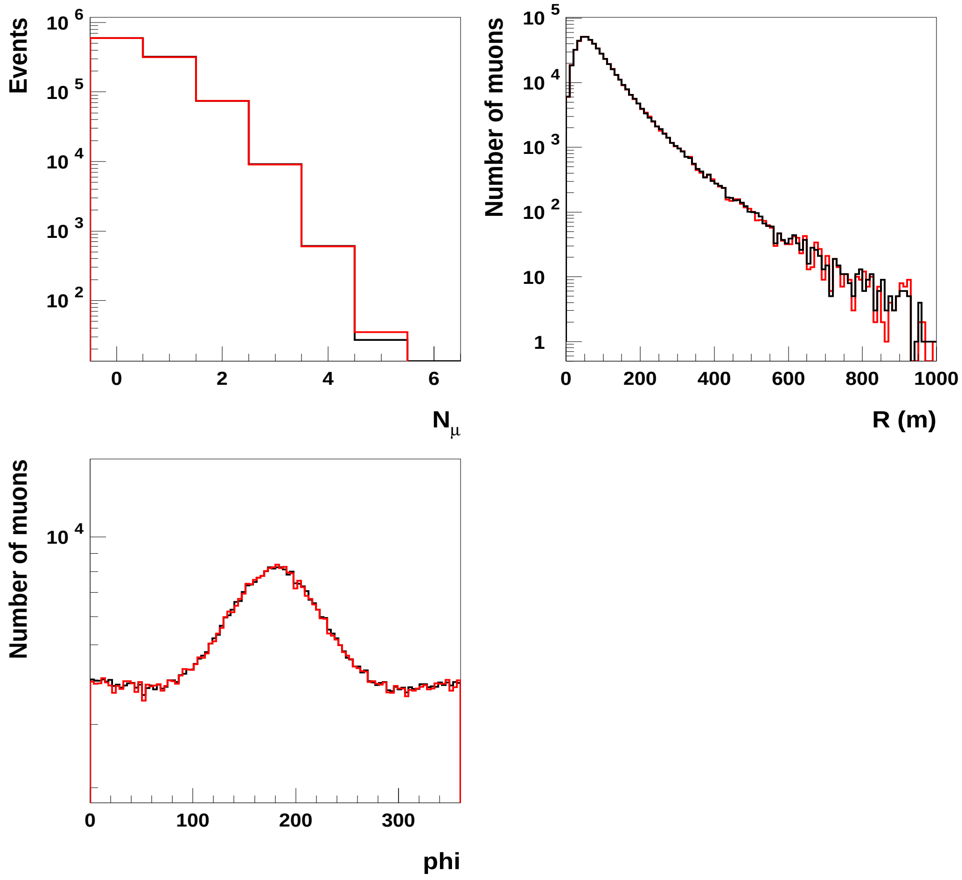

Figure 3: Multiplicity, lateral and azimuthal angle distributions (N_μ, R, and phi) at the surface simulated with DPMJET (black distribution) and generated with the function HRNDM1 (red distribution)

Finally, for events generated with at least two muons, the distances between two generated muons (all posible combinations in one shower, and this for all generated showers with HRNDM1) were computed in both cases a) and b), and compared to the distances between all possible pairs of muons in a shower simulated with CORSIKA (for all simulated showers).

Zenith angle $\theta = 0^0$

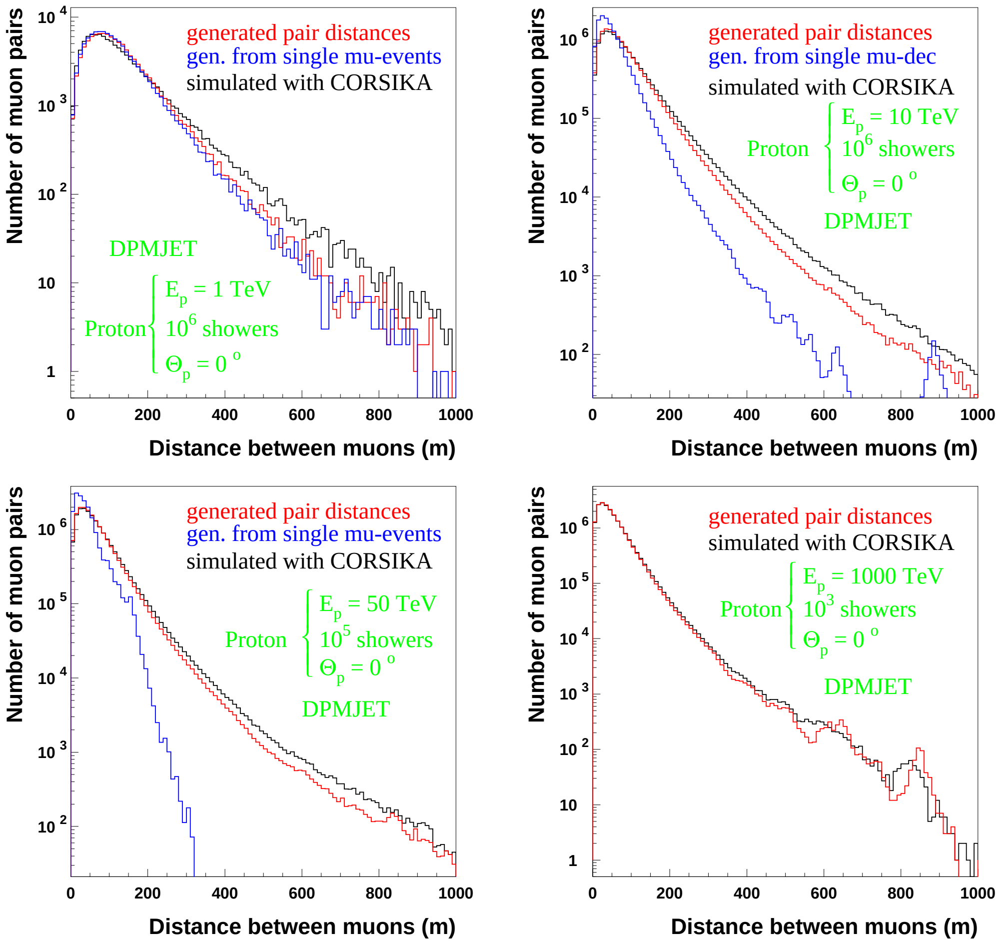

Figure 4: Distance between muons in the same shower for all showers simulated with CORSIKA (DPMJET) at $\theta = 0^0$ (black distribution), generated with the HRNDM1 function from all showers (red distribution), and generated with the HRNDM1 function from single muon showers (blue distribution).

Results of this comparison are presented in figures 4, 5, 6 and 7 for different energies and zenith angles for the case of the DPMJET and VENUS (see figure 7) models.

Zenith angle $\theta = 30^0$

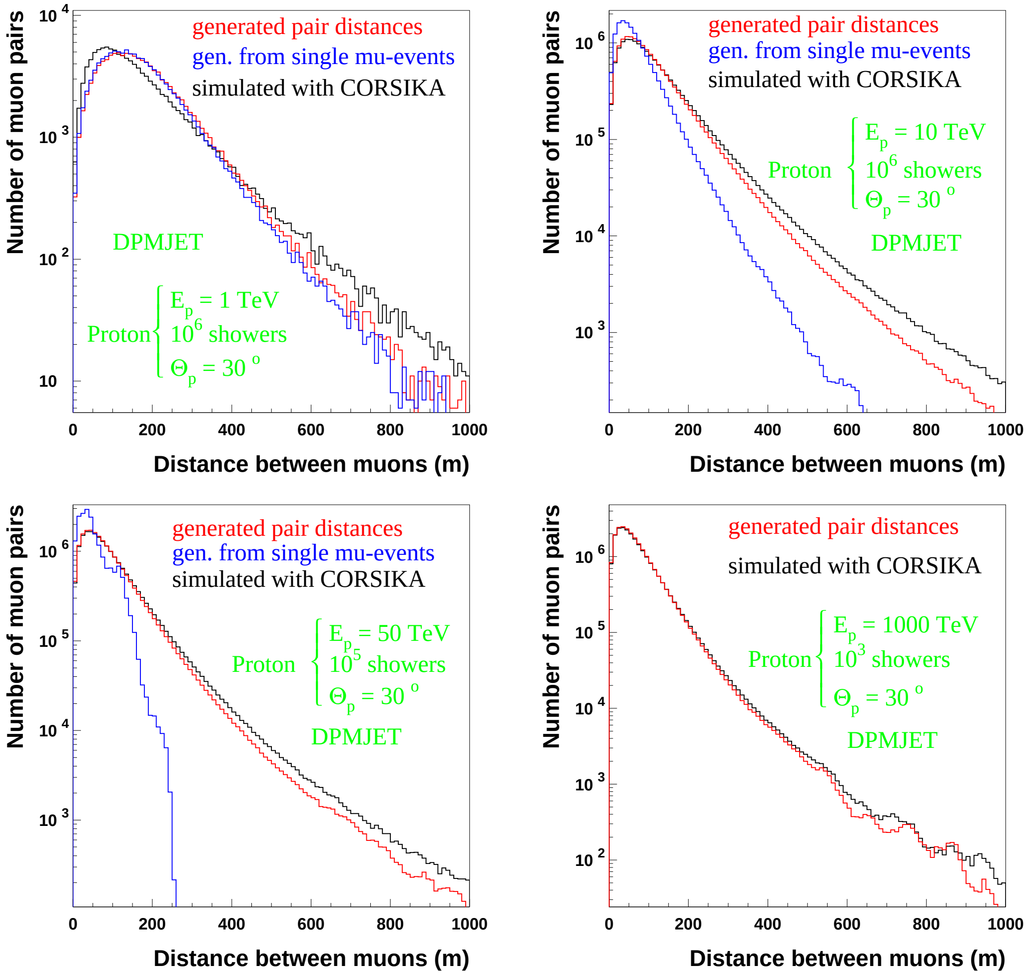

Figure 5: Distance between muons in the same shower for all showers simulated with CORSIKA (DPMJET) at $\theta = 30^0$ (black distribution), generated with the HRNDM1 function from all showers (red distribution), and generated with the HRNDM1 function single muon showers(blue distribution).

From figure 3 it is clearly seen that distributions generated with the HRNDM1 function from the CORSIKA histograms are in a good agreement with the CORSIKA distributions. Nevertheless, when combining the information of generated distributions with the HRNDM1 function to compute the distances between muons, discrepances between the generated and simulated ones are obtained (see figure 4).

Zenith angle $\theta = 50^0$

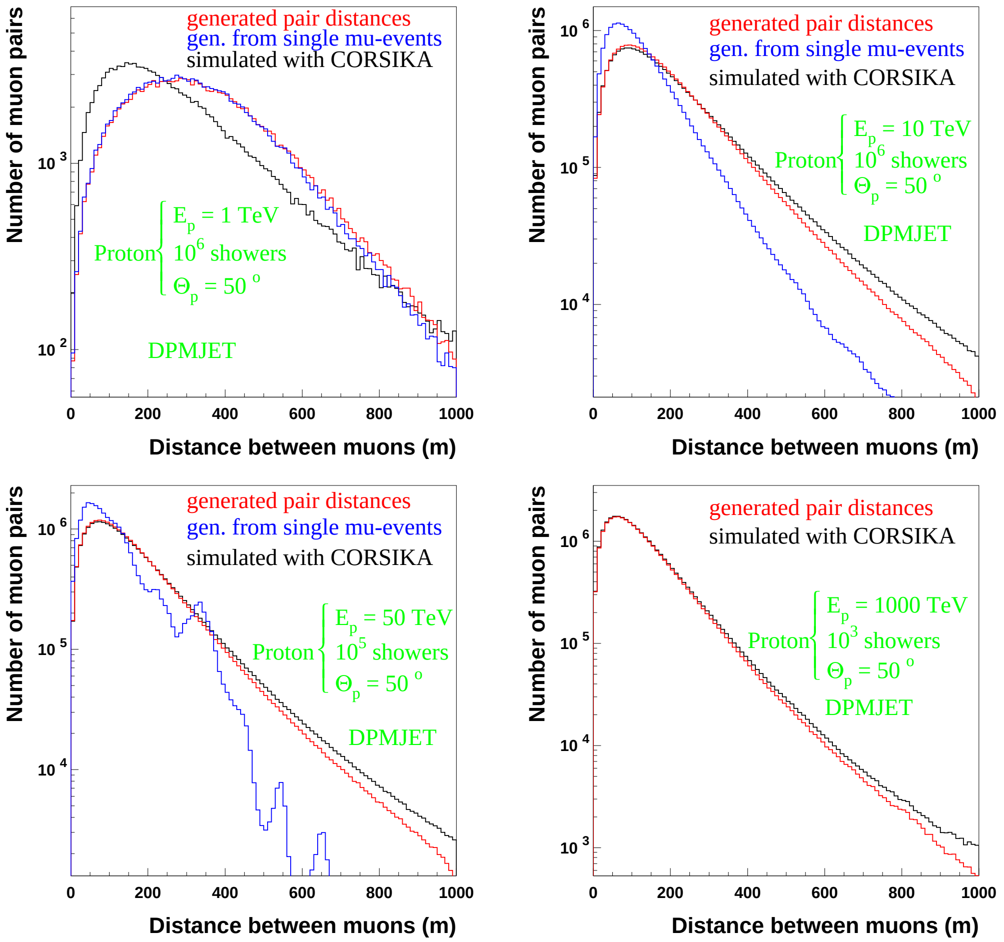

Figure 6: Distance between muons in the same shower for all showers simulated with CORSIKA (DPMJET) at $\theta = 50^0$ (black distribution), generated with the HRNDM1 function from all showers (red distribution), and generated with the HRNDM1 function from single muon showers(blue distribution).

This is also true for different primary energies, zenith angles, and also for different MC models, which is well ilustrated in figures 4, 5, 6, and 7.

VENUS model, Zenith angle $\theta = 0^0$

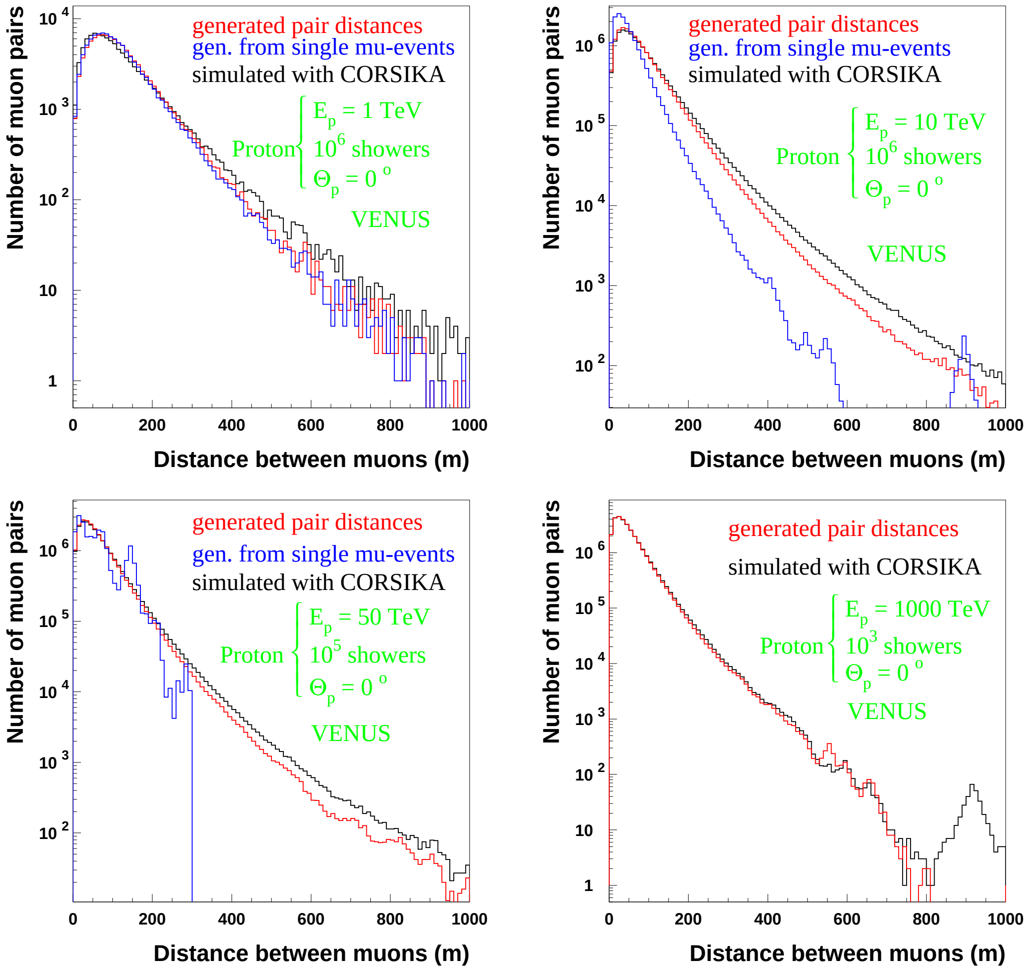

Figure 7: Distance between muons in the same shower for all showers simulated with CORSIKA (VENUS) at $\theta = 0^0$ (black distribution), generated with the HRNDM1 function from all showers (red distribution), and generated with the HRNDM1 function from single muon showers(blue distribution).

This means that the CORSIKA histograms for all these parameters (multiplicity, radial distance from the shower axis, azimuthal angle, and others) can in principle be sampled very successful. But looking at the final result where these parameters are combined, it can be stated that reading them randomly breaks their physical connection. The reason being that all parameters which describe the development of an extensive air shower are strongly correlated.

With increasing energy, the red shape approaches the black one, while the tail remains unsatisfactory. The blue histogram describes the black shape (CORSIKA muon separation distribution) well at low energies, since predominatly single muon events are generated at these energies. With increasing energy, the statistics for single muon events gets poorer and the blue shape describes the black shape worse.

At 1000 TeV there is no blue distribution for the muon separation, because at such energies very few events with one muon are generated and it is not possible to construct in this case a distribution with a well defined shape.

It has been demonstrated that there are correlations in showers with multiple muons. That is why is difficult to reproduce the CORSIKA results with a random function in a fast way.

The analysis of the separation distribution for muons that originate from single muon events (blue distribution) is based on the assumption that between these muons the correlation is totally absent.

It was expected that using the information of these muons, it would be possible to reproduce the CORSIKA muon separation distribution with a random function in a fast way. But looking at the blue distribution it is obvious that also this method is not able to reproduce the CORSIKA results, even worse, it carries very poor information about the development of a shower, being not able to describe the distance between muons at large separations which is clearly observed with increasing the primary energy. This can be explained by the fact that muons from high energy primaries are mostly concentrated near the shower axis, while secondaries originating from low energy primaries are more spread out.

Because the correlation between these parameters is already broken at the level of combining the information of azimuthal angles and radial distances from the shower axis for calculating the coordinates of muons, it was tried to extract randomly the muon coordinates directly from the two dimentional CORSIKA histogram for x and y.

For the multiplicity number randomly selected by the HRNDM1 function from the CORSIKA multiplicity distribution, a x coordinate with its corresponding y coordinate is randomly selected from the CORSIKA x and y distribution with the HRNDM2 function for each muon of the selected multiplicty. The sampling of the x coordinate was performed from a 100 bins

2D histogram and a 1000 bins 2D histogram. With the information of the x and y coordinates for muons, the distance between all possible muon pairs in this event was calculated. The obtained muon separation distribution for all events (red distribution) is compared with the CORSIKA muon separation distribution (black distribution). The result of the comparison is presented in figure 8. An improvement is seen for the red distribution obtained for the 1000 bins xy histogram compared to the one obtained for the 100 bins xy histogram (the left plot), but still the agreement is not fully satifactory. If the muon separation distribution computed from the x and y coordinates directly sampled with the HRNDM2 function from CORSIKA histograms is compared to the muon separation distribution computed from the x and y coordinates that were indirectly obtained from the generated muon lateral and azimuthal distribution, it can be concluded that no clear improvement is achieved.

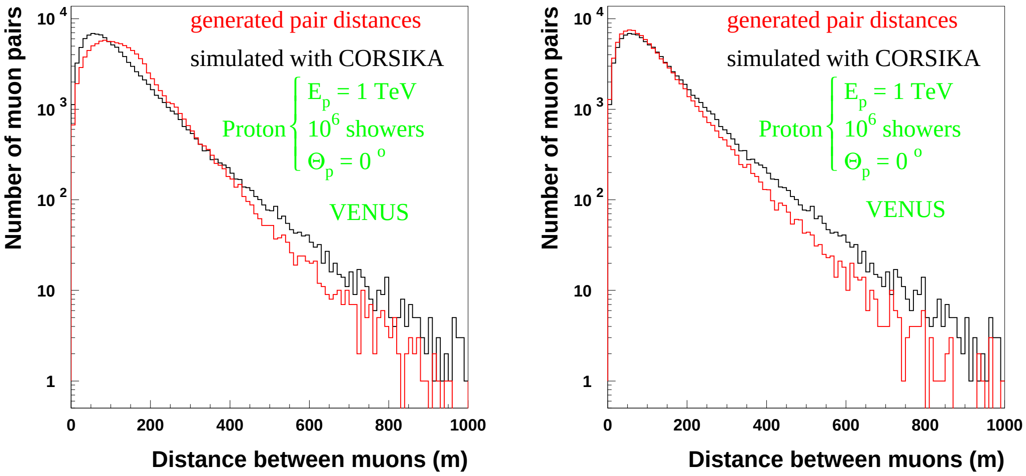

Figure 8: Distances between muons in showers (black distribution) simulated with CORSIKA and between randomly generated muons with x and y coordinates generated according to the 2D xy histogram of 100 bins (the left plot) and 1000 bins (the right plot) with the HRNDM2 function (red distribution)

Second method

Like in the first method, two cases are analysed in parallel.

- 1: From each shower only the first muon is selected and its x and y coordinates are saved in a large array
- 2: From each shower randomly only one muon is selected and its x and y coordinates are saved in a large array
- According to the muon multiplicity distribution obtained with CORSIKA at the surface, new events using the HRNDM1 function are generated and for each new generated event, muons with their x and y coordinates from the prepared large arrays were randomly selected
- The distance between two muons (all posible combinations) were computed for one generated shower and this was performed for all generated showers, and compared to the distance between muons in one shower, for all showers simulated with CORSIKA.

The analysis for the above mentioned two cases is performed separately and results of both cases are compared to initial CORSIKA results.

In figure 9, the distributions of the distances between muons for events simulated with CORSIKA and generated with the function HRNDM1 from CORSIKA are illustrated for vertical proton showers simulated with DPMJET at different energies.

From these plots it can be seen that with increasing energy the distance between muons decreases for the cases of generated events with the HRNDM1 function with muons randomly taken from the array formed by randomly selecting only one muon from each CORSIKA shower and from the array formed by selecting the first muon from each CORSIKA shower.

To understand this behaviour, $2D$ distributions of the x and y coordinates are plotted for muons

- from events simulated with CORSIKA
- from events generated with the function HRNDM1, where the muons are taken from the array formed according to case 1
- from events generated with the function HRNDM1, where the muons are taken from the array formed according to case 2.

The x and y coordinates of muons are presented for vertical proton primary showers simulated at 1 TeV (see figure 10) and at 1000 TeV (see figure 11).

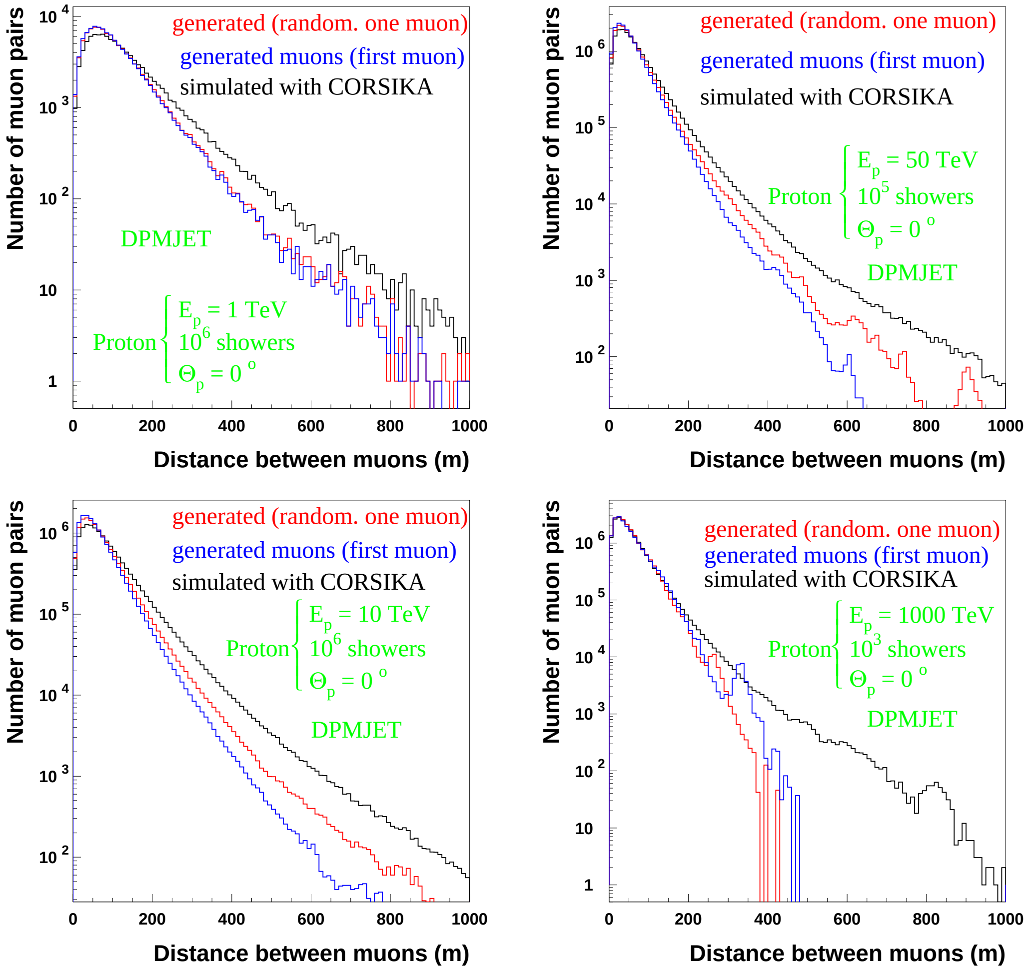

Figure 9: The distributions of distances between muons calculated in one shower, for showers simulated with CORSIKA (DPMJET) at $\theta = 0^0$ (black distribution), for showers generated with the HRNDM1 function that are filled with muons from the array formed by randomly selecting one muon from each CORSIKA shower (red distribution) and for showers generated with the HRNDM1 function that are filled with muons from the array formed by selecteding the first muon from each CORSIKA shower (blue distribution).

x and y coordinates of muons at 1 TeV

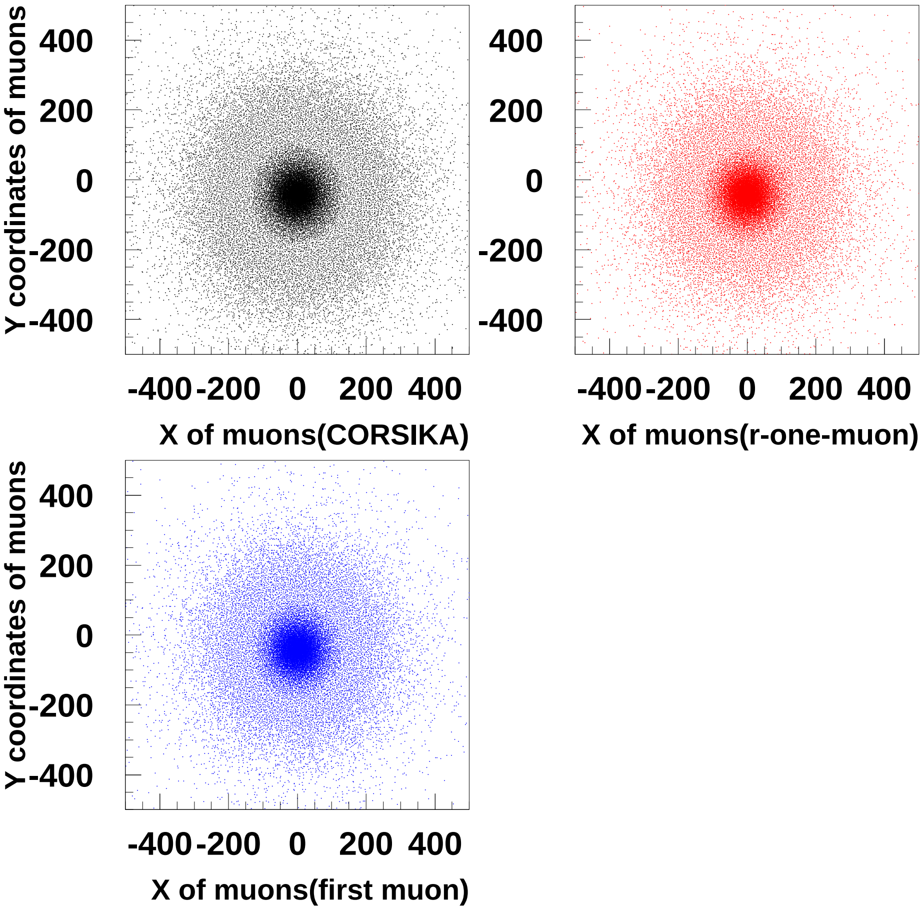

Figure 10: The x [m] and y [m] coordinates of muons for 10^6 primary vertical proton showers simulated at 1 TeV with CORSIKA (DPMJET) (black points), generated with the HRNDM1 function with muons from the array formed by randomly selecting one muon from each CORSIKA shower (red points) and generated with the HRNDM1 function with muons from the array formed by selecting the first muon from each CORSIKA shower(blue points).

x and y coordinates of muons at 1000 TeV

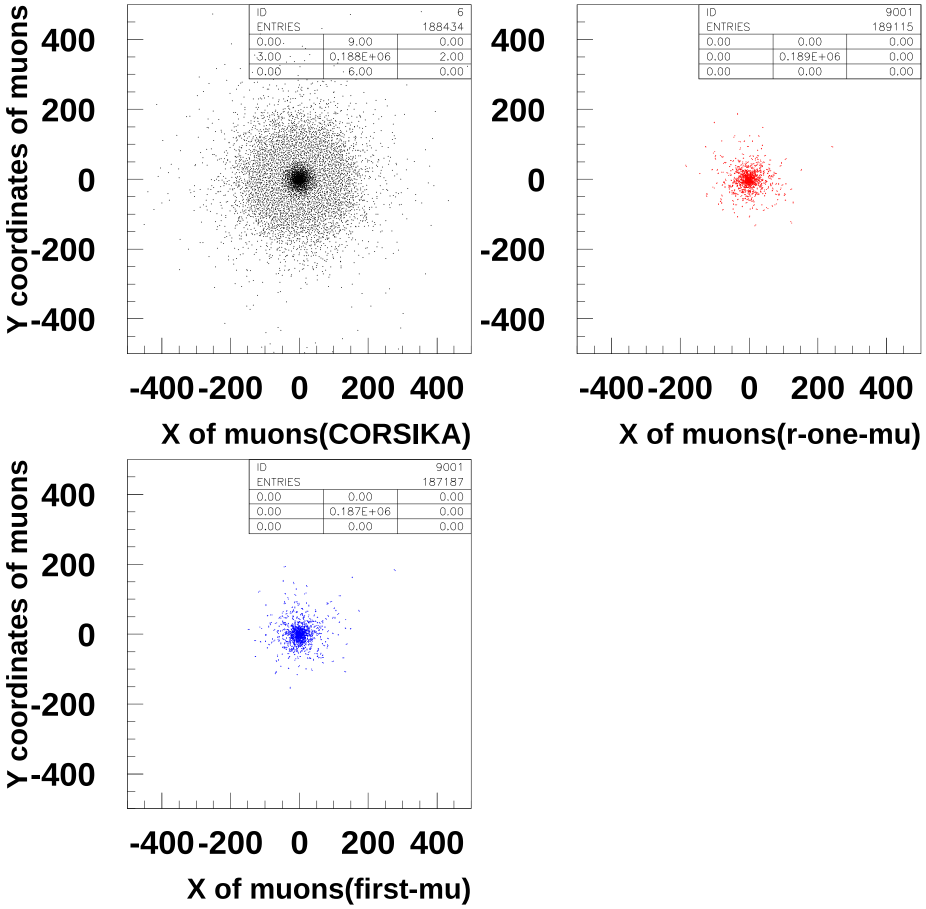

Figure 11: The x [m] and y [m] coordinates of muons for 10^6 primary vertical proton showers simulated at 1000 TeV with CORSIKA (DPMJET) (black points), generated with the HRNDM1 function with muons from the array formed by randomly selecting one muon from each CORSIKA shower (red points) and generated with the HRNDM1 function with muons from the array formed by selected the first muon from each CORSIKA shower(blue points).

From these plots it is observed that for both considered cases of generation of events with HRNDM1, the muons at 1000 TeV energy are concentrated near the shower axis, compared to those at 1 TeV, that is why in this method (second method), the red and blue lines for the distribution of muon distances do not cover the large muon separation interval compared to the CORSIKA distributions (black line) with increasing energy.

Thus, both methods with their particular cases demonstrate that the parameters of interest for this analysis, from which the decoherence distributions are produced using a very fast random function that reads CORSIKA simulated data, are strongly correlated.

A combination of these parameters which were sampled with the fast HRNDM random function from the CORSIKA distributions do not reproduce the initial CORSIKA results.

This analysis inspired the idea to use directly the CORSIKA results for the analysis of high energy muons underground. Details are presented in section 5.3.

Appendix B

Study of the Decoherence Distribution at different Overburdens with CORSIKA

The application of the overburden corrections to the measured coincidence rates is based on the assumption that the decoherence distributions at different depths (small variations of the depth in case of the CosmoALEPH experiment) are more or less identical. To understand and take into account the uncertainty of this assumption, a Monte Carlo study was performed.

According to the proposed method in the Chapter 5 for the analysis of the MC data, the decoherence distributions of muons underground at the depths 320 mwe (125 m), 311 mwe (121.5 m), 323 mwe (126.2 m), 327 mwe (127.734 m) were determined for proton showers simulated with QGSJET. Since the information of the overburden is not included in the MC analysis, different depths require a different energy cut-off, which is calculated according to equation (5.7).

The shapes obtained at different values of overburden were normalized to the reference shape of the decoherence curve at 320 mwe. For the ratios ($r_{327/320}$, $r_{323/320}$, $r_{311/320}$) of coincidence rates obtained at different distances up to 1 km, their deviation from unity was determined (see figure 1).

The next plots (figure 1) present the deviation of the obtained ratios from unity (r - 1) as a function of the distance between the detectors.

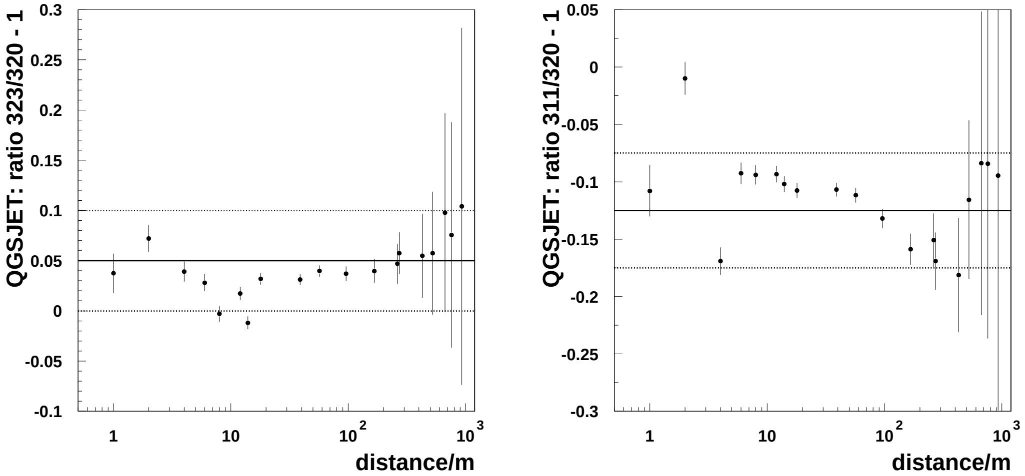

Figure 1: The deviation of the ratios $r_{323/320}$ and $r_{311/320}$ between the decoherence curves obtained at 320, 323, and 311 *mwe* from unity. The simulations were performed for proton showers with QGSJET in energy and zenith angle ranges specified in section 5.1. The errors represent only the statistical fluctuations.

From these plots one sees that there is a correlation between the calculated ratio and the distance between pairs of detectors. This dependence being pronounced at small distances up to 20 *m*. However, the effect is only observed at the level of a band of ± 5 %, clearly seen in each plot. A systematic shift on the y axis is also observed for the calculated ratios, which is expected because the normalization on the reference overburden of 320 *mwe* is performed for different values of the overburden.

To understand how the shape of the decoherence distibution will change for diferent MC models, the same analysis was performed using VENUS and SIBYLL for values of the overburden of 320 *mwe* and 327 *mwe* (see figure 2).

From this analysis it is seen that the observed fluctuations are present also in different MC models, but with the same effect of ± 5 % deviations from a constant shape for the decoherence curve at different values of overburden.

Based on these results, the errors of the overburden correction factors obtained for each scintillator station and ALEPH Hadron Calorimeter were increased by an additional uncertainty of 5 %, since the pairs of these detectors provide coincidence rates from 18 *m* up to 1 *km*.

For the coincidence rate at the small separation of 2.6 *m*, obtained from an independent measurement of cosmic muons in the Time Projection Chamber of the ALEPH detector, an additional error of 10 % is added, since the above analysis shows larger fluctuations at small distances in the decoherence curves at different values of overburden.

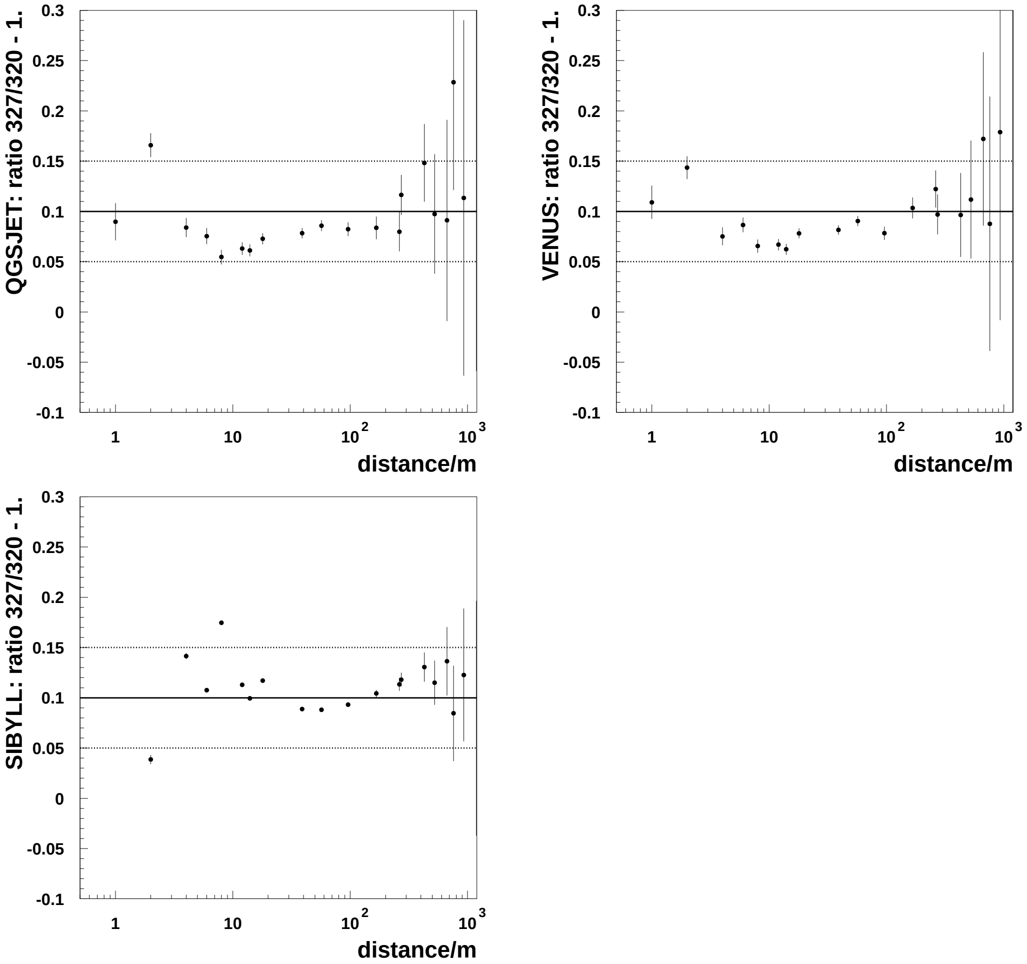

Figure 2: Deviation from unity of the ratio $r_{327/320}$ between the decoherence curves obtained at 320 and 327 *mwe*. The simulations were performed for proton showers with QGSJET, VENUS and SIBYLL in the energy and zenith angle ranges specified in section 5.1. The errors represent only statistical fluctuations.

Appendix C

Transverse Momentum Distributions for different MC Models

The muon transverse momentum was calculated with respect to the vertical incidence for simulated proton, helium and iron primaries with the QGSJET, VENUS, SIBYLL and NEXUS models for the constant mass composition approach.

The shapes of the transverse momentum distributions were fitted best, just as the decoherence distribution, with the Nishimura-Kamata-Greisen (NKG) formula:

$$f(P_t) = a \cdot \left(\frac{P_t}{P_{t_0}}\right)^b \left(1 + \frac{P_t}{P_{t_0}}\right)^c, \tag{9}$$

where a, b, c, and P_{t_0} are parameters obtained from the fit, and P_t [GeV] represents the muon transverse momentum underground at the depth of 320 *mwe*. This analysis reveals the evidence for the strong correlation between the transverse momentum and lateral spread of muons from the shower axis, both being sensitive to the chemical composition of primary cosmic rays.

In the next figures 1 and 2 the results of the fit with the (NKG) formula are presented. The values obtained for the free parameters are given in table 1.

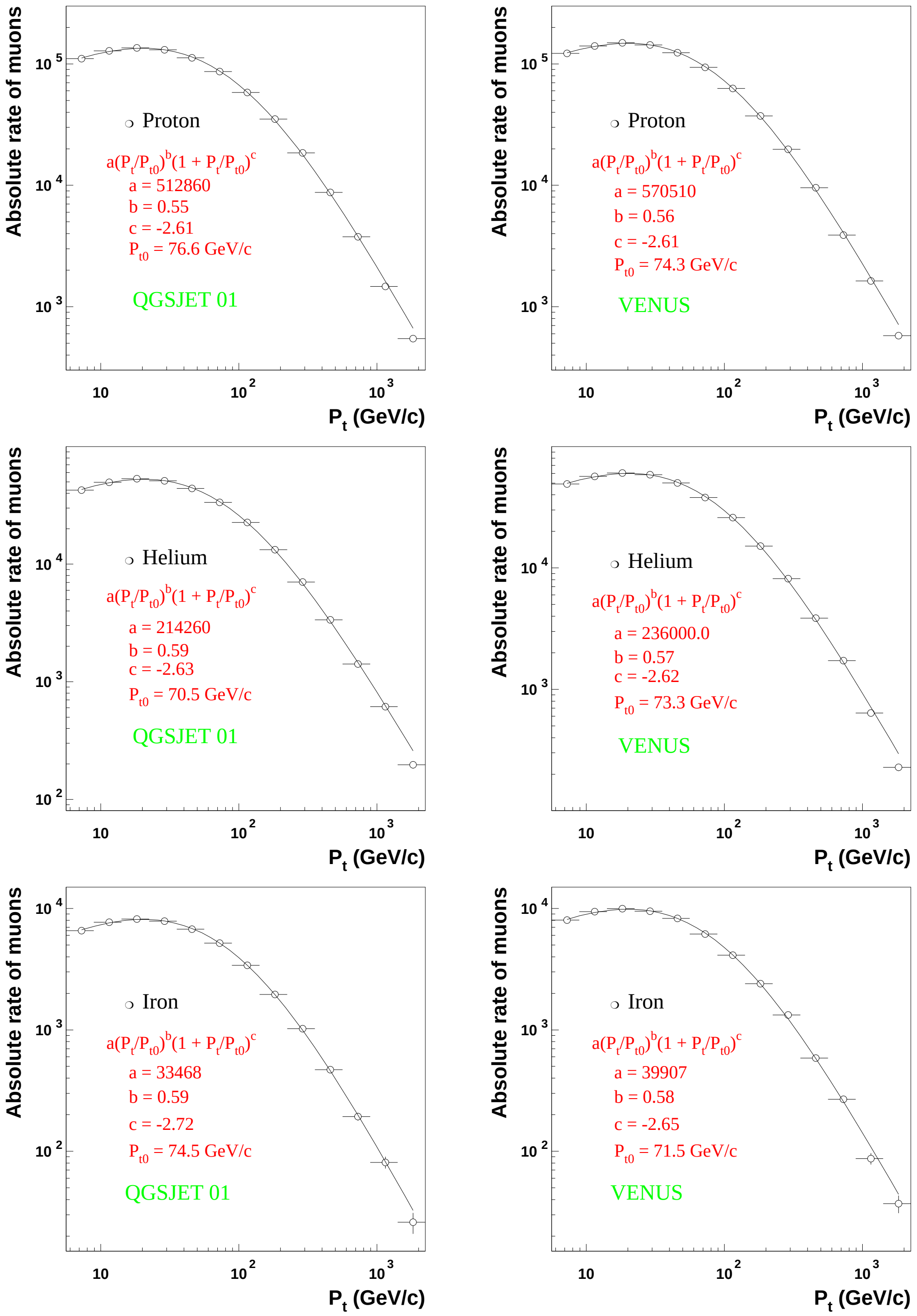

Figure 1: Muon transverse momentum distributions for p, He and Fe fitted with NKG for VENUS and QGSJET.

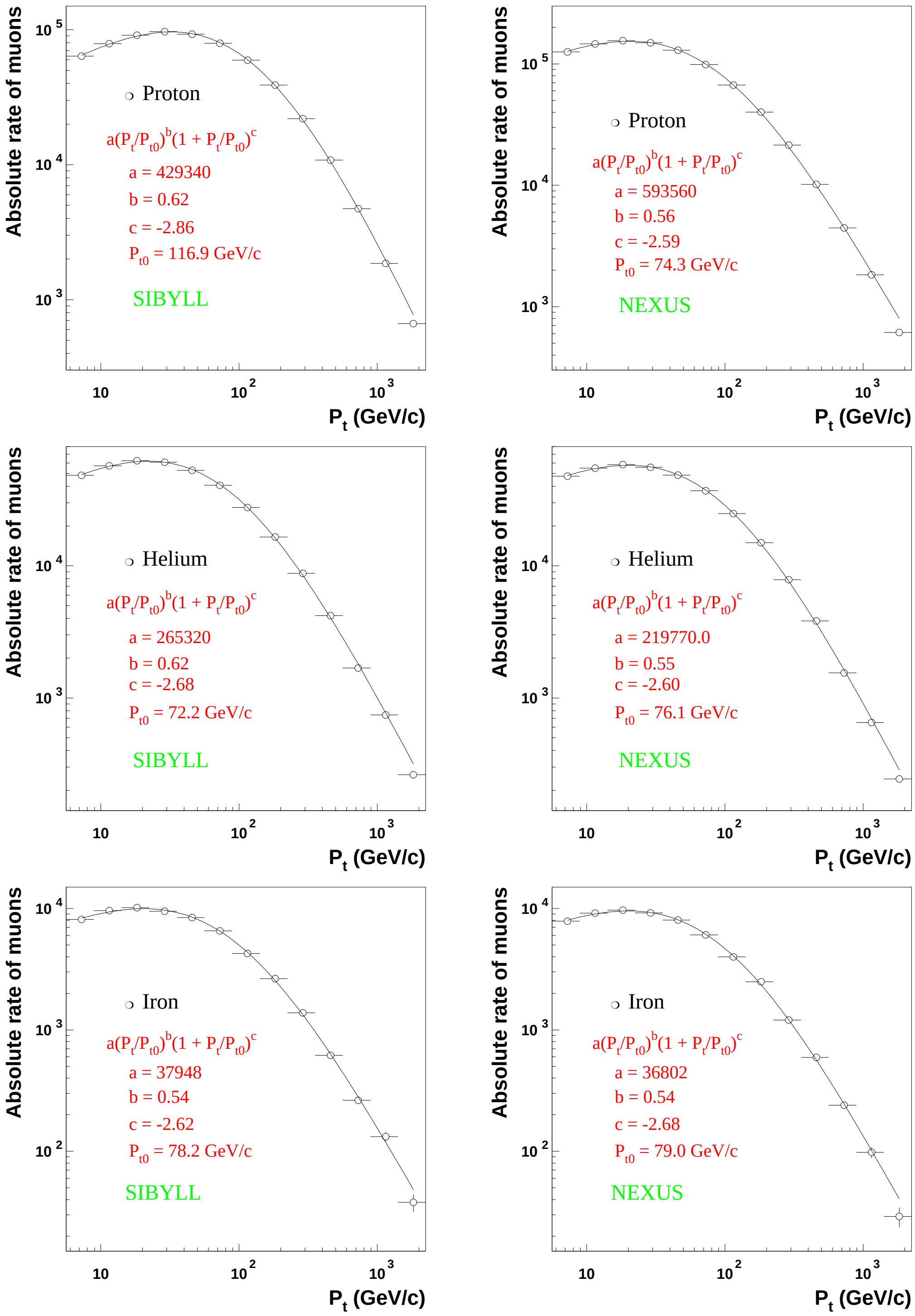

Figure 2: Muon transverse momentum distributions for p, He and Fe fitted with NKG for SIBYLL and NEXUS.

Model	**Elements**	**a**	**b**	**c**	P_{t_0} **[GeV/c]**
QGSJET	**proton**	**512860.0**	**0.546**	**- 2.609**	**76.559**
	helium	**214260.0**	**0.592**	**-2.626**	**70.474**
	iron	**33468.00**	**0.58484**	**- 2.718**	**74.480**
VENUS	**proton**	**570510.0**	**0.554**	**- 2.609**	**74.250**
	helium	**236000.0**	**0.567**	**-2.615**	**73.320**
	iron	**39907.00**	**0.584**	**- 2.653**	**71.497**
SIBYLL	**proton**	**429340.0**	**0.619**	**- 2.855**	**116.89**
	helium	**265320.0**	**0.624**	**-2.676**	**72.201**
	iron	**37948.00**	**0.542**	**- 2.623**	**78.213**
NEXUS	**proton**	**593560.0**	**0.558**	**- 2.591**	**74.279**
	helium	**219770.0**	**0.545**	**-2.602**	**76.082**
	iron	**36802.00**	**0.542**	**- 2.676**	**79.016**

Table 1: Values of the free parameters a, b, c, and P_{t_0} obtained from the fit with the NKG formula (5.21) of the shapes of the transverse momentum distribution of each element simulated with VENUS, QGSJET, SIBYLL and NEXUS for constant mass composition.

Appendix D

JULIA TPC Tracking Algorithm

The reconstruction of a segment track [126] in the TPC is performed in three steps. In the first step, "chains" are found. Chains are radially ordered sets of TPC pad coordinates which are consistent with the hypothesis of lying on the same helix. In the second step, the chains are combined to form so called "track candidates". A track candidate is a set of chains which is consistent with being caused by the same particle. The third step of the tracking is the fitting of all first half arcs of the track candidate. As a result, TPC tracks are formed.

The finding of a chain is performed in four steps:

- find three points consistent with the hypothesis of a helix
- assemble an as large as possible piece of the helix using numerical approximation
- perform a helix fit and use the result to find further points at larger chamber radii
- fit again and use the result to find further points at small chamber radii.

Each of these steps are described in detail in [126].

The linking of chains consists of two modules. The first one takes the decision concerning "who belongs to whom". The second module assembles and orders the chain coordinates to form track candidates. The order of the coordinates is arranged with increasing chamber radius for non spiraling tracks, and along the path of flight for spirals. In the latter case, the flight direction is deduced from the transverse momenta of the chains.

The tasks of the track fitting program are the evaluation of the exact helix parameters, the removal of badly measured points, and the detection of small angle kinks.

In the track fitting procedure five helix parameters are defined:

ω = inverse radius of curvature

$tan\lambda = \frac{dz}{ds_{xy}}$ = tangent of the dip angle

ϕ_0 = emission angle in the x, y plane at the point of closest approach to the z axis

d_0 = impact parameter in the x,y plane

z_0 = z coordinate at $x^2 + y^2 = d_0^2$.

For the determination of the helix parameters, the multiple scattering error is taken into account by increasing the errors on the coordinates according to the arc length within the TPC volume.

The logic built around the track fitting consists of:

- fit the track candidate without modification
- exclude up to two single points according to their contribution to χ^2 of the overall fit
- find a kink
- exclude up to two points by a maximization of the fit probability.

The exclusion of individual points according to their contribution to the value of χ^2 in the track fit simply means, the coordinate with

$$\frac{(r \cdot \phi_{measured} - r \cdot \phi_{fitted})^2}{\sigma^2_{r\phi,measured}} + \frac{(z_{measured} - z_{fitted})^2}{\sigma^2_{z,measured}} = maximum \tag{10}$$

is excluded from the list of points to be fitted.

Due to the uniform magnetic field inside the ALEPH detector, trajectories of charged particles are helices. The routine to fit a helix track consists of

- a circle fit in the x, y plane
- a straight line fit in the $s_{x,y}$, z plane.

The parametrizations, based on the radial structure of the TPC, are expressed for ϕ and z as

$$\phi = \phi_0 + (ssr - sst) \cdot \frac{\pi}{2} + ssr \cdot arcsin\left(\frac{\omega \cdot (r^2 - d_0)}{2 \cdot r \cdot (d_0 \cdot \omega - sst)} + \frac{d_0}{r}\right), \tag{11}$$

where

- $sst = 1$ if track bends clockwise seen from the origin, -1 otherwise
- $ssr = sst$ if the point belongs to the first half of the helix, -sst otherwise

The circle fit parameters are used to calculate the values for $s_{xy}(r)$ which are needed in the straight line fit:

$$s_{xy}(r) = \frac{2}{\omega} \cdot arcsin\left(\frac{\omega}{2} \cdot \sqrt{\frac{r^2 - d_0^2}{1+ \mid \omega \cdot r \mid}}\right) \ . \tag{12}$$

The straight line fit determines the quantities z_0 and $tan(\lambda)$ according to

$$z = z_0 + \frac{2}{\omega} \cdot tan(\lambda) \cdot arcsin\left(\frac{\omega}{2} \cdot \sqrt{\frac{r^2 - d_0^2}{1 - sst \cdot d_0 \cdot \omega}}\right) . \tag{13}$$

The track is fitted by minimizing the distance in the ϕ, z plane between the measured points and the helix curve with a χ^2

$$\chi^2 = \sum_{i,n_{points}} \frac{\phi_i^{fit} - \phi_i^{measured}}{\sigma_{\phi,i}^2} + \sum_{i,n_{points}} \frac{z_i^{fit} - z_i^{measured}}{\sigma_{z,i}^2} + \frac{\alpha^2}{\alpha_0^2} \tag{14}$$

which takes into account the multiple scattering angle α. α_0 is the expected value of α, which is given by

$$\alpha_0 \simeq \frac{0.0141}{p[GeV]} \cdot \sqrt{l} \ ,$$

where l is the length of the material in units of the radiation length.

Bibliography

[1] Grupen, C.: *Astroteilchenphysik*, Vieweg Verlag, 2000

[2] Friedlander, M.: *Cosmic Rays*, Harward University Press, Cambridge, Massachusetts, and London, England 1989

[3] Grupen, C.: *Astroparticle Physics*, Springer- Verlag, Berlin, Heidelberg, 2005

[4] Klaus Blaum, Hendrik Shatz: *Kernmassen und der Ursprung der Elemente*, Physik Journal, Februar 2006 5.Jahrgang, Deutsche Physikalische Gesellschaft

[5] http://www.albany.edu/faculty/rgk/atm101/magnet.htm

[6] D.J.Bird *et al.: Detection of a Cosmic Ray with Measured Energy Well Beyond the Expected Spectral Cutoff due to Cosmic Microwave Radiation*, astro-ph/9410067

[7] N.Hayashida *et al.: Updated AGASA event list above 4 x* 10^{19} eV, astro-ph/0008102 v1 7 Aug 2000

[8] S.P.Knurenko *et al.: Spectrum of cosmic rays with energy above* 10^{17} eV, astro-ph/0411484v1 17 Nov 2004

[9] A.V.Glushkov *et al.: Estimation of Primary Cosmic Ray Energy Registered at the Yakutsk Array*, 28th ICRC Tsukuba 2003

[10] http://www.srl.caltech.edu/ACE/$CRIS_SIS$/cris.html

[11] David B. Kieda: *Cosmic ray composition and muon decoherence at the knee of all-particle cosmic ray spectrum*, Dissertation, University of Pennsylvania, 1989

[12] Heck. D *et al.: CORSIKA: A Monte Carlo Code to Simulate Extensive Air Showers* FORSCHUNGSZENTRUM KARLSRUHE Report: FZKA 6019(1998)

[13] Gaisser, Th.K.: *Cosmic Rays and Particle Physics*, Cambridge University Press, Cambrdge, 1990

[14] Müller, Anke-Susanne: *Erste Untersuchungen ausgedehnter Luftschauer im LEP-Tunnel (CosmoALEPH)*, Diplomarbeit, Universität Mainz, 1996

[15] Hörandel, J.R.: *On the knee in the energy spectrum of cosmic rays*, arXiv:astro-ph/0210453v1, 20Oct2002

[16] Olinto, A.V.: *The origin of the Highest Energy Cosmic Rays*, The University of Chicago, IL 60697, USA

[17] Kampert, K.H. *et al.:Cosmic Rays in the Energy range of the Knee - recent results from KASCADE*, arXiv: astro-ph/0102266 v1 15 Feb 2001

[18] A.D.Erlykin and A.W.Wolfendale: *A single source of cosmic rays in the range* 10^{15} - 10^{16} eV, J.Phys. G:Nucl.Part.Phys. 23 (1997) 979-989

[19] V.I.Yakovlev: *On a possible role of the long-flying component in the seeming absence of the GZK cutoff*, Phys. of Elementary Particles and Atomic Nucleus 2005, T.36

[20] M.Thunman, G.Ingelman: *Charm production and high energy atmospheric muon and neutrino fluxes*, hep-ph/9505417 v1 30 May 1995

[21] Richard Wigmans: *PeV Cosmic Rays: A Window of the Leptonic Era?*, astro-ph/0205360 v2 29 Oct 2002

[22] Pieter L. Biermann and Günter Sigl: *Introduction to Cosmic Rays*, arXiv:astro-ph/0202425, 22Feb2002

[23] Wdowczyk, J., Wolfendale, A. W., Ann. Rev. Nuclear Part. Sci., 39, 43 (1989)

[24] D.J.Bird, *et al.: Evidence for Correlated Changes in the Spectrum and Composition of Cosmic Rays at Extremely High Energies*, Phys.Rev.Lett.,Vol 71, nr. 21, 22 Nov 1993

[25] John N. Bahcall and Eli Waxman: *Has the GZK suppression been discovered ?*,

[26] http://www.iop.org/EJ/article/1367-2630/6/1/140/njp4_1_140.html

[27] Boratav, M.: *Probing theories with cosmic rays*, Europhysics News (2002) Vol.33 No.5

[28] Grieder, P.K.F.: *Cosmic Rays at Earth*, ELSEVIER, 2001

[29] http://www.dsri.dk/ hsv/Noter/solsys99.html

[30] http://www.agu.org/*sci_soc*/cowley.html

[31] Astronomy Picture of the Day: http://antwrp.gsfc.nasa.gov/apod/ap991122.html

[32] http://hubblesite.org/newscenter/archive/1997/34/

[33] http://www.ast.leeds.ac.uk/haverah/dets.shtml

[34] http://imagine.gsfc.nasa.gov/docs/science/ know_l2/cosmic_rays.html

[35] Physik Journal, April 2006 5.Jahrgang, Deutsche Physikalische Gesellschaft

[36] Pijushpani Bhattachajee, Günter Sigl: *Origin and propagation of extremely high energy cosmic rays*, E-Preprint astro-ph/9811011 v2 22 Aug 1999

[37] http://www.engr.uky.edu/ gedney/courses/ee468/expmnt/escope.html

[38] http://www.physics.isu.edu/radinf/dectector1.htm

[39] http://icecube.wisc.edu/brochure/icecube_ brochure.pdf

[40] http://imagine.gsfc.nasa.gov/docs/science/*know*_l1/supernovae.html

[41] Thorsett, S.E.: *The Gravitational Constant, the Chandrasekhar Limit, and Neutron Star Masses*, arXiv:astro-ph/9607003v1, 1 July 1996 arXiv:hep-ph/0206217v5, 25Feb2003

[42] E.Fokitis *et al.: Optical Filter Design for the Fluorescence Detector of the AUGER Project*, JHEP Proceedings, 6th Hellenic School and Workshop on Elementary Particle Physics:, Corfu, Greece, 6-26 Sep 1998

[43] David Griffiths: *Introduction to elementary particles*, Reed College, 1987

[44] Enrico Fermi: *On the Origin of the Cosmic Radiation*, Physical Review Vol. 75, Nr.8, April 15, 1949

[45] http://csep10.phys.utk.edu/astr162/lect/neutron/neutron.html

[46] F.W.Giacobbe: *How a type II supernova explodes*, EJTP 6 (2005) 30-38

[47] Jean-Paul Meyer and Donald C.Ellison: *The origin of present day cosmic rays: Fresh SN Ejecta or Interstellar Medium material? I Cosmic ray composition and SN nucleosyntheses*, astro-ph/9905037 v1 5 May 1999

[48] J,W.Truran *et al.: Neutron Capture Nucleosynthesis in Early Galactic Environments*, to appear in *The First Stars*

[49] S.Goriely and L.Siess: *Nucleosynthesis of s-elements in zero-metal AGB stars*, Astronomy and Astrophysics 378,L25-L28 (2001)

[50] M.Busso *et al.: Nucleosynthesis in Asymptotic Giant Branch Stars: Relevance for Galactic Enrichment and Solar System formation*, Annu.Rev.Astron.Astrophys. 1999, 37:239-309

[51] http://fusedweb.pppl.gov/CPEP/chart_Pages/3.HowFusionWorks.html

[52] C.Morello for the EAS-TOP Collaboration: *Spectrum and mass composition of the cosmic rays around the knee*, Mem.S.A.It. Suppl. Vol. 9, 370, SAIt 2006

[53] S.M.Kasahara *et al.: A study of cosmic ray composition in the knee region using multiple muon events in the Soudan 2 Detector*, hep-ex/9612004 v1 5 Dec 1996

[54] J.W.Fowler *et al.: A measurement of the cosmic ray spectrum and composition at the knee*, astro-ph/0003190 v2 22 Jun 2000

[55] M.A.K.Glasmacher *et al.: The cosmic ray composition between* 10^{14} *and* 10^{16} eV, Astroparticle Physics 12 (1999) 1-17

[56] M.Ambrosio *et al.: High statistics measurement of the underground muon separation at Gran Sasso*, Phys.Rev.D 60 (1999) 032001

[57] J.Malinowski: *Mass composition of primary cosmic ray below the "knee" deduced from analysis of energy distribution of hadrons registered in the Pamir experiment*, 28th ICRC, Tsukuba, Japan, 31 Jul - 7 Aug 2003

[58] H.Tanaka *et al.: A study of nuclear composition of primary cosmic rays above 100 TeV*, 28th ICRC, Tsukuba, Japan, 31 Jul - 7 Aug 2003

[59] Peter L.Biermann: *Cosmic ray interactions and the abundances of the chemical elements*, astro-ph/9609110 v1 17 Sep 1996

[60] S.P.Swordy and D.B.Kieda: *Elemental composition of cosmic rays near the knee by multiparameter measurements of air showers*, astro-ph/9909381 22 Sep 1999

[61] A.D.Erlykin and A.W.Wolfendale: *The nature of the "knee" in the cosmic ray energy spectrum*, J.Phys.G: Nucl.Part.Phys.32 (2006) 1-7

[62] M.Amenomori *et al.: The energy spectrum of the light components (p + He) at the knee obtained by the Tibet air shower core detector*, 29th ICRC Pune (2005)00, 101-104

[63] K.Asakimori *et al.: Cosmic ray proton and helium spectra - results from the JACEE experiment*, LSU Space Science/Particle Astrophysics Preprint 11/3/97

[64] S.Ahlen *et al.: Study of the ultrahigh-energy primary-cosmic-ray composition with the MACRO experiment*, Physical Review D, Vol 46, Nr 3, 1 Aug 1992

[65] Gianni Navarra on behalf of the EAS-TOP Collaboration: *Study of cosmic ray primaries between* 10^{12} *and* 10^{16} eV *from EAS-TOP*, 28th ICRC, Tsukuba, Japan, 31 Jul - 7 Aug 2003

[66] H.T.Freudenreich *et al.: Study of hadrons at the cores of extensive air showers and the elemental composition of cosmic rays at* 10^{15} eV, Physical Review D, Vol 41, Nr 9, 1 May 1990

[67] J.A.Goodman *et al.: Composition of primary cosmic rays above* 10^{13} eV *from the study of time distributions of energetic hadrons near air-shower cores*, Phys.Rev.Letters, Vol 42, Nr 13, 26 March 1979

[68] J.Ahrens *et al.: Measurement of the cosmic ray composition at the knee with the SPACE-2/AMANDA-B12 detectors*, Astroparticle Physics 21 (2004) 565-581

[69] H.R.Adarkar *et al.: Cosmic ray composition from multiple muon data with the KGF underground detector*, Physical Review D, Vol 57, Nr 5, 1 March 1998

[70] Todor Stanev, Peter L.Biermann and Thomas K.Gaisser: *Cosmic Rays: IV. The spectrum and chemical composition above* 10^4 GeV, astro-ph/9303006 v1 11 Mar 1993

[71] A.A.Watson: *The mass composition of cosmic rays above* 10^{17} eV, astro-ph/0410514 v1 21 Oct 2004

[72] M.Ave *et al.: Mass composition of cosmic rays in the range* $2 \cdot 10^{17}$ - $3 \cdot 10^{18}$ *eV measured with the Haverah Park Array*, astro-ph/0203150 v1 10 Mar 2002

[73] A.A.Mikhailov *et al.: Estimate of the mass composition of ultrahigh energy cosmic rays*, 29th ICRC Pune (2005)00, 101-104

[74] James W. Cronin: *Cosmic rays: the most energetic particles in the universe*, Review of Modern Physics, Vol.71, No.2, Centenary 1999

[75] Claus Grupen: *Particle Detectors*, Cambridge University Press, 1996

[76] V. Avati *et al.,* Astropart. Phys. 19 (2003) 513

[77] Nadir Omar Hashim: *Measurement of the vertical cosmic ray muon momentum spectrum with CosmoALEPH*, Dissertation, University of Siegen, 2006

[78] V.Berezinsky: *Puzzles in astrophysics in the past and present*, astro-ph/0107306 v1 17 Jul 2001

[79] Meszaros, P.: *Theories of Gamma-Ray Bursts*, Annu. Rev. Astron. Astrophys. 2002 40, Preprint astro-ph/0111170

[80] Waxman, E. *et al.: Neutrino Afterglow from Gamma-Ray Bursts*, The Astrophysical Journal, 541:707-711, 2000 October 1

[81] Kotaidis, V., Mailov, A. *et al.:Measurements of the Lateral Distribution of the Muon Component of Extensive Air Showers Underground*, The 28th International Cosmic Ray Conference, Tsukuba, Japan, 31 Jul - 7 Aug 2003

[82] Haungs, A. *et al.:Estimate of the Cosmic Ray Composition by a pattern Analysis of the Core of PeV EAS*, 26th ICRC, Salt Lake City, Utah 1999

[83] Kampert, K.H. *et al.:The Physics of the Knee in the Cosmic Ray Spectrum*, Proceedings of ICRC 2001:1 Copernicus Gesellschaft 2001

[84] Hinton, J. A.: Ph.D. thesis, University of Leeds (1998).

[85] http//ast.leeds.ac.uk/ caw/pic_base/pic.html

[86] Kalmykov, N.N., Ostapchenko, S.S.: *The nucleus-nucleus interaction, nuclear fragmentation, and fluctuations of extensive air showers*, Yad. Fiz. 56 (1993) 105; Phys. At. Nucl. 56(3) (1993) 346

[87] Heck, D., Knapp, J., *Extensive Air Shower Simulation with CORSIKA: A User's Guide (Version 6.203 from February 25, 2002)*, FORSCHUNGSZENTRUM KARLSRUHE

[88] Heck, D. *et al.:Recent Additions to the Extensive Air Shower Simulation Code CORSIKA*, 26th ICRC, Salt Lake City, Utah 1999

[89] Knapp, J. *et al.:Extensive Air Shower Simulations at the Highest Energies*, Astroparticle Phys.19(2003)77: astro-ph/0206414

[90] Markus Risse, Dieter Heck: *Energy release in air showers*, Astroparticle Physics 20 (2004) 661-667

[91] R.Engel, T.K.Gaisser, and T.Stanev: *Extrapolation of hadron production models to ultra-high energy*, Proceedings of ICRC, Hamburg, Germany, 7-15 Aug 2001

[92] H.J.Drescher *et al.: Parton-based Gribov-Regge theory*, hep-ph/0007198 v1 18 Jul 2000

[93] S. Ostapcenko: *Enhanced diagrams in high energy hadronic and nuclear scattering*, hep-ph/0504164 v1 19 Apr 2005

[94] S. Ostapcenko: *QGSJET-II: towards reliable description of very high energy hadronic interactions*, hep-ph/0412332 v1 Dec 2004

[95] J.Ranft: *Dual parton model at cosmic ray energies*, Phys.Rev.D, Vol. 51, Nr.1, 1 January 1995

[96] J.Ranft: *Hadronic collisions: physics, models and event generators used for simulating the cosmic ray cascade at the highest energies*, hep-ph/0012171 v1 14 Dec 2000

[97] Heck, D. *et al.:Hadronic interaction models and the air shower simulation program CORSIKA*, Proceedings of 27th ICRC, Hamburg (Germany) 2001

[98] G.Bossard *et al.: Cosmic ray air shower characteristics in the framework of the parton-based Gribov-Regge model NEXUS*, Phys.Rev.D, Vol.63, 054030

[99] Heck, D.: *The Air Shower Simulation Program CORSIKA*, Contribution to Int. Workshop on 'Simulation and Analysis Methods for Large Neutrino Detectors', DESY Zeuthen (Germany), July 6 - 9, 1998

[100] Heck, D.: *Extensive air shower simulations with CORSIKA and the influence of high-energy hadronic interaction models*, Proc. XXX Int. Symp. Multiparticle Dynamics, Tihany (Hungary) 9-15 Oct. 2000, arXiv:astro-ph/0103073 v1 5 Mar 2001

[101] Antoni, T. *et al.:Test of Hadronic Interaction Models in the Forward Region with KASCADE Event Rates*, arXiv:astro-ph/0106494 v1 27 Jun 2001, J.Phys.G: Nucl. Part. Phys. 27 (August 2001) 1785-1998

[102] Antoni, T. *et al.:Test of high-energy interaction models using the hadronic core of EAS*, arXiv:astro-ph/9904287 v1 21 Apr 1999, J.Phys.G: Nucl. Part. Phys. 25 (1999)2161-2175

[103] Anchordoqui, L.A. *et al.:Hadronic interactions models beyond collider energies*, Phys.Rev. D59 (1999) 094003

[104] Alner, G.J. *et al.:A new empirical regularity for multiplicity distributions in place of KNO scaling*, UA5 Collaboration, Physics Letters, Volume 160B, number 1, 2, 3, 3 October 1985

[105] Alner, G.J. *et al.:Scaling violation in multiplicity distributions at 200 and 900 GeV*, UA5 Collaboration, Physics Letters, Volume 167B, number 4, 20 February 1986

[106] Forti, C. *et al.:Simulation of atmospheric cascades and deep-underground muons*, Physical Review D, Volume.42, Number 11, 1 December 1990

[107] Gaisser, Th.K., Stanev, T.: *Cosmic Rays*, Bartol Research Inst., University of Delaware, Revised March 2002

[108] D. Maier: *Zeitkorrelationen im erweiterten ALEPH-Experiment*, Diplom-Arbeit, Uni-Siegen, 1996

[109] Heiko Besier: *Die kosmische Strahlung und ihre Untersuchung im CosmoALEPH-Experiment*, Diplom-Arbeit, Uni-Mainz, 2000

[110] Sascha Schmeling: *CosmoALEPH Handbook*, 2000

[111] Michael Schmelling: *Overburden Corrections for CosmoALEPH*, MPI für Kernphysik, talk, Mainz,1 June 2006

[112] Michael Schmelling: *Efficiency determination for the scintillator stations*, private comunication, 2006

[113] Michael Schmelling: *Some CosmoALEPH Issues...*, 2006, Talk, Mainz

[114] A.-S.Müller and Michael Schmelling: *Efficiencies and Acceptances*, 2005, talk, Mainz

[115] The ALEPH Collaboration: *ALEPH Handbook 1995*, Vol 1, edited by Chris Bowdery

[116] A.-S.Müller: *Determination of HCAL efficiencies*, Institut für Synchrotronstrahlung, Forschungszentrum Karlsruhe, 2004

[117] Michael Schmelling: *The CosmoALEPH Decoherence Curve*, MPI für Kernphysik, August 9,2006

[118] Roland Caspar: *Der CosmoALEPH-Detektor zur Untersuchung ausgedehnter Luftschauer*, Staatsexamensarbeit, Mainz, November 2000

[119] Rodica Tcaciuc: *Systematishe Studien der Myonen-Komponente ausgedenter Luftschauer mit dem CORSIKA-Programm*, Master Arbeit, Universität Siegen 2003

[120] Arif Mailov, Private comunication, Universität Siegen, 2004 - 2006

[121] CERN Program Library Short write ups, CERNLIB, 1996

[122] Claus Grupen *et al.: Measurement of the muon component of extensive air showers at 320 m w.e. underground*, NIM A 510 (2003) 190-193

[123] Petr Travnicek and Arturo Fernandez: *Muon energy cut-off at the Aleph Cavern*, COSMOLHC-005, October 30th, 2000

[124] M.E.J.Newman: *Power laws, Pareto distributions and Zipf's law*, arxiv:cond-mat/0412004 v2 9 Jan 2005

[125] L.N.Bogdanova *et al.: Cosmic muon flux at shallow depths underground*, Institute for theoretical and experimental physics, Moscow

[126] J. Knobloch and P.Norton, *ALEPH 88-46*,Note 88-6, 1988

[127] R. Brun *et al.: CERN GEANT3 Users's guide*, DD/EE/84-1, 1992

[128] F.Ranjard: *GALEPH - Monte Carlo program for ALEPH*, Tech. Rep. ALEPH 88-119, ALEPH internal report 1988

[129] H.Albrecht, E.Blucher and J.Boucrot: *ALPHA: ALEPH physics analysis package*, ALPHA user's guide, 1995

[130] Michael Schmelling, Private comunication, MPI für Kernphysik, Heidelberg, 2006

[131] F.James: *MINUIT function minimization and error analysis*, CERN program library long writeup D506, Version 94.1, 1998

[132] Khaled Rasheed: *An adaptive penalty approach for constrained generic-algoritm optimization*, Department of Computer Science Rutgers, The State University of New Jersey, The Third Annual Conference on Genetic Programming (GP-98):Symposium on Genetic Algorithms (SGA-98), 1998